Exploring Surfactant and Plasticiser Segregation in Thin PVA Films

ARRON BRIDDICK

DURHAM UNIVERSITY

DEPARTMENT OF CHEMISTRY

Thesis

EXPLORING SURFACTANT AND PLASTICISER SEGREGATION IN THIN PVA FILMS

by

Arron Briddick

MChem., Northumbria University, 2013

Submitted for the degree of

Doctor of Philosophy

2017

i. Abstract

Surfactant segregation in solid polymer films is a little studied area of scientific research. This investigation launches an initial exploration into the behaviour of surfactant and plasticiser (glycerol) molecules in a poly(vinyl alcohol) (PVA) matrix. By understanding the nature of segregation within these systems, information regarding the compatibility of components can be gained. A greater understanding of what dictates compatibility and small molecule segregation in polymers is of importance to many industrial products and processes.

Using a series of ion beam analysis and neutron reflectometry experiments the segregation behaviour of three non-ionic, and two ionic surfactants is studied in great detail, both in binary non-plasticised and ternary plasticised PVA films. In order to use these techniques effectively, samples were mostly spin-cast, silicon substrate bound polymer films, of thickness <200 nm.

The non-ionic surfactants studied were a series of poly(oxyethylene glycol) alkyl ethers with a 12-carbon lipophilic tail-group ($C_{12}E_x$). Each of these surfactants exhibited spontaneous segregation to the air and/or substrate interface of the polymer film in binary films with PVA. Upon the introduction of plasticiser under ambient conditions, the amount of surface segregating surfactant is reduced, causing a greater concentration to be present in the bulk. However, when studied under relative humidity control the opposite effect is realised, and the presence of water in the films causes increased surfactant segregation.

The ionic surfactants studied are cetlytrimethylammonium bromide (CTAB) and sodium dodecyl sulphate (SDS). In binary films with PVA, CTAB shows no segregating nature, until glycerol is introduced, at which point substrate and surface segregation is induced. SDS shows development of significant surfactant-plasticiser multi-lamella structures on the surface of the thin films upon the introduction of the glycerol. SDS-glycerol structures like this, with interstitial regions of plasticiser stabilising the surfactant lamellae are unlike anything seen on the surface of a solid polymer film before. Both of these features infer a complex array of interactions with the plasticiser.

Surface energy and compatibility arguments are provided throughout to explain the diverse range of surfactant behaviours discovered in this work. Where surface energy is believed to be the driving force of surface segregation, with lower energy components segregating more, and compatibility to be the force which dictates how segregation behaves upon the introduction of plasticiser. Compatibility arguments are mostly comprised of the hydrogen bonding potential of the compounds within the films, where strong interactions between the polymer, plasticiser and surfactant give rise to increased compatibility, and therefore reduced segregation. Through this work, new, exciting information on the nature of small molecules in polymer systems is realised.

Some of this work has been published in Langmuir;

Briddick, A.; Li, P.; Hughes, A.; Courchay, F.; Martinez, A.; Thompson, R. L. Surfactant and Plasticizer Segregation in Thin Poly(vinyl alcohol) Films. *Langmuir* **2016,** *32* (3), 864-872.

DOI: https://doi.org/10.1021/acs.langmuir.5b03758

A few quotes from people I have grown to respect and admire through my interest in science…

"… star stuff contemplating star stuff …"
Carl Sagan, on humankind (1934 – 1996)

"Lack of comfort means we are on the threshold of new insights."
Lawrence M. Krauss (1954 – …)

"There's real poetry in the real world. Science is the poetry of reality."
Richard Dawkins (1941 – …)

"Everybody does have a book in them, but in most cases that's where it should stay."
Christopher Hitchens (1949 – 2011)

…I hope that's not the case with this one.

ii. Table of Contents

iii. List of Figures

iv. List of Tables

v. List of Numbered Equations

vi. Glossary of Common Abbreviations

%RH	-	Percentage relative humidity
µC	-	Micro Coulomb (electric charge)
A	-	Absorbance
AFM	-	Atomic Force Microscopy
AMU	-	Atomic mass units
$C_{12}E_5$	-	Pentaethylene glycol monododecyl ether
CMC	-	Critical micelle concentration
Conc.	-	Concentration
CTAB	-	Cetyltrimethylammonium bromide
D	-	Deuterium
DH	-	Degree of hydrolysis
DP	-	Degree of polymerisation
ERDA	-	Elastic recoil detection analysis
FTIR	-	Fourier transform infrared spectroscopy
Gly	-	Glycerol
h	-	Planck constant
H-bonding	-	Hydrogen bonding
HLB	-	Hydrophilic-lipophilic balance
HSP	-	Hansen solubility parameter
IBA	-	Ion beam analysis
IR	-	Infra-red spectroscopy
MeV	-	Megaelectronvolt
M_w	-	Molecular Weight
NR	-	Neutron reflectometry
NRA	-	Nuclear reaction analysis
PVA	-	Poly (vinyl alcohol)
PVAc	-	Poly (vinyl acetate)
Q	-	Scattering vector
QNM	-	Quantitative nanomechanical mapping
R	-	Reflectivity
R_a	-	Average roughness
RBS	-	Rutherford backscattering
RI	-	Refractive index
RPM	-	Revolutions per minute
R_q	-	Root means square roughness
RTP	-	Room temperature and pressure
s%	-	Percentage swelling
SDS	-	Sodium dodecyl sulphate
SE	-	Surface energy
SLD	-	Scattering length density
ST	-	Surface tension
T	-	Temperature
T_g	-	Glass transition temperature
Th	-	Thickness
Tm	-	Melting temperature
w%	-	Weight percentage

z*	-	Surface excess
δ (in IR)	-	Bending vibration
ΔG	-	Gibbs free energy
ΔS	-	Entropy
ΔT	-	Enthalpy
θ	-	Scattering angle
ν (in IR)	-	Stretching vibration
$\overline{\upsilon}$	-	Wavenumber

vii. Statement of Copyright

viii. Acknowledgements

First and foremost, I would like to give my sincere thanks to Dr. Richard Thompson, an infinitely caring, understanding and intelligent man who has been an excellent supervisor throughout the entire course of my doctorate. Without him, this project would not have been possible, and I am forever grateful to him for his support, and the opportunity he provided to work in his group.

I would also like to thank; Caitlin, for threatening my life in a way only a charming Glaswegian could if I didn't mention her name here, but also for being a top housemate during my PhD, despite the copious amounts of terrible TV and horror films you made me watch. Rose and Vicki, who I couldn't even separate into two sentences, because they're practically the same person, for being general annoyances, and great friends. Without these three, their constant mockery of my northern accent, the climbing, the wine, the cheese, as well as everything else, my sanity would have been a whole lot less intact, so thank you.

It goes without saying that I owe my family a great deal, despite neither of my parents having entered further education, their support of my aspirations to develop my scientific knowledge and interests to degree level and beyond has always been evident. To my mam, who has supplied me with endless cups of tea, and to my dad, who has been a ceaseless pain in my side, I would not have gotten this far without you, so you also have my eternal gratitude. Of course to my brothers, Shane and Curtis, who if nothing else, provide me with an impetus to be successful, even if it is just so I'm not the worst sibling.

To my other brothers, Andy and Kristian, who have been my closest friends for many years. Cheers for being there through it all, from secondary school, till now, you two have provided me with more backing and encouragement than I could have hoped for from ten friends. Not to mention the laughs (thought I better say something about you both being comedic geniuses or you wouldn't be happy), honestly couldn't ask for two better mates, thanks for everything lads! Cowen, you deserve a mention here too, even though you've moved to Australia, come back at some point yeah… JWC unite!

Without a doubt, the person who has bore the brunt of my thesis writing woes more than any other, has been Megan. You will hate reading this, but your constant support, terrible chat, and again cups of tea have made the final year of this PhD a much easier, more enjoyable experience than it would have been without you. I cannot thank you enough for your understanding nature over the course of this write-up, and yes, I felt as sick writing that as you did reading it.

Also to the Thompson group, especially Ste, who has always lent a hand wherever he could, cheers mate.

ix. Dedication

To Reason and Science

&

To nana Margaret

1. Introduction

Plastics, or polymers, are everywhere. With the number of roles polymers fill in our society having increased exponentially over the past half-century. Advances in polymer science have allowed us to do more than ever thought possible with these relatively simple materials. The prevalence of polymers is undeniable, and their practicality has led to the formation of enormous areas of research in to their characteristics and properties. Through these studies we can customise polymers to fit a seemingly endless range of applications, from stopping a bullet,[1] to carrying groceries.[2] Polymer films make up a large area of the market, ranging in thickness from sub-micron in applications such as protective coatings[3] to super-centimetre in products like acrylic glass.[4] More recently, their use as an encapsulation agent for detergent has been of interest to the industrial partners of this project (Procter and Gamble, P&G). When used in this process, they are termed 'liquid tablet' or 'liquitab'. Films present in liquitabs are usually 50-100 μm thick, and comprised of a series of compounds, primarily a polymer and plasticiser, but with some additional (proprietary) additives. No other material can yet provide the strength, flexibility and water solubility required for this role, other than a polymer, namely poly(vinyl alcohol) (PVA), however it cannot do this job alone.

As with many polymers in industry, we have not only learned to customise the properties of the polymers themselves, but learnt how additives can further this customisation, one such additive being plasticisers. Plasticisers have warranted extensive research of their own, finding and tuning their ideal compatibility to each polymer,[5] without them, and the desirable effects they have on polymeric properties, many applications could not be performed. Ever since plasticisers have been introduced however, there have been problems. Leaching, or blooming/migration of plasticisers from the medium in which they are dispersed has been an issue for a long time.[6] As plasticisers work most effectively when they are free to move throughout the polymer, keeping them from being lost to the environment, whilst maintaining their desired effects on polymeric properties is a significant problem. The amount of plasticiser added to each polymer for its specific role is precisely determined to provide optimum performance for the task the polymer is being designed for. Hence any change in this ideal, specific composition through plasticiser evaporation may affect the polymers performance negatively.

Whether a change in polymeric properties originates from plasticiser loss, or polymer degradation due to environmental factors such as heat, humidity, light, or the chemical environment in which it is placed, it is given the term 'aging'.[7] Generally, aging is considered an unwanted effect since maintaining product functionality for extensive lengths of time is of significant importance. Products made with PVA are sensitive to increased temperature and humidity, causing aging to be significantly accelerated.[8] Aging is especially problematic when the product contains a polymer-polymer weld, which is typically a seal formed between two, interdiffused polymer films, achieved by wetting of one film with a compatible solvent and pressing together. These seals generally become weakened through aging, which could lead to breakage, and ultimately, product failure. This weakening is may be due to aging in the polymer itself, as its macrostructure enters another conformation, facilitated by a change in environmental conditions.[9] It could also be loss of plasticiser, causing an increase in crystallinity, leading to the product becoming

more fragile.[10] A third possibility is migration of compounds from the environment into the film, which is changing the composition of compounds and therefore the polymeric properties, causing the seal to weaken. One or all of these factors could be contributing to aging and this project was tasked to investigate these phenomena. It is not the goal of the project to completely suppress aging however, as there are instances where polymer aging is positive, especially in PVA, biodegradability for example. A breakdown of the polymeric properties by microorganisms, yielding lower molecular weight molecules, is something PVA is capable of,[11] reducing its negative impact on the environment, another reason for it being used in washing applications.

The chemical environment in which a polymer finds itself can play a role in aging, i.e. migration of compounds in to a film. The detergent PVA is used to encapsulate is a complex mixture of surfactants, water softeners, bleach, enzymes, brighteners, fragrances and many other agents. Hence the chance of any one of these compounds having the ability to penetrate the PVA film and change the ideal composition within it is high. Surfactants, the main constituent of detergents, have been shown to migrate, segregate and form complex structures in both solutions and polymers at interfaces.[12-13] Although the interactions between polymers and surfactants in solution have been well-documented in the literature,[14] their interactions in a solid polymer matrix have received relatively little attention. Surfactant migration and aggregation at polymer surfaces is necessary for many industrial applications, as it provides a route by which to functionalise polymer surfaces. Migration of surfactants, which can be relatively dangerous chemicals,[15] to polymer surfaces is also a concern for any consumer-facing product. Not only are surfactants possible health-risks when present in high concentrations, they also possess the ability to form a literal barrier at interfaces. Formation of a surfactant lamellar may hinder the binding potential of any polymer situated either side of the surfactant nanostructure, so there may be some negative effect on polymer seal strength also. This project aims to explore and expand the research area surrounding surfactant segregation in polymer films through experimental investigation of several surfactants' behaviour in polymer matrices, under a variety of environmental and chemical conditions. Through the use of incredibly sensitive techniques such as ion beam analysis and neutron reflectometry, precise spatial resolution of surfactant distribution in polymer films is achieved unlike ever before. This new evidence for the diversity and complexity of surfactant behaviour in polymer films, along with rationalisation of this behaviour through surface energy and compatibility arguments has helped to understand some of the stimuli which control surfactant segregation. A review of the literature surrounding this project is given in the following chapter.

2. Literature Review

2.1. Poly (vinyl alcohol)

The prevalence of poly (vinyl alcohol) (PVA) across a diverse range of industries in today's society is no surprise considering the unique advantages over other polymers it has. Few polymers exhibit the degree of water solubility that PVA does with as little toxicity[16] or as impressive film forming capability.[17] These properties, as well as its resistance to organic solvents and biodegradability[18] have led to PVA being utilised in the food packaging and medical industry, as well as more recently in the laundry industry. There are many examples of medical applications, including implantable and non-implantable devices[19-22] that exploit the polymer's biocompatibility. PVA's primary use in the food packaging industry is the prolonging of food lifetime through production of an airtight seal, preventing contamination. The aforementioned properties combined make PVA the perfect polymer for use as an encapsulation product for detergents and powders in the laundry industry. Companies like the industrial partners of this project (Procter & Gamble) utilise PVA to form a casing around detergent formulations which will dissolve completely when washing with water, and will not cause any source of contamination or threat to biological life when it is drained from the washing machine and flushed away.

2.1.1. Synthesis of PVA

PVA is synthesised from a vinyl acetate monomer as the vinyl alcohol monomer is thermodynamically unstable and tautomerises to acetaldehyde under atmospheric conditions (Figure 2.1.).[23] At room temperature, acetaldehyde is significantly more stable than vinyl alcohol, by 45 $kJmol^{-1}$,[24] hence polymerisation of vinyl acetate must be performed. This is usually done by way of free radical polymerisation,[25] with many initiators, for example potassium peroxydisulfate,[26] being studied to produce poly(vinyl acetate) (PVAc).[27] PVAc synthesis is followed by hydrolysis to achieve PVA, meaning PVA is generally a co-polymer of converted hydroxyl –OH and residual acetate $-OC(=O)CH_3$ groups. Several synthetic routes to hydrolyse PVA have been established, but the main method used in industry is saponification with an aqueous salt solution (Figure 2.2.).[28-30] This method yields PVA of the least toxicity, a quality important in consumer products. The percentage of converted acetate groups is termed the degree of hydrolysis (DH). Although PVA synthesis is not a simple 'one step' reaction mechanism, this process does afford some advantages, as alteration of the DH allows customisation of polymeric properties. The degree of polymerisation (DP) of the original PVAc also plays a large role in polymeric characteristics, as it does with all polymers. Some relationships of polymeric properties to DH and DP are discussed below.

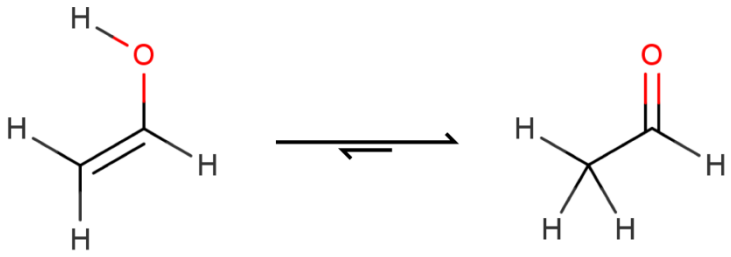

Figure 2.1. MarvinSketch of the favourable tautomerisation of vinyl alcohol to acetaldehyde.

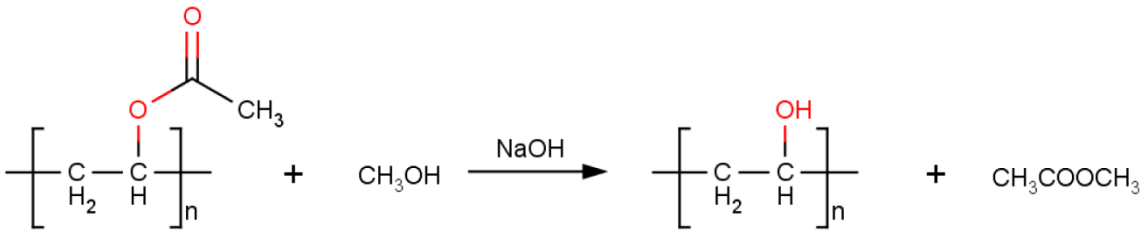

Figure 2.2. Saponification of poly(vinyl acetate).

2.1.2. Physical Properties of PVA and Hydrogen Bonding

As with most properties of PVA, examples of which are solubility, crystallinity, surface energy, tensile strength, elasticity, etc., they are governed by the type and number of hydrogen bonds available for interaction, for example PVA's solubility in water is dependent on DH, temperature and degree of polymerisation (DP).[31] With each one of these factors in some way affecting hydrogen bonding (H-bonding) potential. H-bonding arises when a hydrogen atom is covalently bound to a highly electronegative atom, in this case oxygen, which causes a distortion of the electron cloud surrounding the bond, pulling it towards the electronegative atom (Figure 2.3.). Once the electron cloud is distorted the bond becomes dipolar, having a partially negative (δ-) and partially positive (δ+) end, if a neighbouring molecule also contains a dipole, when opposing charges align an electrostatic attraction is formed.[32] Hydrogen bonding is considered one of the strongest forms of intermolecular forces, with only ion-ion interactions considered stronger. Strong H-bonds are responsible for the unique properties of water such as high surface tension, giving an intermolecular bond strength of 23.3 kJmol^{-1},[33] which is significant considering the bond dissociation of the HO-H bond in water is only 492.2 kJmol^{-1} (converted from 41145.94 cm^{-1}).[34]

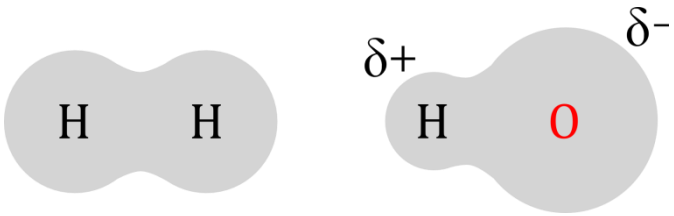

Figure 2.3. Schematic representation of electron cloud distortion caused by electronegative oxygen atom

PVA is capable of significant H-bonding as each monomer contains a strongly polar hydroxyl group. Higher DH resins (> 95%) exhibit increased H-bonding and therefore increased crystallinity as the stereo-regularity of the polymer chains is less disrupted by the presence of the larger acetate groups, allowing significantly more intra/inter-molecular hydrogen bonding (Figure 2.4.).[35] PVA is one of the few polymers capable of exhibiting high crystallinity because of its H-bonding potential.[36] It is has been shown to be approximately atactic, which would normally lead to little crystallinity, but as the size of the hydroxyl functional group is so small, it allows dense packing of the polymer chains and causes increased crystallinity.[37] Indirectly related to crystallinity is the glass transition temperature (T_g), which is the temperature above which amorphous materials transition from a glassy to a rubbery state, exhibiting increased flexibility and softness.[38] This has been shown to be 85 °C for high DH PVA and 58 °C for partially hydrolysed (87-89 %DH) PVA,[39] hence the polymer will exhibit increased flexibility at lower DH, again a factor of the reduced H-bonding. Density is another factor influenced by DH; completely amorphous PVA has a density of 1.19 gcm^{-3}, whereas a completely crystalline resin will have a density of 1.31 gcm^{-3}.[39-40]

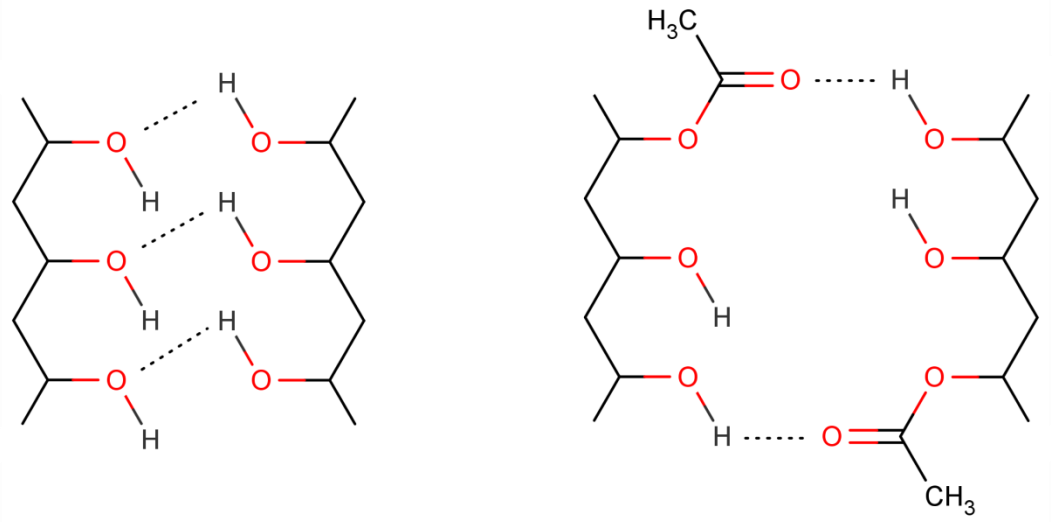

Figure 2.4. Schematic representation of increased H-bonding with high DH PVA (left) and reduced H-bonding with presence of acetate groups (right). Middle bond is not possible due to increased distance between oxygen and hydrogen on opposing chains.

Solubility is one of PVA's most important properties as it is essential not only for film forming but for most of the roles it is tasked to do. PVA has been shown to be soluble in hydrophilic, high polarity solvents such as water, ethylene glycol (EG) and dimethyl sulfoxide (DMSO).[41] Water is the most relevant solvent for this study hence the properties of aqueous PVA are reviewed in greater detail. Solubility is another property which is directly linked to the polymers H-bonding potential with lower DH resins (< 95%) showing a significant increase in solubility, caused by the hydrophobic acetate groups weakening the intra/intermolecular H-bonding between adjacent polymer chains.[42] Solubility has also been shown to decrease with increasing DP for several polymers including PVA,[43] hence with increasing DP greater heating and stirring is required to achieve complete dissolution. Although the total number of hydrogen

bonds in solution remains constant per kg of polymer regardless of polymer molecular weight, the entropy of mixing is greater for lower molecular weights.[44] This is due to the increased number of configurations possible with smaller chains. Unfortunately mechanical properties required for optimum product performance, such as tensile strength are also reduced at lower molecular weight,[45] so a compromise between solubility and practicality must be achieved. Decreased solubility for high DH/DP chains can be overcome by increasing the heat of the solvent, this will provide enough energy to disrupt the hydrogen bonds and hence cause dissolution. However, in laundry applications, there is increasing pressure to make formulations that can be used at low wash temperatures, hence lower DH resins tend to be used.

The surface tension (ST) of dilute, aqueous, PVA solutions has also been directly correlated to DH and DP. Degree of hydrolysis has been shown to decrease the ST as it is reduced, ranging from ~65 mNm^{-1} for a 98-99 %DH polymer to ~45 mNm^{-1} for a 87-89 %DH polymer in a 0.5 w% solution.[46] Decreasing the DP also reduces the ST in aqueous solutions. The surface tension of PVA as a function of structure could be important since it will impact the adsorption of other additives to the PVA surface.

A way of customising these properties of PVA is with the addition of a plasticiser, the addition of plasticisers allows PVA to be used in a number of applications including the aforementioned production of water-soluble, transparent, tough and tear-resistant packaging for detergent encapsulation.

2.1.3. Plasticisation and the Free Volume Theory

Plasticisers are used to infiltrate the polymer matrix, disrupting the non-covalent linkages between polymer chains and hence increasing the space between them.[47] This space is known as free volume. the free volume theory was first put forward by Fox and Flory[48] as a means to explain the reduction of polymer glass transition temperature with the addition of plasticizer. The pair first linked the M_n of polymers to T_g, and therefore free volume, constructing what is now known as the Flory-Fox equation;

$$T_g = T_{g,\infty} - \frac{K}{M_n}$$

Equation 1

where $T_{g,\infty}$ is the maximum T_g that can be achieved at a theoretical infinite molecular weight and K is an empirical parameter related to free volume. It can be seen from this that increasing the molecular weight of a polymer would lead to a larger T_g, this was explained using the free volume around polymer chain-ends. Figure 2.5. displays the free volume associated with a polymer chain-end and monomer, which illustrates the situation where the free volume associated with a chain-end is larger than that for a monomer unit. Therefore by decreasing the molecular weight of the polymer whilst maintaining the total mass the number of chain-ends in the system is increased, this causes an increase in the total free volume between the polymer chains, hence reducing intermolecular interactions and lowering the T_g.[49] Under these circumstances, the constant, K in Equation 1 is positive, which is normally the case,

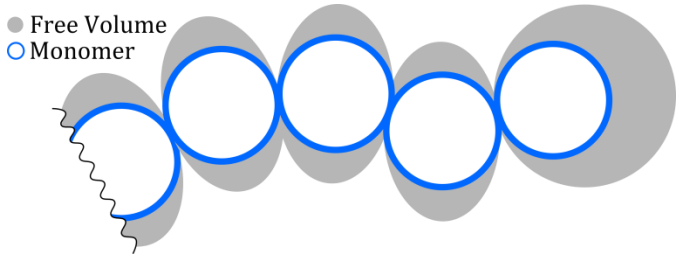

Figure 2.5. Schematic representation of increased free volume at polymer chain ends compared to within the chain, wavy line represents continuation of polymer chain

The addition of glycerol to PVA has been shown to also increase the free volume of the polymer,[50] promoting chain mobility and disrupting H-bonding, and therefore causing T_g to decrease too. The plasticised polymer therefore exhibits increased flexibility and lower tensile strength than the pure polymer.[51] This makes the polymer more malleable and hence easier to manipulate, having significant advantages in applications where flexibility is required. The most common plasticiser used with PVA is glycerol, (or propane-1,2,3-triol) with the formula $C_3H_8O_3$.[52] This is the most suitable plasticiser for PVA due to its low molecular weight, high polarity and large potential for intermolecular hydrogen bonding, as well as low toxicity. These characteristics increase the free volume of a PVA system when introduced, causing the polymeric network to become less dense due to the decrease in intermolecular (PVA-PVA) H-bonds, hence improving the flexibility of the polymer.[53] The physical properties of the plasticiser are critical in determining its compatibility with a polymer and specific care has to be taken with plasticiser selection. There have been several theories put forward for the reasons behind plasticiser selectivity, compatibility with the polymer and the overall mechanism of plasticization. One of which is the Flory-Huggins[54-55] solubility parameters, these can be used to predict polymer-plasticiser compatibility in the same way as they are used for predicting polymer-solvent interactions, using the equation below;

$$\ln a_1 = \ln(1 - v_2) + \left(1 - \frac{1}{x}\right) v_2 + \mu v_2^2$$

Equation 2

where v_2 is the polymer volume fraction, x is the volume ratio between polymer and solvent molecule, and μ is a semi-empirical constant. It was shown that if μ exceeds a critical value, usually between 0.5 and 0.55 for most polymers then phase separation will occur. Even if μ is < 0.5 for a system and the two compounds exhibit sufficient compatibility and mixing initially, due to the mobility of small plasticisers in large polymer matrices this state is not stable for an infinite amount of time as plasticisers have the potential to be lost to the atmosphere with time.[56-57]

Plasticiser migration and loss to the environment is a significant problem for any polymer system which contains a plasticiser.[58] Not only will the physical properties of the polymer be affected by a change in plasticiser concentration, but in some applications if toxic or environmentally hazardous plasticisers are used, leaching of these from the polymer matrix over time is a significant health risk. There has been interest in ionic liquids as plasticisers due to their low volatility, however most are likely too toxic and expensive for laundry applications.[59] The phenomenon of plasticiser migration has received

much attention in the medical and food packaging industry[60] due to the toxicity of some plasticisers. If a toxic plasticiser is present then monitoring of the plasticiser's migration patterns is of considerable concern to health agencies as they aim to avoid contamination of food and medical equipment. This has led to the investigation of many routes to immobilise plasticisers whilst also maintaining the desired physical properties.[61-63]

Plasticizer loss from PVA can take three main forms; evaporation through the surface-air interface,[64] extraction through contact with a liquid (solvent, oil, or water),[65] or migration in to a neighbouring non-plasticized polymer.[66] Loss via evaporation is the only mechanism of direct concern to the samples analysed in this project, as the polymer films are not placed in direct contact with liquid or solid environments, but are exposed to various gaseous atmospheres. The rate of evaporation at the surface-air interface depends on the partial pressure of plasticizer vapour over the film surface. The relative partial vapour pressure (ratio of pressure above the system to the presence over the pure plasticizer) increases with concentration, if the vapour pressure over a polymer/plasticizer blend is nearing that over the pure plasticizer this indicates poor compatibility or a high concentration of plasticizer.[66] The amount of plasticizer present above the system is largely influenced by the volatility of the plasticizer; a volatile compound will evaporate rapidly, causing a decrease in the amount of plasticizer at the surface-air interface. This causes a concentration gradient which facilitates the migration of additional plasticizer to the surface and out of the matrix, decreasing the mechanical function of the blend.[67] Plasticizers are generally chosen to have a high boiling point (BPT) so evaporation is slow; the rate of evaporation (W) can be calculated from the Hertz equation;[68]

$$W = \frac{p}{\sqrt{2MkT}}$$

Equation 3

where p is partial pressure of the plasticizer at temperature T, M molecular weight of the plasticizer and k is the rate constant of transfer of low M_w substance from material. As the BPT of a liquid is inversely proportional to the vapour pressure,[69] it can be seen from Equation 3 that molecules with a high BPT will give a low vapour pressure, and hence a slower rate of evaporation (W). The BPT for glycerol is 290 °C,[70] hence plasticiser evaporation should not occur readily at room temperature. When plasticizer deposition does occur at the solid-gas interface prior to evaporation however, the process is known as blooming. Here small amounts of plasticizer are deposited on the surface of the polymer; in severe cases of incompatibility small droplets can be observed.

Water can also act as a plasticiser,[50] which is generally present in polymer films either by being retained from processing or absorbed from the atmosphere. As the boiling point of water is lower, and the compound is also lighter, it would be expected that the rate of evaporation for water from a polymer matrix would be significantly faster than glycerol. As both glycerol and water are non-toxic, leaching of the plasticiser in to its environment bares no safety risks; it is only the effects on the mechanical properties of the polymer which is of concern. If plasticiser is lost from the matrix it may create regions of insufficiently plasticised polymer, which in turn will lead to non-ideal physical properties such as a decrease in impact strength. This means the polymer will be more brittle, and may lead to increased

susceptibility to rupturing during movement heavy processes such as transport. Migration within a polymer matrix has also been shown to be an issue for another group of compounds, surfactants.

2.2. Surfactants

Surfactants, whose name is derived from "surface active agents", are relatively small compounds (<500 $gmol^{-1}$) in comparison to polymers. They are comprised typically of a hydrophilic head-group and hydrophobic tail-group. The tail-groups of surfactants are usually simple hydrocarbon chains which are greater than 10 carbons in length, making them lipophilic. It is the difference in hydrophilicity of these two regions that enable their use as detergents, where the lipophilic tail-group binds to oily substances such as greases, leaving the hydrophilic head group exposed. Upon rinsing with water the head-group is solubilised, taking the tail-group and oily residue with it, hence removing the stain.[71] Generally the head-groups of surfactants contain more functionality, with a wide variety of possible moieties; these can fall in to one of four groups, non-ionic, cationic, anionic or zwitterionic (amphoteric). In contrast to the tail-group the head-groups are generally have high polarity (hydrophilic), giving them good compatibility with polar solvents.[72] The size and composition of the head-group is key to determining surfactant functionality, they can range from relatively short and bulky head-groups, like the ones found in sodium dodecyl suphate (SDS) to longer, more chain-like head-groups, such as the one present in pentaethylene glycol monododecyl ether ($C_{12}E_5$) (Figure 2.6.). Both of these surfactants, as well as cetyltrimethyl ammonium bromide (CTAB), plus variants of the non-ionic $C_{12}E_4$ and $C_{12}E_6$ are studied in this project.

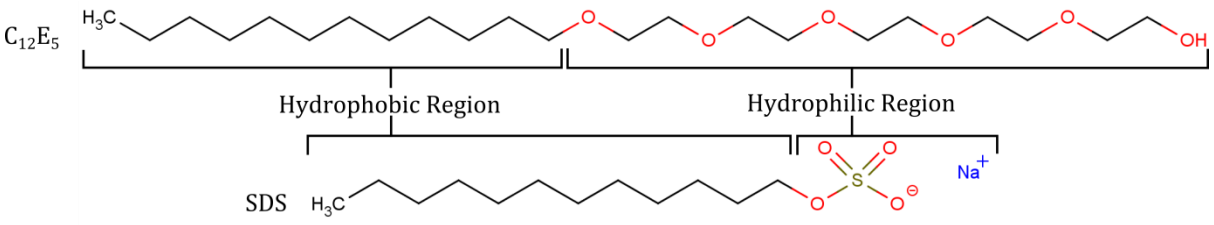

Figure 2.6. Hydrophobic tail-groups and hydrophilic head-groups of $C_{12}E_5$ and SDS

The molecular weight relationship between the head and tail group is given the name hydrophilic-lipophilic balance (HLB). HLB has been shown to be an insightful parameter when defining properties such as solubility[73] and the oil-water partition coefficient (KWO)[74] of surfactants, which are essential in determining a surfactant's suitability to its task. For non-ionic surfactants, HLB is given by the Griffin equation;

$$HLB = 20 \cdot \frac{M_h}{M_w}$$

Equation 4

where M_h is the molecular mass of the hydrophobic portion of the molecule and M_w is the molecular weight of the entire molecule. Higher HLB surfactants are therefore more hydrophilic, and lower more

lipophilic. For ionic surfactants, the Griffin method has been shown to be less accurate, and instead the Davies method is preferred;[75]

$$HLB = 7 + \sum_{i=1}^{m} H_i - n \times 0.475$$

Equation 5

where; m is the number of hydrophilic groups, H_i is the value of the ith hydrophilic groups (from literature) and n is the number of lipophilic groups in the surfactant. There exists a general scale for HLB which can be used to determine what applications a surfactant is likely to be effective in (Figure 2.7.).[76] The HLB for the surfactants used in this study are given in Table 2.1. As can be seen the HLBs for the non-ionic surfactants are generally higher than the ionic surfactants, making them more suitable for use as detergents.

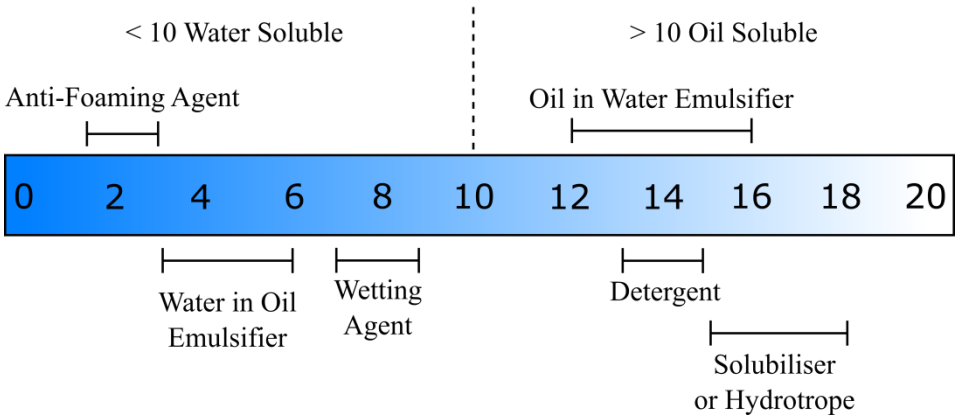

Figure 2.7. Griffin[77] HLB scale to determine surfactant functionality

Table 2.1. HLB of surfactants used, (NI) – non-ionic, (I) – ionic

Surfactant	HLB
$C_{12}E_6$ (NI)	12.5
$C_{12}E_5$ (NI)	11.7
$C_{12}E_4$ (NI)	10.7
SDS (I)	8.3
CTAB (I)	6.9
SDBS (I)	5.9

2.2.1. Surface Adsorption and Segregation

As the name suggests, surfactants are very surface active, meaning that they accumulate at surfaces and interfaces. This property can be described through surface tension arguments. Surface tension is defined as the excess surface free energy per unit area, or the minimum amount of work required to create a new unit are of the interface. In a simple homogeneous liquid-air system, the cohesive forces shared with neighbouring molecules are equal for those in the bulk as they are surrounded evenly in all directions. Liquid molecules at the surface however have no neighbouring liquid molecules above them, and hence bonds must be broken to increase the surface area. The work required to do this defines the surface tension. This increase in attractive forces is what defines surface tension.[78] Surfactants are surface active in aqueous solutions because their hydrophobic portions have an unfavourable interaction with the polar solvent, hence it requires less energy for a surfactant molecule to migrate to the surface, than it does a water molecule. Therefore migration will happen spontaneously, in order to minimise contact of the hydrophobic tail-group with the polar solvent the surfactant will orientate itself with the tail-group pointing out of the liquid-air interface.[79] As migration progresses and the concentration of surfactant at the interface increases a monolayer is formed, this causes an energetically favourable reduction in the surface tension at the interface (Figure 2.9.). If the concentration of surfactant is sufficiently high, then surfactant structures within the bulk begin to form, the concentration at which this happens varies regarding surfactant structural properties, (HLB, polarity, etc.) and is termed the critical micelle concentration (CMC).[80] This point is clearly visible on a plot of concentration versus surface tension (Figure 2.8.), as the point at which the surface tension is no longer reduced with increasing surfactant concentration. This is because increasing the surfactant concentration about the CMC has little effect on the activity.

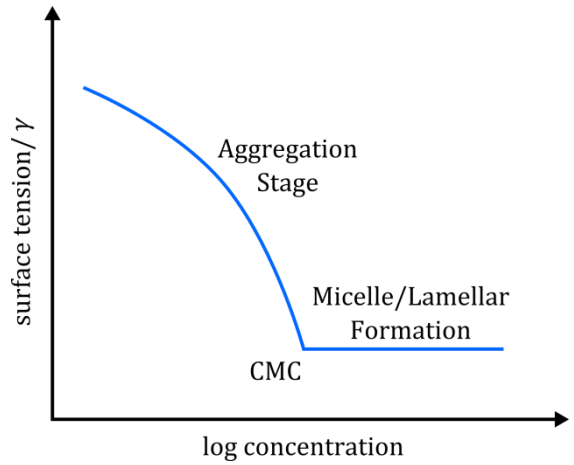

Figure 2.8. General representation of surface tension with increasing surfactant concentration, indicating the critical micelle concentration (CMC)

2.2.2. Surfactant Micelles and Lamellae

In the most basic form the thermodynamics of surfactant micelle formation are described using the Gibbs-Helmholtz equation;

$$\Delta G_m = \Delta H_m - T\Delta S_m$$

Equation 6

where ΔG_m is the Gibbs free energy of micellisation, ΔH_m the enthalpy of micellisation and ΔS_m the entropy of micellisation.[81] Generally there is a small increase in enthalpy of the system for formation of micelles; hence thermally micelle formation is unfavourable. In contrast however there is a large increase in ΔS_m upon micellisation, giving a negative ΔG_m. This means micelle formation will lead to a reduced free energy (a more stable system), hence will occur spontaneously. This is because the entropically unfavourable ordering of water around hydrophobic groups to preserve H-bonds is reduced. If surfactant concentration is increased far beyond the CMC, the surfactant can form liquid crystalline phases.[82] These phases are referred to as lyotopic liquid crystals and can exist in several possible forms; elongated micelles, hexagonal phase, cubic phase and lamellar phase (L_α). Generally as concentration increases the liquid crystals will form in the previous order, with a lamellar phase being formed at the highest concentration. When any surfactant agglomeration has formed, as a surface mono-layer, or liquid crystal, it exists as a dynamic equilibrium where surfactant molecules from the bulk and surfactant structure will constantly interchange, represented by the equilibrium arrows in Figure 2.9.[83] More in-depth information on the thermodynamics of micelle and liquid crystal formation is given in the review by Nagarajan and Ruckenstein.[84] While this is very well established behaviour in water, the corresponding behaviour in PVA has never been addressed.

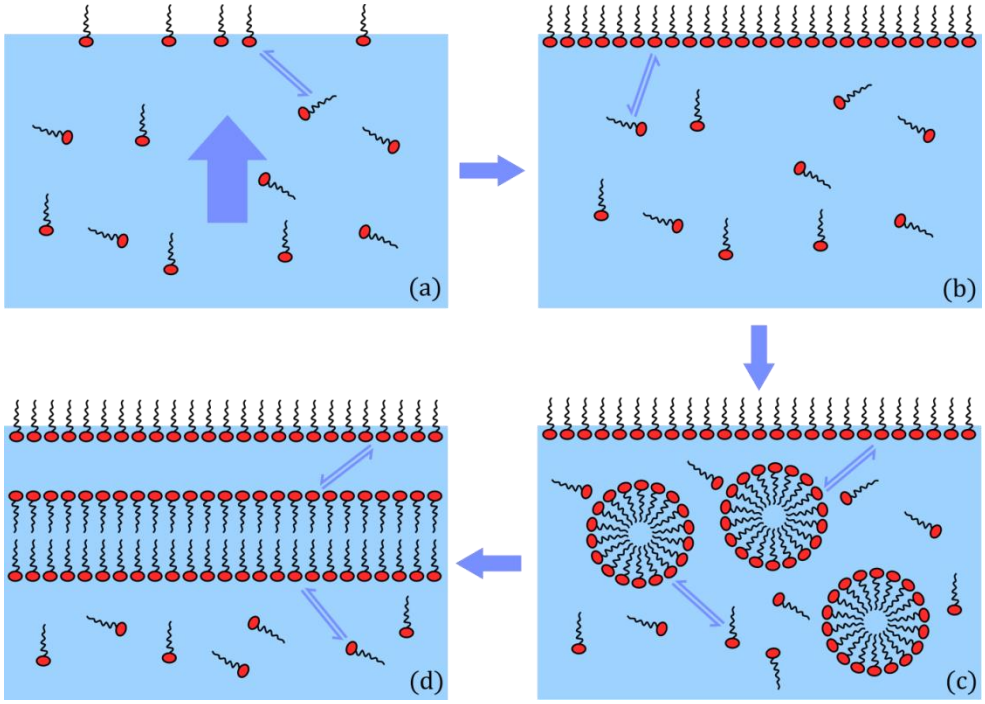

Figure 2.9. Schematic representation of surfactant in an aqueous medium, (a) low surfactant concentration, start of surface segregation, (b) formation of surfactant monolayer, (c) increased surfactant concentration, formation of micelle, (d) high surfactant concentration, formation of a lamellar

Surfactants will not only migrate to surfaces, but also to contrasting interfaces in solution.[85] This is especially useful in the formation of emulsions, where the surfactant forms a flexible (due to low interfacial tension) barrier between two immiscible fluids, such as oil and water. In the same way that was described for the water-air system, surfactant will migrate to the interface as it requires less energy to produce interfacial area, the build-up of surfactant at the interface then reduces the interfacial tension between the two phases.[86] Micelles will again form once the CMC is reached, except here they will form around a droplet of either water or oil. This provides a protective barrier between the two fluids, meaning that interaction between them is significantly reduced. This therefore allows small droplets of one fluid to move freely and be dispersed in the other, hindering phase separation, which is essential for detergent formulations and many cosmetic products.[87] The chemical nature of the surfactant and the two immiscible media is what determines whether a water-in-oil (W/O) or oil-in-water (O/W) emulsion is formed; both are visible in Figure 2.10. Because surfactants spontaneously have a preferred monolayer curvature, formation of W/O and O/W at the same time is unusual, the schematic is merely used to represent both situations. Collection of surfactant at solid-liquid interfaces has also received much attention in the literature; however the system of interest in this study has gone surprisingly unstudied, adsorption of surfactant at a solid-air interface.

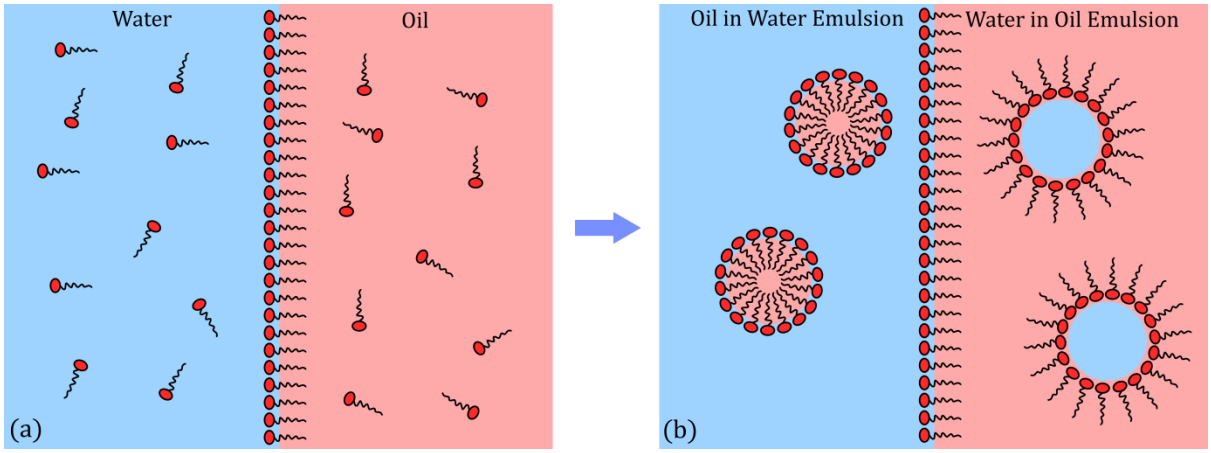

Figure 2.10. Schematic representation of either a water-in-oil (WIO) or oil-in-water (OIW) emulsion upon addition of surfactant to two immiscible fluids

2.3. Compatibility of Components

The effect of surfactants on two immiscible fluids has been discussed, but what determines whether one compound is miscible/immiscible? Compatibility arguments are discussed in the following section which attempt to explain this behaviour. When determining the compatibility of two materials the Hansen solubility parameter (HSP) of each material is often consulted. Hansen famously stated that 'like dissolves like' and devised the HSP calculation by splitting the Hildebrand solubility parameter in to three components to describe the interaction between molecules;[88]

$$\delta = \sqrt{\left(\delta_d^2 + \delta_p^2 + \delta_h^2\right)}$$

Equation 7

where δ is the total Hildebrand parameter, δ_d is the dispersion component, δ_p is the polar component and δ_h is the hydrogen bonding component. Although this parameter performs best when the molecules are considered spherical, it can still provide a good approximation as to whether solvation will occur with non-spherical molecules too (i.e. polymers). HSPs can also be used to predict the effectiveness of a plasticiser as the Flory-Huggins parameters (Equation 2) can; if the polymer and plasticiser exhibit a similar HSP then sufficient compatibility should be observed.[89] The effectiveness of the plasticisers glycerol and urea on PVA have been studied, where urea was found to be a more suitable plasticiser.[90] Comparing the HSP values for each of the compounds to PVA (Table 2.2.) it can be seen that this result is not surprising, as urea exhibits a HSP much closer to PVA than glycerol does. The authors conclude that it is the ability of urea to form stronger H-bonds to PVA in comparison to glycerol that increases compatibility, the δ_h also suggests this as it is much closer to PVA's δ_h. Prolonged exposure to urea can however lead to dermatitis,[91] hence it is not likely to be used in laundry product formulations. The relationship and ability to form H-bonds between PVA, glycerol and water is investigated in surfactant containing systems in the humidity sections of chapters 5 and 6, as well as the molecular interactions chapter 7.

Table 2.2. Hansen solubility parameters for PVA and some known plasticisers of PVA, values obtained from Handbook of Solubility Parameters[92]

Compound	δ	δ_d	δ_p	δ_h
PVA	23.7	17.5	12.5	10
Urea	20.9	12.0	10.5	13.5
Glycerol	36.2	17.4	12.1	29.3
Water	47.8	15.6	16.0	42.3

2.4. Relative Humidity Control

The interactions between PVA and glycerol are studied throughout this project, with glycerol's effects on surfactant segregation of significant importance. As part of the investigation in this area, these relationships were studied under relative humidity control. This was done using saturated salt solutions in sealed vessels, which works as the water vapour concentration, and therefore the percentage relative humidity (%RH) over a salt solution is less that over pure water.[93] Vapour pressure is something that exists over any liquid, but in the case of water it can be considered that over any aqueous solution there will exist some amount of gaseous water, giving rise to a vapour pressure. Molecules of water at the surface of a solution are constantly changing from the solution to gaseous state (evaporation) and vice versa (condensation). When a solution exists in an open container the rate of evaporation is large compared to the rate of condensation, hence the amount of solution will become reduced over time. However when a solution exists in a sealed chamber, a dynamic equilibrium can be reached where the rate of evaporation equals the rate of condensation, hence the water vapour pressure over the liquid water is saturated (contains a fixed number of water molecules), and therefore humidity is stable. Upon addition of a salt to the solvent, the process of evaporation is hindered, whereas condensation is not, causing the solution to exhibit reduced vapour pressure. The amount of hindrance exhibited on the solvent (water) is determined by the chemical nature of the salt, therefore the number of water molecules in the atmosphere at equilibrium (relative humidity) can be controlled depending on the salt used. The concentration of the salt (solute) can also have an effect on the boiling point of a solvent. This effect is described in terms of boiling-point elevation (ΔT_b), assuming the salt is non-volatile, ΔT_b is given by;[94]

$$\Delta T_b = K_b \cdot b_B$$

Equation 8

where K_b is the ebullioscopic constant and b_B is the molality (moles of solute per kilogram of solvent) of the solution. The ebullioscopic constant is determined for a solvent using the following expression;

$$K_b = R\,T_b^2 \cdot \frac{M}{\Delta_{vap}H}$$

Equation 9

Where R is the molar gas constant, T_b is the normal boiling point temperature of the solvent, M is the molar mass of the solvent and $\Delta_{vap}H$ is the molar enthalpy of vaporisation of the solvent at its boiling

point. The K_b of water is 0.512, hence addition of a salt will increase the molality of the solution, causing the boiling point to also increase. These values can be used to calculate the degree by which boiling point, and hence vapour pressure and relative humidity will be affected upon addition of a salt.

Temperature is also influential on the vapour pressure of water, where heating will cause an increase (evaporation) and cooling will cause a decrease (condensation). This effect is also seen in dilute aqueous salt solutions however, so if a stable environment cannot be achieved it is necessary to saturate the solutions to help maintain a consistent atmosphere (%RH) regardless of temperature.[95]

2.5. Molecular Vibrations

Molecular interactions are investigated in chapter 7 with infrared spectroscopy, therefore some basic theory on molecular vibrations, which are utilised to perform the analysis, are discussed below. There exist three types of motion in any molecule; translational, where the molecule as a whole moves in a single direction, rotational, where the molecule as a whole spins or rotates and vibrational, where the bonds between individual atoms within a molecule move.[96] There are several types of molecular vibrations which exist in molecules that contain more than two atoms, for example the vibrations for a methylene ($-CH_2-$) group are listed in Figure 2.11.[97] Typically one full vibration cycle takes approximately 10^{-15} seconds to complete, and the typical frequencies of these vibrations range from approximately 10^{13} to 10^{15} Hz, which corresponds to wavenumbers of ~300-3000 cm^{-1}.[98]

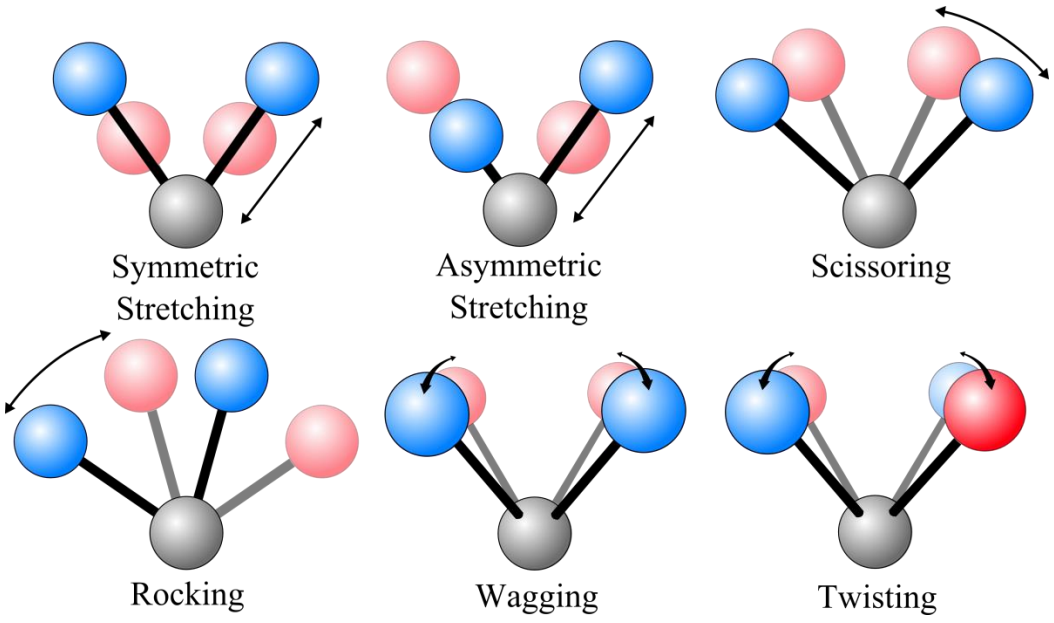

Figure 2.11. Schematic representations of bond vibrational modes, blue – start position, red – end position

Infra-red spectroscopy (IR) works by probing the different vibrations in a molecule through absorption of electromagnetic radiation, in the form of light. In its most basic form, IR uses a white light source which has been separated into individual wavelengths and passed through a sample. Each wavelength of light is comprised of photons which have the same energy, and if a sample contains a

molecular vibration which has the exact same excitation energy as the photon energy, the photons will be absorbed by the sample and excite electrons within it.[99] The absorbance (A) is defined as;

$$A = log_{10}\frac{I}{I_0}$$

Equation 10

where I is the intensity of light transmitted through the sample and I_0 is the intensity of light irradiating the sample. The concentration of the absorbing species is included in the Beer-Lambert law;

$$A = \varepsilon cl$$

Equation 11

where ε is the absorption coefficient, c is the concentration and l is the path length of light through the sample. These values are hence used to quantify the concentration, or strength, of the vibration which correlates to that wavelength within a molecule. If there is strong absorbance at a particular wavelength it indicates that only a small number of the incident photons have reached the detector on the other side of the sample, therefore the sample contains a large amount of vibrations which correspond to that specific change in vibrational energy level. The theory behind this is discussed more in more detail in the following section.

As discussed the photon energy (E) is what is varied in order to produce an IR spectrum, this therefore generally constitutes the controlled variable (x-axis) for most IR spectra. The units of this are not discussed directly in terms of E however, and are instead usually expressed in terms of frequency (f) or wavelength (λ). These three physical properties are all directly correlated using Equation 12,Equation 13 and Equation 14.[100]

$$f = \frac{c}{\lambda}$$

Equation 12

$$f = \frac{E}{h}$$

Equation 13

$$E = \frac{hc}{\lambda}$$

Equation 14

where; h is the Planck constant and c is the speed of light in a vacuum. Conventionally, and for this investigation, the units of frequency used are reciprocal centimetres or the number of waves in a length of one centimetre ($\overline{\upsilon}$, cm^{-1}) given by;

$$\overline{\upsilon} = \frac{1}{\lambda}$$

Equation 15

which can also be described as wavenumber. The wavenumber of a vibrational mode can be calculated using Hooke's Law as it applies to a covalent bond;

$$\overline{\upsilon} = \frac{1}{2\pi c}\sqrt{\frac{k}{\mu}}$$

Equation 16

where k is the force constant, used to provide a measure of the 'stiffness', or strength of the bond and μ is the reduced mass, which incorporates the atomic masses of the atoms, given by;

$$\mu = \frac{m_1 \cdot m_2}{m_1 + m_2}$$

Equation 17

where m_1 and m_2 are the masses of the atoms either side of the bond, giving Equation 18;

$$\overline{\upsilon} = \frac{1}{2\pi c}\sqrt{\frac{k(m_1 + m_2)}{m_1 \cdot m_2}}$$

Equation 18

for $\overline{\upsilon}$ to be cm^{-1}, the speed of light must be in cms^{-1}, the force constant in $ergcm^{-2}$ and the reduced mass in grams. The force constant can also be described as the spring constant as bonds follow Hooke's Law;

$$F = -kx$$

Equation 19

where F is the restoring force of the spring and x is the displacement of the spring from its equilibrium position. This can therefore be rearranged to give;

$$k = -\frac{F}{x}$$

Equation 20

for calculating the spring constant. It can be seen from the previous equations that the wavenumber of a given vibrational mode is defined from the composition of the bond, and can therefore be used to identify what moieties are present in a sample.

For example, if a compound contains a C-H stretch (νCH), as most compounds do, the wavenumber of the vibrational mode can be calculated using Equation 18, where the masses of C and H are 1.99×10^{-23} g and 1.67×10^{-24} g respectively. The force constant (k) for a C-H stretch was calculated by to be 29.4 eV $Å^{-2}$,[101] giving a value of 4.71×10^{5} erg cm^{-2}. Calculated using the following conversions; 1 eV = 1.602×10^{-12} erg and $1cm^{-2} = 1\times10^{16}$ $Å^{-2}$. The final wavenumber is given in reciprocal centimetres (cm^{-1}) as 1 erg ≡ 1 dyne cm ≡ 1 gcm^2s^{-2}, causing the units to cancel as shown above. From this it is possible to see that if the force constant (bond strength) increases the stretching frequency, and hence wavenumber, will also increase, therefore more coordinated bonds will generally appear at higher wavenumber. Increasing the reduced mass of the bonded atoms will cause a decrease in the observed wavenumber through the expressions above, which is why deuterium labelling can be used in conjunction with IR for a number of applications.[102-104]

The strength of photon absorption is controlled by a molecules dipole moment. The dipole moment of each bond is determined by the magnitude of the charge difference between its two atoms, as well as the distance between them, hence bond vibration results in a change in dipole moment. This fluctuation in dipole moment produces an electric field and if the electric field of the photon (from the light source) matches that of the bond, excitation occurs.[105] The total dipole moment for a molecule is the vector sum of each individual bond dipole (2.1.2.) within that compound. A stronger bond dipole will result in a greater number of photons being absorbed, hence absorption bands for polar moieties are much easier to detect. Compounds without polar groups will produce IR spectra with little to no absorption. When photons are absorbed at a particular wavenumber, the molecule gains energy and is moved from the ground vibrational state (lowest vibrational energy) to an excited vibrational state (higher vibrational energy). This results in a respective change to the vibrational mode which absorbs this energy, where a stretching mode will exhibit an increase in bond length between the two atoms with excitation, and a bending mode will exhibit an increase in the bond angle. In order to excite a molecule, the energy of the photon must be equal to the energy difference between the two vibrational states (ΔE);

$$\Delta E = hv$$

Equation 21

where; h is the Planck constant and v is the frequency of the photon. Therefore as the energy of the photons which are interacting with sample is varied to cover the entire range, a strong absorption at a particular wavenumber indicates a strong presence of the moiety related to that wavenumber.

Some related vibrations produce two absorption peaks in very close proximity; this is generally accounted for by the presence of an asymmetric and symmetric stretch of the same type of bond. With a symmetric stretch, for example in a CH_2 group, the distance between the carbon and hydrogen atom increases simultaneously, then decreases simultaneously. As the distance between oppositely charged atoms contributes to a bonds dipole moment, a symmetric stretch causes a relatively significant change in dipole moment as both bonds extend at the same time. This in turn leads to a reduction in the wavenumber at which symmetric stretches are seen as the wavenumber relates to bond strength. Increased photon photo absorption is also observed for these vibrations as a feature of the large change in dipole moment. These effects are not observed with an asymmetric stretch as a constant state is achieved as when one bond extends, the other retracts. It is this reason why asymmetric stretches will often appear stronger than their symmetric counterparts.

FTIR has been shown to be especially adept at defining the strength of H-bonding by a number of characteristic changes in the spectrum.[106-107] Firstly, as the strength of a vibrational mode indicates how strongly it will absorb IR radiation, it can be influenced by changes in the surrounding environment, so an increase/decrease in absorption intensity can provide information on H-bonding. Broadening of peak width in IR is another indicator, stretching modes such as the O-H stretch (νOH), C-H stretch (νCH) and C-O stretch νCO will see an increase in the range of spring constants when H-bonded. Variance in vibration spring constant will cause variance in vibration wavenumber through Equation 16, which will then result in a broadening of the respective band as an array of wavenumbers are representative of a single vibrational mode. This phenomenon is observed when looking at compounds such as alcohols in the

gaseous state.[108] As H-bonding cannot occur in a vapour, the free νOH stretch appears as a sharp, narrow band as oppose to the conventional broad band associated with a H-bonded νOH stretch. Bending modes will conversely see a narrowing of their respective bands as bending becomes more difficult when H-bonded. The wavenumber of a bond vibration is another indicator, as wavenumber is inversely proportional to wavelength, and subsequently energy, stronger bonds vibrate at higher wavenumber (Equation 16). When bonds such as the O-H stretch partake in H-bonding, their strength is reduced, which causes the representative band to shift to lower wavenumber (red shift). This is due to the electrostatic interaction between H-bond donor ($X\text{-}H^{\delta+}$) and H-bond acceptor ($Y^{\delta-}$) atoms which causes X-H lengthening as $Y^{\delta-}$ pulls $H^{\delta+}$ closer to it.[109] Therefore all stretching modes will shift to a lower wavenumber with H-bonding. Oppositely, any bending modes will see an increase in their wavenumber if they are taking part in H-bonding as it becomes more difficult to bend the bond, causing the potential surface to become narrower. A large increase in dipole moment response can also be observed with increased H-bonding.

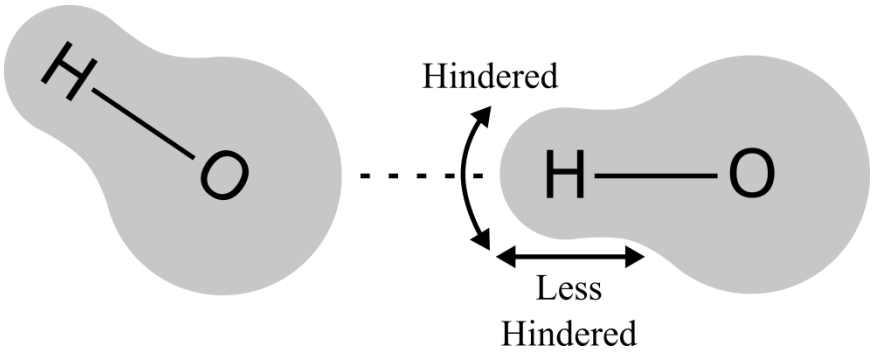

Figure 2.12. Schematic representation of how hydrogen bonding of hydroxyl group causes stretching vibrational modes to become weaker, and hence have a lower wavenumber, and how bending vibrations become more difficult, causing wavenumber to increase

2.6. Project Aims

The aims of this project are to explore the relatively unknown segregation behaviour of surfactants and plasticisers in a PVA matrix. Small molecule migration and segregation in polymers is a phenomenon of significant importance in many industrial applications. For plasticisers, loss to the environment is of concern to many products due to negative effects on the polymeric properties of the material, as well as the toxicity of some plasticisers. For surfactants, aggregation at polymer surfaces can have a significant impact on the surface functionality of polymer films, as well as their appearance and feel. The factors that control the segregation behaviour of these compounds in a polymer matrix, especially surfactants, is not well-understood. It is believed that probing the segregation behaviour and nature of interactions between surfactants, plasticisers and the PVA matrix will shed light on the forces which control these processes.

Chapter 4 – plasticiser evaporation and absorption aims to study the behaviour of a well-established PVA plasticiser (glycerol) within the matrix. As plasticiser loss to the environment is a cause for concern for many polymer systems, an initial investigation in to the rate at which the plasticiser evaporates is set to be launched. This should provide information on not only the rate of glycerol evaporation in PVA but also the rate at which it can redistribute inside the polymer matrix. The effect of properties relevant to the function of PVA such as degree of hydrolysis, are also to be investigated.

Chapter 5 - Non-ionic surfactant segregation in PVA film is set to study exactly that. As mentioned, PVA often come into contact with surfactant rich environments, as well as usually containing some surfactants left over from emulsion polymerisations. The behaviour of surfactants in the polymer matrix lacks thorough investigation; hence this chapter will probe the behaviour of some non-ionic surfactants in PVA, and attempt to uncover some of the forces behind their behaviour. By varying surfactant properties such as HLB, and environmental properties such as relative humidity, more information is hoped to be gained on the segregating nature of the small molecules in the polymer matrix.

Chapter 6 - Ionic surfactant segregation in PVA film has similar aims to the previous chapter, whilst also having the goal to probe any differences in segregation behaviour between non-ionic and ionic surfactants caused by the variance in head-group moieties and HLB. It is well known that both non-ionic and ionic surfactants will form aggregated lyotropic mesophases in solution, but their ability to do so in solid polymer matrices has also received little literature attention. This phenomenon is set to be investigated for both ionic and non-ionic surfactants using neutron reflectometry.

Chapter 7 - Molecular Interactions - Hydrogen Bonding via FTIR is set to provide experimental evidence for the intermolecular forces which dictate the favourable/unfavourable nature of interactions between the four main components to be studied; PVA, glycerol, surfactant and water. As all of these compounds are generally capable of significant hydrogen bonding, this form of molecular interaction is to be the focus of this chapter. H-bonding is known to be detectable with FTIR, therefore this technique will be primarily used here.

Some theory behind the processes which occur in polymer, plasticiser and surfactant systems has been discussed in the previous chapter; the following chapter will focus more on the theory behind the experimental techniques used in this project.

3. Materials and Methods

3.1. Sample Preparation

Generally samples exist in one of two forms within this investigation. Thin (< 300 nm), substrate-bound polymer films doped with plasticiser and/or surfactant were used to investigate segregation behaviour with IBA/NR. Additionally thick (> 10 μm), free standing polymer films were used to produce a model version of the thicker polymer films used in industry. Each sample preparation method is discussed below.

3.1.1. Model Thick (> 10 μm) Films

In order to study the fundamental behaviour that relates to commercial PVA films, it is necessary to simplify the film to a small number of well-defined components. To do this a 4 %(w/v) aqueous solution of PVA resin (Sigma-Aldrich P8136, M_w = 30–70 kg/mol, DH = 87–90%), similar in properties to what is used industrially[110] was made by heating in deionised water, conductivity ~0.5 μS cm^{-1}, with stirring at 75 °C for ~2 hours until completely dissolved. To plasticise these systems an aqueous 4 %(w/v) solution of plasticiser (glycerol ≥ 99%, Aldrich) was then added in the desired weight percentage and stirred overnight. To prepare a film of ~76 μm, 18 cm^3 of solution was added to a 10 cm diameter polystyrene petri dish and dried inside a vacuum oven at 80 °C / 800 mbar for ~90 minutes or until all solution was removed from the petri dish and only a solid film remained. The average film thickness was controlled by varying the volume of solution deposited per unit area. To produce thinner (~15 μm) films capable of being studied with FTIR in transmission geometry the same method is performed using 5 cm^3 stock solution.

3.1.2. Thin (< 300 nm), Spin-Cast Films

In order to study segregation behaviour of compounds such as surfactant and plasticiser in polymers with scattering techniques, significantly thinner (< 300 nm) films were produced. Model films were again studied in order to simplify the system and enable easier interpretation of segregation behaviour. To produce films of this sort a 4 %(w/v) aqueous solution of a PVA was again formulated and combined with 4%(w/v) solutions of glycerol and/or surfactant and stirred overnight. Surfactant solutions, particularly the anionic ones, may become hazy when stirring. This is most likely due to the formation of self-assembled surfactant mesophases, heating slightly for approximately 15 minutes will cause the mesophase to dissipate[111] and produce a clear aqueous solution. Combining the surfactant solution with the polymer solution will also cause the mesophase to disband, forming an isotropic phase again. Films of < 300 nm were achieved by spin-casting on to cleaned silicon wafers of approximately 3 x 3 cm, which had been cut using a diamond-tipped pen. The substrate is kept in place during sample preparation by a vacuum which is applied to the underside of the silicon wafer using a compressed airline. There are generally 3 stages involved in the process of producing a spin-cast film. The first stage is a washing

phase, here the silicon wafer is rotated at high speed (> 1500 RPM) and a jet of organic solvent, usually acetone, is applied via a wash bottle to remove any residual organic material, plus any shards of silicon left over from the scoring of the wafer. The next step is the addition phase; here the sample solution is applied to the cleaned wafer, depending on the surface tension of solvent used for polymer dissolution, the speed of this stage can vary. If the solvent has relatively low surface tension, it will spread effectively on the wafer, giving even coverage at slow rotational speed (< 100 RPM). Due to the high surface tension of the solvent in this case (water), at low speed the solution would not wet the substrate surface fully, running off a single side only. To combat this problem the substrate had to be stopped completely in order to apply an even coating of solution to the entire wafer. Once the substrate was loaded with polymeric solution, the drying phase could commence. Rotational speed of this stage is largely responsible for the final thickness of the dried film; a slower rotation throws less of the solution off the edges of the substrate, causing an increase in thickness, and vice versa. The films produced generally ranged from 150 to 300 nm with spinning speeds of 800 – 1300 RPM.

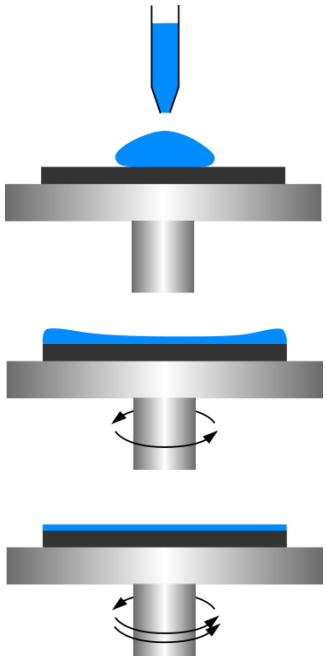

Figure 3.1. Schematic representation of solution drying via spin coating.

3.2. Scattering Techniques

In order to achieve depth profiles of the elements present in the thin films, and hence track their migration and segregation within the samples the two main scattering techniques used were ion beam analysis and neutron reflectometry. A relatively brief overview of the theoretical foundation and experimental set-up of the two techniques is discussed in the following sections. For more in-depth information please consult the ion beam analysis reviews by Jeynes and Colaux,[112-113] as well as the neutron reflectometry review by Zhou and Chen.[114]

3.2.1. Ion Beam Analysis (IBA)

Ion beam analysis is a well-established collection of techniques used to reliably determine elemental composition versus depth profiles for labelled components in < 1μm thin films. It has seen use in several research areas, examples of which are; fingerprint and gunshot residue analysis,[115] elemental profiling of gold artefacts,[116] characterising cementitious materials[117] and elemental analysis of cells and biomaterials.[118] The IBA family is mainly made up of nuclear scattering techniques; Rutherford backscattering spectrometry (RBS), non-Rutherford (elastic) backscattering (EBS), elastic recoil detection analysis (ERDA) and nuclear reaction analysis (NRA). It also includes some photon emission techniques such as particle induced x-ray emission (PIXE) and particle induced gamma-ray emission (PIGE). The two emission techniques have excellent elemental resolution but poor depth resolution, so are therefore not useful for the depth profiling of thin films of known composition. Therefore, the techniques mainly used in this study are RBS, ERDA and NRA, for their simplicity and accuracy when depth profiling light elements in a heavy matrix. Durham University has one of two IBA set-ups in the U.K., including a National Electrostatics Corporation 5SDH pelletron accelerator and RC43 end-station. In order to perform IBA the entire system must be kept under relatively high vacuum (< 4×10^{-6} Torr). At these low pressures, evaporation occurs at a significant rate, causing the low molecular weight components of the thin films to be removed rapidly. To maintain sample integrity during experiments films were cooled to below −50 °C using liquid nitrogen. This was achieved by attaching the silicon wafer to a metal sample holder by screwing two smaller plates on top of the wafer (Figure 3.2.), which is subsequently screwed into a sample holder rod. This allows the user to submerge the sample into liquid nitrogen safely, and once cooled lower the sample into the endstation (Figure 3.3c.) for analysis. The details of each IBA technique are discussed in the following sections.

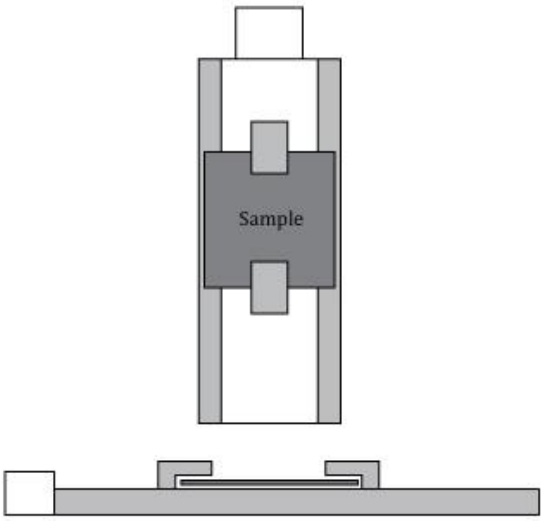

Figure 3.2. Schematic representation of silicon wafer sample holder which is lowered into the 'endchamber' for analysis

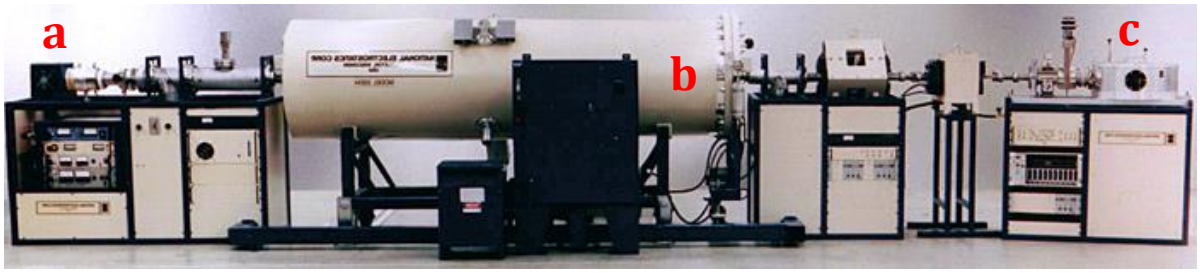

Figure 3.3. Photograph of IBA set-up, labelled parts are a – ionisation chamber, b – Pelletron accelerator and c – endstation.

a. Rutherford Backscattering

RBS is particularly well suited to the detection of heavy elements within a sample. In a typical RBS experiment, an incident $^4He^+$ beam of 1.5 MeV is directed at a sample 80° to the sample normal. Once impacting the sample, backscattering of the helium ions occurs and a detector with a nominal energy resolution of 17 keV at 170° to the incident beam measures the energy and number of backscattered helium ions. A schematic representation of this process is displayed in Figure 3.4.

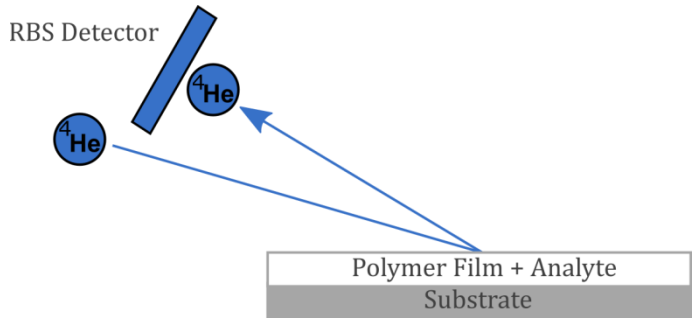

Figure 3.4. Schematic representation of Rutherford backscattering (RBS) analysis and geometry

The information gathered by the detector can then be interpreted to give an elemental and hence molecular composition profile for each individual component within a sample. Under these experimental conditions, RBS provides a depth resolution of ~15 nm. The raw output of all IBA data is given as counts per channel versus channel. Channel corresponds to the energy of each backscattered helium ion and hence the depth within the sample at which it was scattered, plus the mass of the target nucleus. In this set-up, typically energy (E) = 9.6 keV/channel + 40 keV. The gain is defined by the amplification electronics and the constant is the energy lost by the recoiling particles as they traverse the detector window. As an ion beam travels through matter it loses energy from two forms of collisions, inelastic collisions with electrons (S_e electronic stopping) where interaction excites or ionises the target atoms, causing the incident particle to lose energy. Energy is also lost through elastic collisions with target nuclei (S_n nuclear stopping), which lead to a change of direction of the incident ion in a 'billiard ball' fashion, the sum of these two contributions gives the total stopping power (S);

$$S = S_n + S_e$$

Equation 22

At low beam energy (< 100 keV) nuclear stopping power dominates the expression, whereas at higher energy the stopping power due to interaction with target nuclei becomes negligible and electronic stopping power is more prevalent hence; $S \approx S_e$.[119] Stopping power will increase with increasing beam energy until a maximum is reached, after which any further increase will cause stopping power to decrease as other factors such as radiation stopping power come in to play.[120] As the beam energies used in this study range from 0.7 – 1.5 MeV the initial primary stopping power is that of electrons, with nuclear scattering becoming apparent once the incident ions have lost sufficient energy. The expression for stopping power is given as the energy (E) loss per unit path length (x);

$$S(E) = -\frac{dE}{dx}$$

Equation 23

Using the program SRIM – The Stopping and Range of Ions in Matter,[121] the typical electronic and nuclear stopping power for a 1.5 MeV ^4He beam in PVA are 236.81 and 0.25 keVμm^{-1} respectively. As can be seen the electronic stopping power is much greater than the nuclear. The mass of the target atoms is the largest contributor to stopping power, where the energy of the backscattered projectile (E_1) can be calculated by scaling the energy of the incident ion (E_0) by the elastic scattering kinematic factor (K_S);

$$E_1 = K_S E_0$$

Equation 24

where K_S is given by;

$$K_S = \frac{E_1}{E_0} = \left[\frac{\pm\sqrt{M_2^2 - M_1^2 \sin^2\theta} + M_1 \cos\theta}{M_2 + M_1}\right]^2$$

Equation 25

where θ is the scattering angle, M_1 is mass of incident nucleus, M_2 is mass of the target nucleus. As the incident nucleus is always $^4He^+$ in this study, for backscattering, the mass of $M_1 < M_2$, therefore only the plus sign is physically meaningful for RBS in Equation 25. The kinematic factor for a typical element such as carbon is hence smaller than K_1 for a heavier element such as bromine (utilised in 6.1.), causing helium backscattered by bromine to be detected at higher energy,

The distance the incident beam has travelled within the sample also affects the energy of the backscattered projectile. Helium ions detected with a higher energy have lost relatively little of their energy as they have impacted the sample, meaning they have been scattered from the surface or near-surface regions. As the energy of the detected helium decreases, this indicates a greater interaction with the sample; hence the beam has travelled further in to the sample before scattering, having therefore lost more energy. This direct correlation of scattering depth to backscattered ion energy is what enables accurate depth profiling of heavy elements within a sample. The feature of energy loss can however complicate analysis when relatively rough films are studied, discussed later in chapter 4. Backscattered

yield (measured in counts per channel) for each element is proportional to its concentration, as a greater number of backscattered ions with a specific energy means a higher concentration of the heavy element at that depth within the sample. In an environment such as the one generally used in this study (a spin cast PVA film on a silicon wafer) backscattering is dominated by the silicon substrate as the polymer film is significantly thinner than the substrate on which it is bound. Therefore to explicitly detect an element in a film on a Si wafer with RBS, it must be significantly heavier in mass than Si.

b. Elastic Recoil Detection Analysis

ERDA differs from RBS as it exploits the forward scattering of elements lighter than the incident beam in order to produce a depth profile. Typically a 1.5 MeV $^4He^+$ beam is used for ERDA as was done for RBS, allowing the two techniques to be measured simultaneously.[122] The primary forward scattered elements are those lighter than 4 atomic mass units (AMU). Anything heavier than this that is also forward scattered is eliminated from the detector by use of a 5 μm PET range foil, which filters out higher atomic number nuclei, including the helium incident ions. In order to provide a contrast within the material to detect distribution of individual components, deuterium labelling is utilised. Deuterium labelling (^1H to D) has been proven to be an effective method of compound isolation whilst having very little effect on the physicochemical properties of the labelled component.[123] As the mass of deuterium is < 4 AMU, it is also forward scattered along with hydrogen (Figure 3.5.). The energy of the recoiled atoms (E_2) can be calculated in relation to the incident ion energy (E_0) by use the kinematic elastic recoil factor (K_R), given as;

$$K_R = \frac{E_2}{E_0} = \frac{4M_1M_2}{(M_1 + M_2)^2}\cos^2\phi$$

Equation 26

where M_1 is mass of incident nucleus and M_2 is mass of recoiling nucleus at an angle ϕ. As the incident beam is always $^4He^+$ and the scattering angle is constant, usually fixed at 30°, it can be seen from this equation that any increase in mass will cause the backscattered ion to have more energy. Using Equation 26 the energy separation of D and H scattering is explained in terms of atomic mass;

$$H = \frac{4\ {}^4He \cdot\ {}^1H}{\left({}^4He + {}^1H\right)^2}\cos^2 30 = 0.48$$

$$D = \frac{4\ {}^4He \cdot D}{\left({}^4He + D\right)^2}\cos^2 30 = 0.67$$

hence;

$$for\ H: E_2 = 0.48\ E_0$$

$$for\ D: E_2 = 0.67\ E_0$$

therefore forward scattered deuterium will be detected at higher energy in comparison to forward scattered hydrogen. The incident beam loses energy as it traverses the sample in the same way as it does for RBS, hence higher energy H and D has been scattered from the surface of the film, and lower energy has been scattered from deeper within the film. A schematic representation of the scattering geometry for ERDA is shown in the Figure 3.5.

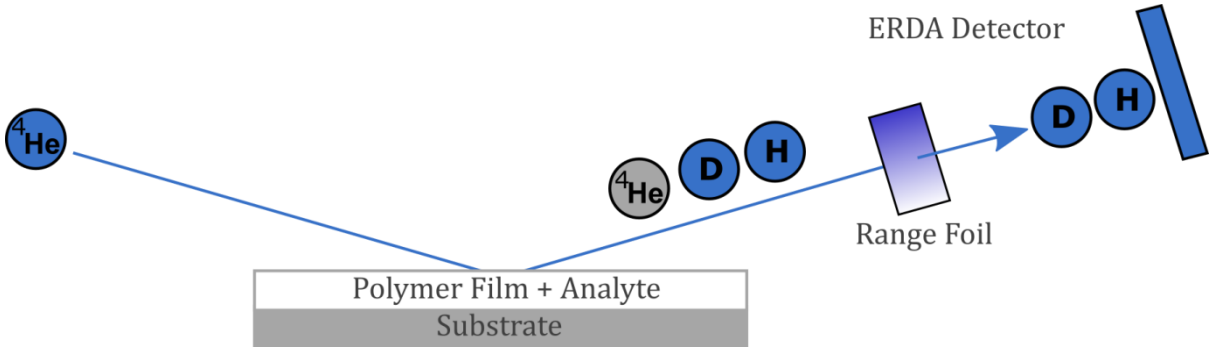

Figure 3.5. Schematic representation of elastic recoil detection analysis (ERDA) mechanism and geometry

c. Nuclear Reaction Analysis

The final branch of IBA used in this study is nuclear reaction analysis (NRA); the same detector used for RBS is used here, hence a similar geometry and gain (E = 9.5 keV/channel + 40 keV) is utilised. NRA excels when the individual analysis of deuterium distribution within a sample is required. Such cases that may require this method of analysis are when a sample is very thick or if a low energy beam is required. If samples are thick (> 1 μm), ERDA is unable to fully resolve the hydrogen and deuterium scattering, making comprehensive analysis of deuterium distribution difficult, an example of this within this study is found in 4.3., and in the literature in the Composto IBA review.[124] In order to isolate deuterium distribution, a $^{3}He^{+}$ incident beam is used which can, as the branch name suggests, cause a nuclear reaction. For a reaction to occur, the incident helium ion must have enough energy to overcome the Coulombic repulsion, if this requirement is filled, transfer of a neutron from deuterium to helium occurs, producing a high energy proton ($^{3}He + D \rightarrow {}^{4}He + H + 18.352$ MeV).[125] Other nuclear reactions can be used to probe elemental distribution, for example with Li and F, but this is the only one that is useful for the samples studied in this investigation. The energy and number of ejected protons can be used to determine depth and concentration in a similar way to the previous techniques. As NRA does not require a grazing angle for analysis, it can penetrate further into the sample compared to ERDA. It can also achieve a greater depth resolution of ~8 nm as no range foil is required in backscattering geometry.

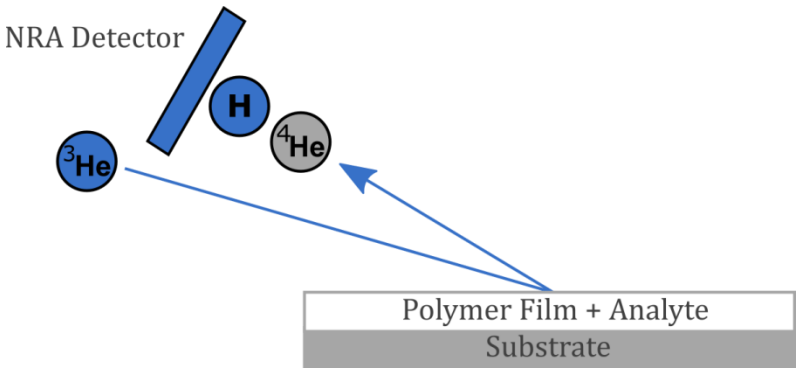

Figure 3.6. Schematic representation of nuclear reaction analysis (NRA) mechanism and geometry

d. Beam Damage

Although not intentionally destructive techniques, it can be seen from the previous two sections that both ERDA and NRA cause atoms to be scattered from the sample. Although RBS does not detect forward scattered atoms, it uses a similar experimental set-up and beam to RBS, hence will still forward scatter. Loss of atoms from the material by this route is termed beam damage. Beam damage from helium ion beams has been reported for both Si and Cu substrates,[126] polyimide films[127] and polystyrene.[128] $^4He^+$ beam damage has not been studied in PVA films, however its effects on PVA electrospun fibres has. It was found that upon irradiation with a $^4He^+$ beam the elastic modulus of the polymer was degraded by 63%.[129] These findings suggest that beam damage is likely to be relatively significant in PVA films also. An extensive review of beam damage in IBA is given in the Spirit Handbook.[130]

Figure 3.7. displays the ERDA scattering data from a 30 w% d_5-glycerol PVA thin film analysed with a 1.5 MeV $^4He^+$ beam. In order to demonstrate the destructive effect of prolonged sample irradiation with an ion beam, ten separate, sequential 1 μC scans were performed on the same location of the film. The peak at ~1.2 MeV is representative of forward scattered hydrogen, and the peak at ~1.7 MeV of deuterium. As can be seen, as the cumulative charge increases, the counts per channel for each element decrease. This is especially visible in the back edge of the H-scattering at 1.0-1.2 MeV, this shift of the data indicates a decrease in film thickness with prolonged analysis, showing the destructive power of the ion beam for plasticised PVA films. To establish a suitable charge to analyse future samples with, the counts for both H and D were summed and plotted against the cumulative charge (Figure 3.8.). A decay of H and D concentration (counts per channel) within the film is shown with increasing irradiation. This decrease is a function of there being more polymer for the beam to interact with initially, hence the concentration of each element detected is high. Once damage has commenced and progresses, there is less polymer and glycerol to scatter H and D from, hence the concentration, and counts per channel decrease. It was deemed from this experiment that 2 μC of charge would provide data of good statistical quality without causing significant damage to thin polymer films, hence 2 μC is used for most analysis throughout this work.

If data of insufficient statistical quality is acquired with 2 μC however, it is possible to improve it without additional sample damage. The detected scattering from several locations on a single film can be summed in a single measurement. To do this a 2 μC scan is taken at a single location on the film, the

analysis is paused and the sample is moved in the z-direction (vertically), then without resetting the profile as if a new samples was being studied, another 2 μC is taken and the data simply continues to collect as if a 4 μC scan had been performed. This process can be repeated until the data is of satisfactory quality, or there is no further room for analysis on an undamaged portion of the sample. As a typical sample is approximately 3 x 3 cm, and the beam damage profile caused by the $^{4}He^{+}$ beam is generally 2.0 cm in length and 0.5 cm in height at incident angles of 70-88°, around 6 experiments can have their counts 'stacked' on a single film.

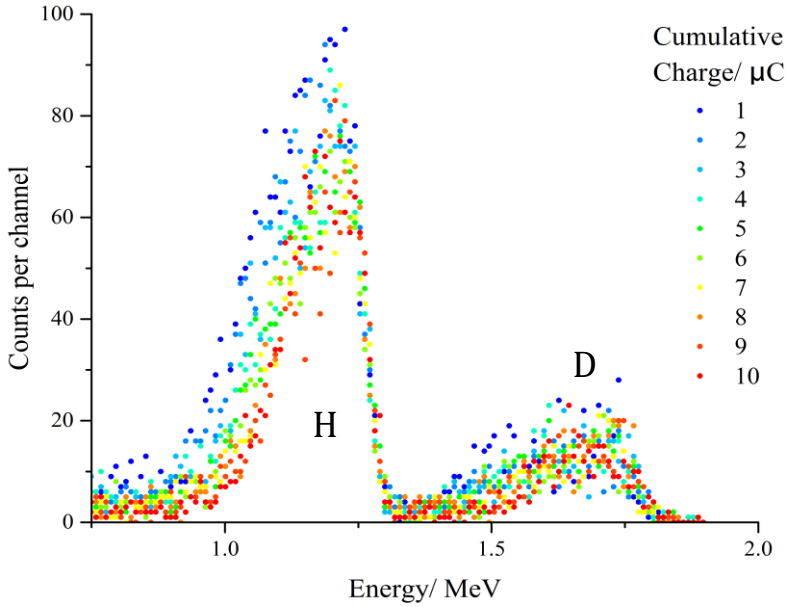

Figure 3.7. ERDA beam damage experiment, 10 x 1 μC sequential scans performed on the same area of a 30 w% d_5-glycerol plasticised PVA film.

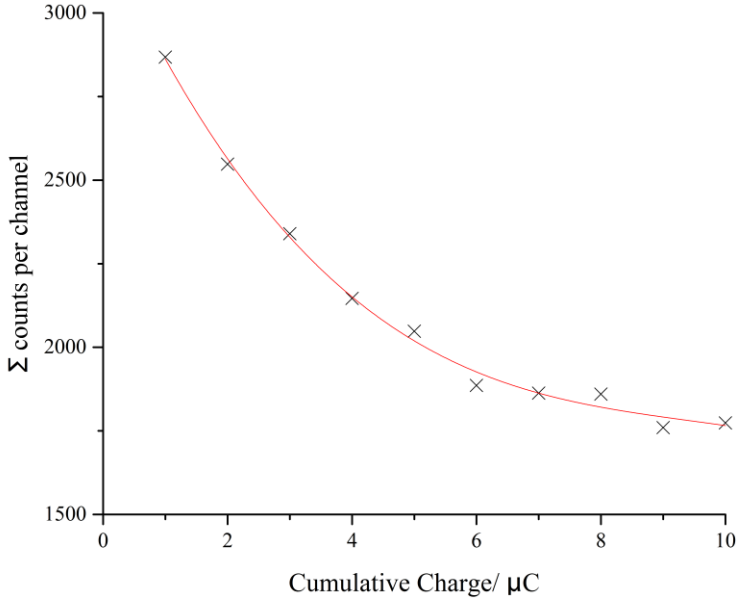

Figure 3.8. Sum of the total counts per channel from both H and D scattering (taken from Figure 3.7.), against the cumulative charge, 4th order polynomial applied to the data to give a rough line of best fit

3.2.2. Neutron Reflectometry

Vertical concentration profiles of components within the spin-cast films were also determined by neutron reflectometry (NR) using the SURF and INTER reflectometers at the Science and Technology Facilities Council (STFC) facility ISIS. This technique provides significantly better depth resolution (~0.5 nm)[131] compared to IBA, as well as the ability to study samples under atmospheric conditions as the technique does not require a vacuum to operate. In general, neutron reflectivity data is given in the form of the scattering vector Q (Å^{-1}) versus reflectivity (R). The magnitude of the scattering vector is the modulus of the resultant scattering between the incident and scattered wave-vectors. These values can be described with a scattering triangle (Figure 3.9.), where the scattering vector is given by $Q = k - k'$. Scattering here is elastic and energy is conserved throughout interaction with the sample, hence $k = k'$. Reflectivity is given by calculating the number of neutrons reflected at a given scattering vector over the number of incident neutrons, giving a measure of depth.

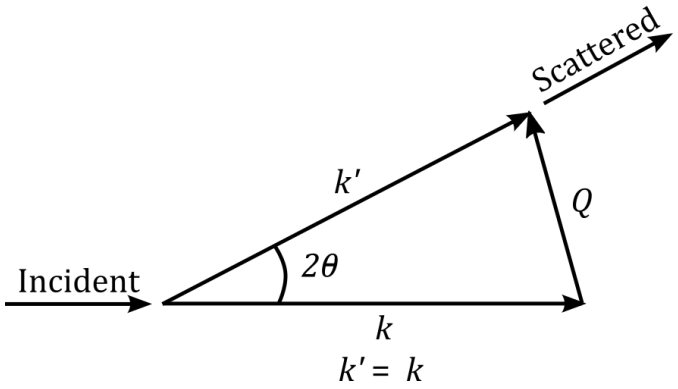

Figure 3.9. Scattering triangles for elastic scattering where the incident neutron neither gains nor loses energy

As the angle between the incident beam and the sample (incidence angle) is generally fixed at a defined angle, typically in the range 0.3-1.5°, to perform neutron reflectometry over a significant Q range the wavelength of the incident neutron beam is varied. NR is a specular technique, therefore the scattering vector only has a z-component (perpendicular to the sample normal) so is renamed Q_z. This parameter describes the momentum transfer after reflection from a sample has occurred;

$$Q_z = 4\pi \, sin\frac{\theta}{\lambda}$$

Equation 27

where λ is the neutron wavelength and θ is the angle of incidence. By substituting Bragg's law of diffraction;

$$n\lambda = 2d \, sin\theta$$

Equation 28

in to the previous equation the following expression is realised;,

$$d = \frac{2\pi}{Q}$$

Equation 29

where d is a distance. Using these considerations, if there are multiple scattering planes parallel to a surface present within a material, a Bragg peak within the data can be used to study the distance between each scattering plane. This is termed Bragg scattering and is used to provide key length scales and distances/separations which have been utilised to define; surfactant nanostructure,[132] block co-polymer distribution[133] and degree of cross-linking.[134]

Specular reflectometry concerns neutron scattering where the angle of incidence is equal to the angle between the reflected beam and sample (angle of reflection). The use of specular reflection at very small angle of incidence which are close to the critical angle (where neutrons are totally reflected from a smooth surface, usually < 1°) allows probing of structures larger than the atomic dimensions associated with other neutron scattering techniques. It does this by being extra sensitive to differences in refractive index (RI) between interfaces as it traverses the material. Neutron RI is directly related to the scattering length density of a material so can be used to provide information about the composition of interfaces and surfaces. To define the interaction of a neutron beam with a thin polymer film and how scattering length density is used to probe structure the schematic in Figure 3.10. is presented.

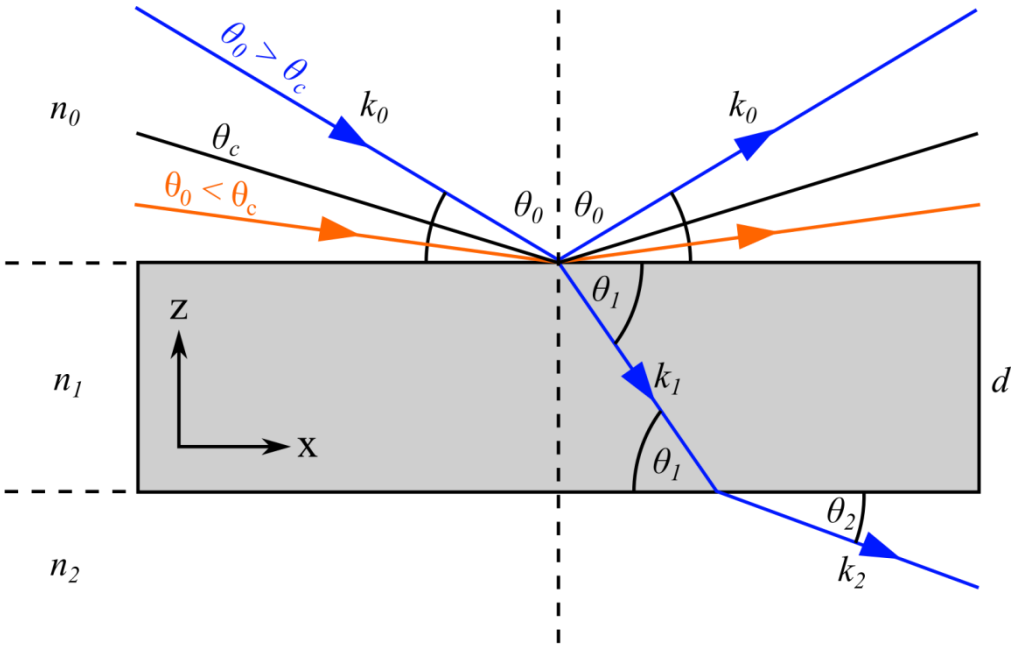

Figure 3.10. Example of neutron reflection and refraction by a thin film of thickness d and refractive index n_1, between two regions of refractive index n_0 and n_2, representing a thin polymer film on a silicon substrate.

Note that for neutrons n is always close to 1 and $\theta_0 \approx \theta_1 \approx \theta_2$ The refractive index of the polymer film is defined in the same way as is done with electromagnetic waves with RI (n) being given by;

$$n = \frac{k_1}{k_0}$$

Equation 30

where k_1 and k_0 are the neutron wavevectors either side of the interface. The refractive index for neutrons is commonly written as;

$$n = 1 - \frac{\lambda^2 \delta}{2\pi}$$

Equation 31

where δ is the scattering length density (SLD) and λ is the neutron wavelength. As in most cases $n < 1$, neutrons are externally reflected by most materials. The SLD (δ) is defined as a measure of the scattering power of a material and is calculated using the following expression;

$$\delta = \sum_i n_i b_i \cdot \frac{\rho \, N_A}{M_w}$$

Equation 32

where n_i is number of atoms in molecule i, b_i is scattering length of nucleus i, ρ is bulk density of the scattering body, M_w is molecular weight and N_A is Avogadro constant. When calculating SLD for polymers, it is necessary to calculate SLD for one repeat unit. Using these expressions and the bound coherent scattering lengths for ^{1}H (-3.74 $\times 10^{-15}$ m) and D (6.67 $\times 10^{-15}$ m),[135] it is clear to see how using deuterium labelling can create a contrast in SLD which causes an easily detectable change in refractive index within the sample. To probe changes in RI below the surface refraction must occur, hence to calculate the angle below which total reflection occurs (critical angle, θ_c), Snell's law;

$$n = \frac{\cos\theta_0}{\cos\theta_1}$$

Equation 33

can be used;

$$\cos\theta_c = \frac{n_2}{n_1}$$

Equation 34

the relationship between the critical angle, neutron wavelength and SLD is then given by Equation 35.

$$\theta_c = \lambda \sqrt{\frac{\delta}{\pi}}$$

Equation 35

When $\theta < \theta_c$ total external reflection occurs and reflectivity $R = 1$ (Figure 3.10.). For $\theta > \theta_c$ Fresnel's Law applies to determine the reflectivity;

$$R = |r|^2 = \left|\frac{n_0 \sin\theta_0 - n_1 \sin\theta_1}{n_0 \sin\theta_0 + n_1 \sin\theta_1}\right|$$

Equation 36

this expression is then extended when a film of multiple layers and interfaces is analysed to provide reflectivity and thickness measurements for each specific layer, further information on this is provided by Zhou and Chen.[114]

Sample preparation was similar to that for IBA experiments, except that the films were somewhat thinner (~70 nm) to maximize the sensitivity of the measurement to changes in film thickness from the Kiessig fringes in the reflectivity profiles (Figure 3.11.). NR also provides a direct measure of film surface roughness, something that must be implemented in to the fits with IBA. $R(Q)$ was measured from before the critical edge ($Q \approx 0.01$ Å^{-1}) to the point at which the signal is indistinguishable from the background ($Q \approx 0.25$ Å^{-1}). On the SURF reflectometer this measurement required three angles of incidence (Φ = 0.25, 0.65, 1.5) and approximately 2 hours of acquisition time per sample to obtain data of sufficient statistical quality over the entire Q range. The latter factor imposes a requirement that films must be stable for at least several hours, as any alteration in film thickness during measurements would make accurate interpretation of the data impossible. Neutron experiments carried out on the INTER reflectometer have a reduced acquisition time (~1 hour, 15 minutes) compared to SURF as the newer target station 2 (TS2) beamline at ISIS is much more efficient than the older TS1. To maximise the number of samples studied in a 24 hour period, and to avoid a sample change-over every 1.25 hours, generally 4 samples were analysed in series using an automated sample changing stage. Although experiments on each reflectometer have different times of acquisition the results achieved should not differ as both instruments offer the same spatial resolution. Raw data were rebinned into increments of δQ/Q of 0.015, this step was necessary to minimise statistical noise in the data while preserving the experimental resolution of δQ/Q ~0.03.

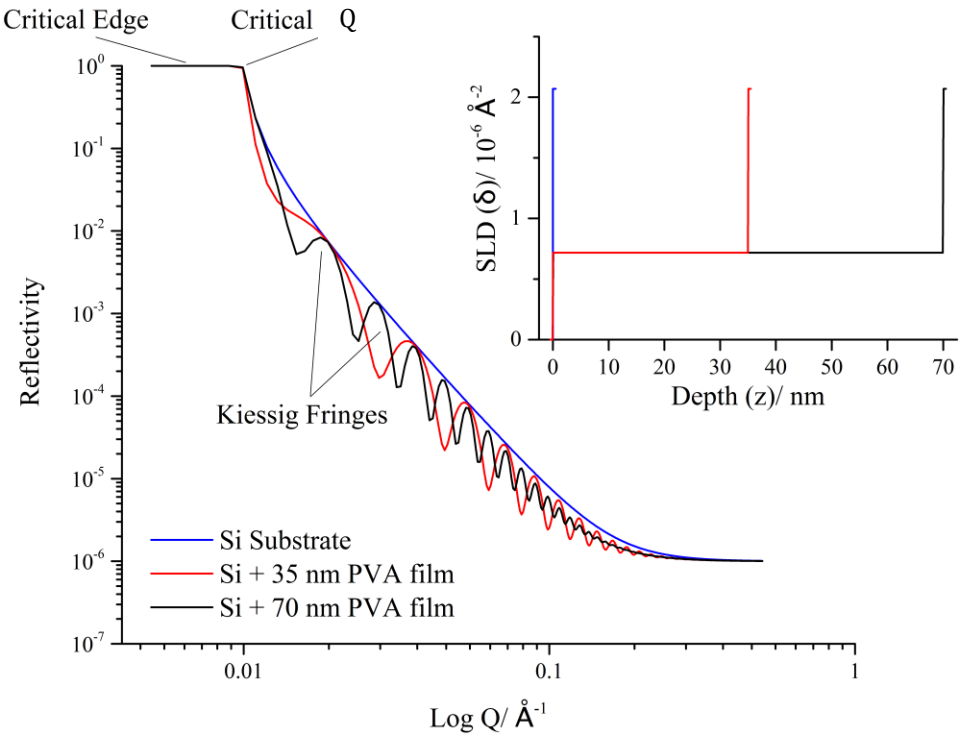

Figure 3.11. Calculated reflectivity profiles for a silicon substrate (solid, blue), a smooth 35 nm PVA film on a silicon substrate (solid, red) a smooth 70 nm PVA film on a silicon substrate (solid, black) produced with MotoFit (resolution $\delta Q/Q$ = 4%, background = 1 x10^{-6})

3.3. Fitting Software

Without the use of computer software to analyse the data produced via IBA and NR accurate interpretation of results would be impossible. The software used in these circumstances is however not completely automated; comprehensive knowledge of the elements within the samples and the structures they are likely to form is required in order to apply a preliminary 'simulation', hence the need for well-defined model systems. This simulation is a predicted depth profile for the sample, from which the software will vary the input thickness and concentration (IBA) or SLD (NR) to produce a fit to the data with the least χ^2. More information on how the utilised software performs this process and converts the output in to a concentration profile is given below.

3.3.1. DataFurnace

All ion beam analysis data were analysed with the Surrey University DataFurnace[136] software (WiNDF v9.3.68, running NDF v9.6a) to determine the concentration versus depth profiles. Several files are required to perform a fit; a structure, geometry and simulation file must all be constructed in order for the software to function. The geometry file defines the experimental set-up, including the branch of IBA, energy of the incident beam, scattering geometry, as well as other calibration parameters. Rutherford scattering cross sections were assumed for the RBS analysis, and NRA data were analysed

using the scattering cross sections of Möller and Besenbacher.[137] The structure file contains the 'logical elements' present within the sample. The logical elements are the constituent compounds that make up the sample, within this file their density in gcm^{-3} is defined, as well as the depth range in which they are permitted to reside. All compounds must be defined within the structure file or they cannot exist within the simulation. The output of DataFurnace is a composition versus atomic percentage profile where each molecule defined in the structure is presented as an atom, having the average composition of the molecule, (e.g. water, H_2O is represented in the output as atoms of $H_{0.667}$ $O_{0.313}$. Densities of compounds used within this project are given in Table 3.1. The simulation file contains a predicted concentration versus depth profile which is used as a basis to perform analysis from. There are two primary methods for producing a fit from these files, layer fit and functional fit.

The layer fitting methodology requires the sample concentration profile to be segregated in to layers. Each layer is given a thickness and starting concentration of each logical element within it. To avoid over-parameterisation, model composition profiles were restricted to either two or three layers, the minimum number of layers required to accurately fit the data. The thickness and composition of these layers is then allowed to vary to obtain the best possible fit to the experimental data, a confidence limit of 0.025 is generally set within DataFurnace, ensuring each fit has a χ^2 of < 0.25. Where a satisfactory fit cannot be achieved because of the tailing off of the data (diffuse edge), roughness considerations can be implemented to accommodate for this. An example of IBA data where this is the case is given in 4.2. DataFurnace provides five roughness models, but only the first is used in this project. Where roughness is caused by the inhomogeneity in a layer's thickness and assuming the previous layer does not affect the thickness of the following one, the roughness contributions of each layer (δX_i) can be used to calculate a total roughness contribution (ΔX^{inh}). Total roughness at the interface between the n^{th} layer and the following one is given by;

$$\Delta X^{inh} = \sqrt{\sum_{i=1}^{n} \delta X_i^2}$$

Equation 37

the δX_i for each layer is taken as the standard deviation of the layer thickness, a value which is input by the user. The corresponding energy resolution is added to the energy resolution at the interface between layer *i* and the next one, in order to cause a blurring of the boundaries between each layer.

If the inclusion of a roughness parameter does not yield a satisfactory fit other methods can be employed. When distribution of a compound within a sample is not segregated in to layers, but shows a gradual increase/decrease, a functional fit can be used to describe the distribution with more accuracy. In comparison to the layer fit which varies the concentration and thickness of a set number of layers, the functional fit uses a given equation, in this case an exponential, and varies the parameters of said equation to achieve the best fit. This work concerns surface active compounds whose concentration profile decays with increasing depth, hence Equation 38 is appropriate;

$$\phi(z) = \phi_b + (\phi_s - \phi_b)\mathrm{e}^{\left(\frac{z}{\lambda}\right)^{-\beta}}$$

Equation 38

where ϕ_s is concentration of component at the surface, ϕ_b is concentration of component in the bulk and λ is the decay length of excess. Performing a functional fit in DataFurnace is not without its disadvantages, although in principle the function should be capable of describing a surface excess. When implementing functional forms for $\phi(z)$ the fit can become unstable and additional layers can be added to the produced depth profile without the user's control, this feature is however a relatively new addition to DataFurnace and is still under development. Therefore functional fitting is best suited to samples which exhibit lack of a thick, segregated surface excess and contain an exponential decay of detected counts with increasing depth. In most cases an exponential decay does not accompany a thick surface excess as if a pure layer is forming on the surface of thin films then there is a strong impetus for segregation within the film, so a gradually changing concentration is unlikely. This fitting methodology is utilised in 5.1.3.

3.3.2. IGOR & MotoFit

All neutron reflectometry data were analysed with the fitting package Motofit, supported by IGOR Pro (v6.37). Similarly to DataFurnace, MotoFit normally uses a series of layers with a pre-defined thickness and SLD, it also requires a predicted depth profile to be established prior to fitting. Once the simulation is within a reasonable degree of agreement with the data fitting can proceed, the SLD, thickness and roughness of each layer is optimised to produce the best fit. MotoFit offers a larger degree of customisability when fitting compared to DataFurnace, where any setting within any layer can be omitted from the fitting procedure. For example as each sample is formed on a silicon substrate, the SLD of which is 2.07×10^{-6} Å^{-2}, a thick layer of silicon is added to the base of each fit where the thickness and SLD is not permitted to vary. Exposed silicon wafers will also have a native oxide layer which has a SLD of 4.18×10^{-6} Å^{-2} and typical thickness of < 3.5 nm, so in this case the SLD of this layer can be fixed, as it is known, and the thickness is allowed to vary with the fit. This silica layer is consistent with results that have been inferred from previous experiments on silicon substrates.[138-140] The remaining scattering length densities of the organic components present in the films were calculated using Equation 32.

Densities for most compounds studied were obtained from the literature; however for some of the more exotic deuterated surfactants, there exists no literature value for density. In these cases the density for the hydrogenous surfactant was scaled by the ratio of deuterated to hydrogenous molecular weight, assuming the same molecular volume;

$$\rho_D = \frac{\rho_H \cdot M_W^D}{M_W^H}$$

Equation 39

where ρ_D is density of deuterated compound, ρ_H is density of hydrogenous compound, M_W^D is molar mass of deuterated compound and M_W^H is molar mass of hydrogenous compound. Table 3.1. lists the calculated densities, molecular weights, $\sum_i n_i b_i$ and SLDs for all compounds used in this study. The density of the PVA

resin primarily used in this study is 87-89%, as crystallinity is shown to be reduced with lower DH resins, its density is estimated to be ~1.19 gcm^{-3}.[39-40]

Table 3.1. Coherent scattering lengths used to calculate $\sum_i n_i b_i$ were obtained from the National Institute of Science and Technology (NIST) database,[135] *deuterated density calculated using M_w ratio (Equation 39) as no literature value was available

Component	Density/ gcm^{-3}	M_w/ $gmol^{-1}$	$\sum_i n_i b_i$/ 10^{-4} Å	SLD/ 10^{-6} $Å^{-2}$
PVA	1.19[141]	44.05	0.41	0.72
H_2O	1.00	18.02	-0.17	-0.56
D_2O	1.11	20.03	1.91	6.39
Si	2.33[142]	28.09	0.42	2.07
SiO_2	2.65[143]	60.08	1.58	4.18
Glycerol	1.26[70]	92.09	0.74	0.61
d_5-glycerol	1.33[144]	97.12	5.95	4.91
$C_{12}E_4$	0.95	362.54	0.48	0.08
d_{25}-$C_{12}E_4$	1.02	387.70	26.5	4.18
$C_{12}E_5$	0.96[145]	406.60	0.89	0.13
d_{25}-$C_{12}E_5$	1.02*	431.75	26.9	3.84
$C_{12}E_6$	0.98	450.65	1.31	0.17
d_{25}-$C_{12}E_6$	1.03	475.80	27.3	3.56
SDS	1.01[146]	288.38	1.59	0.36
d_{25}-SDS	1.10*	431.75	27.6	5.83

As can be seen in Table 3.1., deuteration of components provides a significant increase in SLD, by at least 3×10^{-6} $Å^{-2}$. Therefore by labelling only one species within a sample the SLD profile obtained from the scattering data provides a comprehensive description of the labelled compounds distribution within the sample. Slight issues arise when considering SiO_2 at the substrate interface however as SiO_2 has a similar SLD to the deuterated compounds. A previously stated a layer of 1-3.5 nm of SiO_2 generally resides on each of the substrate silicon wafers which can make determining exact concentrations of the deuterated compounds at the silicon interface difficult. Fortunately the labelled components within this study do not appear to exhibit substrate segregation when analysed with NR. Fitting in MotoFit produces a SLD versus depth profile, which must be exported and converted to a concentration (at. %) to enable comparison to IBA data. This is done by subtracting the background SLD of each hydrogenous compound within the sample, and dividing by SLD of the deuterated compound being observed; For example when considering a three component film containing a deuterated component (*x*), hydrogenous plasticiser (*y*) and hydrogenous PVA (*z*);

$$[x] = \frac{\delta - [y]\delta_y - [z]\delta_z}{\delta_x}$$

Equation 40

where δ is the calculated SLD obtained from MotoFit, δ_x is SLD of deuterated compound, $[x]$ is concentration of deuterated compound (at. %), δ_y, δ_z are SLDs of hydrogenous components and $[x], [y]$ are concentrations of hydrogenous components (w%). An example calculation for a deuterated SDS plasticised film is given below, taken from the 20% d_{25}-SDS, 20% h-glycerol data in Figure 6.14. The first layer from this sample has a calculated SLD of 5.75 which gives [d_{25}-SDS] = 5.75 – [(0.2 x 0.61) – (0.6 x 0.72)]/5.83 = 0.89, or 89%, signifying an almost pure layer of d_{25}-SDS at the depth which the SLD was detected. The fitted parameters for each neutron experiment can be found in the Supporting Information 12.2.

3.4. Additional Techniques

Although scattering techniques comprise the bulk of analysis done throughout this project several other techniques have been employed in an effort to support IBA/NR findings.

3.4.1. Ellipsometry

Ellipsometry was used to study thin film thickness for spin-cast samples. The Sentech® SE 500 ellipsometer uses specular reflection of polarised light to detect changes in polarisation after interacting with a sample, compared to a model that the user has input. If there is excessive disagreement between the model and the sample, accurate readings cannot be obtained. Therefore the properties of the film (refractive index, approximated thickness) must be known prior to analysis. The refractive index (RI) of PVA has been shown to decrease with increasing wavelength (λ),[147] reaching a plateau of 1.5 above 600 nm. The ellipsometer uses a He-Ne laser, which gives a wavelength of 632.8 nm,[148] therefore 1.5 was used as the RI for PVA in the ellipsometry model. Prior to precise measurement by ellipsometry approximate film thickness can either be estimated by observing the colour of the film, with dark blue films being < 100 nm, light blue 100-200 nm and yellow > 200 nm, or studied using a film thickness probe (FTP) in conjunction with the ellipsometer. The SE 500 is designed to study films of < 25 μm, and will struggle with films of greater thickness, as well as films < 200 nm thick.

3.4.2. Atomic Force Microscopy (AFM)

The surfaces of thin polymer films have been widely studied using AFM,[149-150] allowing not only a detailed image of the surface to be obtained, but also providing mechanical characterisation of properties such as adhesion. A Bruker MM8 AFM capable of scanning areas of 15 x 15 μm, was used for all samples in this study. Figure 3.12. displays a schematic representation of the general AFM set-up. In order to detect surface features of the films a silicon probe (or cantilever) is used to tap the surface of the film and

create an image. Bruker ScanAsyst-Air silicon tip on nitride lever cantilevers were used which had a tip length and width of 115 µm and 25 µm respectively, as well as a spring constant of < 0.4 Nm^{-1}. The effective radius of a probe tip is usually <10 nm, which defines the lateral resolution limit. Vertical resolution is affected by building vibration and thermal noise, but is ~0.3 nm. The advantage of the Bruker system is that it allows intermittent contact of the probe with the surface by moving of the sample relative to the probe, compared with older systems where the probe is dragged across a stationary surface. Movement of the sample is controlled by an attached piezoelectric scanner. A piezoelectric material contracts and expands proportionally in response to an applied voltage, the polarity of the voltage is what dictates whether the material expands or contracts. These scanners are used in atomic force microscopy as full 3-dimensional control is needed when examining the surface. The split photodiode detector in Figure 3.12. measures cantilever deflection via the difference in the laser position from the resting position of the probe to when it is affected by the sample. The optical arrangement of the laser and cantilever greatly amplifies the deflection of the cantilever, this is necessary as cantilever deflection is generally on the vertical order of < 100 nm. It therefore requires two very closely spaced photodiodes with the separate output signals collected and correlated by a differential amplifier. This amplifies the difference between the two voltages but does not increase the value of the particular voltages, hence allowing very sensitive detection of cantilever movement.

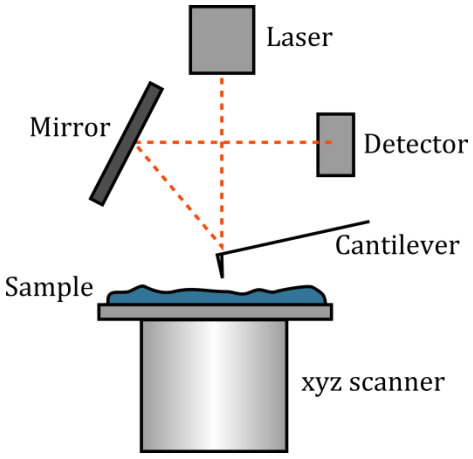

Figure 3.12. Schematic representation of AFM sample set-up including xyz piezoelectric scanner

In order to obtain mechanical data from the sample a force distance curve (Figure 3.13.) is taken each time the probe contacts the sample. The force-distance curve provides a simplified descriptor of the force exerted on the probe during analysis and can be analysed to measure the deformation of the sample, from which other surface properties can be determined (see schematic, Figure 3.13.). Starting at the largest piezo z-position (furthest away from the sample), as the z-position decreases and the probe approaches the sample (red arrow) there is no force (0 nN), attractive or repulsive on the probe until it is within sufficient distance of the sample. The point denoted by the sharp increase in attractive force is present as the probe 'snaps on' to the surface due to attractive forces between the probe and sample. After this point sample continues to be pushed further in to the probe and the cantilever begins to deflect, causing an

increase in the repulsive force. After the probe has reached a maximum deflection the sample is retracted (blue arrow), as the sample is pulled away from the probe it does not detach at the same point at which it contacted it. Instead additional force must be applied in order to fully remove the probe from the sample. This additional force is termed the tip-sample adhesion force and from this an adhesion map of the sample is formulated. As this must be done for every point on a scan the desired resolution of the image or 'samples per line' as it is termed in AFM can largely affect acquisition time for a single plot. Generally 512 samples per line were used to collect good quality images and hence a single plot could take up to 10 minutes to complete. Other measurements such as contact mode are faster (2-3 lines/second), but the advantage of Bruker's PeakForce mode is that gains are automated, reducing the difficulty of capturing an image. The raw data of each image is 'flattened' using NanoScope Analysis (v 1.1.) to remove the natural curvature of height caused as the sample is rastered in respect to the cantilever. Additional information can also be obtained from the lateral movement of the probe in AFM, by sliding the probe along a flat surface and monitoring lateral force variations molecular migration on the single molecules scale can be achieved,[151-152] this is termed friction force microscopy (FFM).

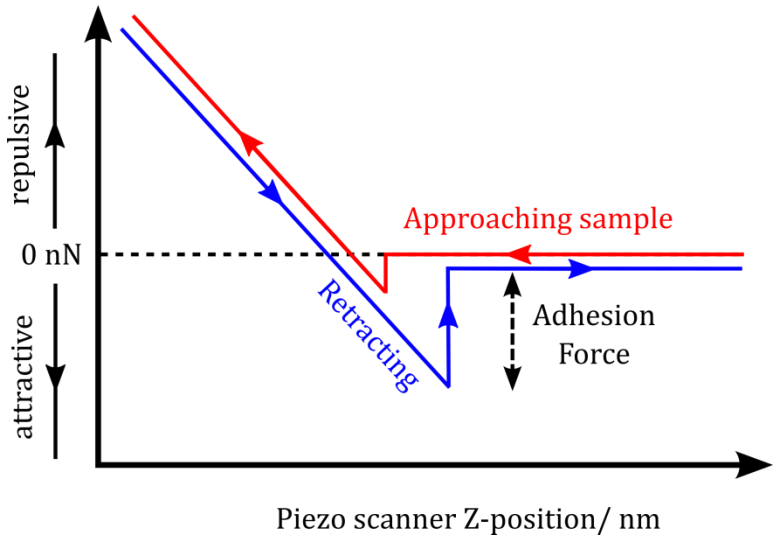

Figure 3.13. Force-distance curve showing adhesion force of the cantilever as it is retracted from the sample in QNM mode.

The NanoScope Analysis software provides a number of features to give quantitative values for surface properties, as smooth scattering surfaces and the evolution of surface features on thin films are of interest here it was used to provide a measure of surface roughness. Average roughness (R_a) is the simplest parameter to obtain which quantifies surface roughness. It is derived by calculating an arithmetic average of the absolute values of the surface height deviations measured from the mean plane of the image;

$$R_a = \frac{1}{L}\int_0^L |Z(x)|dx$$

Equation 41

where L is the evaluation length and $Z(x)$ is the profile height function analysed in terms of height (Z) and position (x). Although this parameter is easily obtained, it has certain limitations. As it is simply a mean absolute profile of the surface height it cannot distinguish between a film that is 'peaked' and a film that is 'troughed', for example the two films (1 and 2) shown in Figure 3.14. would exhibit identical R_a as the differentiation from mean height is the same for both, although the surface structures are very different. Where R_a is most useful is the determination of whether a surface has become more or less rough compared to a previous sample, for example film 3 in Figure 3.14. would exhibit a mean value for surface height (mean line) similar to what was seen for film 1 as both the peaks and troughs have increased by a similar intensity, but its R_a would show an increase as the deviation from this mean has increased.

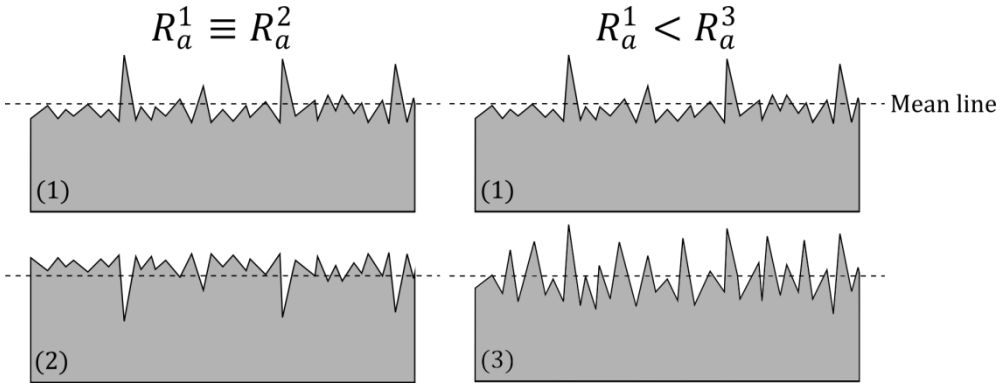

Figure 3.14. Schematic representation of average roughness (R_a) limitations and advantages

Efforts have been made to improve the reliability of this parameter; hence root mean square (RMS) roughness (R_q) was formulated. RMS roughness has proven adept at detecting self-assembly of molecules,[153] hence should be useful in determining the nature of compounds at the surfaces of the thin films studied here. The only difference when calculating R_q compared to R_a is that the amplitude of each peak and trough is squared;

$$R_q = \sqrt{\frac{1}{L}\int_0^L |Z^2(x)|dx}$$

Equation 42

making the parameter more sensitive to larger deviations from the mean line. This means that R_q values will be higher than R_a values, represented in Figure 3.15., it is also the measure of roughness which NR is sensitive to, which is useful for comparison between measurement techniques. Therefore as standard R_q values will be used to discuss changes in roughness for the thin PVA films studied. Another useful

parameter is kurtosis, this describes the 'peakedness' of the data, i.e. a large kurtosis would indicate a small number of very intense features (platykurtoic), compared to a lower or negative kurtosis, which would suggest a greater number of more moderate height features (leptokurtic).[154] Kurtosis can therefore be used to differentiate between surfaces which have different shapes, but the same R_a value.

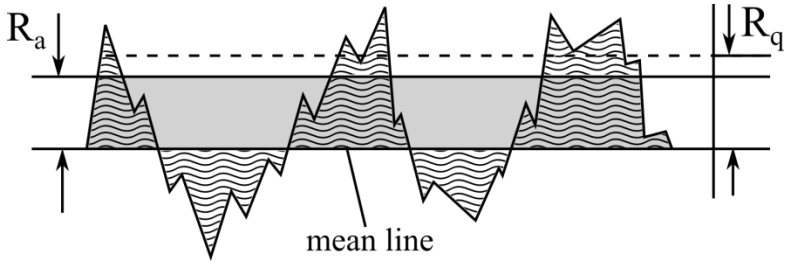

Figure 3.15. Schematic representation of average roughness (R_a) and root means square roughness (R_q)

3.4.3. Fourier Transform Infra-Red (FTIR) Spectroscopy

A PerkinElmer *Spectrum Two* FTIR spectrometer was used to study changes in the absorption spectra for both liquid and solid samples. In its most simple form, IR spectroscopy involves shining a monochromatic light at a sample and measuring the amount of light absorbed. This is done for multiple wavelengths and a spectrum is produced. Understandably this process requires significant acquisition time to cover the conventional wavenumber range of 400-4000 cm^{-1}. In order to reduce this time and improve the signal-to-noise ratio associated with each spectrum FTIR was developed. FTIR works by shining a light source containing multiple wavelengths of light at once and through a Fourier transform works backwards to separate each wavelength and produce a spectrum. To study H-bonding in liquid samples via FTIR (7.1.) a single reflection ATR accessory is used with the spectrometer. The accessory has a horizontal plate and screw down clamp to ensure good contact of the sample with the ATR crystal. The use of an ATR diamond crystal allows focusing of the light beam and intensifies the absorbed signals. Initial solutions were made by mixing distilled water with glycerol (≥ 99%, Aldrich) to achieve solutions of 0-100 w% glycerol content, with increments of 10 w% glycerol. Approximately 5 g of each solution was made and allowed to stir overnight in a sealed sample vial. Each solution was then analysed, where a background scan and 8 analysis scans of each sample were collated to give the final spectra. To probe the effects of additives such as $C_{12}E_5$ and PVA, 10 w% of each was added to the glycerol-water solutions and allowed to stir overnight. After which solutions were analysed in the same way as the binary systems.

For the study of 76 μm commercial films the use of an ATR attachment is not ideal. A depth penetration of approximately 2 μm is achieved with this set-up, so only the near-surface regions of the polymer can be probed. In order to study the entire thickness of the film the FTIR was used in transmission geometry. This involves the film being suspended in the beam by a makeshift FTIR attachment, created using a single piece of cardboard cut to the necessary dimensions, with a hole to allow the beam to pass through. The film was attached via double-sided adhesive tape, placed into the FTIR and 8 scans were collated and analysed. A schematic representation of this is found in Figure 3.16.

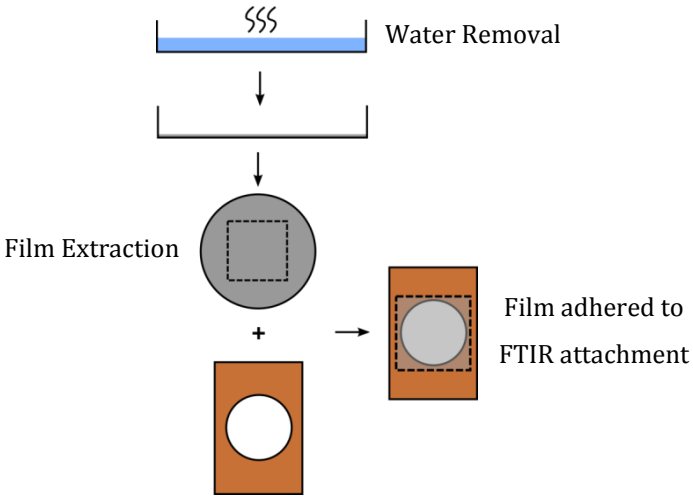

Figure 3.16. Schematic representation of PVA solution casting, film formation and FTIR attachment set-up

4. Plasticiser Evaporation & Absorption

4.1. Volatility of Low Molecular Weight Components

It is well understood that plasticisers are mobile molecules added to a polymer matrix. This mobility can lead to significant problems when specific mechanical properties, defined by plasticiser concentration, are required for a polymer to perform its task. As it means the plasticiser is normally capable of escaping the polymer matrix by a number of routes. In this chapter, for the first time, glycerol migration and loss to the environment in thin PVA films is studied, employing ellipsometry, IBA and NR techniques to do so. In an effort to understand the migration and segregation of compounds such as plasticisers in PVA films, vertical concentration profiles, which give information on the positioning of a labelled component throughout the entire depth of the film are obtained. In order to achieve these using scattering techniques, samples of sufficient quality are needed, usually acquired by spin-coating polymer films from solution.

Initial polymer films were produced via spin coating an aqueous solution of 4 %(w/v) PVA (Sigma-Aldrich 341584, M_w = 89–98 $kgmol^{-1}$, DH = 99+%) on to a cleaned silicon wafer, the thickness of these films was then measured with ellipsometry. Film thickness was measured over the course of several days and it was found that the thickness of pure PVA films remained stable under atmospheric conditions, as a solid polymer film containing no additives would be expected to (Figure 4.1., solid squares, black). Any variation in the pure PVA film thickness over the course of the experiment can be accounted for by experimental error in the ellipsometer readings, or perhaps a change in temperature/humidity which has caused the film to swell/shrink slightly. It was not until the plasticiser glycerol was introduced to the system that a systematic decrease in Th was recorded.

Figure 4.1. shows how films of varying degree of plasticisation decrease in thickness over time when left to dry under atmospheric conditions. Three measurements were taken on each thin film and the results averaged. A few notable trends occur, with increasing plasticiser concentration, initial film thickness (Th_0) decreases. This is due to the presence of less polymer in the final solution as it becomes more dilute with increased plasticiser concentration, as well as the reduced viscosity of dilute solutions, which will contribute to production of thinner, spin-cast films. It also appears that the time taken to reach equilibrium is affected by the starting concentration of plasticiser, with higher concentrations requiring more equilibration time. This suggests glycerol leaves the polymer matrix at a fixed rate, independent of starting thickness and solvent volume. Films of 5 and 10 w% glycerol appear to reach equilibrium after 3 days, 15 and 20 w% taking 5 days and 30 w% reaching equilibrium after approximately a week. Equilibrium film thickness (Th_E) was calculated by taking an average of the last three data points, which in turn allowed calculation of a percentage reduction in film thickness for each glycerol concentration. Plotting glycerol concentration against Th_0/Th_E gives an extremely well correlated plot (Figure 4.2.), signifying that if more glycerol is present in the film upon formation, a greater decrease in film thickness will be observed. This correlation implies that the reduction in film thickness over the course of the experiment is caused by glycerol evaporating from the film. If loss of the

plasticiser is the sole cause of the reduction in film thickness then it can also be gauged from these results that a thin (< 200 nm) PVA film retains 2-5 w% of plasticiser under ambient conditions (room temperature and pressure - RTP) once equilibrium or steady state thickness has been reached. This is very different to what is found industrially, where stable films are achieved with plasticiser concentrations over 20 w%.[155] However the macroscopic surface area to relatively small film thickness would cause plasticiser to be lost more noticeably. It is also possible that as glycerol is slightly more dense (1.26 gcm^{-3}) compared to PVA (1.19 gcm^{-3}), it accounts for less than its weight percent as a thickness percent. This would mean that the equilibrium is reached when all glycerol is lost, rather than a small amount being retained by the polymer.

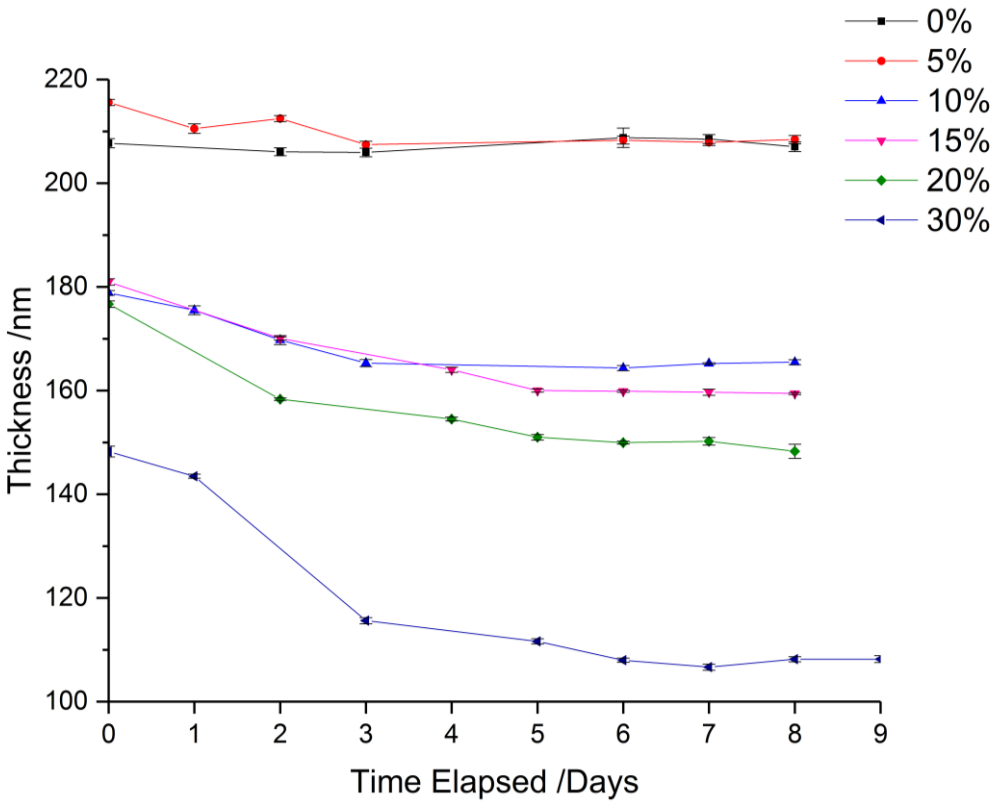

Figure 4.1. Thickness measurements taken over the course of 9 days on thin PVA films containing varying concentrations (w/w %) of glycerol.

Table 4.1. Thickness values for thin spin cast films containing varying amounts of plasticiser at both their starting thickness and equilibrium thickness.

Glycerol Conc./ %	Th_0/ nm	Th_E/ nm	Th_0/Th_E/ %	Glycerol Remaining/ %
0	207.7	208.1	-0.2	-
5	215.6	208.2	3.4	1.6
10	178.9	165.4	7.5	2.5
15	181.0	159.7	11.8	3.2
20	176.7	149.5	15.4	4.6

30	148.2	107.6	27.4	2.6

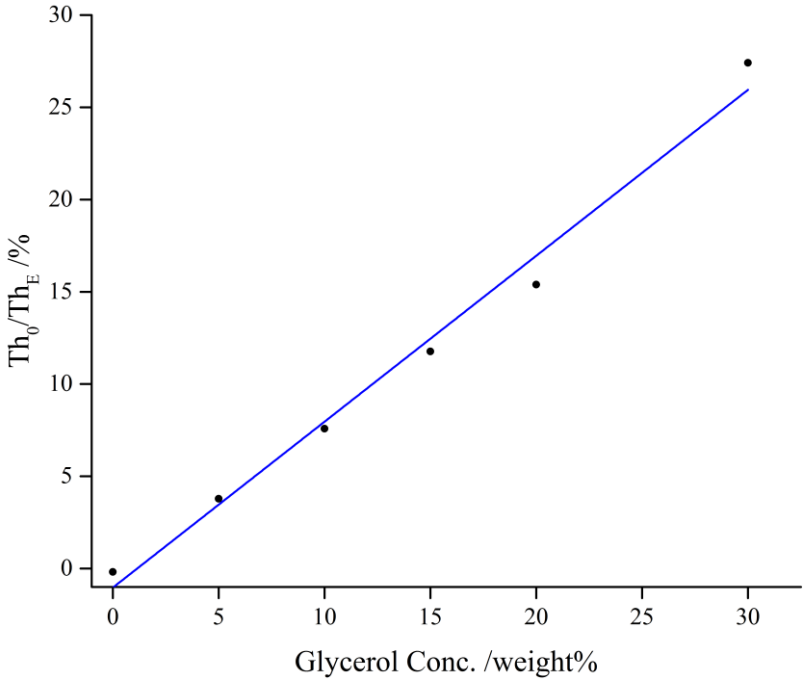

Figure 4.2. Correlation between the atomic percentage of plasticiser in each film and the fractional decrease in thickness from sample preparation to equilibrium

The decrease in film thickness is better depicted by normalising each film to its starting thickness, therefore removing the discrepancies between starting film thickness (Figure 4.3.). It is also easier to visualise the rate at which equilibrium is reached in these samples. A mastercurve of offset data can then be produced by taking the maximum glycerol concentration (30 w%) and scaling each data set to this. For instance, the 20 w% data starts at the point where the 30 w% film has lost 10% of its mass, hence has a normalised thickness of 0.9. The 15 w% data starts at 0.85, the value expected after the 30 w% film had lost half of its glycerol, and the trend continues in this manner. The agreement between all curves shows that the composition profile of glycerol in a 30 w% film after it has lost half of its glycerol is the same as the starting composition of a film 15 w% film. This implies a consistent rate of plasticiser loss regardless of initial concentration, showing that evaporation rate is the rate limiting factor when concerning plasticiser loss, not the amount of plasticiser in the film.

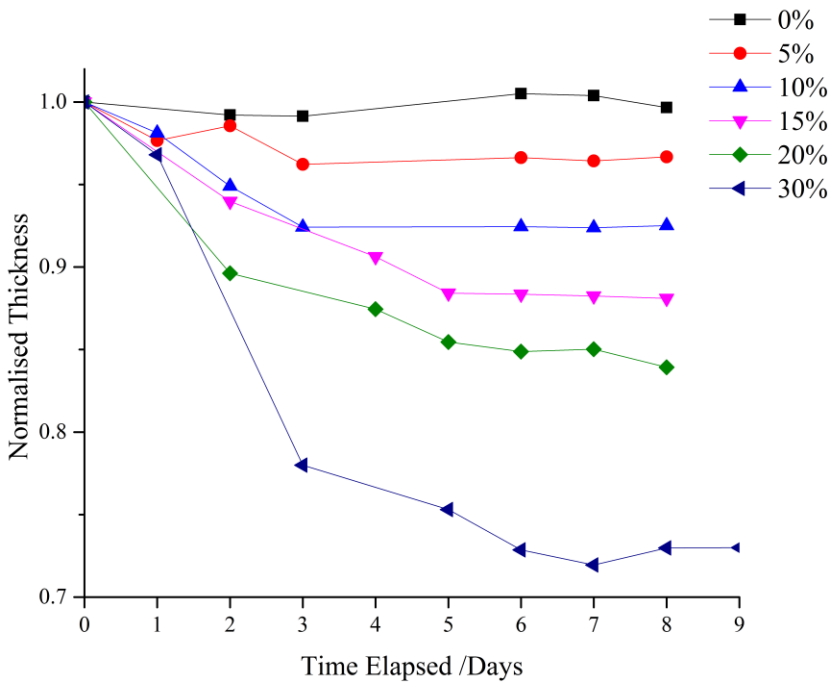

Figure 4.3. Thickness values of for each concentration of glycerol, normalised against their starting thickness.

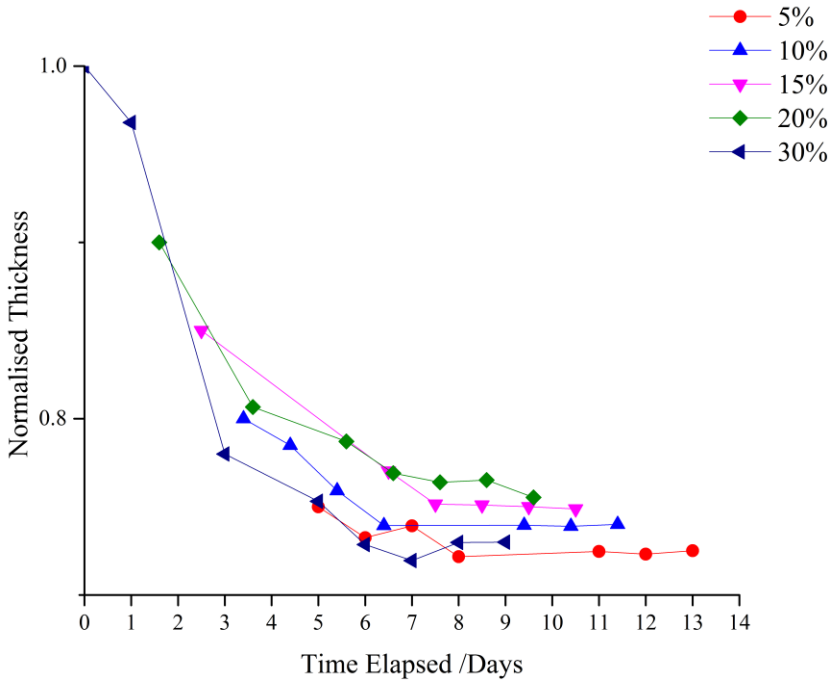

Figure 4.4. Mastercurve of offset data for varying concentrations of glycerol in thin PVA films.

The influence of PVA resin degree of hydrolysis on glycerol loss was explored by repeating similar experiments using Sigma-Aldrich P8136 (M_w = 30–70 kgmol^{-1}, DH = 87–90%). The lower DH and molecular weight bring the physical properties of the polymer more in-line with those used in industry, where lower DH polymers are chosen for their reduced crystallinity and increased flexibility/solubility.[156] From this point on in the study this partially hydrolysed PVA resin is used to conduct all experiments. A

mastercurve was produced in the same way as before and when comparing it to that of the higher DH resin it can be seen that the new resin loses plasticiser quicker, reaching equilibrium at approximately 5 days as opposed to 10-12 days (Figure 4.5.).

Fitting of the mastercurves was achieved using an exponential function to describe the decay of film thickness with increasing time;

$$a(t) = a_\infty + (a_0 - a_\infty)e^{-\frac{t}{t_{\frac{1}{2}}}}$$

Equation 43

where t is the time in days, a_0 is the maximum normalised thickness (1), a_∞ is the minimum normalised thickness and $t_{½}$ is the half-life. Fitting the data using this function until the lowest χ^2 is reached (0.006 for 87-89 %DH and 0.013 for the 99+ %DH) gives a half-life ($t_{½}$) of the plasticiser decay. The calculated half-life for the 87-89 %DH resin is 1.90 days, and for the 99+ %DH resin 2.75 days. Therefore it can be seen that the rate of glycerol loss from a plasticised, high DH PVA film is considerably slower than from a low DH film.

This suggests that the plasticiser is more mobile in the low DH polymer, which may be expected as a lower DH PVA has an increased number of acetate groups, lowering the extent of H-bonding between polymer chains and reducing crystallinity. Glycerol also has less affinity for the acetate groups due to reduced H-bonding potential, so would migrate with greater ease. A reduction in crystallinity means that the polymer chains are more mobile and can flow more easily; this increased freedom of movement within the system will also increase the ability of glycerol to migrate. Diffusion is also thought to occur primarily through the amorphous regions of semi-crystalline polymers,[157] hence as the amorphous regions are larger for the low DH polymer, diffusion will occur with greater ease. Increased crystallinity in polymer films has been shown to decrease permeability of gas molecules also,[158] so it is not unusual that glycerol exhibits a similar trend. It is notable that there is significantly more agreement between the data points of the mastercurve for the lower DH resin compared to the higher DH. This could be a feature of the reduced mobility in the 99+% hydrolysed polymer as the limited mobility of the plasticiser may cause uneven distribution during drying. Although suitable film forming conditions have been realised via spin coating, the instability of thin PVA films containing additives has also been demonstrated. To investigate glycerol migration patterns further two of the primary techniques used in this project, ion beam analysis and neutron reflectometry are employed. These techniques allow information to be obtained on glycerol distribution within a thin film, which could provide an insight into the routes by which the plasticiser is evaporating.

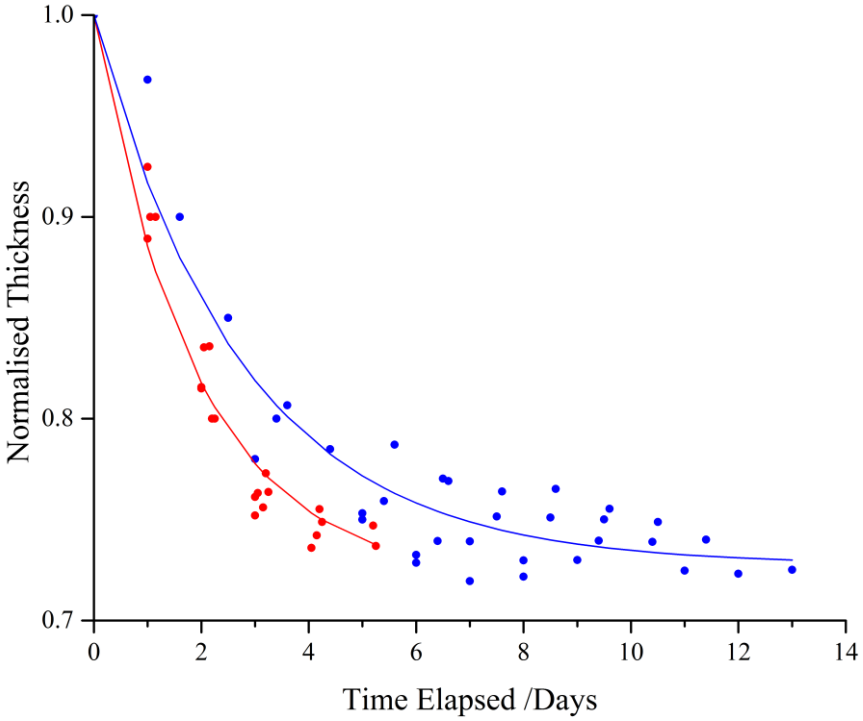

Figure 4.5. Plot of combined mastercurves for Sigma-Aldrich 341584, high DH, 99+% resin (blue) and P8136, low DH, 87-89% resin (red), an approximate line of best fit is displayed for each data set. Fits to data achieved with Origin 2015 Sr2, 5th order polynomial.

4.2. Glycerol Distribution in Thin PVA Films

As discovered in the previous section, if low M_w components such as glycerol are present in thin films, they are susceptible to being lost to the environment. The distribution of these components within the polymer film may help to uncover any concentration gradients present and highlight the areas of the film where plasticiser is most likely to be lost from. One such way to achieve this is with IBA. In order to perform IBA a high vacuum is required throughout the system; therefore any volatiles such as the plasticiser will be lost at a much quicker rate than they would be under standard conditions (RTP). To combat this and maintain sample structure throughout the experiment, films must be vitrified by submerging in liquid nitrogen prior to analysis. As glycerol contains no elements which distinguish it from PVA, a deuterated analogue was used (d_5-glycerol, CK Isotopes). Deuterium labelling allows the ion beam to be used in the NRA configuration, which can explicitly probe deuterium distribution within a sample via the methods previously described. Care must be taken not to use a glycerol with deuterated hydroxyl groups as to avoid isotope exchange between labile OH and OD groups on the plasticiser, polymer and solvent. This precaution maintains the ability to resolve the small molecules from the polymer matrix. 1,1,2,3,3-d_5 glycerol was chosen so that only non-labile C–D bonds were deuterated. The deuterated plasticiser was added to solution the same way as described earlier.

A spin-cast film was irradiated with a beam of 0.7 MeV $^3He^+$ ions at 80° to the sample normal and the energy spectrum of resulting, backscattered protons analysed. Figure 4.6. displays the concentration versus depth profile, raw data and DataFurnace fit (inset) for a thin 87-89% DH PVA film, loaded with 30

w% deuterated (d_5) glycerol. The error bars (here and hereafter) are from the Poisson statistics, i.e. the square root of absolute counts per channel. The sharp onset in the spectrum at 12.77 MeV corresponds to deuterium found at the surface of the film. The gradual decline in proton yield (counts per channel) after this point is due to the decrease in nuclear reaction scattering cross section as the beam penetrates the sample and loses energy. Due to the inverse kinematics of the nuclear reaction in backscattering geometry the protons produced from the surface appear at lower energy in the spectra.[159] The depth profile shows a flat concentration profile for glycerol within these films, indicating homogeneous distribution, which is expected for a sufficiently compatible plasticiser. The slight discrepancy between the fit and the data points at ~13.1 MeV is a feature of sample roughness. A rough sample effectively causes a variance in film thickness, which means incident ions will travel a range of distances before encountering the substrate, beyond which there is no deuterium, causing counts to tail off when approaching the substrate interface. A schematic representation of this can be seen in Figure 4.7. The even distribution shown by Figure 4.6. also indicates that evaporation is slow compared to the rate of diffusion in the PVA film as no concentration gradient is visible, hence formation of a plasticiser wetting layer is unlikely.

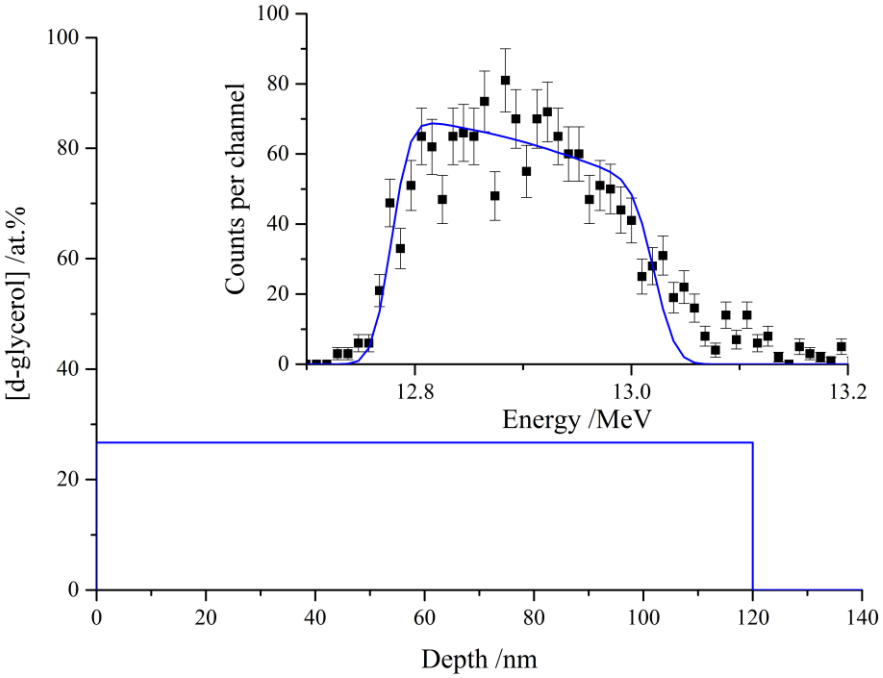

Figure 4.6. NRA (proton spectrum) for 30% d_5-glycerol in a thin PVA film. The fitted curve corresponds to the composition versus depth profile of d_5-glycerol.

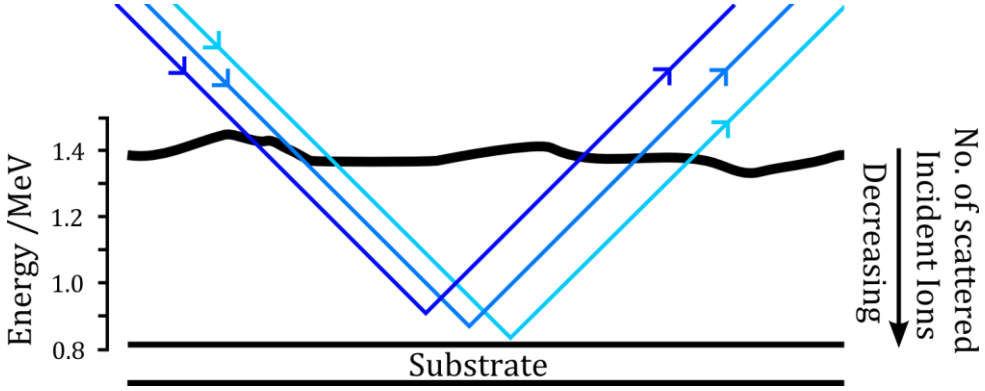

Figure 4.7. Schematic representation of how roughness causes variance in film thickness, reducing counts seen at lower energies, hence making the lower energy edge of the data diffuse.

Neutron reflectometry can provide greater insight in to additive segregation as it provides a better depth resolution of ~0.5 nm, allows study of samples under atmospheric conditions and also gives a direct measurement of roughness, a feature which the films have exhibited. The specular reflectivity, R(Q), was measured from before the critical edge ($Q \approx 0.01$ Å^{-1}) to the point at which the signal is indistinguishable from the background ($Q \approx 0.25$ Å^{-1}). In order to obtain data of sufficient quality over the complete Q range each sample required analysis at three angles of incidence, taking roughly 2 hours to complete. If any change in film thickness was to occur during this time the fringes in the data would become washed out and accurate interpretation of the results would be impossible. Although a definite change in film thickness with time was discovered previously, in comparison to the thickness lost at equilibrium, the change over the course of a few hours is minimal. Based on Figure 4.5. it can be estimated that film thickness loss for a sample with 20 w% glycerol would be ~1% within a 2-6 hour time period, and much less for a film containing 10 w% glycerol. It was therefore deemed that the plasticiser loss during experimental time (2-6 hours) would be insufficient to cause any alteration to the measurement.

Figure 4.8. displays the vertical concentration profile of 10 w% glycerol within a spin-cast PVA film, the raw data and fit achieved with MotoFit are shown in the inset. The error bats arise from the Poisson statistics of the raw count rate detected per Q increment. There is good agreement between the fit and the data, producing a flat concentration profile similar to the one seen with IBA. The initial output from MotoFit is given in the form of a SLD profile, which is converted to an atomic percentage by the methods discussed in chapter 3.3.2. These results confirm the lack of a wetting layer which would lead to an increased glycerol evaporation rate, instead the plasticiser leaves the film at a constant rate whilst maintaining even distribution. This must mean that the rate of evaporation from the surface is slow compared to the rate of redistribution within a film of 70 nm.

The findings so far have indicated that both IBA and NR are suitable techniques to accurately study additive distribution in thin PVA films, both under vacuum and ambient conditions. The agreement between the techniques gives confidence in the results gained from IBA, and provides evidence that submerging the samples in liquid nitrogen prior to analysis has no significant effects on additive distribution. Going forward IBA is generally used as a preliminary experiment, to probe the distribution

of several compounds, and when results indicate interesting behaviour, NR is used to investigate the concentration profiles in more detail. IBA is not without its advantages over NR however, [113] one of which is the size of the incident beam. At incident angles of 70-88° the area on a sample needed for analysis is approximately 2.0 cm in length and 0.5 cm in height. By comparison, an entire 5.5 cm diameter block is needed for NR, meaning that analysis on much smaller, less uniform and rougher samples can be done with IBA. This provides an ability to do analysis on samples like the ones described in the following section. IBA is also more sensitive to gradual changes in composition.[160]

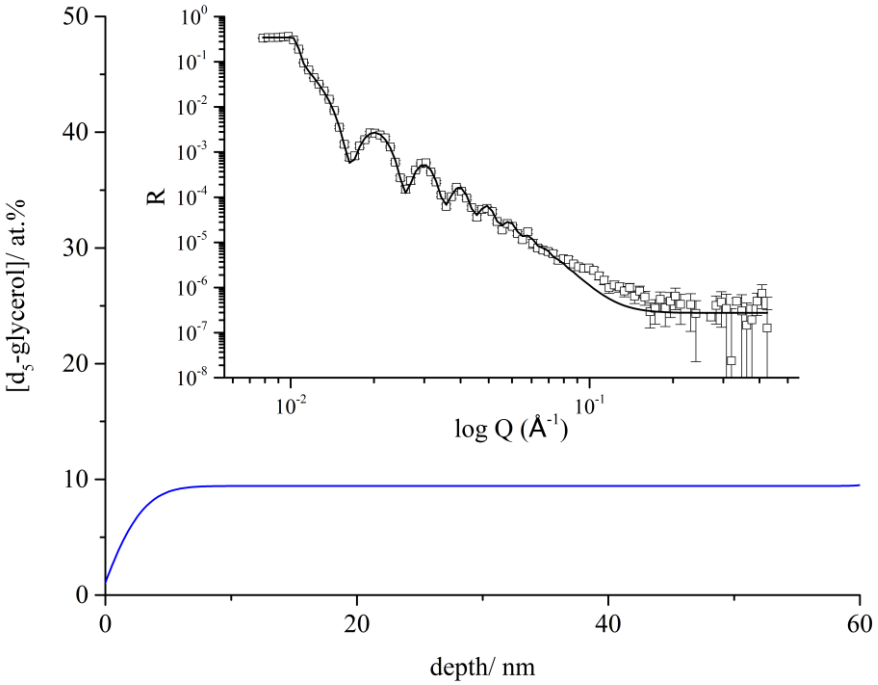

Figure 4.8. Neutron reflectometry data and fit (inset) and corresponding composition profile for 10% d_5-glycerol in thin PVA films

4.3. Barrier Transfer Experiments in Commercial PVA Film

So far plasticiser distribution in thin, spin-cast films has been explored and found to be homogeneous regardless of plasticiser concentration or film thickness. However, it is also of interest in this project to understand the distribution of small molecules in much thicker (76 µm) industrial films, therefore some efforts have been dedicated to exploring more industrially relevant films. Plasticiser loss to the atmosphere and to contacting solutions for thicker films has been studied by several authors[161-163] who state that it can take months for plasticiser exudation to be evident, with exudation usually detected by presence of an oily film on the surface of the polymer. Although glycerol evaporation was detected over a much shorter timescale in thin films, it is likely that by decreasing film thickness while maintaining a macroscopic surface area (3 x 3 cm) to thickness (< 200 nm) ratio an accelerated picture of what migration/evaporation trends may be expected in the thicker films is being studied. Industrial films however are not simple binary (PVA, glycerol) mixtures, and contain many other additives which could be influential on the rate at which components such as glycerol migrate, therefore attempting to draw a

scaling factor from these values to directly compare spin cast films to industrial films may lead to inaccurate results.

It would also be impossible to replicate industrial film composition in spin cast form as some of the larger additives such as silica particles would interfere with film forming. Here we study the ability of glycerol to migrate (or absorb) into the polymer rather than out of it. This is particularly relevant concerning liquitabs, as a portion of glycerol is present in the detergent of which the polymer film encapsulates.[164] This is done to ensure that glycerol does not leach into the detergent, and also to replenish any glycerol that is lost to the atmosphere over the product's lifetime, hence maintaining mechanical properties. If the absorption rate for glycerol into PVA from an area of high concentration is significantly quicker than the rate at which it is lost then it would be unlikely that depletion of glycerol within the film would cause product failure. To study industrially relevant migration a roll of film was supplied by P&G Belgium (MonoSol, M8630), from which samples were cut and analysed with IBA. As the industrial film curls due to the stresses applied when packing and rolling they cannot conveniently be analysed by IBA without some modification. The migration study was scheduled to monitor glycerol migration over the course of a week so prepared films had to be stable for a significant amount of time. To ensure flat, stable films capable of forward scattering; films were attached to a silicon wafer of the same size using double sided adhesive tape (Figure 4.9.). The orientation of the films is of importance when performing this type of experiment as the MonoSol films have a single side coated with silica nanoparticles in order to avoid film cohesion when wound into a roll for transit. This creates a shiny and matt surface to each film, for consumer purposes, but also mechanical advantage, the shiny Si coated side is used as the external surface of the product. Hence migration of molecules from the matt to shiny surface is of interest, as the matt is commonly used as the liquid interface in detergent products. ERDA was used over NRA for this experiment as ERDA allows a direct comparison between the amount of forward scattered hydrogen and deuterium ions (from d_5-glycerol), which enables reliable, quantitative data to be obtained. The data is then converted to a plasticiser concentration depth profile using the molecular weights and densities of the compounds present.

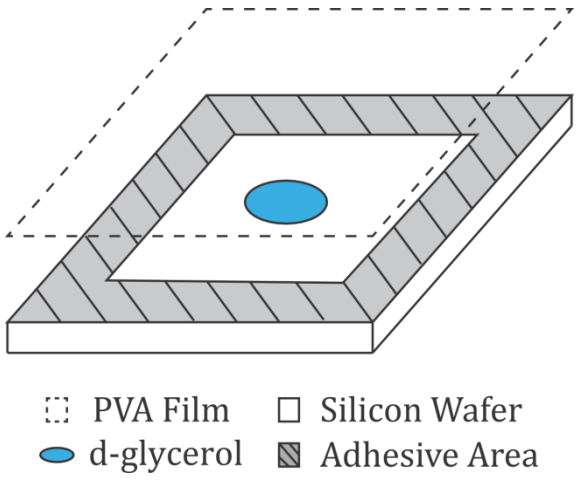

Figure 4.9. Schematic representation of how flat industrial films were maintained by fixing the PVA in place with double sided adhesive tape.

ERDA with a 1.5 MeV ^{4}He beam and 5 μm PET range foil can achieve depth penetration of up to 150 nm; hence any deuterium detected is located in the near-surface region of the 76 μm film, having travelled from the underside. Scattering from the samples after being left under atmospheric conditions for a time period of 1-6 hours is displayed in Figure 4.10. Results with energy below ~1.0 MeV are due to forward scattered hydrogen, and above representative of deuterium. Although the film used to create each sample is from the same roll, and should therefore exhibit very similar hydrogen scattering profiles, it is difficult to ensure each sample is irradiated with the same total integrated beam current (electric charge, μC). It is also very difficult to ensure identical alignment for each sample, which leads to small variations in the energy of detected recoils. Therefore fitting software such as DataFurnace must be used to account for this variation. From first glance however, the general consistency of the hydrogen scattering profile between samples can be compared to the clear increase in counts seen with time in the deuterium scattering. This signifies more deuterium has been detected, and hence more glycerol is being detected in the near-surface region of the film. Fitting each dataset with DataFurnace provides accurate quantification of deuterium within the sample. Each ERDA depth profile produced a homogeneous layer of glycerol, which increased in concentration with time. Using these calculated concentrations with time the amount of glycerol transfer (δ) in grams per metre squared per day ($gm^{-2}day^{-1}$) can be realised;

$$\delta = \frac{[\alpha].M_w.\rho.\varepsilon}{[\alpha].M_w + [\beta].M_w}.10000$$

Equation 44

where; $[\alpha]$ is concentration of d_5-glycerol (at. %), $[\beta]$ is concentration of PVA (at. %), ρ is average density of the sample (gcm^{-3}) and ε is film thickness (cm). Plotting these values against the time lapsed in days gives a gradient which is equivalent to the amount of glycerol transferred. Data for 1-6 hours can be seen in Figure 4.12. The discrepancy between the fits and collected data <1.0 MeV is perhaps due to the beam damage imparted on the sample during analysis, or an imperfect calculation of sample stopping power. The 'kink' in the fits at ~0.45 MeV is due to a weak resonance in the $^{1}H(^{4}He, ^{1}H)^{4}He$ scattering, but is not resolved in the noise of the data.

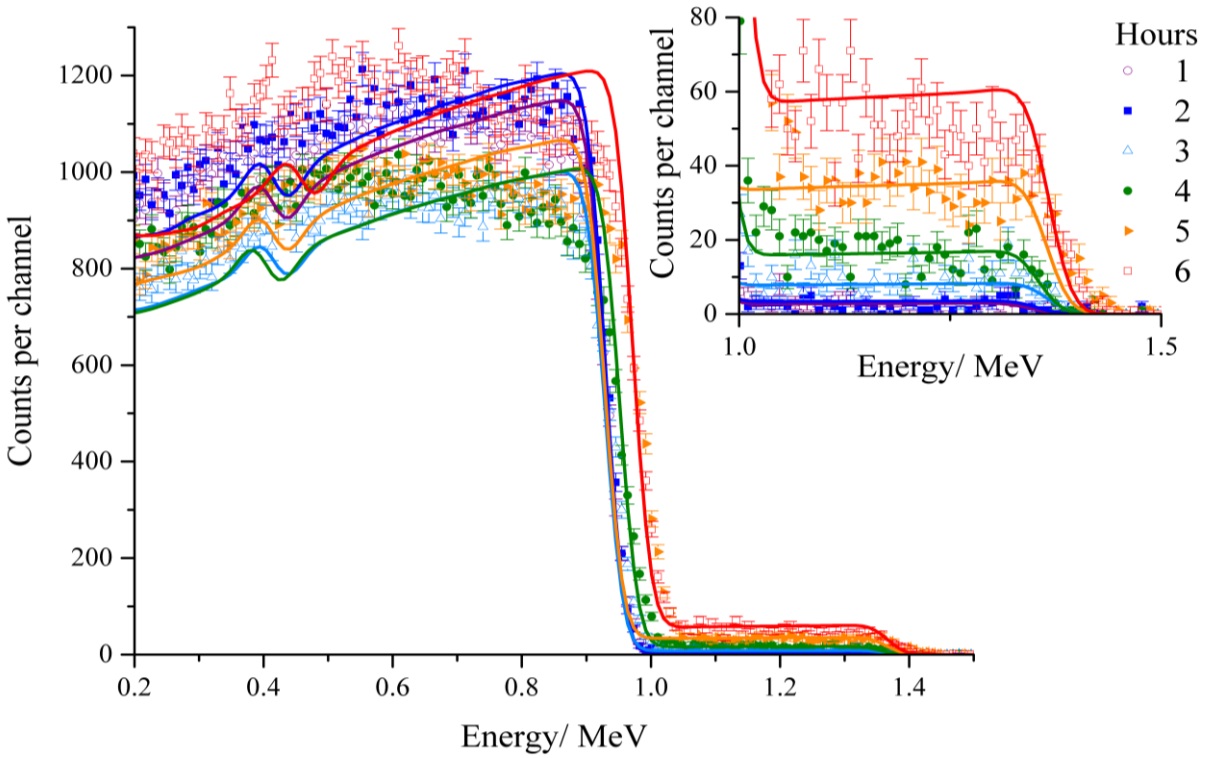

Figure 4.10. Barrier transfer ERDA data for migration timescale of 1-6 hours, with a zoomed plot of the deuterium resultant scattering shown in the inset.

After obtaining data for samples that had been allowed 1-6 hours to equilibrate, the time period was extended to 7 days (Figure 4.11.). The charge variance between samples in this group of experiments was much greater than previously, thought to be due to the films exhibiting more defects over the extended time period. Not only does the number of counts vary significantly; there is no particular trend that can be seen in the deuterium region at first glance. Without the variance in charge being accounted for in DataFurnace, effective analysis of this data would have proved difficult. A plot of calculated glycerol surface density with time can be seen in Figure 4.12., from which the gradient of a linear line of best fit can be used to calculate an absorption rate. The data shows an initial rate of absorption of 30.7 $gm^{-2}day^{-1}$ in the first 6 hours, which slows to 2.3 $gm^{-2}day^{-1}$ thereafter. If the time period was extended beyond 7 days it may be expected that the rate of absorption will plateau when a maximum glycerol concentration is reached within the film, however the data shows no evidence of this point within the first week.

The approximate size of a liquitab is 5 x 5 cm, giving a total surface area of ~50 cm^2. Therefore as 1 $gm^{-2} \equiv 0.1$ $mgcm^{-2}$, it can be said that the amount of glycerol transfer per liquitab per day is 153.5 mg in the first 24 hours, and 11.3 mg per day after the initial 24 hour period. Both values are significant quantities of glycerol, more than what could be feasibly lost from an industrial film within the time period studied. Therefore it can be said that as long as there remains enough glycerol in the bulk detergent solution, the rate at which it can be absorbed into an industrial PVA film outweighs the rate at which it could be lost. So unless the glycerol in the solution is depleted within the products natural lifetime, de-plasticisation of the film is unlikely to be the cause of product failure.

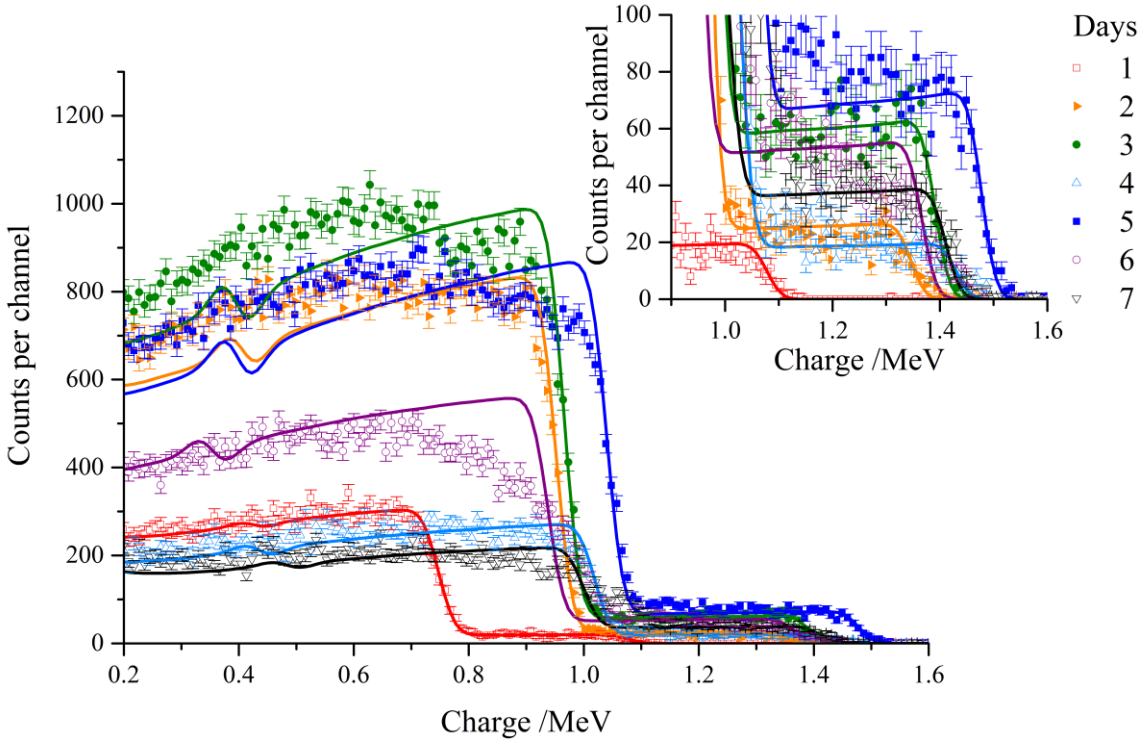

Figure 4.11. Barrier transfer ERDA data for migration timescale of 1-7 days, with a zoomed plot of the deuterium resultant scattering shown in the inset.

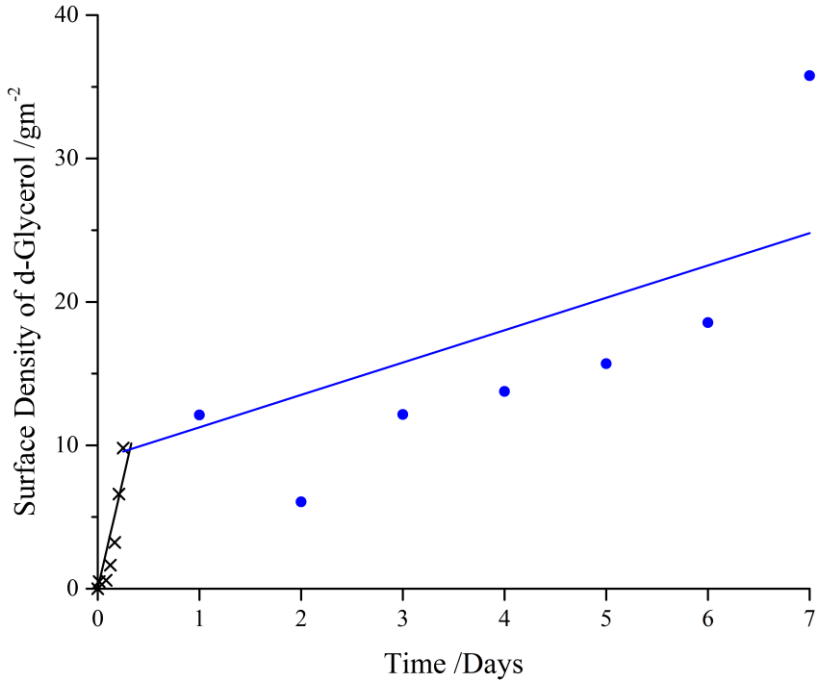

Figure 4.12. Near-surface concentration of d_5-glycerol accumulated after migration through a 76 µm commercial PVA film. A line of best fit is shown for each dataset, 1-6 hours (black) and 1-7 days (blue) giving absorption rates of [d-Gly / gm^{-2}] = 30.70 (time/days) and 2.26 (time/days) respectively.

Several conclusions can be drawn from the work performed throughout this chapter for thin spin-cast plasticised PVA films and thicker belt-cast plasticised industrial PVA films. It has been shown that glycerol exhibits homogeneous distribution in spin-cast PVA films, consistent with good suitability to plasticise PVA. It is possible to quantify glycerol evaporation in thin films through ellipsometry measurements at room temperature and atmospheric pressure. For thin films of high DH PVA, the rate of glycerol loss appears relatively significant, losing most of its mass and reaching equilibrium after approximately 5 days. Increasing the DH of the polymer causes the evaporation rate to decrease – reaching equilibrium at approximately 10 days. The evaporation rate is however slow compared to the redistribution rate of glycerol in PVA as no concentration gradient of the plasticiser was seen with scattering techniques. Evaporative loss of glycerol from PVA is also slow compared to the rate of glycerol replenishment from a glycerol source.

Another major component of detergent formulations, other than glycerol, is surfactants, which are also able to migrate into thick PVA films, being found on the surface of liquitabs after prolonged storage. Despite this phenomenon, and related observation of 'blooming' of fat in chocolate etc., surfactant migration and segregation in solid polymer films has received little attention in the literature. The following chapters address the behaviour of non-ionic and ionic surfactants in thin PVA films.

5. Non-ionic Surfactant Segregation in PVA Film

Non-ionic surfactants make up the bulk of surfactants used in industry, accounting for approximately a third of the global surfactant market. To give an idea of the industrial scale of surfactant usage, the surfactant market for personal care alone was estimated at US$6.49 billion in 2016.[165] Non-ionics generally tend to be long, linear compounds, which exhibit surfactant-like properties due to the presence of a long hydrocarbon chain (lipophilic) at one end of the molecule, and a long, oxygen-containing (hydrophilic, commonly a polyoxyethylene) chain at the other end.[166] The lack of a counter-ion means these compounds do not produce ions in aqueous solutions, allowing them to exhibit excellent miscibility and good solubility at low temperatures, meaning they can be placed into many commercial products with a low risk of phase separation.[167] They can be found in cosmetics as oil in water emulsifiers due to their generally high HLB,[168] or in cleaning products such as those used in hand dishwashing or shampoo to boost foaming.[169]

As these compounds are not found in the natural environment, when found on the surface of a product such a liquitab, they can only be present as a result of migration from within the product to the outer surface. There are two possible sources of surfactant origin, either in the detergent (or 'juice', as it is called in industry), as a cleaning agent, or from within the films themselves, which are doped with surfactant during manufacture. Regardless of the source of surfactant, their ability to collect in relatively high concentrations at interfaces may be a window in to discovering the reasons behind seal failure. We aim to shed light on this subject area, and for the first time investigate what dictates surfactant migration tendencies in polymer films. It has already been shown that IBA and NR are excellent tools for exploring the way smaller molecules behave in a larger matrix, therefore scattering techniques will remain at the forefront of this investigation. Some of the work on $C_{12}E_5$ segregation described in this chapter has been published in our initial work.[170]

5.1. Pentaethylene Glycol Monododecylether ($C_{12}E_5$) Segregation in Thin PVA Films

The segregation behaviour of $C_{12}E_5$ in non-plasticised and plasticised PVA films under a variety of atmospheric conditions is studied in the following chapter. Deuteration of compounds has proved a successful method to study segregation so far, hence a deuterated analogue (d_{25}-$C_{12}E_5$) prepared by Dr. Peixun Li at Rutherford Appleton Labs (RAL) was used in these experiments. Significant deuteration of the surfactant is required in order for it to be detectable in low concentrations by IBA; this can be most easily done by Williamson synthesis from a deuterated alkyl bromide.[171-172] This produces a surfactant with a deuterated alkyl chain and hydrogenous pentaethylene glycol region, having a percentage deuteration of > 50%. Distribution of the surfactant in both binary (non-plasticised) and ternary (plasticised) PVA films will be discussed.

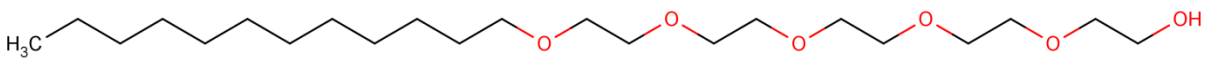

Figure 5.1. MarvinSketch structure of pentaethylene glycol monododecyl ether ($C_{12}E_5$).

5.1.1. Distribution in Binary Films

As the surfactant is deuterated ERDA and NRA are both suitable IBA techniques to probe the vertical depth distribution, ERDA giving greater quantification of surfactant amounts and NRA giving better resolution of surfactant structure within the sample. ERDA was performed first on a sample containing 25 w% d_{25}-$C_{12}E_5$ in PVA. The resulting scattering is displayed in Figure 5.2. with the calculated DataFurnace fits. The depth profiles produced by these fits are displayed in Figure 5.3. Counts seen below 0.55 MeV are representative of hydrogen within the sample, and above 0.55 MeV representative of deuterium. The yield seen for hydrogen is much greater than deuterium as is expected for a partially deuterated surfactant present in relatively low weight percent in a hydrogenous matrix. Therefore displaying the plot in Log_{10}Counts (Figure 5.2., inset) allows better comparison between the scattering profiles. Two separate fits are required to achieve a depth profile when performing ERDA, one for each of the forward scattered elements. Although the fits are separate, they are also interrelated as the composition profile of one component cannot be changed with changing the other. These are shown in red and black for hydrogen and deuterium respectively. The deuterium profile shows two peaks at approximately 0.59 and 0.64 MeV, indicating two distinct layers of enrichment in the composition profile of surfactant. Resolved with DataFurnace these peaks are converted to a d_{25}-$C_{12}E_5$ surface excess of 41nm thickness, 24 at. % and a silicon (substrate) excess of 25 nm thickness, 80 at. %. The hydrogen distribution shows a single peak in the spectrum, which may be construed as a homogeneous layer without DataFurnace fitting. However it is possible to see from depth profile that there exist two regions of depleted hydrogen which correspond to the excesses of surfactant. To study this segregation further with improved depth resolution (~8 nm) complimentary NRA experiments were performed with varying weight percentage of surfactant.

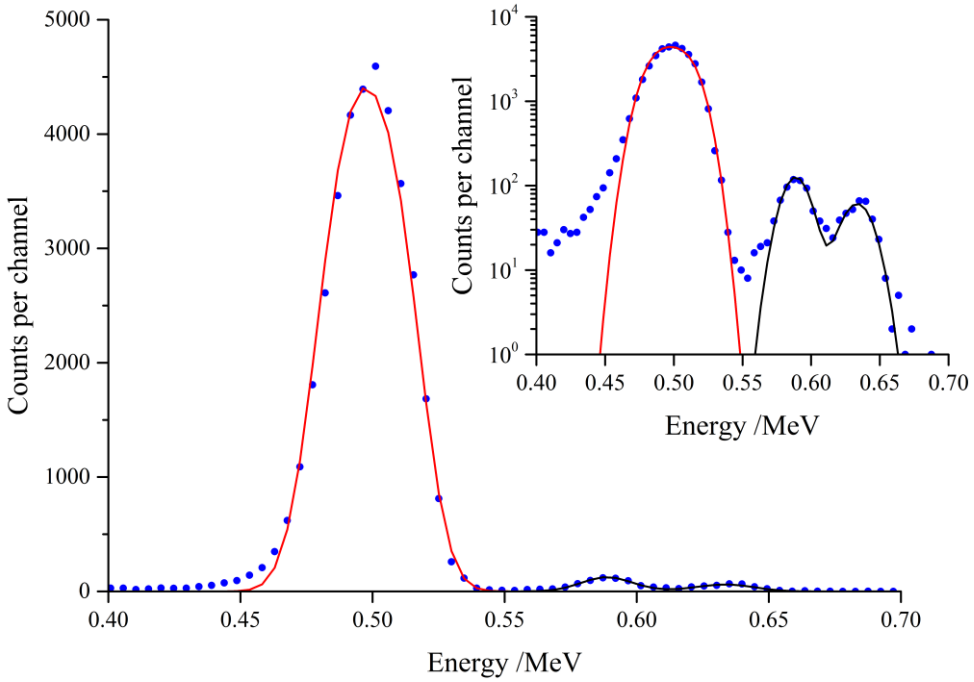

Figure 5.2. ERDA scattering for a thin PVA film containing 25 w% of d_{25}-$C_{12}E_5$ with DataFurnace fits, log plot shown in the inset.

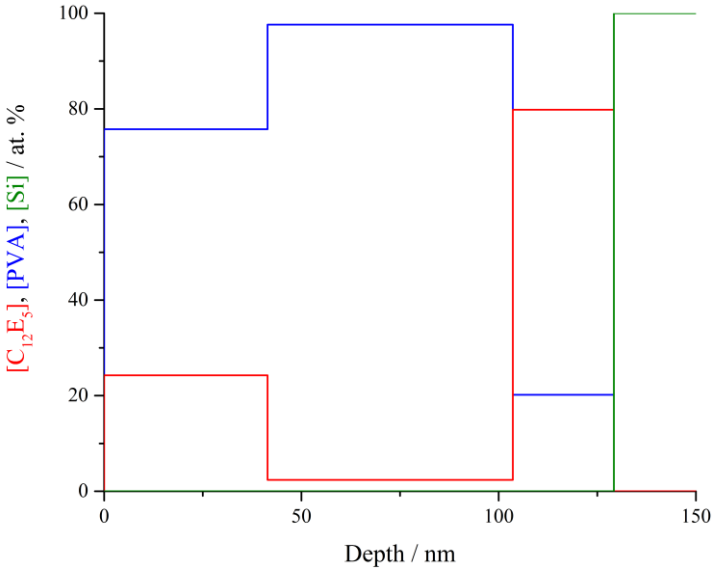

Figure 5.3. Distribution of d_{25}-$C_{12}E_5$ in a thin PVA film produced with DataFurnace, displaying each logical element (LE); LE1 – d_{25}-$C_{12}E_5$ (red), LE2 – PVA (blue) and LE3 – Si (green).

The concentration of surfactant was chosen to be 5, 15 and 25 w%. Comparing results from ERDA and NRA for the 25%, formation of the surface excess is still apparent, but with the increased sensitivity of NRA the composition profile changes dramatically. Thickness of the surface excess was reduced from 41 nm to 8 nm, and the concentration of the surface concentration increased from 24% to 77%. Note that the reduced surface excess thickness of 8 nm is comparable to the resolution of NRA, therefore precise purity is still not exactly determined. These results do however suggest that an almost pure layer of

surfactant is being formed at the surface of the PVA film during spin-coating. The substrate excess remains comparatively similar regardless of the IBA technique used. An excess is defined as;

$$z^* = \int_0^\infty \varphi(z) - \varphi_b dz$$

Equation 45

where φ_b is the bulk concentration adjacent to the surface excess region, and $\varphi(z)$ is the depth (z) dependent volume fraction profile of the near surface region. Plotting of z* values helps to quantify changes in surface excess with parameters such as concentration. If the excess contains more than one surfactant-rich layer then summing the z* values for each consecutive layer provides a representation of total surface excess. z* values for Figure 5.4. are 4.7, 6.8 and 7.2 nm for 5, 15 and 25 % d_{25}-$C_{12}E_5$, indicating an increase in the amount of surfactant seen at the surface with increasing concentration. Surface tension measurements on aqueous surfactant solutions have shown that surface tension will decrease with increasing surfactant concentration, signifying an increase in the concentration of surfactant within the surface excess,[173] mirroring the results found with polymer films here. However, the concentrations are much higher in these PVA films than would typically be measured in water.

Considering the surface energy (SE) values of the components present in the film can help to explain why this segregation behaviour is observed. A number of surface energies of PVA have been reported; two sources quote it as 37 mNm^{-1} at 20 °C, where SE was calculated from the molecular constitution[174] and glass transition (T_g)[175] of the polymer. Another source which also calculates SE from T_g gave a value of 49 mNm^{-1}.[176] The SE has also been calculated from acid-base analysis[177] and the parachor parameter[178] to give values of 42 and 59 mNm^{-1} respectively. This disagreement between sources is not only a measure of the variety of techniques used to calculate SE but also a result of PVA's properties being largely dependent on its polymeric characteristics, particularly DH. As different sources typically compare different resins, it is difficult to compare the precise DH of each material to the one being used in this study. However the SE of PVA has been shown to decrease with decreasing DH,[179] therefore as the PVA used in this study contains at least 10% PVAc, it can be presumed that the partially hydrolysed polymer resin would give a SE value towards the lower end of the established values. SE has also been shown to increase with increasing molecular weight for several polymers such as polystyrene, polypropylene and polethylene.[180-182] As the PVA resin used in this study is of relatively low M_w it also suggests the SE of PVA is likely to be at the lower end of the scale. Going forward the SE of the PVA resin used in this study will be assumed to be approximately 40 mNm^{-1}. As $C_{12}E_5$ is a liquid it is not possible to measure surface energy, however the surface tension (ST) has been well-studied. $C_{12}E_5$ has a limiting surface tension of 29.9 mNm^{-1} at concentrations of ≥ 0.1 mM in water,[183] which is considerably lower than any measured value for the SE of PVA. This means that surface adsorption of d_{25}-$C_{12}E_5$ in PVA is favoured by the reduction in SE of the entire system caused by agglomeration of the non-ionic surfactant at the air interface. If the ST/SE of the surfactant was higher than that of PVA, there would be no favourable reduction of sample SE by segregation and the surfactant may be expected to exhibit homogeneous distribution.

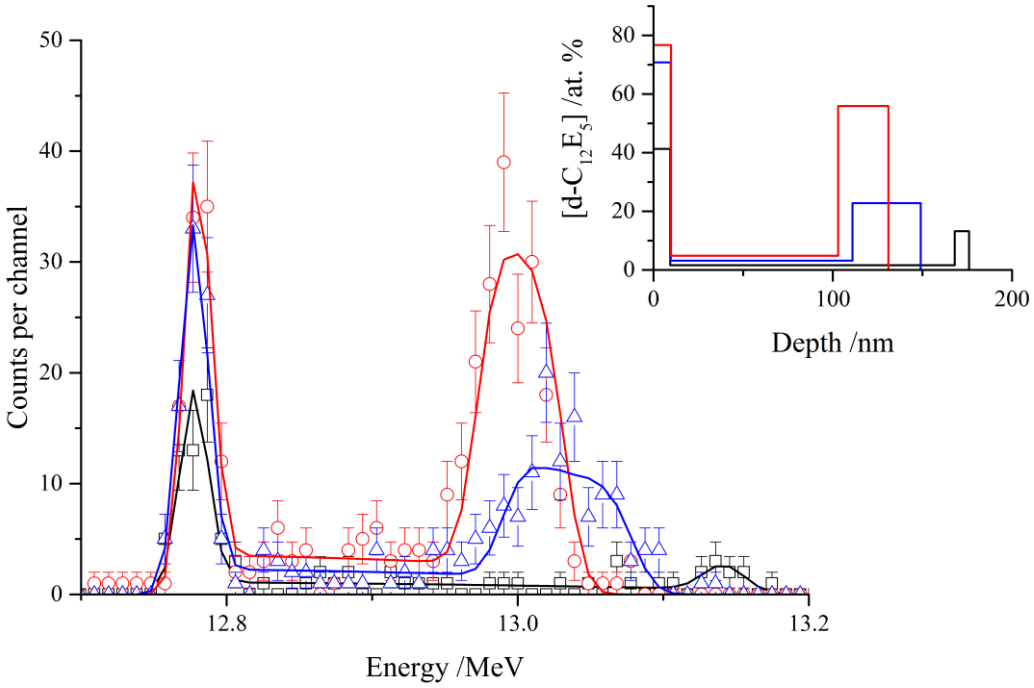

Figure 5.4. NRA data and DataFurnace fits for 5 (black, open squares), 15 (blue, open triangles) and 25 (red, open circles) w% d_{25}-$C_{12}E_5$ in PVA, produced depth profiles shown in the inset.

To investigate the spontaneous segregation of d_{25}-$C_{12}E_5$ further, neutron reflectometry (NR) was used to allow the replication of the previous experiments with even greater precision under ambient conditions. Figure 5.5. displays reflectivity data (offset) for 10, 20 and 30% d_{25}-$C_{12}E_5$ in PVA, as well fits achieved with MotoFit. Although the depth profiles appear slightly different when comparing the two techniques, the overall conclusion is consistent between analysis methods; d_{25}-$C_{12}E_5$ has again been shown to segregate to the surface and interface of thin PVA films. The surface excess appears thinner, and less concentrated when analysed with NR. This is likely to be a feature of the decreased film thickness necessary for neutron experiments, or caused by inclusion of a roughness parameter in NR fitting. Although the surface excess measured is thinner, the impact of surface excess formation on the bulk concentration is still significant. An increase in the amount of surfactant seen at the surface as concentration increases is also evident again.

Another interesting feature has presented itself at the highest concentration where the thickness of the surface excess increases significantly. It is unexpected that the concentration of surfactant at the surface does not increase above 60 at. % when there is an abundance of d_{25}-$C_{12}E_5$ in the system, which would be capable of forming a complete wetting layer. A similar feature was also apparent in the NRA data where the concentration of surfactant at the surface does not increase beyond ~75 at. %. When studying the sample with IBA, the additional surfactant is found at the silicon interface rather than just below the surface excess. This may be a result of the increased timescale of NR experiments, wherein surfactant initially present at the substrate excess after spin-coating migrates to the surface as the molecules are free to move under atmospheric conditions, rather than being vitrified for IBA. Quantification of the surface excess by both techniques shows formation of a significant surfactant layer which contains some quantity of PVA (25-40 w%, depending on the technique). The total value of z* far

exceeds what would be possible for a single layer of surfactant at the surface. The maximum all-trans length of a $C_{12}E_5$ molecule is ~3.7 nm (calculated using MarvinSpace with MarvinSketch v 6.2.0.), therefore even if the surfactant was orientated perpendicular to the plane of the PVA film, two end-on-end surfactants would not provide the necessary length to produce a surface excess of ~8 nm.

Experimental and computational studies of $C_{12}E_5$ adsorption on water show that the surfactant forms single layers with the hydrophobic tails pointing out at a tilted angle, so an end-on-end orientation is very unlikely. Although the orientation of the surfactants cannot be resolved with NRA or NR for a PVA containing system, the significance of the surface excess is apparent. As there was some evidence to suggest surfactant migration over time when comparing the NRA to NR results, an investigation in to surfactant distribution with time was launched.

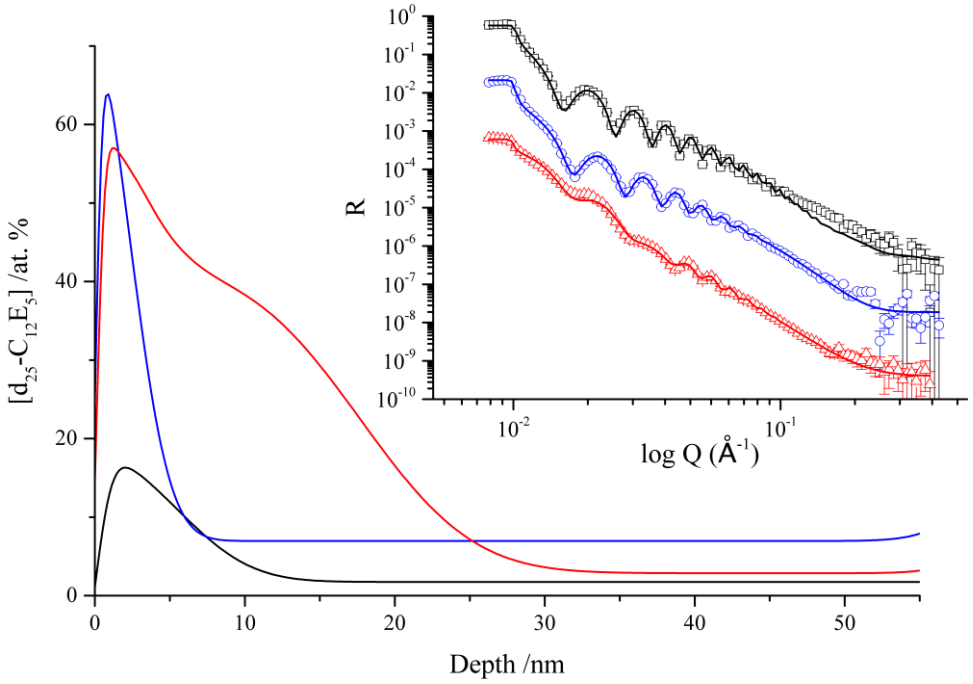

Figure 5.5. Near-surface composition profiles (main body), NR data and MotoFit fits (inset) for 10 (black, open squares), 20 (blue, open circles) and 30 (red, open triangles) w% d_{25}-$C_{12}E_5$ in PVA

5.1.2. Variation of Non-Ionic Surfactant Distribution over Time

Glycerol has been shown to be volatile in thin films, with most of its mass being lost after 3-5 days, so it is not unreasonable to assume the non-ionic surfactant may be subject to a similar evaporation rate. NR also suggests qualitatively different behaviour of the non-ionic surfactant from NRA (lack of substrate excess), this implies that as NR samples are not vitrified immediately after forming, and have increased equilibration time, that a change in surfactant distribution over time is likely occurring. A solution containing 25 w% d_{25}-$C_{12}E_5$ was spin cast to give films of approximately 140 nm thickness. Samples were allowed to equilibrate under ambient conditions for a set time, after which they were vitrified in liquid nitrogen and analysed via ERDA. Figure 5.6. shows the resulting scattering for each sample, offset so that the plots are displayed from top to bottom as equilibration time is increased. The time increments used

were 0, 1, 3, 6, 24 and 48 hours, deuterium and hydrogen scattering for each sample is displayed in Figure 5.6. In order to view both scattering profiles simultaneously they are plotted in log form. However viewing the scattering as a log plot does not allow small changes in counts to be seen easily; therefore a non-log plot of the deuterium region only can be seen in Figure 5.7. Evident from this plot is a clear decrease in the overall counts for deuterium as samples are allowed more time equilibrate. Despite this decrease with time the overall profile remains largely intact. Fitting with DataFurnace enables these changes to be quantified, accounting for any fluctuation in charge between samples; the depth profiles for each fit are displayed in Figure 5.8.

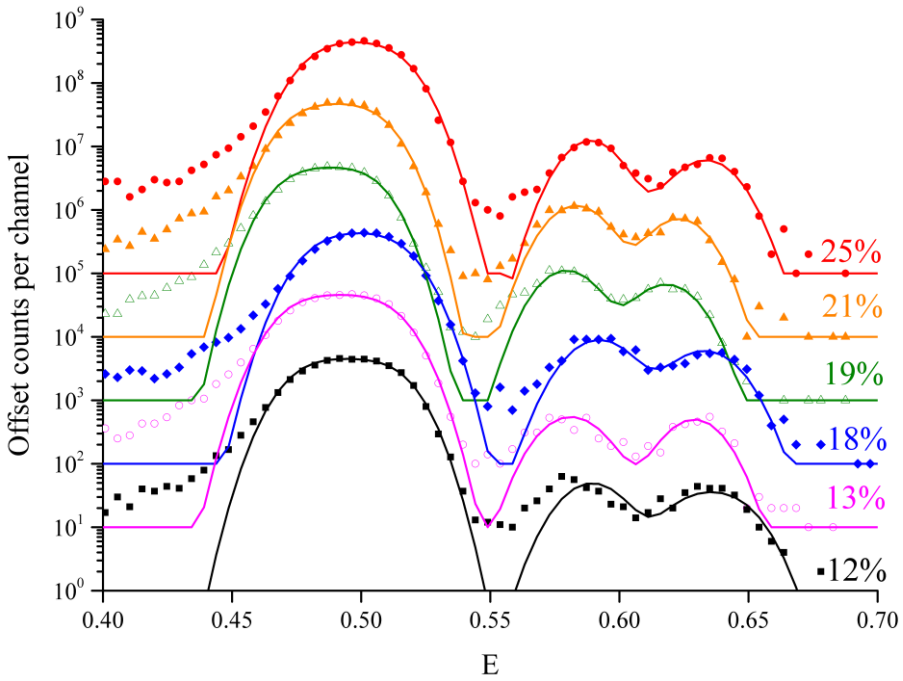

Figure 5.6. Offset ERDA data and DataFurnace fits for 25% d_{25}-$C_{12}E_5$ in PVA after being cured under atmospheric conditions for 0, 1, 3, 6, 24 and 48 hours, going from top to bottom.

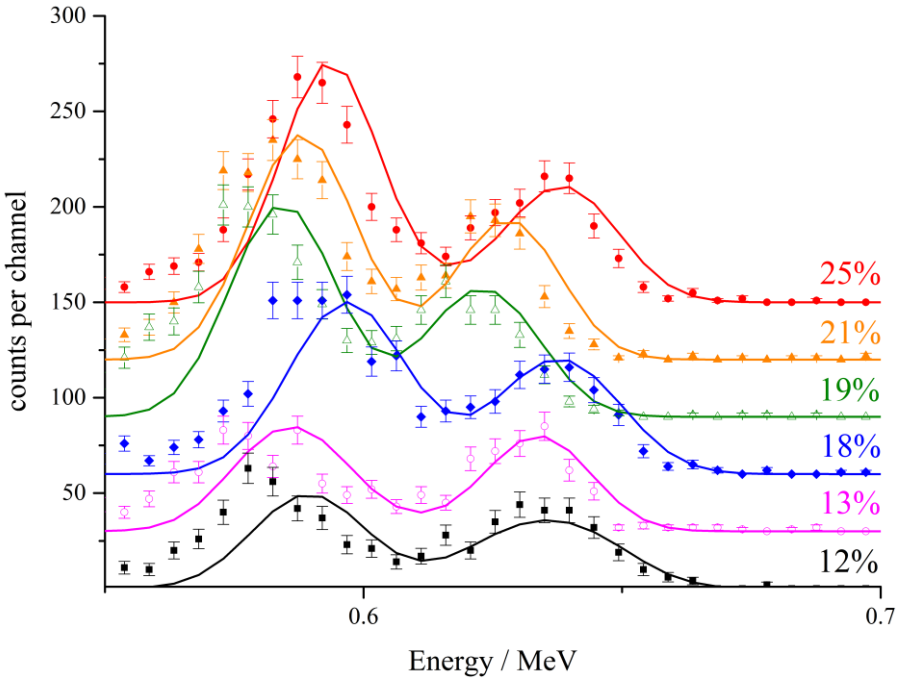

Figure 5.7. Offset ERDA data and DataFurnace fits for deuterium only in samples of 25% d_{25}-$C_{12}E_5$ in PVA after being cured under atmospheric conditions for 0 (top), 1, 3, 6, 24 and 48 hours (bottom). The total concentration of deuterated surfactant detected at each interval is given at the end of each plot.

The depth profiles have a similar distribution to what was found with ERDA in the previous section, where for both a substrate and surface excess are apparent for each sample, with the surface excess being less concentrated than the substrate excess. Interestingly this result is the opposite to what was found with NRA and NR, where the surface excess is more concentrated. Figure 5.7. includes the overall concentration of d_{25}-$C_{12}E_5$ (σ) remaining in the film at the point of analysis, which has been calculated using the depth profiles produced in DataFurnace (Figure 5.8.), for example with the 25 w% data;

Table 5.1. Example calculation of total surfactant concentration from thickness and concentration parameters derived from the DataFurnace depth profile.

Layer	[d_{25}-$C_{12}E_5$] /at. %	Thickness /nm	[d_{25}-$C_{12}E_5$] .Thickness
1	24.3	41	996.3
2	2.4	63	151.2
3	79.8	26	2074.8
Σ		130	3222.3

$$\sigma = \frac{\Sigma\, dC_{12}E_5.Th}{\Sigma\, Th} = 24.8\ \%$$

Equation 46

where Th is the thickness of each individual layer.

Normalising the surfactant concentration (σ) values at each time interval to the starting concentration allows the evolution of the depth profile with time to be studied. Figure 5.9. shows the normalised values for both the surface and interface excess, both of which show a decrease in the amount of surfactant detected over time, suggesting that d_{25}-$C_{12}E_5$ is being lost from the film. The initial rate of loss is greater, slowing with time and plateauing after approximately 3 days. This timescale is very similar to the time taken for glycerol loss to become static, which is surprising as the surfactant has a much higher molecular weight so would be expected to be less volatile. It is possible that because the surfactant has reduced polarity compared to glycerol due to the large hydrocarbon chain, this may cause less favourable interaction with PVA. This could make the surfactant more volatile and compensate for the hindrance of the increased molecular weight, possibly causing both compounds to exhibit similar evaporation rates. It appears that the macroscopic surface area to thickness ratio in these thin, spin-cast films can cause even reasonably heavy molecules to be lost to the atmosphere at a significant rate. The way in which the distribution changes over time is also interesting as the substrate excess decreases more significantly in comparison to the surface excess. Intuitively surfactant would be expected to be lost from the surface as it is exposed to the atmosphere. Being collected on the surface would leave the surfactant more susceptible to factors such as temperature, humidity and air-flow, which may increase the rate of evaporation. One explanation to this reduction at the substrate excess could be that the surfactant is migrating through the depleted region between each excess as the sample maintains its surface energy and composition of surfactant at the surface as it lost to the environment. This may seem unlikely as the films are mostly solid polymer and a significant amount of d_{25}-$C_{12}E_5$ is lost in the first hour, hence migration would have to be possible in large quantities. However glycerol has been shown to possess the ability to migrate quickly through this medium so it is plausible that the surfactant can also exhibit rapid migration through the polymer.

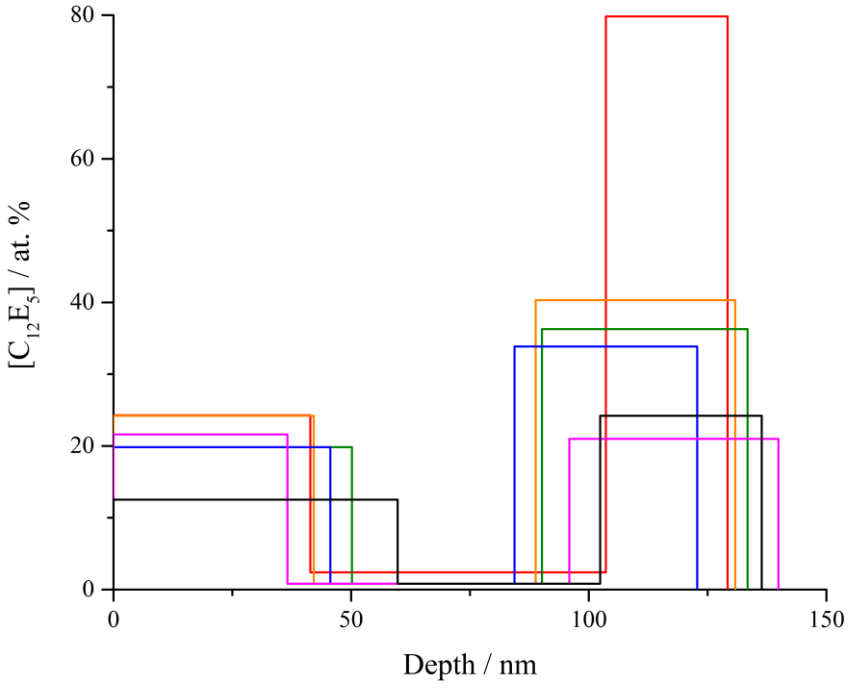

Figure 5.8. Calculated depth profiles achieved with DataFurnace for timescales including 0 hour (red), 1 hour (orange), 3 hours (green), 6 hours (blue), 24 hours (pink) and 48 hours (black).

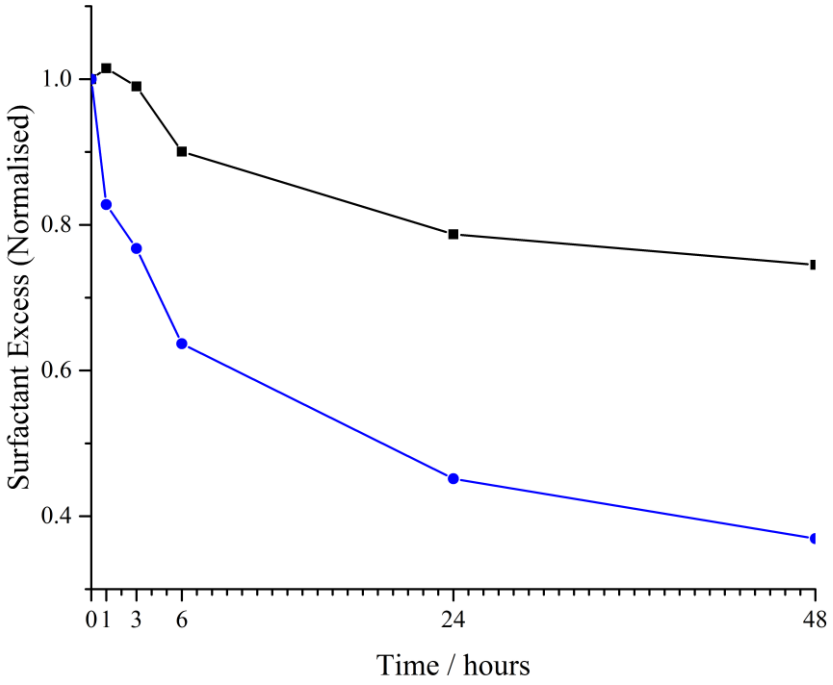

Figure 5.9. Normalised percentage concentration d_{25}-$C_{12}E_5$ values for each sample plotted against equilibration time for both the surface (black) and substrate (blue) excess.

5.1.3. Distribution in Ternary PVA Films

As plasticisers are present in almost all commercial PVA films used in industry it was of interest to study the effects of plasticisation on surfactant distribution by introducing glycerol to the films. Glycerol was added to the PVA/surfactant solutions and spin cast. NRA has been shown to be more accurate and in greater agreement with NR, therefore it was used over ERDA to study distribution of deuterated compounds in ternary films. As 20 w% of plasticiser is the quantity generally used in industrial films, this concentration was explored as well as 10% either side of this ideal quantity to gain an understanding of how an under and over-plasticised film might behave. All films were analysed immediately after spin-casting and the raw data, fits and depth profiles are displayed in Figure 5.10. The first trend of note is the reduction in film thickness with increasing plasticiser content. This is because any added glycerol is replacing the equivalent concentration of polymer in solution as the surfactant concentration is kept constant throughout (30%), hence films will become thinner. Initial non-plasticised results were very similar to what was documented previously, with a highly concentrated, thin surface excess and less concentrated but thicker substrate excess of surfactant. It is very clear from these results that plasticisation causes a systematic reduction in surface activity of the non-ionic surfactant, reducing the mass fraction of d_{25}-$C_{12}E_5$ from ~90 at. % to as low as ~55 at. %. Increased compatibility between surfactant and polymer in the bulk of the film can also be seen with plasticisation as the bulk

concentration of d_{25}-$C_{12}E_5$ increases from 5 at. % to 8-9 at. % when significant plasticiser (≥ 20 w%) is present.

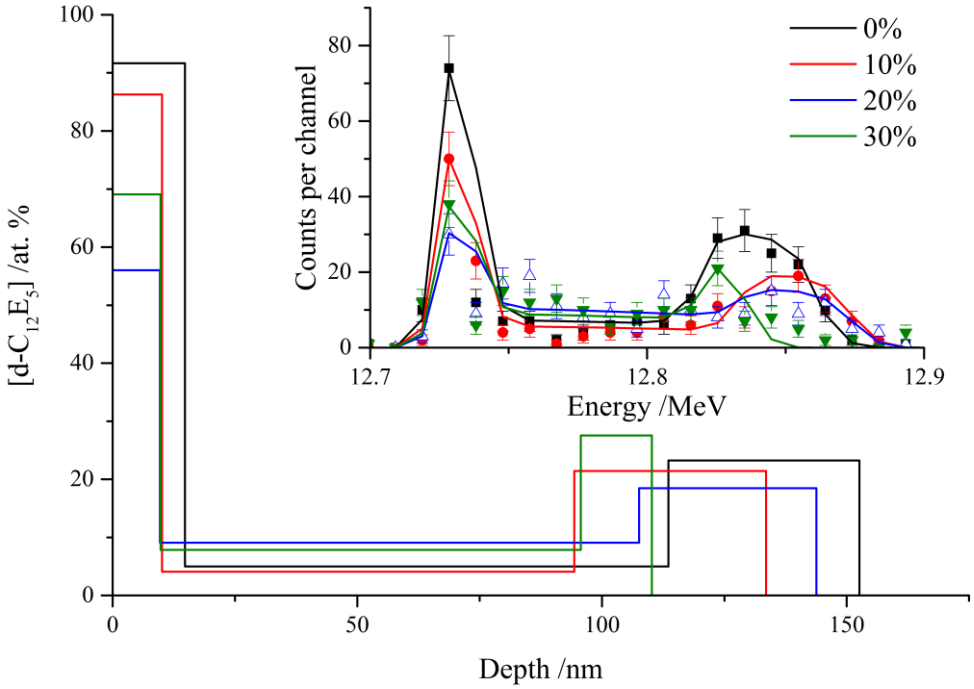

Figure 5.10. Concentration profiles of 30% d_{25}-$C_{12}E_5$ in mixed PVA/glycerol films as a function of glycerol content. Glycerol concentrations are indicated in the main figure. NRA data and fits are shown in the inset.

Complementary NR experiments were carried out to investigate this phenomenon further. Due to the restricted beam-time, only one plasticiser concentration was explored. The concentration of d_{25}-$C_{12}E_5$ was kept constant at 20 w%, and NR data was acquired in both a non-plasticised PVA film, plus a film containing 20 w% of hydrogenous glycerol. The labelled components were then exchanged; deuterated surfactant (d_{25}-$C_{12}E_5$) for hydrogenous (h–$C_{12}E_5$), and hydrogenous glycerol (h-glycerol) for deuterated (d_5-glycerol). So now techniques used to observe deuterium distribution would correspond to glycerol's position within the film and not the surfactant's. Neutron reflectivity data, fits and calculated depth profiles are displayed in Figure 5.11. The NR data confirmed the findings of the NRA experiments as there is a clear reduction in the amount of d_{25}-$C_{12}E_5$ seen at the surface when comparing a non-plasticised PVA film to a plasticised film. What is more unusual however, is the result of the labelling exchange experiment. Although the distribution of glycerol in thin PVA films was found to be homogeneous in the previous chapter, here the calculated depth profile for d_5-glycerol exhibits a surface excess of plasticiser in the presence of $C_{12}E_5$ (Figure 5.11c.). The concentration of plasticiser shows a ~10 at. % increase in the 10 nm surface region of the film, which suggests the surfactant and plasticiser are co-located, as the d_{25}-$C_{12}E_5$ excess was also found in this region. These findings further suggest some individual interaction between the surfactant and plasticiser which causes increased compatibility between the two compounds. It is possible that a $C_{12}E_5$-glycerol complex is formed at the surface of the film which draws glycerol from the bulk and causes it to segregate.

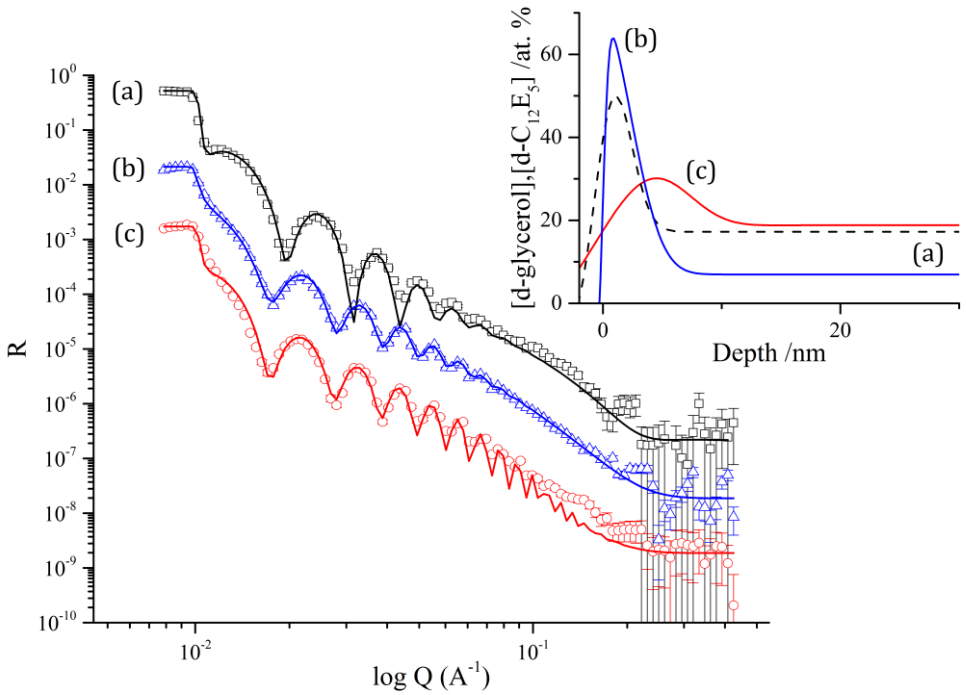

Figure 5.11. NR data, fits and composition profiles for (a) 20% d_{25}-$C_{12}E_5$ and 20% glycerol in PVA, (b) 20% d_{25}-$C_{12}E_5$ in PVA (reproduced from Figure 5.5) and (c) 20% $C_{12}E_5$ and 20% d_5-glycerol in PVA. The composition profiles for each dataset correspond to the deuterated element of that sample.

IBA was then used to probe the effect of varying hydrogenous surfactant concentration on glycerol distribution further. Solutions were made that contained 20 w% of d_5-glycerol, accompanied by 1, 2, 5, 10 and 20% of h–$C_{12}E_5$ in PVA and spin cast. The data displayed in Figure 5.12. shows 20 w% d_5-glycerol and 1 w% h–$C_{12}E_5$ in PVA. Initially conventional layer fit methodology was applied to this data, displayed as the red dotted line in both the fit and depth profile in Figure 5.12. The computational simplicity of the layer fit model makes fitting of a gradual change in concentration very difficult, adding more layers to the model might describe the data better, however increasing the number of variables in the fit is not only more taxing on computer power, but also allows much more room for the software to create errors. Fortunately it is possible to fit the data with a functional fit, described more in 3.3.1. The calculated fit and depth profile achieved using the functional fit is displayed as a blue solid line in Figure 5.12. As can be seen the functional fit describes the data with greater accuracy, indicating the ability of even small amounts such as 1 w% h–$C_{12}E_5$ to perturb the homogeneous distribution of glycerol. The presence of surfactant causes a 5% increase in glycerol seen at the surface of the film (25 at. %), which gradually decreases to 15% over ~250 nm.

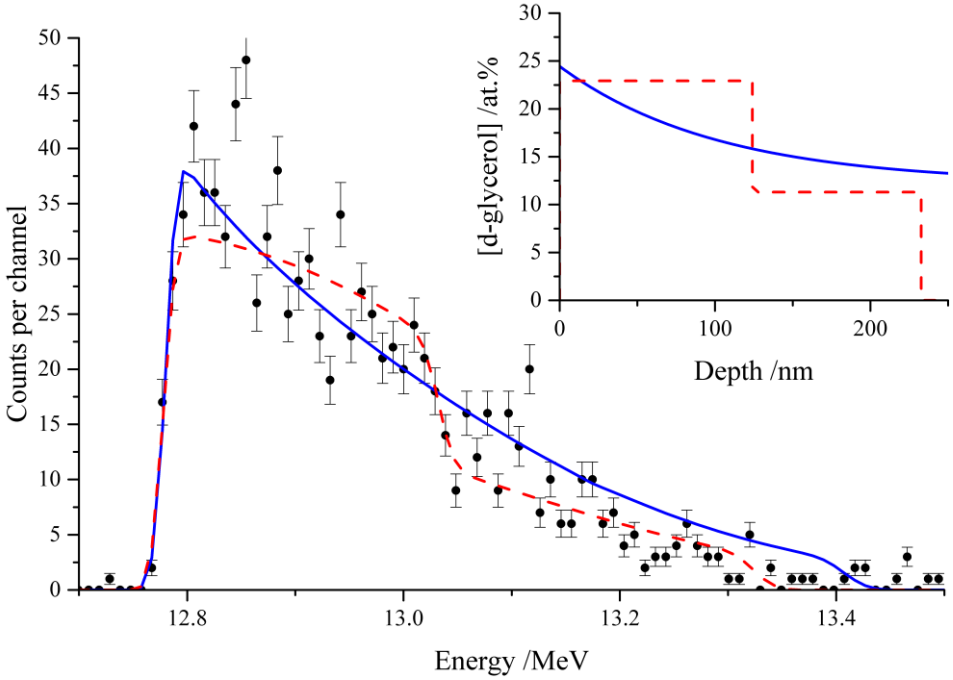

Figure 5.12. NRA data with layer fit (red, dashed line) and functional fit (blue, solid line) for 1% h–$C_{12}E_5$, 20% d_5-glycerol in a thin PVA film, with respective depth profiles shown in the inset.

Increasing the concentration of h–$C_{12}E_5$ in each film perturbs the distribution of plasticiser further, causing increased surface segregation (Figure 5.13.). All glycerol found at the surface of the film is drawn from the bulk, depicted by the proportional decrease in glycerol concentration between 100 and 250 nm as surfactant concentration increases. As the functional fit describes the depth distribution of a component by exporting a number of parameters which define an exponential decay formula, it does not give a limiting film thickness in the profile. Therefore it is necessary to do at least once layer fit to estimate film thickness, which can then be used to determine where the exponential decay meets the substrate and the film ends, in this case 230 nm.

Plasticisation is confirmed to reduce the significance of the surfactant surface excess by NR and NRA, although the magnitude of the reduction detected with NR was less than what was detected with NRA. Exchange of the labelled species has illuminated the ability of non-ionic surfactants to distort homogeneous plasticiser distribution in thin plasticised films, which suggests formation of a surfactant-plasticiser complex. The reorganisation of plasticiser may have implications on the mechanical properties of films which contain even a small amount of surfactant, as homogeneous plasticiser distribution is necessary to maintain polymer functionality for most applications. As the changes in the surface structure of thin PVA films with plasticisation or surfactant addition has been shown to be so significant with scattering techniques, it would be surprising if detection of some change in surface properties was not resolvable with other methods. Atomic force microscopy allows detailed surface imaging on the nanometre scale, hence this technique was used in an attempt to visualise the changes in surface properties discovered so far.

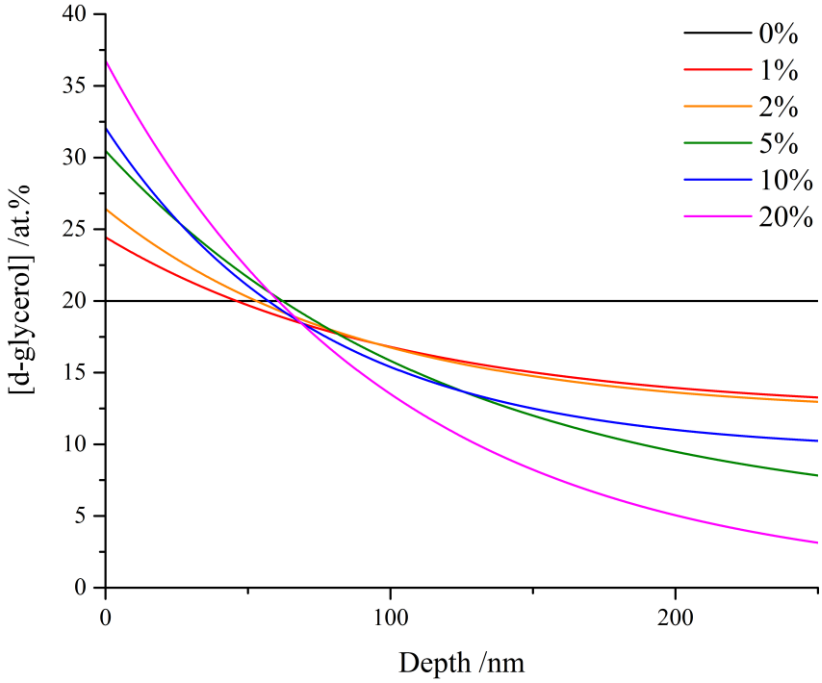

Figure 5.13. Functional fit depth profiles with 20 w% d_5-glycerol and 1-20 w% h–$C_{12}E_5$ in thin PVA films.

5.1.4. Surface Topography of Thin Films

Atomic force microscopy (AFM) is not only used for surface imaging, but can also be used to study several mechanical properties alongside imaging depending on the type of analysis performed. Using quantitative nanomechanical mapping (QNM) the effects of plasticisation and surfactant addition on the height and adhesion profiles of thin films is studied. The mechanics of QNM are discussed in more detail in 3.4.2. Plasticisation was investigated in binary films with PVA initially (Figure 5.14.); which shows a 3D adhesion plot superimposed on to a 3D height map for a film spin-cast from a 4 w% aqueous PVA solution. Here, we note that because of the uncertain range of penetration of the probe into the plasticised PVA surface and the inhomogeneous composition profiles, the adhesion maps are essentially qualitative in nature. To establish if each AFM image was a true representation of the surface nature of the entire film, five separate scans were taken at various points on the film, and the profiles compared. If there was very little variation between the observed plots, then the best quality image was generally chosen and plotted in the figures below. AFM confirms the presence of relatively smooth films via spin coating, as the range of the height map never exceeds a half-length of 1.0 nm. Hence the distance from the highest to the lowest point on a film is never found to be greater than 2.0 nm, which is relatively small compared to the average film thickness (~200 nm). Adhesion is displayed in nanonewtons (nN), the scale of which can be used to identify the strength of adhesion measured from the force curve. As visible in Figure 5.14., the adhesion profile tends to correlate with the height map, with features running in the same direction. As QNM has not been applied to thin PVA films before it is difficult to interpret whether the values obtained are comparatively small or large to what would be expected from a PVA film on Si substrate, hence the data is qualitative. As a pure PVA film is the most basic film investigated in this

project, this will be used as a baseline to compare all subsequent films to. The calculated parameters for each film are displayed in Table 5.2.

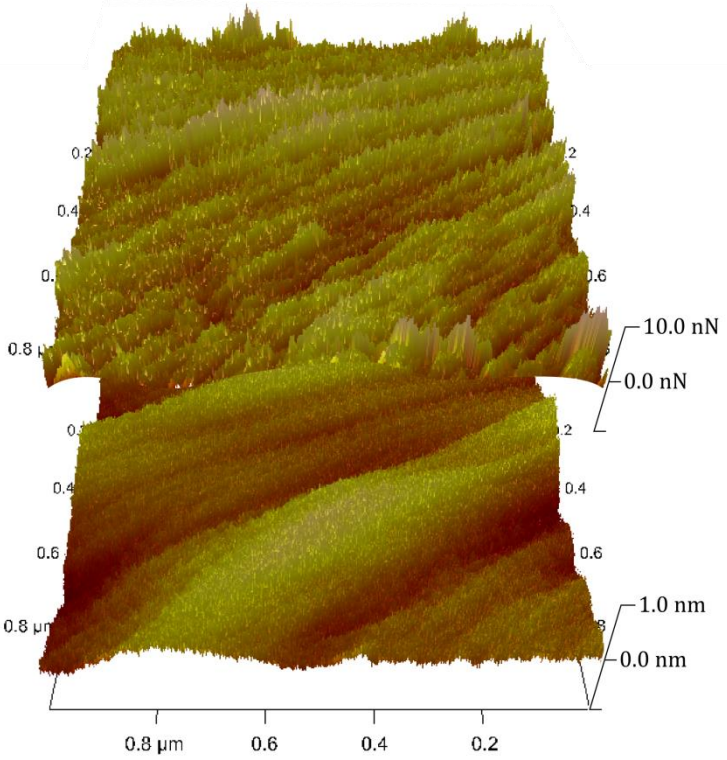

Figure 5.14. AFM topographic height map (bottom) and adhesion (top) for a thin spin-cast pure PVA film on silica substrate.

Table 5.2. List of parameters obtained from NanoScope analysis of each AFM topographic surface map.

Sample	Height Range/ nm	Adhesion Range/ nN	R_q/ nm	R_a/ nm	Kurtosis
PVA	1.0	10.0	0.19	0.15	3.34
PVA + Glycerol	1.7	17.5	0.25	0.19	5.36
PVA + $C_{12}E_5$	1.8	16.7	0.51	0.36	6.39
PVA + $C_{12}E_5$ + Glycerol	1.0	8.0	0.24	0.19	2.84

Figure 5.15. shows the corresponding measurement, performed on a PVA film which contains 20 w% of glycerol as a plasticiser. The addition of plasticiser to the pure polymer film causes slight variations in the appearance of the films surface which can be quantified through surface height and adhesion. Firstly the half axis distance for the height map has increased from 1.0 to 1.7 nm, and the adhesion plot has seen a similar increase from 10.0 nN to 17.5 nN. This implies that the height range of the features seen on the surface of the film has increased slightly, and these features themselves have a greater range of tackiness than a pure PVA film. Adhesion has been empirically related to glass transition (T_g) in polymers[184] where the maximum energy of adhesion (W_m/ Jm^{-2}) for a polymer is reached at approximately 50 to 70 °C above

the T_g. As the inclusion of plasticisers reduces the T_g of PVA (58 °C)[39] towards the measurement temperature, the W_m is also reduced, causing the polymer to become tackier, which is supported by these findings. It is also possible that as the plasticiser will swell the polymer, any deviations from a completely planar surface present in the non-plasticised films are enhanced upon plasticisation, resulting in the increased height range seen for plasticised samples. However, this is quite a small effect.

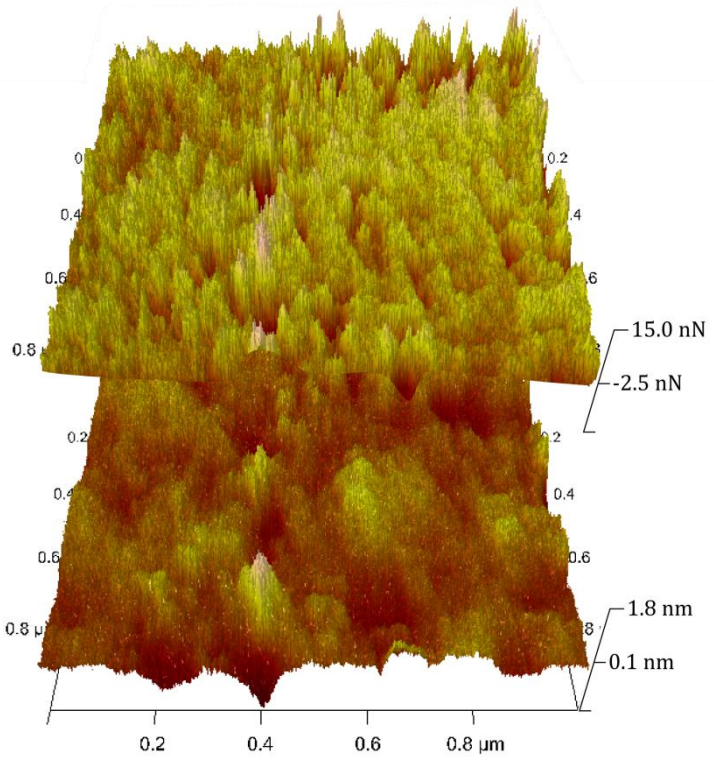

Figure 5.15. AFM topographic height map (bottom) and adhesion (top) for a thin spin-cast 20% glycerol, 80% PVA film on silica substrate.

20 w% of h-$C_{12}E_5$ was added to both pure and plasticised PVA films to study the effects on surface properties. Figure 5.16. shows the height and adhesion map for a binary surfactant-polymer film. Both plots appear very different to those presented for a PVA-only film, which is unsurprising given the knowledge of $C_{12}E_5$ surface activity gained from NRA and NR. The height and adhesion range, R_a, R_q and kurtosis all increase significantly when adding surfactant to the film, showing that not only does the surface become rougher, the features seen on the surface also become larger. This is plainly visible from Figure 5.16. which shows a relatively smooth film with deep voids in the height map. What is interesting is that when comparing the height to adhesion map these voids correspond to the most adhesive regions of the film. The height of these features is also interesting, having a depth of ~2 nm, they are comparatively smaller than the 8 nm d_{25}-$C_{12}E_5$ surface excess documented with NRA, this may be caused by the AFM being insensitive to the bulk of the surfactant layer on the surface of the film, wherein it only detects features in close proximity to the solid PVA film. In comparison to the all-trans length of a $C_{12}E_5$ molecule (~3.7 nm) and the documented average $C_{12}E_5$ layer thickness (4.2 nm) found on the surface of silica when placed in a solution above the CMC,[185] it is also small. This suggests that the surfactant is not

able to orientate perpendicular to the plane of the film, or form structured agglomerates on the surface of non-plasticised PVA films. Figure 5.17. depicts a top-down view of the two plots which clearly indicates overlapping of the height and adhesion features. There also appears to be an area surrounding these regions where adhesion is significantly reduced, almost creating an island of adhesion. This phenomenon may be explained by the melting temperature of the surfactant. Although an exact melting temperature for $C_{12}E_5$ could not be found, the surfactant is a liquid at room temperature which suggests it is below 20 °C. A similar surfactant, hexaethylene glycol monododecyl ether ($C_{12}E_6$) has been shown to have a melting point of 27.2 °C,[186] so $C_{12}E_5$ should be slightly lower than this. If any wells of surfactant in the liquid state are present on the surface of the film then adhesion will increase as the probe sticks to it. The decrease in height associated with these regions would also be accounted for by a liquid surfactant structure at the films surface as the probe would penetrate through any liquid regions before reaching solid PVA, giving the impression of decreased height. These results differ significantly from other studies of $C_{12}E_5$ structure on substrates, where hemi-spherical micelles were shown to form on the surface of graphite both experimentally[187] and with molecular simulations.[188] These experiments were carried out on a substrate submerged in a surfactant containing solution however; therefore different surface and interfacial interaction would be expected to lead to different structures.

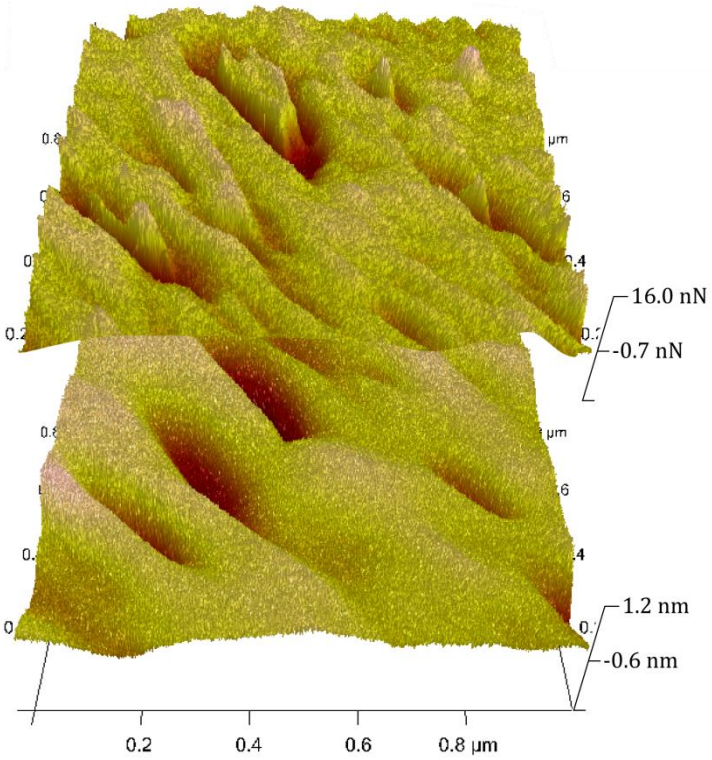

Figure 5.16. AFM topographic height map (bottom) and adhesion (top) for a thin spin-cast 20% $C_{12}E_5$, 80% PVA film on silica substrate.

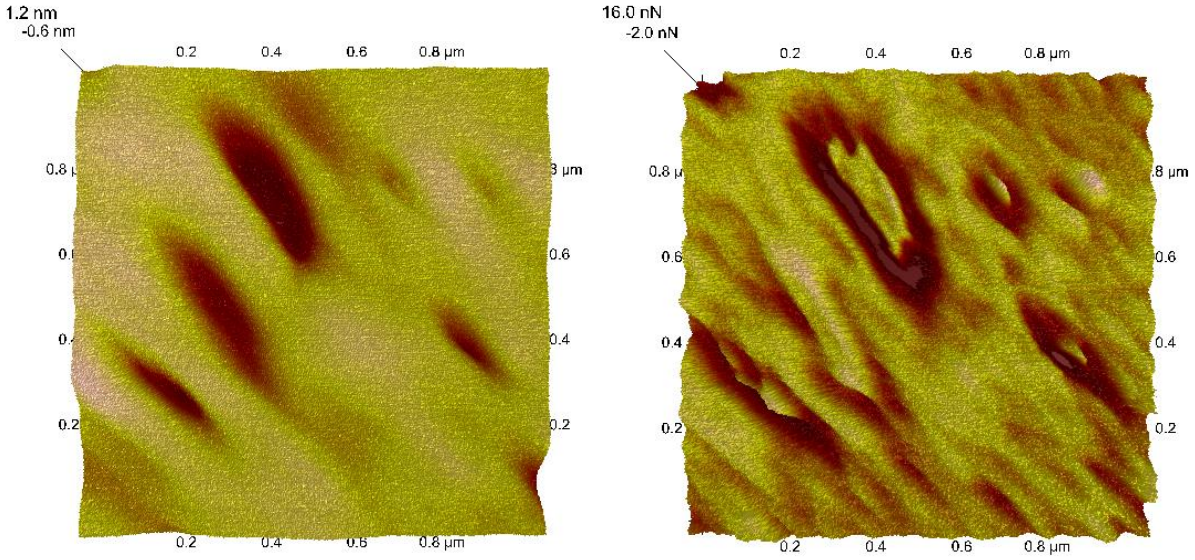

Figure 5.17. Top-down view of the height (left) and adhesion (right) maps for 20% $C_{12}E_5$ in 80% PVA spin cast thin film on a silica substrate.

Another possibility is that where the amount of $C_{12}E_5$ on the surface does not readily make an integer number of layers, a mixed surfactant structure is formed. This is known for PS-PMMA block-copolymer films[189] and is represented in Figure 5.18. This would explain the deviations in the height map in Figure 5.17., if a significant layer of surfactant was present on the surface of the film then any regions where the surfactant molecules were not arranged in lamellae would cause the reduced height seen. The addition of glycerol to surfactant containing films causes a reduction in these features, and makes the film appear more like the pure PVA film seen in Figure 5.14. Glycerol addition in the pure film caused an increase in R_a and kurtosis, whereas in this case it causes a reduction. It is known from the IBA and NR studies that glycerol decreases the magnitude of $C_{12}E_5$ surface excess seen in these films, as well as increasing the amount of surfactant seen in the bulk. It would appear that these results are reflected in the AFM images, as the presence of surface structures caused by surfactant on the surface of the film is reduced upon glycerol addition, suggesting less surfactant is present at the surface.

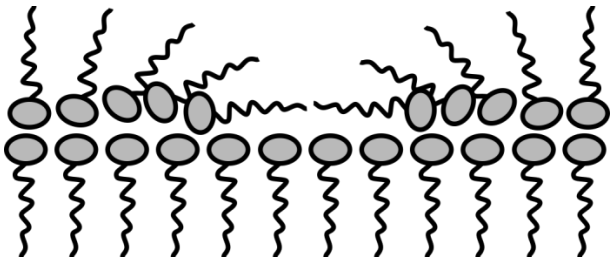

Figure 5.18. Schematic representation of possible mixed surfactant structure on the surface of the polymer film

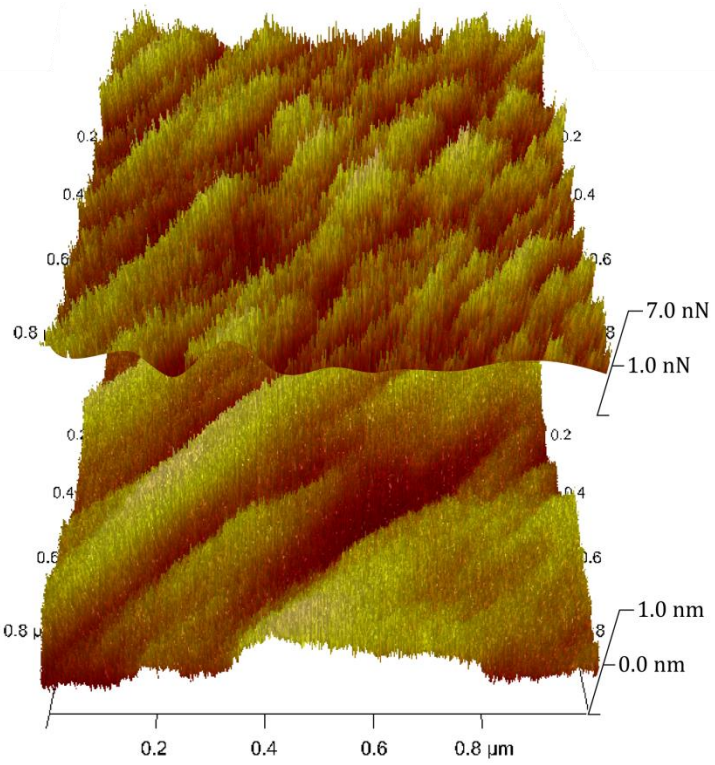

Figure 5.19. AFM topographic height map (bottom) and adhesion (top) for a thin spin-cast 20% $C_{12}E_5$, 20% glycerol, 60% PVA film on silica substrate.

5.1.5. Influence of Humidity on $C_{12}E_5$ Segregation

It has clearly been shown that plasticisation with glycerol can alter a film's properties significantly, but glycerol is not the only plasticiser known to be present in these films. Water also plays a vital role in maintaining film stability in industrial films by acting as a plasticiser. As polymeric properties (T_g, tensile strength, flexibility, etc.) are largely dependent on plasticiser concentration, any fluctuation in humidity and hence water (plasticiser) content of films can have a significant impact on film behaviour. It is proposed that the presence of increased water in the atmosphere will not only affect the physical properties of the polymer, but in turn also affect compatibility with surfactants, causing surfactant structures on the film's surface to change and leading to an increase/decrease in film permeability. Therefore an investigation was launched to probe the effects of humidity on thin, spin-cast films such as the ones studied so far in this work. Saturated salt solutions were used to control the humidity in a sealed chamber. Solutions of potassium acetate (CH_3CO_2K), magnesium chloride ($MgCl_2$), magnesium nitrate ($Mg(NO_3)_2$) and potassium chloride (KCl) were used to give a relative humidity (RH) of 23, 33, 55 and 85% respectively.[190]

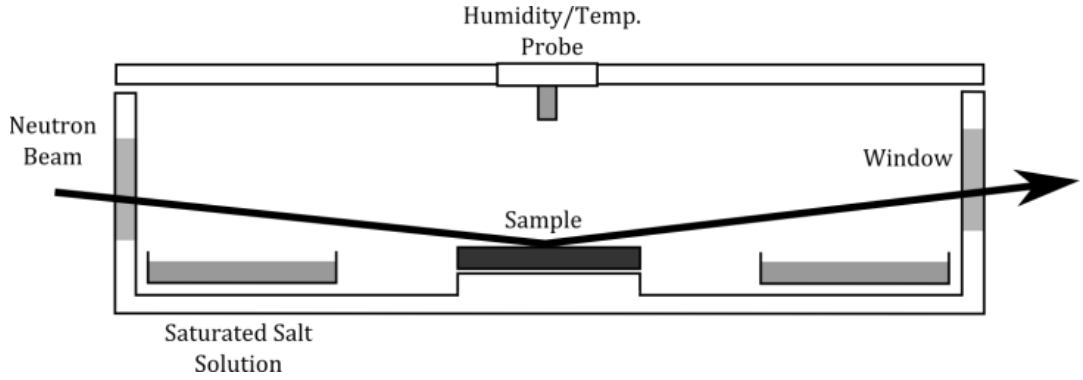

Figure 5.20. Schematic representation of 'UFO' cell used to control the relative humidity surrounding a sample.

Prior to NR experiments, care was taken to ensure that films were stable for long enough to attain reliable data. From the film thickness studies in chapter 3 and $C_{12}E_5$ NR data presented so far in the current chapter it was apparent that film stability should be maintained for at least 24 hours. As an NR experiment on INTER takes approximately 1.25 hours, it was also necessary to ensure the saturated salt solutions stabilised the atmosphere within the UFO cell quickly as a consistent humidity should be reached before analysis begins. By monitoring the humidity via a probe inserted into the cell directly above the sample it was found that a stable humidity was reached after approximately 15 minutes. It takes roughly 30 minutes to lock the instrument and align the samples with NR so this was deemed sufficient enough time to start analysis directly after this procedure. To gain a baseline measurement and test the effectiveness of the humidity cells a pure PVA film was analysed first. In order for the film to contain a contrasting element to define a critical edge during analysis, PVA was dissolved in D_2O rather than H_2O as it is known that the polymer retains a reasonable quantity of water (~7 w%) in the industrial films, therefore some water retention should occur in spin cast films also. Also isotope exchange between the labile OH groups of PVA and OD groups of the solvent will occur, hence the polymer should also exhibit an increased SLD. Figure 5.21. displays the raw data, fits and D_2O concentration versus depth profiles achieved for four separate spin-cast PVA in D_2O films, each subjected to varying relative humidity environments of 23, 33, 55 and 85 %RH.

Although the data does not vary much between samples, the difference in spacing of the fringes at low Q is telling of a change in film thickness. This is obvious from the depth profile as the peak visible at the highest depth of each film, caused by a thin SiO_2 layer on the silicon substrate shifts by ~5 nm per humidity interval, a clear indicator of water absorption in the thin films. The relationship between the swelling ratio and humidity is given in Figure 5.22., where the swelling ratio is calculated by normalising each film thickness to the thickness at the lowest humidity (23 %RH). The relationship is relatively linear, indicating that the film is able to absorb moisture roughly in proportion to the water vapour pressure regardless of humidity, and that a maximum absorption is not reached at any stage, which would be indicated by a plateau. The large increase in film thickness displayed at 85 %RH is perhaps due to the larger increment (30 %RH) between 85 and 55 %RH compared to the smaller increments (10 and 22 %RH) between 23, 33 and 55 %RH respectively. It is however possible that the increase in film thickness

was amplified by a washing out of the Kiessig fringes at low Q for the 85 %RH sample. The fitted parameters in the supporting information (12.2) show that the roughness parameter associated with this fit was significantly larger (6.6 nm) in comparison to the fits for lower humidity (1-2 nm). This suggests the films surface is becoming relatively rough at higher humidity, possibly due to water absorption on the surface of the film, or by becoming excessively plasticised. Plasticisation with glycerol was shown to cause a small increase of surface roughness with AFM, so it is not unreasonable that plasticisation with water could have a similar effect. The calculated SLD and deuterium concentration is notably reduced at higher humidity (55 and 85 %RH). It is possible that this is due to the presence of additional hydrogenous water (from the atmosphere) in the film, this will likely result in exchange of labile PVA OD with water OH, causing the SLD of the polymer, and hence the sample, to be reduced. It is evident from these results that the humidity chambers are effective at controlling the atmosphere around the sample, and that water absorption in to the sample is occurring, which will have a significant effect on surfactant behaviour.

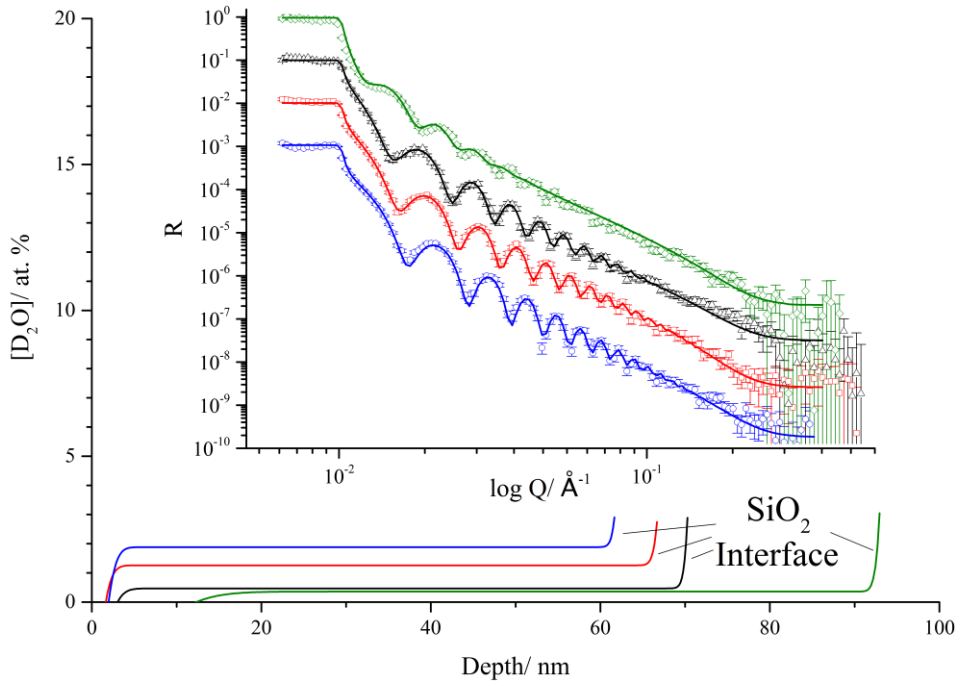

Figure 5.21. NR data (offset), fits and composition profiles for D_2O, PVA films subjected to 23%RH (blue), 33%RH (red), 55%RH (black) and 85%RH (green) environments.

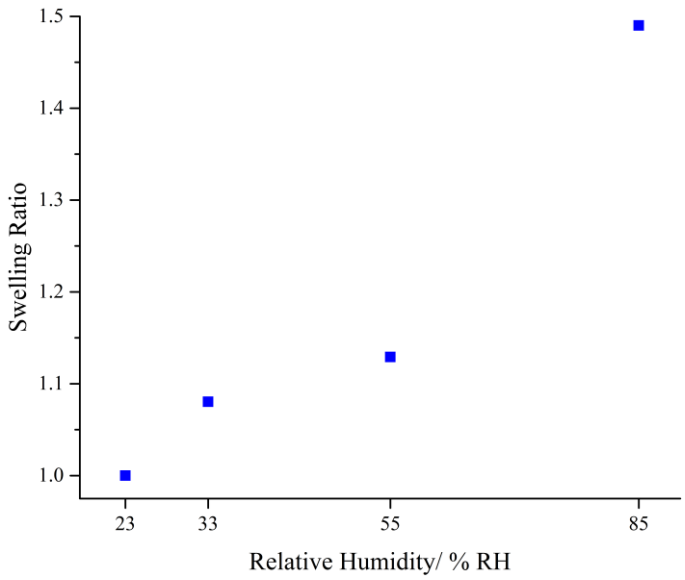

Figure 5.22. Positive relationship between relative humidity and percentage swelling indicating absorption of water from the atmosphere in thin, spin-cast PVA films

$C_{12}E_5$ has previously been shown to surface segregate when in non-plasticised and plasticised PVA films. Figure 5.23. displays data, fits and composition profiles for four separate 20 w% d_{25}-$C_{12}E_5$ non-plasticised films. Each film was subjected to increasing relative humidity as was done for the PVA-only films. Again an increase of film thickness with increasing humidity is observed, showing evidence of water absorption in the surfactant containing films. The most interesting feature of the data in Figure 9 is the evolution of a broad Bragg peak at high *Q*, normally indicative of increased ordering within a system. Although surface segregation was detected earlier for d_{25}-$C_{12}E_5$ in PVA films, this Bragg peak did not present itself. The most logical region for surfactant ordering to occur is within the surface excess, where it is present in high concentrations. Therefore additional layers were added to the fit of alternating high and low SLD, the fit was then run and the depth profiles in Figure 5.23. produced. These depth profiles may appear different to what has been seen previously as the roughness parameter obtained with NR has been omitted by plotting the depth profile from the thickness and SLD values only (Appendix 12.2.). This is done to remove any ambiguity regarding layer thickness and composition when analysing the surface excesses, as significant film roughness can lead to a blurring of the boundaries between highly contrasting SLD layers, which makes accurate interpretation of the structure difficult. By producing profiles like this evidence of ordering within the surface excess of each sample is clear; showing layers of almost pure surfactant separated by lower SLD layers. There is also an increase in ordering with increasing humidity seen as the concentration of surfactant in each layer rises with humidity; presence of an extra surfactant rich layer is also visible in the 85 %RH sample. The fact that surface ordering of surfactant was not detected in the initial neutron experiment studied under ambient conditions suggests that this is a result of prolonged equilibration in the humid environment the samples are placed in. These results suggest a decrease in compatibility between surfactant and PVA as the polymer is plasticised with water under increased humidity, causing the surfactant to segregate in to almost pure layers. As glycerol was shown to have a positive effect on surfactant-polymer compatibility when studied under ambient conditions

(chapter 5.1.3.), it was of interest to see how these two opposing effects would play against each other when a glycerol plasticised, $C_{12}E_5$ containing, PVA film was subjected to increased humidity.

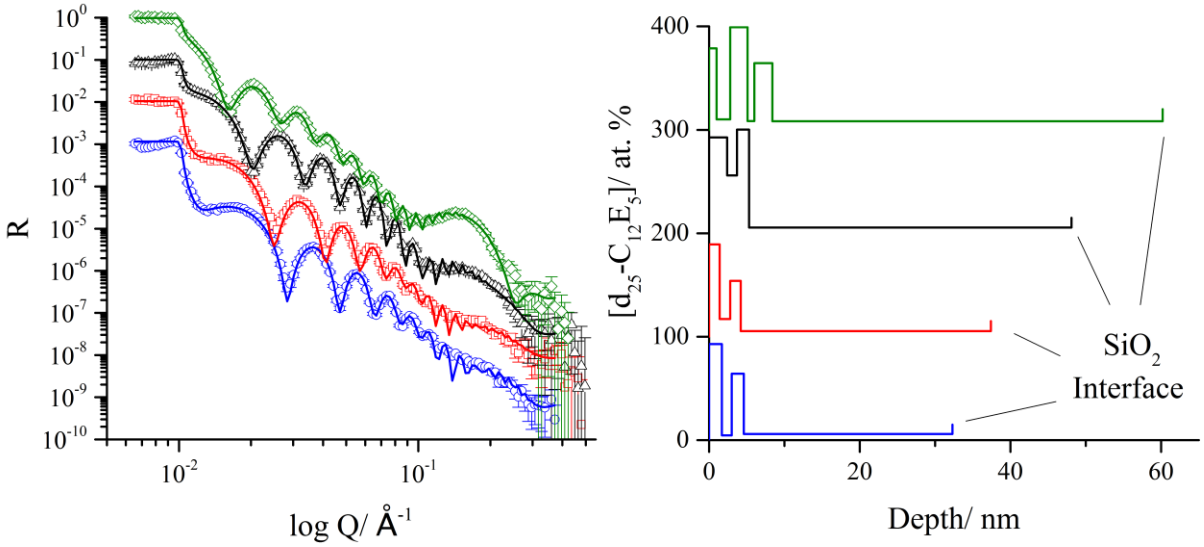

Figure 5.23. NR data (offset), fits and composition profiles for 20 w% d_{25}-$C_{12}E_5$ PVA films subjected to 23%RH (blue), 33%RH (red), 55%RH (black) and 85%RH (green) environments. Each increment on the depth profile accounts for 0 to 100 at. % of d_{25}-$C_{12}E_5$.

Four films containing 20 w% d_{25}-$C_{12}E_5$ and 20 w% h-glycerol were spin-cast and analysed with NR (Figure 5.24.). Interestingly when studied under RH control, glycerol exhibits the opposite effect to what was seen previously, where now rather than increasing compatibility between components, it decreases it. On average, z^* increases by ~50% for each sample upon the addition of glycerol, indicating a significant decrease in the compatibility of the surfactant with the polymer matrix. It is possible that these effects are actually from a greater degree of water plasticisation in the films permitted by the addition of glycerol. A measurement performed by Laura Martin, a former intern student in the chemistry department at Durham University showed that pure glycerol can absorb up to 13% of its own mass in water from the atmosphere. Considering the difference in molecular weight of water to glycerol that is almost a 2:3 molar ratio of glycerol to water, so the uptake is considerable. $C_{12}E_5$'s critical micelle concentration (CMC) has been shown to be 0.04 mM in water, and 0.4 mM in a 90 w% glycerol/water solution,[191] therefore micelles are formed at much lower concentrations in aqueous solutions, suggesting less compatibility with water in comparison to glycerol. If glycerol is co-located with the surfactant in the film as the previous results suggest, then when films are exposed to a humid atmosphere glycerol will absorb water, which will in turn increase the likelihood of $C_{12}E_5$ micelle formation. Although it is worth noting that the concentration of surfactant in the adsorbed layer is much greater than the CMC, even in glycerol containing solutions, it is not unreasonable to suggest that an increase in water concentration is likely to encourage aggregation into lyotropic mesophases. If micelles are forming within the polymer matrix upon water absorption, they are less likely to be compatible with the polymer due to their

negative effect on polymer free volume in comparison to the individual surfactant molecules, hence may encourage surface segregation further.

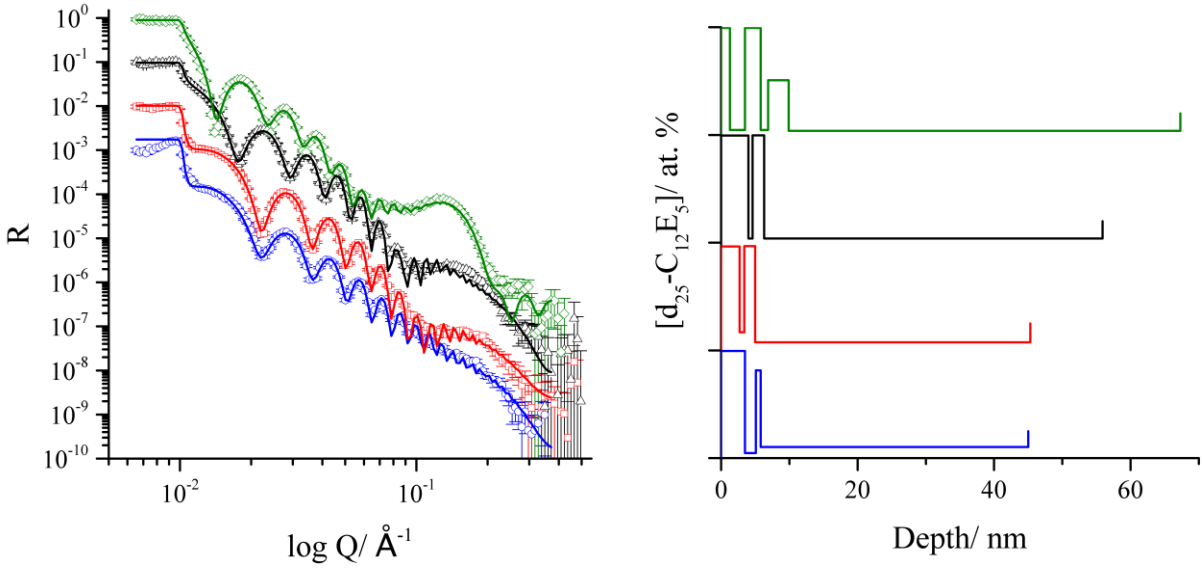

Figure 5.24. NR data (offset), fits and composition profiles for 20 w% d_{25}-$C_{12}E_5$, 20% h-glycerol PVA films subjected to 23%RH (blue), 33%RH (red), 55%RH (black) and 85%RH (green) environments. Each increment on the depth profile accounts for 0 to 100 at. % of d_{25}-$C_{12}E_5$.

Exchanging the deuterated compounds allows the study of plasticiser behaviour within the ternary surfactant samples. Not only is the distribution of plasticiser within the film interesting as it may be involved in micelle formation by water absorption, but previously it was also found that when performing similar experiments under ambient conditions some plasticiser exhibited surface segregation. Evidence for a small surface excess of glycerol is again apparent from the depth profiles presented in Figure 5.25., present at all relative humidity values studied. There is also evidence for some structuring of glycerol in the excess for the 33 %RH sample, visible in the data by the presence of a Bragg peak at high *Q*. The previous IBA work in this chapter on $C_{12}E_5$ containing films showed no evidence of glycerol surface structuring, but it is almost certain that this level of ordering is not detectable with NRA, as the maximum resolution achievable with NRA is ~10 nm. This is large in comparison to the thickness of each surface excess detected with NR, as well as the thickness of the PVA films (~150 nm). It is unusual that this level of structuring is only seen at 33 %RH, and hinted at with the 85 %RH sample, whereas 23 and 55 %RH show a surface excess of d_5-glycerol, but no structuring within it, as this does not suggest any particular trend between relative humidity and surfactant excess ordering.

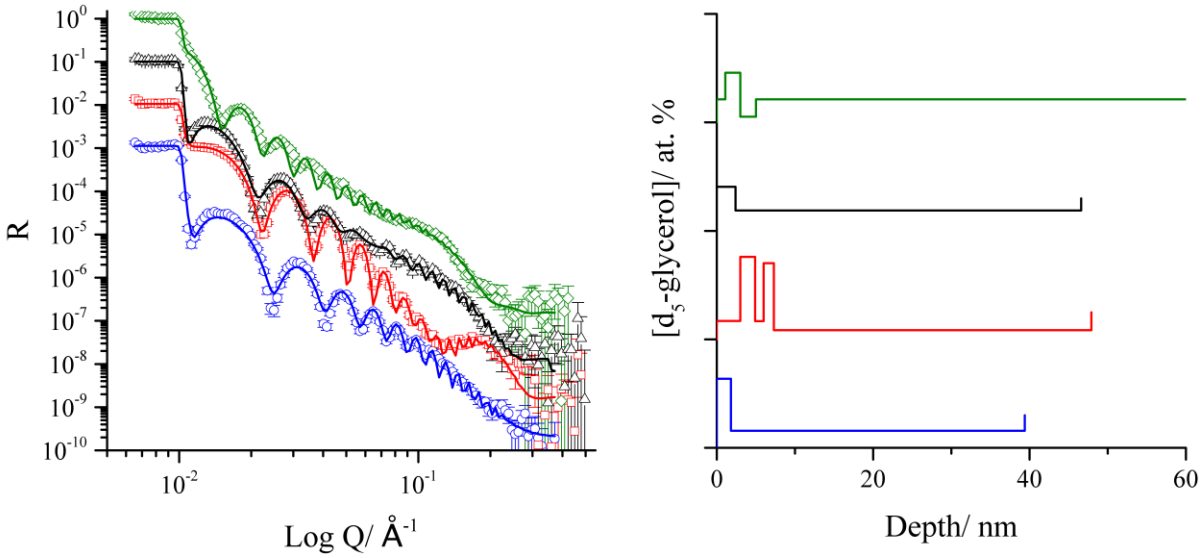

Figure 5.25. NR data (offset), fits and composition profiles for 20 w% h-$C_{12}E_5$, 20% d_5-glycerol PVA films subjected to 23%RH (blue), 33%RH (red), 55%RH (black) and 85%RH (green) environments. Each increment on the depth profile accounts for 0 to 100 at. % of d_5-glycerol.

Although the d_{25}-$C_{12}E_5$ and d_5-glycerol samples at 33 %RH are completely separate, the agreement between their depth profiles when plotted without roughness is significant. By inverting the concentration profile for the deuterated glycerol sample and overlaying it against the deuterated surfactant sample (Figure 5.26.) it appears as though there are intermittent layers of $C_{12}E_5$ and glycerol on the surface of the thin films. The most probable surfactant-glycerol conformation to exist in this case is a series of surfactant lamellae, separated by regions of glycerol. $C_{12}E_5$ has been shown to form lamellae at high concentrations (> 55%) in aqueous solutions containing polymer through molecular simulations,[192] and although the overall concentration in solution is only 20 w%, the concentration of surfactant in the surface excess (> 90 at. %) is more than sufficient for lamellae to form. This suggests that the presence of polar molecules within the matrix allows increased structuring at the surface. This would help to explain the series of surfactant-rich layers seen in the binary $C_{12}E_5$-PVA films, as surfactant structuring is only present under RH control, when there is significant water within the system. This suggests that it is either a pure layer of water which supports the surfactant layers on the surface of the film, or a layer of water-plasticised PVA. The fact that the glycerol structuring is only observed at 33 %RH is also interesting; it could be that this sample was smoother than the rest, which allowed better resolution to be obtained from NR as there was less variation in film thickness at the surface, giving more uniform scattering. Another possibility is that changing RH changes the lyotropic behaviour of $C_{12}E_5$/glycerol structures and only 33 %RH gives clear enough lamellae, parallel to the surface for the structuring to be seen. NR has confirmed the presence of a $C_{12}E_5$ surface excess in thin PVA films under all environments studied, as well as a non-homogeneous distribution of plasticiser at a range of relative humidity values.

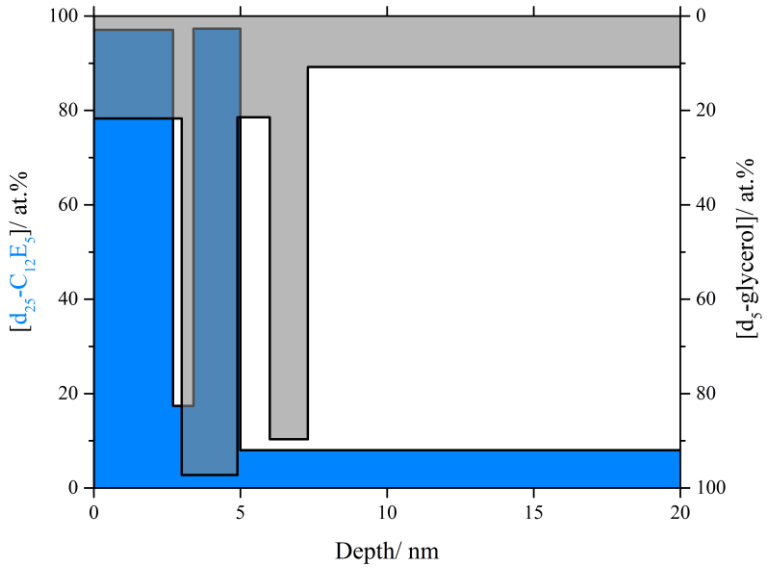

Figure 5.26. NR depth profiles 20% d_{25}-$C_{12}E_5$, 20% glycerol (blue) and 20% d_5-glycerol, 20% h-$C_{12}E_5$ (grey, inverted) with removal of the roughness parameters focusing on the near surface region (0-20 nm).

5.1.6. Summary of $C_{12}E_5$ Segregation Behaviour

So far the segregation behaviour of the non-ionic surfactant d_{25}-$C_{12}E_5$ in PVA has been investigated with several techniques. Unlike the plasticiser glycerol, this surfactant has been shown to exhibit spontaneous segregation when placed in thin PVA films. $C_{12}E_5$ will not only segregate to the air interface as would be expected for a surface active compound such as a surfactant, but has also been found in significant concentration at the substrate interface. The results presented so far suggest that the surface energy of components within the PVA matrix dictates segregation behaviour, with lower surface energy compounds segregating more readily. Compatibility of the components present within each sample has also shown to be of importance when determining the extent of surfactant surface segregation, expressed by the change in surfactant behaviour upon the inclusion of molecules such as the plasticisers glycerol and water. Evidence of a surfactant-glycerol complex has also been found, showing the ability of $C_{12}E_5$ to perturb the homogeneous distribution of plasticiser within the sample. This may have major implications for film stability as any deviation from a homogeneous distribution will cause areas insufficiently plasticised polymer, leading to increased fragility and increasing the likelihood of film fracture/failure, it could also lead to an undesirable tacky feel on the surface of the film. The effect of humidity on the magnitude of the surfactant surface excess (z*) in thin films has also been explored and is summarised in Figure 5.27. It was found that increasing humidity causes surface segregation of the surfactant to be enhanced, forming complex structures on the surface of the film. This would suggest that as a surfactant-glycerol complex is shown to form, greater surfactant segregation would cause greater glycerol segregation. However labelling of the plasticiser has shown that glycerol segregation is reduced at higher humidity (Figure 5.27.), which suggests that water, absorbed from the atmosphere takes over glycerol's role in the interstitial surfactant surface excess regions, allowing more glycerol to be present in the bulk. This suggests that there exists an ideal humidity for film stability where the amount of surface

segregating surfactant is at a minimum, and the amount of glycerol present in the bulk is at a maximum. Despite this it is clear that the problem of glycerol segregation in thin films is prevalent throughout the entire humidity range. It is thought that altering the surfactant's compatibility with the plasticiser and polymer by adjusting the hydrophilic-lipophilic balance (HLB) could shed light on a possible means to suppress segregation of both the surfactant and plasticiser in thin polymer films.

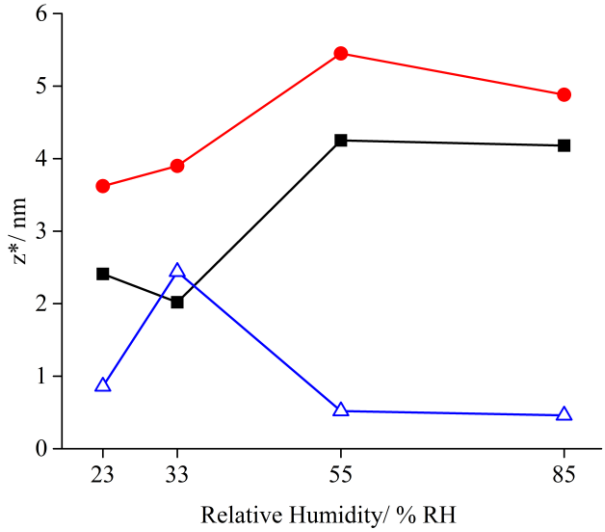

Figure 5.27. Surfactant surface excess as a function of %RH for 20% d_{25}-$C_{12}E_5$ (filled squares, black), 20% d_{25}-$C_{12}E_5$ with 20% h-glycerol (filled circles, red) and 20% h-$C_{12}E_5$ with 20% d_5-glycerol (open triangles, blue) in thin PVA films

5.2. Effects of Surfactant Hydrophilic-Lipophilic Balance on Segregation and Nanostructure

The HLB was varied for the non-ionic surfactant $C_{12}E_5$ by comparison with samples have one fewer or one more ethoxy groupremoving or adding an ether group to give tetraethylene glycol monododecylether ($C_{12}E_4$) and hexaethylene glycol monododecylether ($C_{12}E_6$) respectively (Figure 5.28.). As this process is altering the size of the polyoxyethylene chain and therefore the polar surfactant head-group, it is expected that the compatibility with polar materials such as water, PVA and glycerol will be directly correlated to changes in HLB. Deuterated analogies of these materials were supplied by the deuteration lab at ISIS and produced using the same reaction mechanism as done for $C_{12}E_5$ by simply exchanging the non-deuterated ether for a longer or shorter compound in the Williamson synthesis.[171-172] The effects of HLB on surfactant behaviour may help to more accurately identify the forces dictating surfactant migration in these thin films. Table 5.3. lists HLB values for the non-ionic surfactants as well as other physical properties. The M_w, density and SLD are all obtained from Table 3.1., displayed in chapter 3, with the rest of the parameters being obtained from various literature resources.

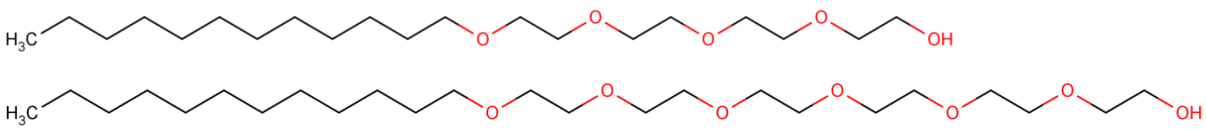

Figure 5.28. MarvinSketch of hydrogenous $C_{12}E_4$ and $C_{12}E_6$ exhibiting same length hydrocarbon region

Table 5.3 Comparison of non-ionic surfactant physical properties, [a] calculated using Equation 4, [b] Persson,[193] [c] Kjellin et al.,[183] [d] Wijaya et al.,[194] [e] Patel et al.[195]

Property	$C_{12}E_4$	$C_{12}E_5$	$C_{12}E_6$
Molecular Weight	362.5	406.6	450.7
HLB	10.66[a]	11.67[a]	12.49[a]
Density/ gcm^{-3}	0.950	0.963	0.976
SLD/ $x10^{-6}$	4.18	3.84	3.56
ST (in water)/ mNm^{-1}	27.6[b]	29.9[c]	31.9[d]
CMC/ $x10^{-5}$ M at 25°C	4.6[e]	5.8[e]	8.0[e]

5.2.1. Influence of Humidity on Surfactant Structure and Distribution in Binary PVA Films

The same experimental conditions used to study surfactant segregation for $C_{12}E_5$ in PVA films were also used for $C_{12}E_4$ and $C_{12}E_6$ containing films; d_{25}-$C_{12}E_4$ was first studied in non-plasticised PVA films. A surface excess of surfactant is visible in Figure 5.29. for all humidity values. This is expected as the physical properties of the surfactant do not change drastically with the removal of an ether group so similar behaviour might be expected in a hydrophilic matrix. The distribution of d_{25}-$C_{12}E_6$ (Figure 5.30.) also shows a surface excess at all humidity values, appearing significantly more concentrated than the lower HLB surfactant. The magnitude of the surface excess is again described in terms of z*. Figure 5.31. displays the z* values for all non-ionic surfactants studied so far in binary films with PVA. Both $C_{12}E_5$ and $C_{12}E_6$ show an increase in the number of surfactant molecules within the surface excess as humidity increases, whereas $C_{12}E_4$ exhibits almost no change in segregation behaviour under varying humidity. When comparing $C_{12}E_4$ to the higher molecular weight surfactants a decrease in surface segregation is visible at all humidity values. As the compound has a reduced molecular weight, surface tension and density, compared to the other surfactants it was expected that increased surface segregation would be visible. Compatibility arguments would also support increased segregation as the surfactant has a smaller HLB compared to $C_{12}E_5$ and $C_{12}E_6$, making it less polar, and therefore less compatible with the polar polymer matrix. Although surfactant molecules should be aggregated at these concentrations in all samples, the reduced CMC of $C_{12}E_4$ in water (Table 5.3.) is indicative of its decreased compatibility with polar systems, hence CMC can be directly related to compatibility with the polar polymer. A decreased compatibility with PVA would likely cause increased segregation compared to the other surfactants.

Therefore the surfactant CMC would also support increased segregation for $C_{12}E_4$. As all documented properties suggest the surfactant should exhibit the opposite behaviour to what is detected, there must be some other factor at play, overpowering the effects of the physical properties and causing the surfactant to show reduced surface segregation.

It is also intriguing to see that where $C_{12}E_5$ containing samples were shown to have at least two surfactant-rich layers in binary films, only a single surfactant layer is visible in $C_{12}E_4$ containing samples. The concentration of this surfactant layer does not appear to be affected significantly by humidity at any value studied. There is a notable reduction in the bulk concentration of surfactant at 85 %RH however, indicating decreased surfactant compatibility at the highest humidity. The average thickness of the surfactant layers present on the surface of the polymer films is approximately 1.33 nm, calculated from the fitting parameters. Molecular dynamics simulations have shown the thickness of an adsorbed layer of $C_{12}E_4$ on an ethylammonium nitrate surface to be 1.70 nm.[196] Although this surface is chemically different to PVA, it is polar like the polymer; hence it is plausible that the surfactants would orientate in a similar way, with their hydrophobic tail-groups pointing out of the surface. As the average $C_{12}E_4$ layer thickness from these results and simulated $C_{12}E_4$ surface excess thickness do not differ considerably it appears that a monolayer of $C_{12}E_4$ is present on the polymer film's surface.

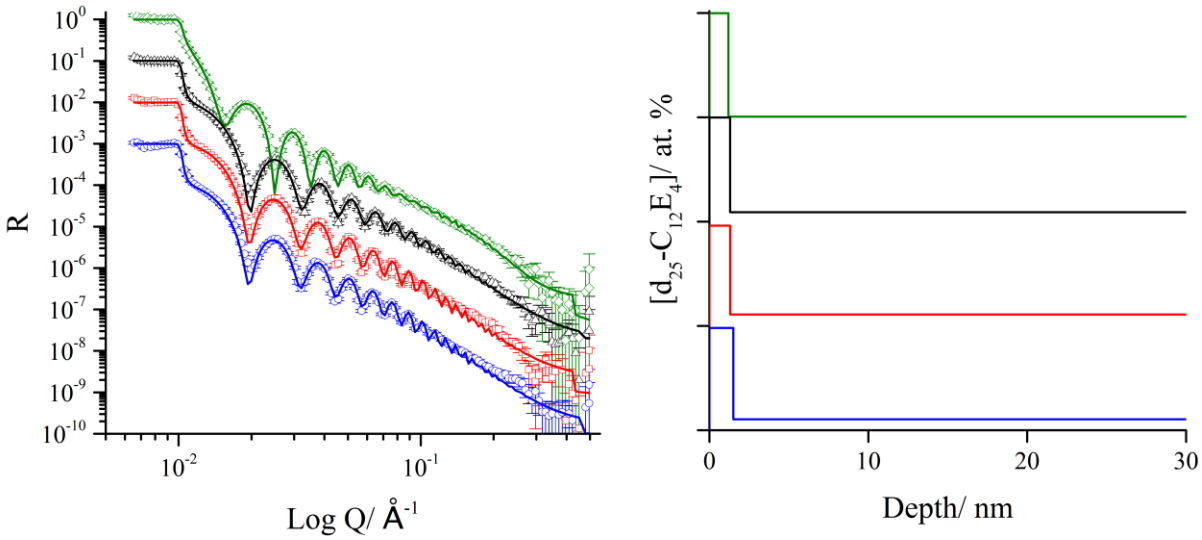

Figure 5.29. NR data (offset), fits and composition profiles for 20 w% d_{25}-$C_{12}E_4$, PVA films subjected to 23%RH (blue), 33%RH (red), 55%RH (black) and 85%RH (green) environments. Each increment on the depth profile accounts for 0 to 100 at. % of d_{25}-$C_{12}E_4$.

The segregation behaviour of $C_{12}E_6$ in thin PVA films is the opposite to what is expected. The increased HLB should cause the surfactant to be more compatible with the polymer matrix, which should suppress segregation. The z* values in Figure 5.31 however show an increase for 3 of the 4 humidity percentages studied compared to $C_{12}E_5$, with only 55 %RH exhibiting a reduction. This suggests decreased compatibility with the polymer compared to the other surfactants when all of the aforementioned physical properties (M_w, density, surface tension, CMC) imply that an increase in compatibility should be seen for $C_{12}E_6$. The higher molecular weight surfactant does however exhibit a

more similar trend to the $C_{12}E_5$ with increasing humidity in comparison to $C_{12}E_4$, wherein the thickness, concentration and number of surfactant layers on the surface increases with increasing humidity.

It is proposed that the size of the surfactant structures forming within the non-plasticised films dominates segregation behaviour and overpowers the opposing effects of physical properties. Although the exact surfactant nanostructure forming within each film is difficult to predict, it can be theorised that as surfactant concentration in the films is much greater than the CMC, it is unlikely that spherical micelles are present, as larger structures are formed at higher concentrations.[197] Cylindrical micelles of $C_{12}E_5$ have been shown to form in aqueous solution.[198] If this is also occurring in these films under humidity control, then an adjustment made to the surfactant chain length would have a corresponding effect on cylindrical micelle diameter.[199] $C_{12}E_4$ would exhibit a reduced diameter compared to $C_{12}E_5$, which would have a less negative impact on the free volume of the polymer, making the surfactant nanostructure more compatible with the polymer matrix. $C_{12}E_6$ would have a larger diameter than the other surfactants, meaning it would reduce free volume within the system more. Therefore it would be less energetically favourable for the surfactant structure to remain within the matrix as opposed to being situated on the surface of the film compared to the smaller surfactants, hence leading to increased surface segregation. Another possible explanation for this phenomenon is that although the ethoxy groups of the surfactant have an increased compatibility with the polymer compared to the hydrocarbon chain, they still have somewhat unfavourable interactions with PVA. This would mean that the smaller surfactant would have fewer unfavourable interactions with the polymer, simply due to its reduced molecular weight.

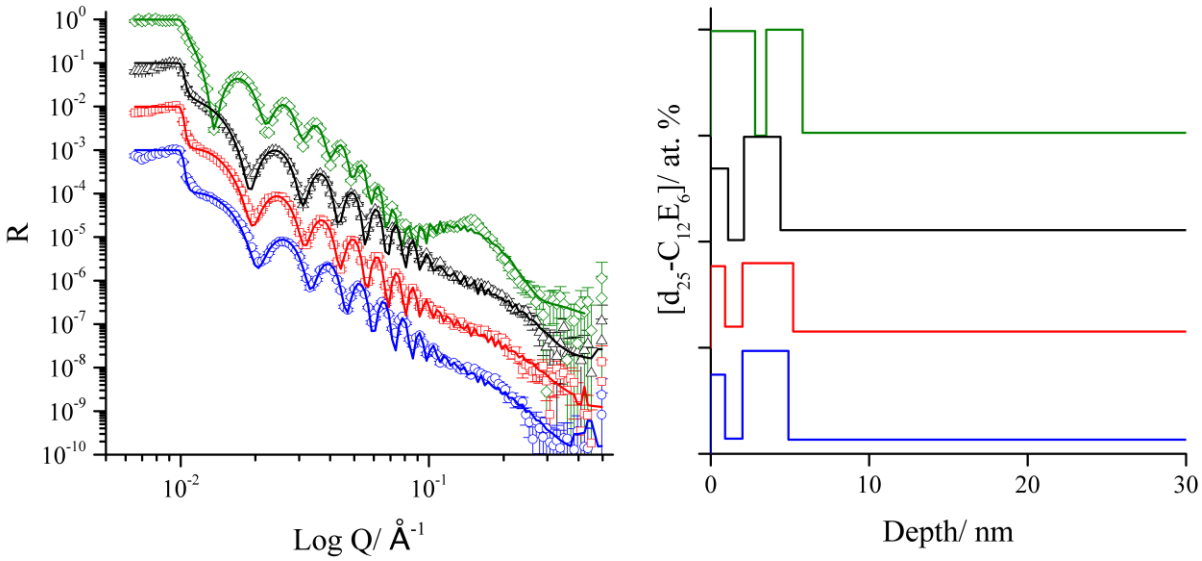

Figure 5.30. NR data (offset), fits and composition profiles for 20 w% d_{25}-$C_{12}E_6$, PVA films subjected to 23%RH (blue), 33%RH (red), 55%RH (black) and 85%RH (green) environments. Each increment on the depth profile accounts for 0 to 100 at. % of d_{25}-$C_{12}E_6$.

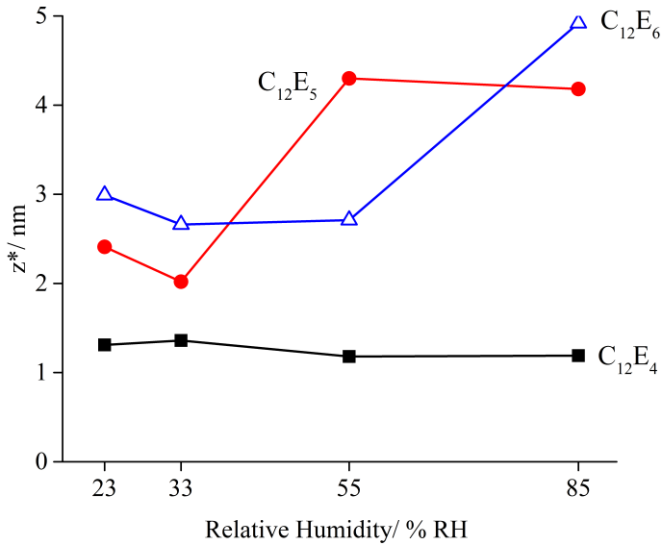

Figure 5.31. z* of d_{25}-$C_{12}E_4$ (black), d_{25}-$C_{12}E_5$ (red) and d_{25}-$C_{12}E_6$ (blue) in thin PVA films against relative humidity.

5.2.2. Surfactant Distribution in Ternary Plasticised Films with Humidity

The interaction of the plasticisers glycerol and water with the surfactant has been shown to be important in determining surfactant segregation in $C_{12}E_5$ containing films, hence similar experiments were performed with plasticised films containing $C_{12}E_4$ and $C_{12}E_6$. Figure 5.32. displays the data, fits and depth profiles for the glycerol containing samples, it can be seen the addition of glycerol causes a substantial increase in the amount of segregated surfactant, similarly to what was seen for $C_{12}E_5$, suggesting a decrease in compatibility between surfactant and PVA upon plasticisation when studied under humidity control. At all humidity values (23, 33 and 55 %RH) a double surface excess is now present, which was not detected in the non-plasticised samples. This appears to be a feature of the reduced surfactant-polymer compatibility, as more surfactant attempts to it segregate to the surface. As the additional surfactant cannot add to the pure layer of $C_{12}E_4$ already at the surface, the addition of glycerol causes another surfactant layer to be formed directly below the surface excess. The depleted SLD region between the surfactant layers has been shown to be comprised of glycerol molecules for $C_{12}E_5$ containing films in chapter 5.1.5. It is likely that a similar phenomenon is also seen here for $C_{12}E_4$ containing, plasticised films, where the formation of surfactant lamella is facilitated by the presence of polar molecules within the polymer matrix. Unfortunately there was an error during the measurement of the 85 %RH, $C_{12}E_4$, plasticised sample hence a depth profile is not given for this data, making it difficult to see any trend in $C_{12}E_4$ segregation in plasticised films with varying humidity. Exchanging of the labelled components (Figure 5.33.) uncovered a surface excess of glycerol, as was expected from the presence of highly-concentrated surfactant layers with depleted SLD regions between them, so formation of a surfactant-plasticiser complex is demonstrated again with $C_{12}E_4$. No evidence of structuring within the

glycerol excess is visible here however as was seen with $C_{12}E_5$, so it is difficult to define a surfactant-glycerol nanostructure at the surface.

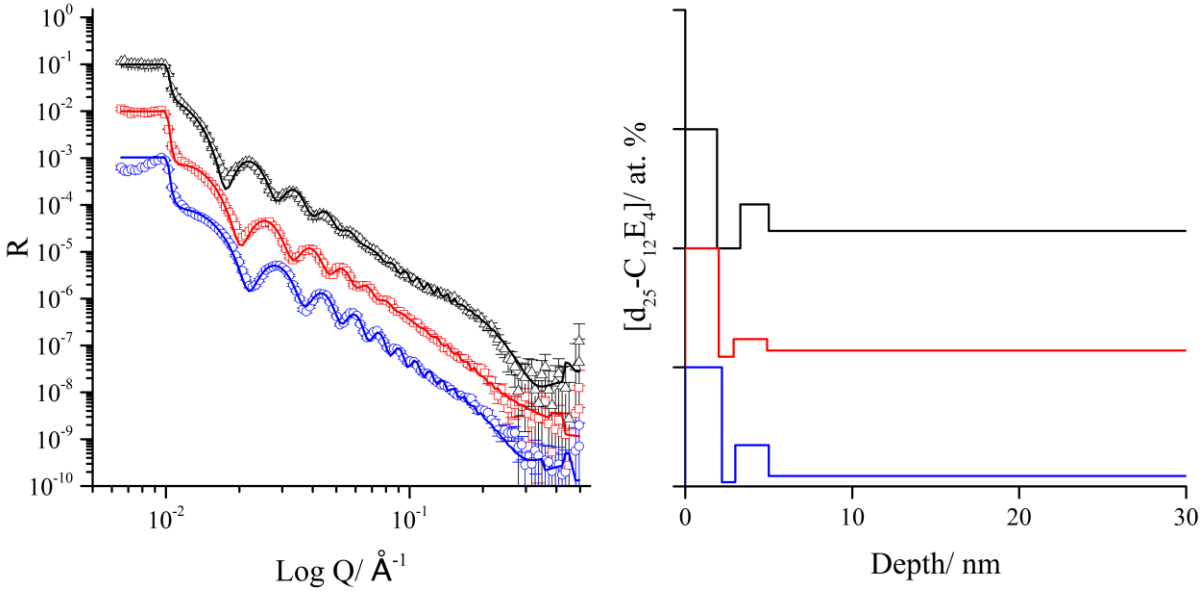

Figure 5.32. NR data (offset), fits and composition profiles for 20 w% d_{25}-$C_{12}E_4$, 20% h-glycerol PVA films subjected to 23%RH (blue), 33%RH (red), 55%RH (black) and 85%RH (green) environments. Each increment on the depth profile accounts for 0 to 100 at. % of d_{25}-$C_{12}E_4$.

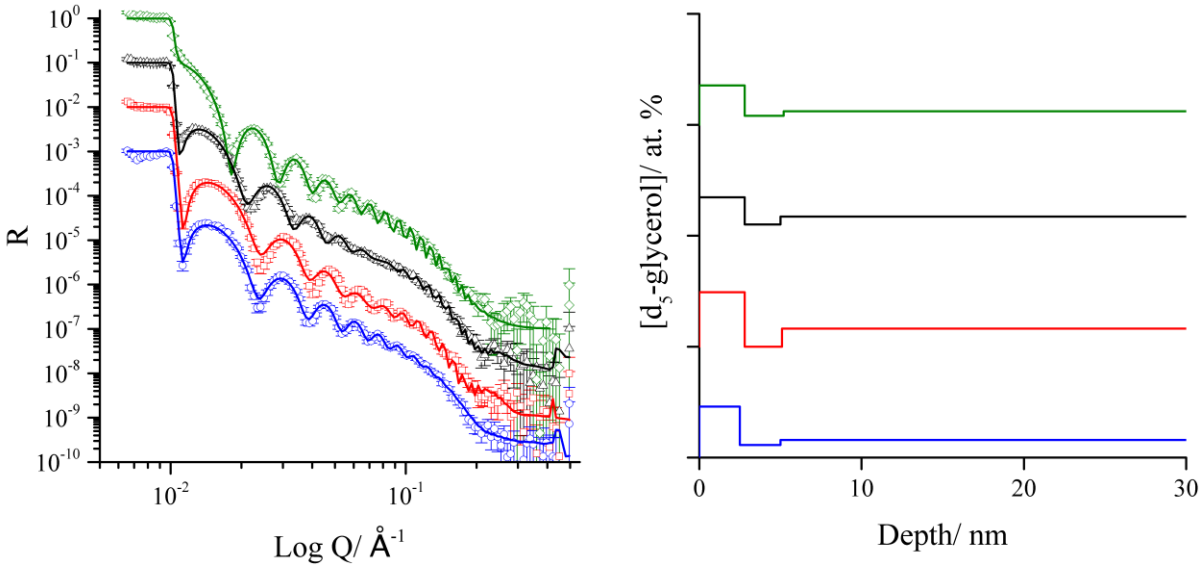

Figure 5.33. NR data (offset), fits and composition profiles for 20 w% h-$C_{12}E_4$, 20% d_5-glycerol PVA films subjected to 23%RH (blue), 33%RH (red), 55%RH (black) and 85%RH (green) environments. Each increment on the depth profile accounts for 0 to 100 at. % of d_5-glycerol.

Figure 5.34. displays the data, fits and concentration profiles for 20% d_{25}-$C_{12}E_6$ with 20% h-glycerol samples. Interestingly where $C_{12}E_6$ containing, non-plasticised films exhibited greater segregation compared to the $C_{12}E_5$ films, the opposite behaviour is found with plasticised films. This would suggest

that the larger surfactant has increased compatibility with the film in plasticised samples compared to the $C_{12}E_5$ plasticised samples. The increased HLB of $C_{12}E_6$ should cause more favourable interactions with the polar polymer and plasticiser, which could be the reason for the reduced segregation. It is worth noting that significant segregation is still visible however, it is just reduced in comparison to the behaviour of $C_{12}E_5$. The relationship between segregation and humidity is similar to what was seen for $C_{12}E_5$ where both the number and concentration of surface segregated surfactant layers increases with increasing humidity.

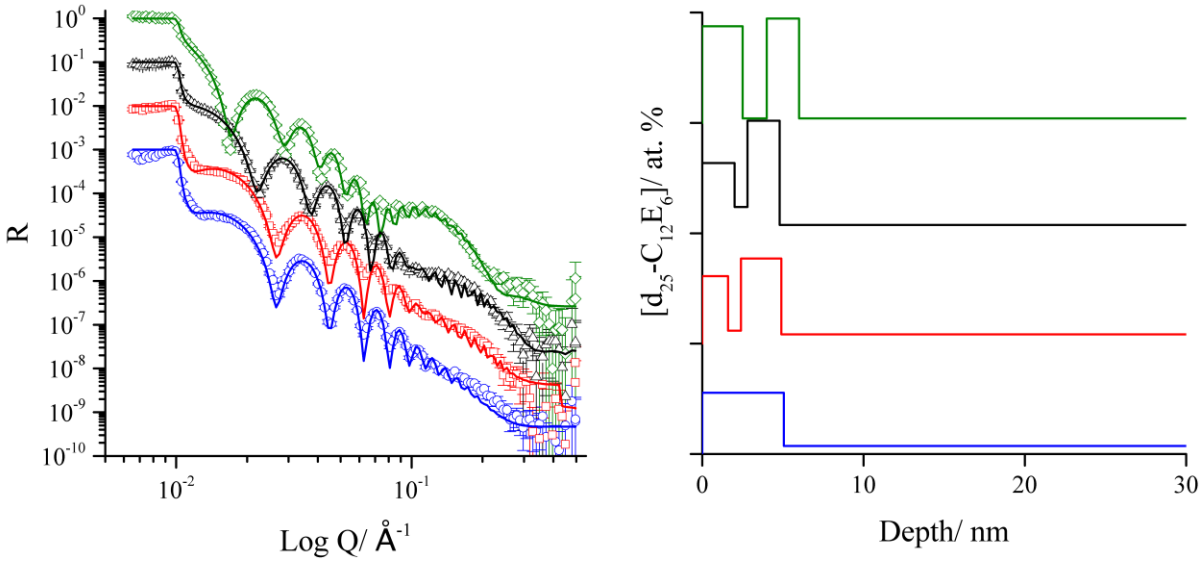

Figure 5.34. NR data (offset), fits and composition profiles for 20 w% d_{25}-$C_{12}E_6$, 20% h-glycerol films subjected to 23%RH (blue), 33%RH (red), 55%RH (black) and 85%RH (green) environments. Each increment on the depth profile accounts for 0 to 100 at. % of d_{25}-$C_{12}E_6$.

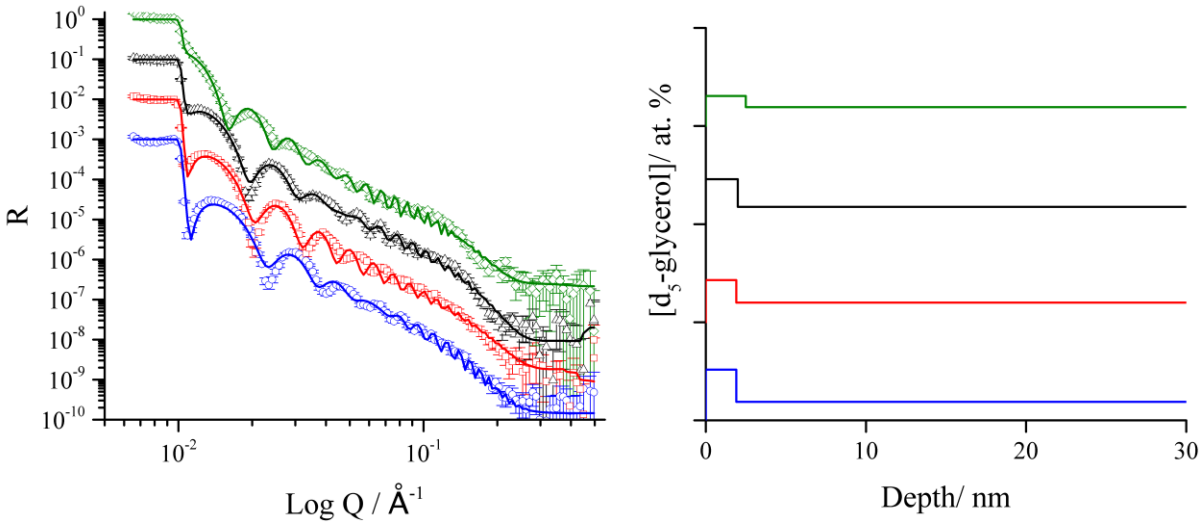

Figure 5.35. NR data (offset), fits and composition profiles for 20 w% h-$C_{12}E_6$, 20% d_5-glycerol PVA films subjected to 23%RH (blue), 33%RH (red), 55%RH (black) and 85%RH (green) environments. Each increment on the depth profile accounts for 0 to 100 at. % of d_5-glycerol.

When observing deuterated glycerol distribution with $C_{12}E_6$ a surface excess of glycerol is again seen in Figure 5.35., indicating some favourable interaction between $C_{12}E_6$ and the plasticiser. Compared to the other surfactants however the concentration of glycerol seen at the surface is small, indicating that the interaction between the higher molecular weight surfactant and plasticiser is correspondingly reduced. What is unique about this sample set is that a clear relationship between humidity and deuterated plasticiser distribution is present in the ternary films. Figure 5.36 displays the z* for all $C_{12}E_6$ containing samples, where it can be seen that as humidity increases, the amount of d_5-glycerol present at the surface decreases. This finding reveals more information on the interactions between surfactant, glycerol and water at the films surface. As the $C_{12}E_5$ results suggested that a slab of polar molecules (in that case glycerol) exists in between the surfactant-rich layers in order for surface structuring to occur, then similar structuring should occur in the case of $C_{12}E_6$. As more surfactant is present in the surface excess as relative humidity increases then more polar molecules are required to shield the surfactant head-groups from each other. It is clear from the d_5-glycerol, h-$C_{12}E_6$ sample that it is not glycerol which occupies this region as the amount of plasticiser present at the surface (z*) decreases with increasing relative humidity; it therefore must be water (absorbed from the atmosphere) which makes up the interstitial regions between surfactant layers. Figure 5.37. shows a schematic representation of how water molecules can replace glycerol in the interstitial layers with increasing humidity, leading to increased surfactant surface structuring. This suggests that either water is more effective at shielding the polar interactions of the surfactant head-groups compared to glycerol, or simply that the concentration of water within the film is greater than that of plasticiser at higher humidity concentrations, so it is more likely to occupy these regions.

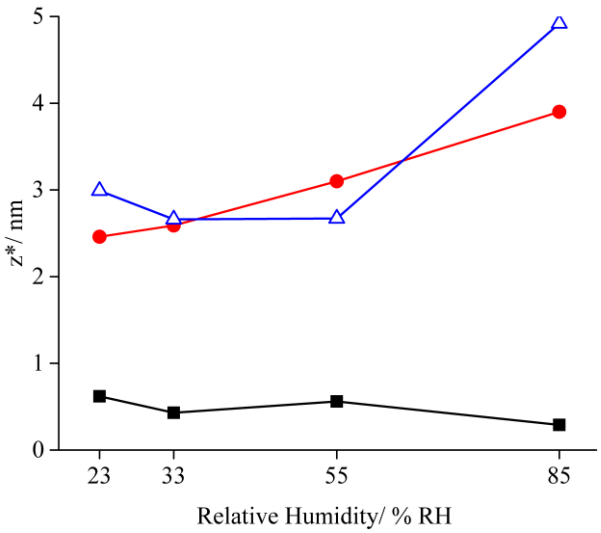

Figure 5.36. z* of d_{25}-$C_{12}E_6$ (blue), d_{25}-$C_{12}E_6$ with h-glycerol (red) and d_5-glycerol with h-$C_{12}E_6$ (black) in thin PVA films against relative humidity.

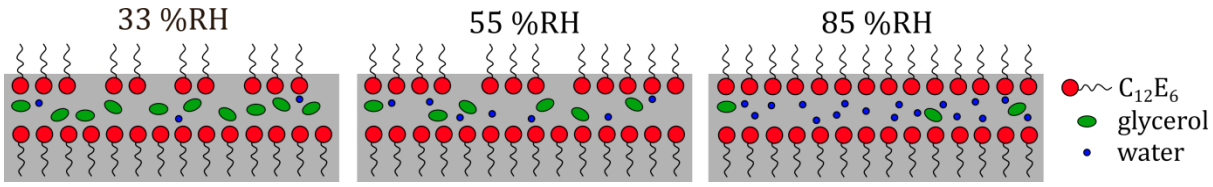

Figure 5.37. Schematic representation of increasing surfactant surface excess concentration with increasing relative humidity, as well as replacement of glycerol with water in the interstitial region

5.2.3. Summary of HLB Findings

In an attempt to summarise the findings across all non-ionic surfactant containing samples studied under humidity control Table 5.4., Table 5.5. and Table 5.6. are presented. These tables represent the magnitude the surface excess (d_{25}-$C_{12}E_5$ or d_5-glycerol) rescaled from the maximum and minimum values across the entire sample range, to 0-10. These values were then colour coded, red (0) being the smallest z* value and green (10) being the largest. For binary films of surfactant and PVA it can be seen from Table 5.4. that the surfactant surface excess increases as a function of both relative humidity and HLB. It is theorised that the relationship between surfactant molecular weight and segregation is established by size of surfactant nanostructures forming in the PVA film. Although the exact nanostructure is not predictable from this form of NR experiment, it appears that the greater negative effect on free volume within the system that a larger surfactant nanostructure would have is a logical reason for the increased migration seen with $C_{12}E_6$, and the reduced migration seen with $C_{12}E_4$. Surface excess as a function of humidity appears to be a result of plasticisation via water absorbed from the atmosphere. The increased water absorption in binary films causes a decrease in compatibilty between the surfactant and polymer, facilitating increased surface segregation.

The NR results from plasticised samples under RH control also show a general increase in segregation under increased relative humidity. For most plasticised samples, especially the $C_{12}E_5$ samples, they appear to show increased surfactant segregation compared to their non-plasticised counterparts. This is theorised to be due to the ability of glycerol to absorb a significant portion of its own mass in water. Therefore allowing increased water absorption into films where this increased plasticisation by water causes further segregation. From these results it would appear that the non-ionic surfactants have a reduced compatibility with water compared to glycerol in thin PVA films.

As glycerol cannot aggregate and form liquid crystals as the non-ionic surfactants do, it is not surprising that Table 5.6. shows reduced z* values compared to the other two tables as it is the surface excess of glycerol being studied in this case. For most cases in this sample set there does not exist a strong correlation between surface segregation and either HLB or humidity. However by plotting the table in the colour-coded format it is possible to see there is a general reduction in surface segregation as samples move towards the lower right corner. This general reduction in surface segregation with increasing humidity for $C_{12}E_6$ ternary samples was especially useful in highlighting the ability of water from the atmosphere to replace glycerol in the interstitial regions between surfactant-rich layers, facilitating increased surfactant segregation. It is clear from these results that humidity has significant

and intriguing effects on non-ionic surfactant surface and bulk distribution in thin films. Therefore the study naturally led to the investigation of how these factors effect ionic surfactant segreation too.

Table 5.4. Rescaled (from 0-10) z* surface excess values for all deuterated non-ionic surfactant containing, binary PVA films where 0 is the smallest amount of segregation and 10 is the largest, colour scale applied via conditional formatting

	HLB	Relative Humidity/ %			
		23	33	55	85
d_{25}-$C_{12}E_4$	10.7	1.1	1.5	1.7	1.6
d_{25}-$C_{12}E_5$	11.7	4.1	3.4	7.7	7.5
d_{25}-$C_{12}E_6$	12.5	5.2	4.6	4.7	9.0

Table 5.5. Rescaled (from 0-10) z* surface excess values for all deuterated non-ionic surfactant and hydrogenous glycerol containing, ternary PVA films

	HLB	Relative Humidity/ %			
		23	33	55	85
d_{25}-$C_{12}E_4$	10.7	4.1	3.1	3.3	-
d_{25}-$C_{12}E_5$	11.7	6.4	7.0	10.0	8.9
d_{25}-$C_{12}E_6$	12.5	4.2	4.5	5.4	7.0

Table 5.6. Rescaled (from 0-10) z* surface excess values for all hydrogenous non-ionic surfactant and deuterated glycerol containing, ternary PVA films

	HLB	Relative Humidity/ %			
		23	33	55	85
d_{25}-$C_{12}E_4$	10.7	1.1	1.2	0.5	0.7
d_{25}-$C_{12}E_5$	11.7	1.1	4.1	0.4	0.3
d_{25}-$C_{12}E_6$	12.5	0.7	0.3	0.5	0.0

6. Ionic Surfactant Segregation in PVA Film

Ionic surfactants are of importance for many products and processes including; DNA extraction,[200] synthesis of gold nanoparticles,[201] hair conditioning products,[202] insecticides,[203] as well as commonly being used in detergent formulations[204] and fabric softeners,[205] making their interactions with PVA film in soluble unit does formulations of significant interest to this project. The study of ionic surfactants affords certain advantages over non-ionics when analysing their segregation behaviour with scattering techniques. The presence of relatively large counter-ions which usually accompany the charged tail-groups of ionic surfactants allows other IBA techniques such as RBS to be used. As these counter-ions differ significantly in atomic weight from other elements present within the sample, backscattered helium ions in RBS experiments from these elements have very different energy to those backscattered from lighter elements. If the contrast between the counter-ion and polymer matrix is large enough, then the scattering from the counter-ion can be completely isolated, allowing complete depth distribution of the surfactant throughout the entire film to be analysed. The advantage of this is that no labelling of the additive is required, significantly reducing the cost of the experiment, as well as increasing the range of surfactants that can be studied.

6.1. Cetyltrimethylammonium Bromide (CTAB) Segregation in Thin PVA Films

Although cationic surfactants are not used as detergents, they are commonly found in fabric softeners,[206] which are used in conjunction with many laundry cleaning products, such as liquitabs. One surfactant that is readily available and well-studied in the literature,[207-209] whilst also possessing a counter-ion with sufficient difference in mass from the C, H, O which make up PVA, is CTAB. The presence of the large bromide (Br^-) counter-ion on each surfactant molecule provides enough contrast from the polymer and plasticiser to enable its depth profile to be measured by RBS. CTAB is a favoured surfactant for the extraction of DNA as it can simultaneously solubilise a cell membrane and denature enzymes that would hydrolyse DNA, meaning that DNA remains largely intact during the process.[200] The surfactant has also been used as a template to create mesoporous materials which have found use as catalysis substrates due to their extremely large internal surface area.[210] Some of the results in the following section (6.1.) were also published in the initial paper on surfactant segregation.[170]

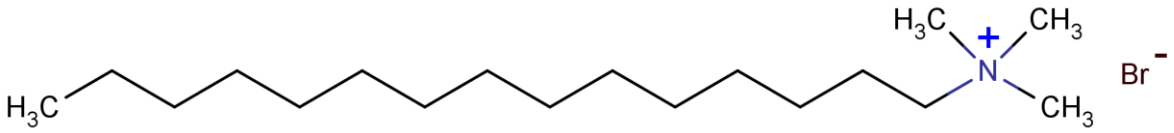

Figure 6.1. Chemical structure of cetyl trimethylammonium bromide (CTAB)

6.1.1. CTAB Segregation in Binary PVA Films

RBS spectra of a thin PVA film containing 25 w% CTAB can be seen in Figure 6.2. Recoils detected below 0.6 MeV are due to scattering from lighter elements such as C, O and Si, with Si dominating scattering as it is present in the most abundance as the substrate. Recoils detected in the region between 0.7 and 1.3 MeV exclusively arise from the Br^- ions present in the surfactant. Not only can conventional fits be produced with DataFurnace, as described in chapters 4 and 5, but when analysing a sample with RBS, 'separated spectra' are also obtainable. These display the relevant scattering from each element (Figure 6.2). As can be seen, Si backscattering dominates the spectrum, hence viewing the scattering on a log scale allows bromide scattering to be more visible (Figure 6.3.). The lower energy edge of the Br^- scattering (0.7 MeV) is notably more diffuse than the high-energy edge (1.3 MeV). This is a feature of film roughness, caused by variation in film thickness as discussed in chapter 4.2. Scattering from the surface of the film produces helium ions of a higher energy than those scattered from deeper in the film, as the incident beam loses energy as it traverses the sample, therefore the variation in counts per channel with energy is related to the variation in concentration with depth.

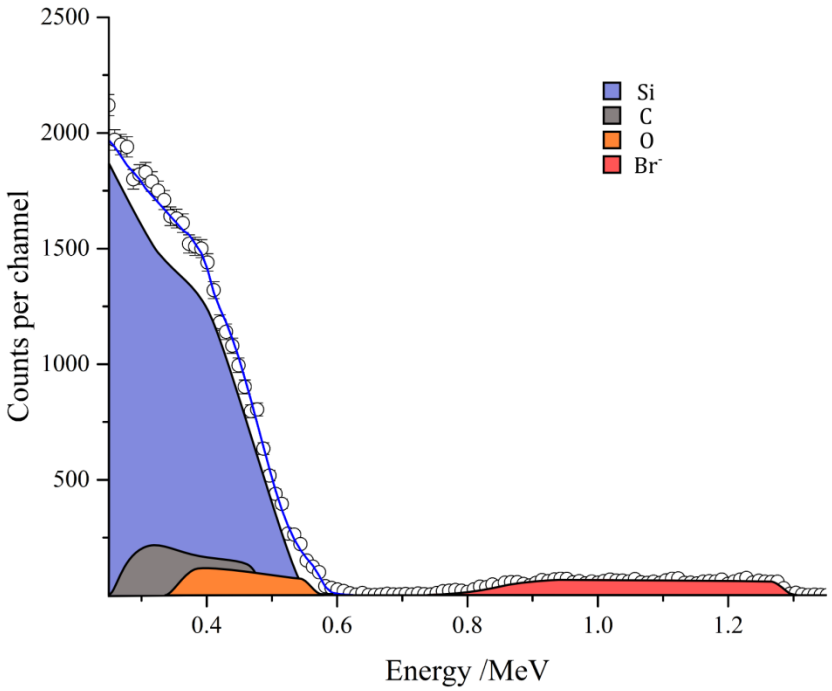

Figure 6.2. Separated RBS spectra displaying the backscattering from each individual element within the sample.

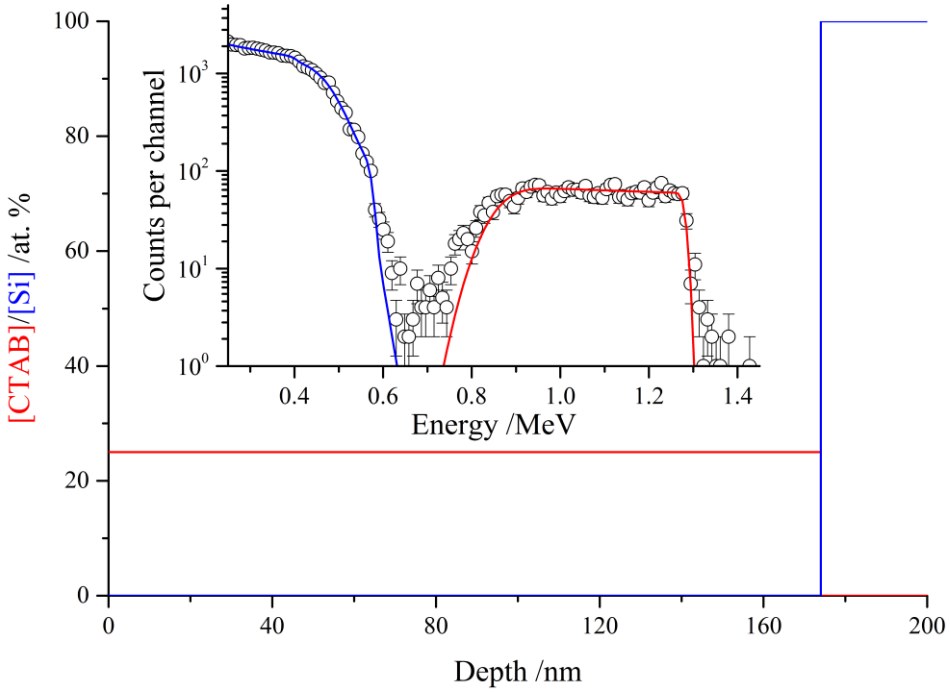

Figure 6.3. RBS data and fits (inset) for 25% CTAB in a thin PVA film, depth profile for CTAB (red) and Silicon (blue) also shown.

CTAB shows an even distribution in a non-plasticised film; in contrast to the behaviour seen for the non-ionic surfactants. Again surface energy values may provide some insight in to why CTAB behaviour in a PVA film is somewhat different to the behaviour of d_{25}-$C_{12}E_5$. As previously discussed, an estimated SE of the PVA used in this study is ~40 mNm^{-1}, unfortunately no value for the SE of CTAB in its pure form could be found in the literature. This is likely to be because it would be difficult to find a series of contact fluids that would be sufficiently incompatible with CTAB to enable reliable contact angle analysis. Much work has been done on the surface tension of CTAB in solution however, where it has been shown that in aqueous solutions CTAB can reduce the ST of water from 72 mNm^{-1} to a limiting surface tension of 32-26 mNm^{-1} when present in concentrations above the critical micelle concentration (0.92 – 1.0 mM).[211] These ST values were achieved when KCl was added to the solution, which screens the charged groups of the surfactant from each other, allowing closer packing. While caution must be taken when comparing ST for an aqueous solution of CTAB to the SE of PVA, it is plausible that (because no such additional ions were present) CTAB has a similar ST to PVA. If the ST/SE values of the two components are similar then migration of CTAB to the surface would cause no significant reduction of film ST, and hence would not occur spontaneously.

6.1.2. CTAB Segregation in Ternary, Plasticised PVA Films

In chapter 5, it was seen that the addition of plasticiser increased surfactant-polymer compatibility with $C_{12}E_5$ under ambient conditions. It has been hypothesised that this is mostly due to favourable interactions between the PVA, surfactant and glycerol, caused by the presence of significant H-bonding

sites. As CTAB contains much fewer polar bonds compared to the non-ionic, it is predicted that CTAB may exhibit decreased compatibility with the plasticiser glycerol in comparison to the ethylene glycol monododecyl ether variants. By keeping the surfactant concentration constant at 25 w% and varying the concentration of glycerol at 10, 20 and 30% the effect of plasticisation is probed. Scattering from the bromide ion and DataFurnace fits are displayed in Figure 6.4. At lower concentrations of plasticiser (≤ 10%) the data appears much the same as for a non-plasticised film. However when significant levels of plasticiser are found which mirror the volumes used in industry (≥ 20%) an intense peak forms in the data at ~1.3 MeV, with another peak of lower intensity at ~0.9 MeV. The reason for the decreased intensity of the peak at lower energy is explained in the same way as the diffuse edge of the data at lower energies, where the loss of resolution is due to film thickness variation, causing the peak at lower energy to be smeared out. Fitting of these two peaks with DataFurnace accommodates for this decrease in resolution, producing depth profiles which contain two highly concentrated excesses of surfactant at both the air and substrate interface (Figure 6.5.). Each excess is at least 10 nm thick and has a CTAB concentration of >50 at. %, indicating significant segregation has been activated at higher plasticiser concentrations. These findings support the theory that it is not only surface energy which is controlling migration tendencies. If SE differences were the only impetus for migration then this large change in surfactant behaviour would not be explained. While the addition of glycerol to the film might contribute to a small increase in the overall SE of the film, as glycerol ST > PVA SE, it would only be marginal as PVA is still by far the most abundant compound in the film, and therefore SE would remain dominated by PVA. Compatibility arguments can help to explain this phenomenon; if the addition of glycerol, which has a greater affinity and compatibility with PVA due to its hydrogen bonding sites in comparison to CTAB, outcompetes CTAB for its favourable interaction with the amorphous regions of the polymer, then this may cause segregation to be initiated at higher concentrations. This effect may not be seen at plasticiser concentrations of ≤ 10% as there exists enough space within the polymer matrix to accommodate both molecules, when the critical concentration of glycerol is exceeded however, CTAB is excluded from the bulk of the PVA film, causing it to segregate to each interface.

It is also possible that the addition of glycerol is speeding up the migration of CTAB from the polymer film. If the migration rate of CTAB to the surface is slow, because of the increased viscosity of spin-cast polymer films,[212] it may be that the addition of plasticiser simply speeds up migration, to a rate where visible migration and agglomeration at the surface and substrate interface is visible in the 30-60 seconds between film spin-casting and vitrifying with liquid nitrogen. Plasticisers have been shown to decrease the viscosity of polymers,[213] therefore this explanation could also stand for describing the segregation of CTAB upon plasticisation.

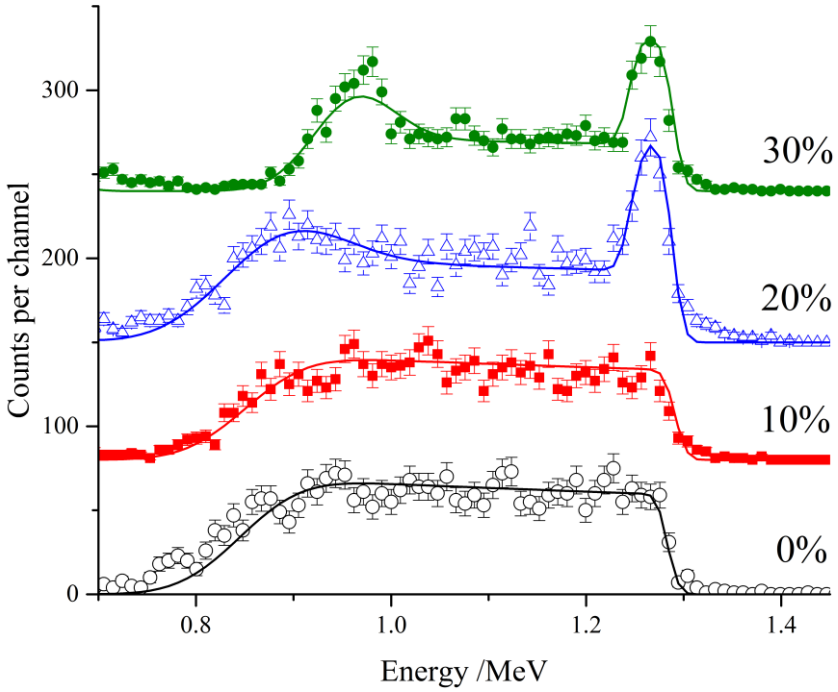

Figure 6.4. RBS data and fits for the depth distribution of 25% CTAB in mixed PVA/glycerol films as a function of glycerol content. Data are offset for clarity and annotated with glycerol content.

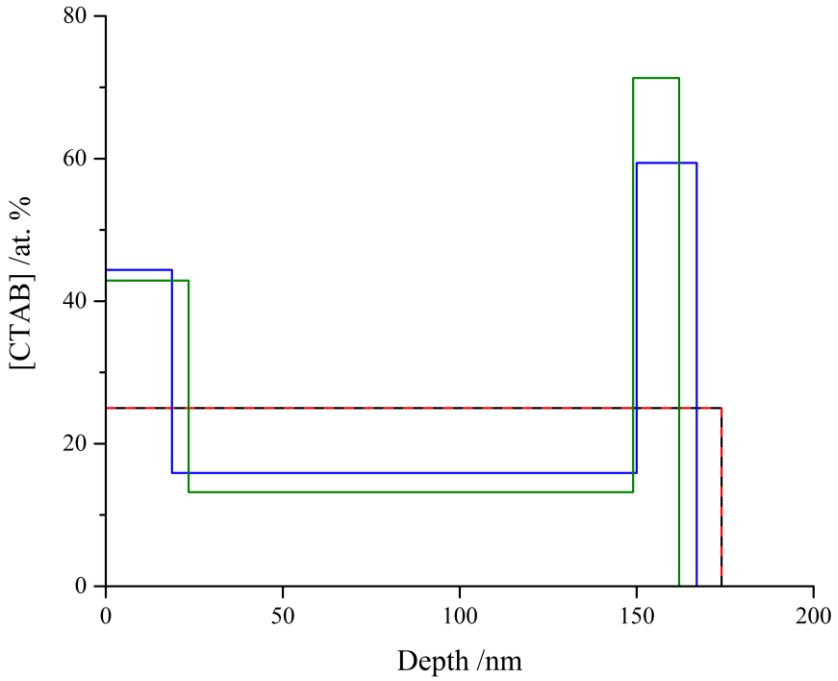

Figure 6.5. Depth profiles corresponding to the previous DataFurnace fits: black (0%), red (10%), blue (20%) and green (30%).

The presence of surfactant in a ternary film was shown to have a significant effect on plasticiser distribution in the previous chapter, causing the homogeneous distribution of glycerol to be perturbed when even small concentrations of non-ionic were present at the surface. As CTAB shows surface segregation in thin films when plasticised, it is possible that the distribution of glycerol in ternary films

will also exhibit non-homogeneous behaviour. The concentration of CTAB was kept constant at 20 w% whilst the amount of plasticiser in the film was varied at 10, 20 and 30 w%. Figure 6.6. displays the data, fits and concentration profiles (inset), it can be seen that despite the segregation behaviour displayed in the CTAB profiles in Figure 6.5., only homogeneous distribution is seen for the plasticiser. These results imply there is no favourable interaction between the surfactant and plasticiser, which is entirely consistent with the hypothesis that CTAB segregation is driven by incompatibility with glycerol, possibly due to the lack of H-bonding sites compared to $C_{12}E_5$. Judging by the thickness of the glycerol layer (~130-150 nm) there does however appear to be some partitioning of plasticiser within the films, for example taking the total thickness of the 20% h-glycerol sample from the previous figure and subtracting the thickness of both excesses gives 131 nm. Considering the variance in film thickness between samples this is quite similar to the thickness of the glycerol layers found when deuterating the plasticiser, suggesting glycerol does not span the entire width of the polymer film, and instead resides mainly in the region between each surface excess. Compatibility of the plasticiser and CTAB is clearly an issue within the film, with the two compounds having difficulty to co-locate. The discrepancy between the fit and the data at ~12.8 MeV for the 30 w% d_5-glycerol sample could correspond to a region of reduced plasticiser concentration related to where CTAB is enriched.

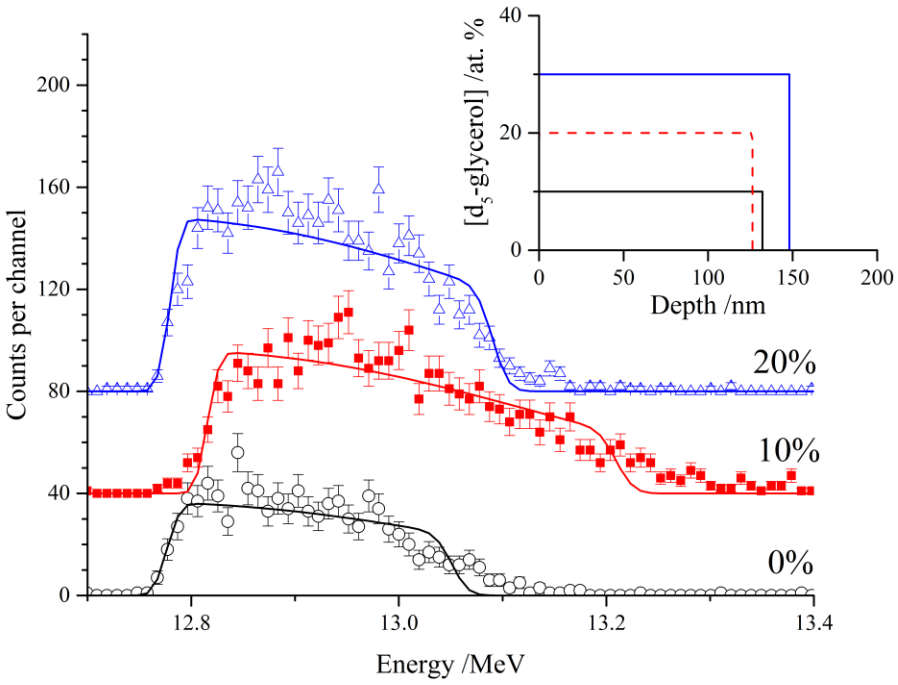

Figure 6.6. NRA data and fits for 10 (open circles, black), 20 (closed squares, red) and 30% (open triangles, blue) d_5-glycerol plus 20% CTAB in thin PVA films, produced depth profiles are shown in the inset.

6.1.3. Summary of CTAB Segregation Patterns

By investigating the first cationic surfactant in this study some interesting trends have been uncovered. In binary films CTAB has been shown to exhibit homogeneous distribution, which had not been displayed for any surfactant so far. This is thought to be due to its increased surface tension compared to other surfactants, hence migration to the surface results in no favourable change in the SE of the system. Up to now the addition of plasticiser has only had the ability to either enhance or reduce the segregating nature of a surfactant in thin PVA films, but here it has demonstrated the ability to completely change the nature of CTAB, causing it to become surface active when it does not show segregation tendencies in binary PVA films. The plasticiser was shown to have no effect in low concentrations, another trait which has not been discovered before, as even small amounts of glycerol have been shown to effect surfactant segregation in chapter 5. The fact that CTAB only exhibits segregation upon plasticisation with glycerol, which it has little impetus for favourable interaction with due to the lack of H-bonding sites, supports the theory that compatibility of components is something which has a significant effect in determining segregation behaviour. If cationic surfactants can exhibit such activation behaviour it is of interest to explore the nature of anionic surfactants also.

6.2. Segregation of Sodium Dodecylsulphate (SDS) in PVA Film

One of the most prominent ionic surfactants in the academic literature[214-216] is sodium dodecylsulphate (SDS). SDS contains a Na^+ counter-ion as opposed to CTAB's Br^-, making it an anionic surfactant. Although the counter-ion was used to monitor surfactant distribution for CTAB, Na^+ is not the heaviest element within the surfactant. Sulfur has the largest atomic mass and should therefore provide the best basis for analysis with RBS, as it has the highest contrast to the other elements present. However as it is significantly lighter than Br^-, the contrast between the surfactant and other elements present will be less. It will therefore be more challenging to fully separate its scattering from Si. SDS can be found in many heavy duty detergents used in industry due to its effectiveness when removing oily residues from a variety of materials, although linear alkylbenzene sulphonates (LAS) are more commonly used in modern formulations.[217] Although SDS is not included in the laundry detergent used in liquitabs, it offers a wide array of background literature due to its presence as a model surfactant for many studies.[214-216] SDS has been used to customise the properties of polymer films before,[218] where it was shown to effect the tensile strength, elongation at break of plasticised soy protein isolate films even in small concentrations. SDS is generally not found in detergent products due to the presence of the sodium counter-ion which can affect the pH of the detergent and therefore the efficiency of any enzymes present.[219] However, despite these effects SDS has never had its distribution within polymer films be analysed. In the following sections, for the first time SDS segregation behaviour and distribution in PVA films is explored.

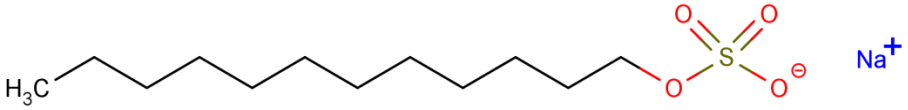

Figure 6.7. Chemical structure of sodium dodecyl sulphate (SDS)

6.2.1. Segregation of SDS in Binary Films

Initial segregation studies were performed using RBS as, if isolation of the surfactant distribution was possible with this technique, a deuterated analogue of the material would not be required. Figure 6.8. shows the backscattering spectrum from a sample containing 20 w% h-SDS in PVA. Scattering above 0.7 MeV is from the heavier elements in the sample, and below 0.7 MeV from Si, C and O. Upon initial viewing of the raw data it was thought that SDS was present in higher concentrations at both the air interface (0.95 MeV) and the silicon interface (0.75 MeV) due to the increase in counts seen at these energies. However, this was disproven upon fitting with DataFurnace by exporting a separated spectrum (Figure 6.9.). From the linear separated spectra, there is evidence of a surface excess of SDS shown by the increase in counts at 0.95 MeV, although it is not conclusive within the error of the measurement. What was initially thought to be a substrate excess of surfactant was in fact a reiteration of the surface excess caused by backscattering of ^{4}He from the sodium counter-ion, emphasising the need for careful fitting of IBA data. It became apparent from these results that a deuterated analogue of the surfactant must be obtained in order to isolate its distribution from the PVA matrix, as overlapping of scattering profiles for different elements would make accurate interpretation very difficult. A sample of d_{25}-SDS was obtained from RAL for use with neutron experiments. In order to perform a preliminary experiment as a prelude to submitting a neutron proposal, 0.5 g of the deuterated surfactant was sent to Durham from Dr. Peixun Li (STFC, ISIS facility).

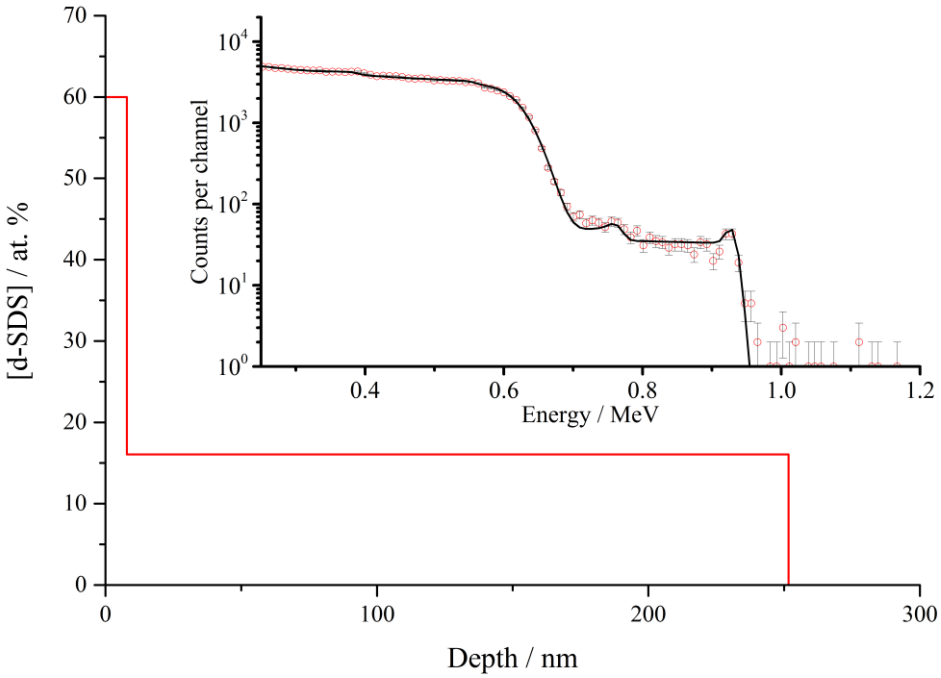

Figure 6.8. RBS data and fits for 20% h-SDS in a thin PVA film (inset) and produced depth profile.

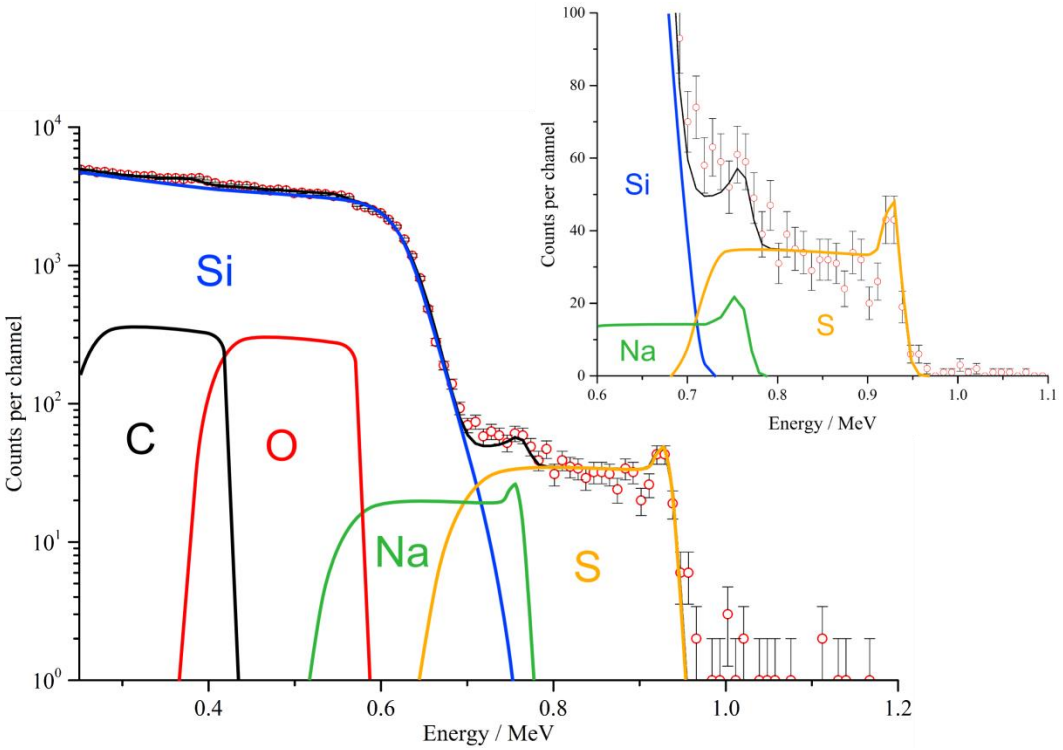

Figure 6.9. Separated RBS spectra of the previous data, displaying each of the constituent elements present in the sample with a zoomed and non-logarithmic plot shown in the inset.

NRA experiments with d_{25}-SDS were performed on binary films of surfactant and PVA. Figure 6.10. shows the data obtained for 10 and 20 w% d_{25}-SDS in PVA. Clear evidence of surface activity of SDS is confirmed, forming an excess of 18 nm and 23, 43 at. % for 10 and 20 w% d_{25}-SDS, respectively. To explain this spontaneous segregation behaviour, surface energy/tension arguments are used. Much work has been done on the calculation of surface tension for SDS, both in its 'pure' form and in aqueous solution. Mysels[220] quotes values from several authors with pure SDS surface tension values ranging from 48.4 - 52.5 mNm^{-1}, obtained using the maximum-bubble-pressure method. These values are generally higher than that established for PVA, so spontaneous migration may not be expected, but migration is plainly visible in the experimentation. Aqueous solutions of SDS do however exhibit the lower surface tension values that might be expected from the spontaneous migration seen in the IBA experiments. Solutions of > 5×10^{-3} M exhibited surface tension values of < 35 mNm^{-1},[221] significantly lower than the SE established for PVA. As the surfactant is dispersed in a larger polymer matrix, surface tension values in solution are perhaps more relevant than those calculated for the pure surfactant. A powerful feature of NRA is that it allows the surface excess of the surfactant to be determined directly, and it appears that there is a layer of ~18 nm of ~50 at. % deuterated surfactant at the air surface. Although the surface layer is only ~50 at. %, the total thickness of the layer is very significant. Molecular simulations have shown the average length of an SDS molecule to be 1.36 ± 0.07 nm,[222] therefore the layer observed is much thicker than could be accounted for by a monolayer of surfactant at the surface. Although NRA lacks the resolution required to characterise the orientation of the d_{25}-SDS molecules, it clearly reveals the presence of multilayer adsorption at the surface, suggesting presence of a surfactant wetting layer.

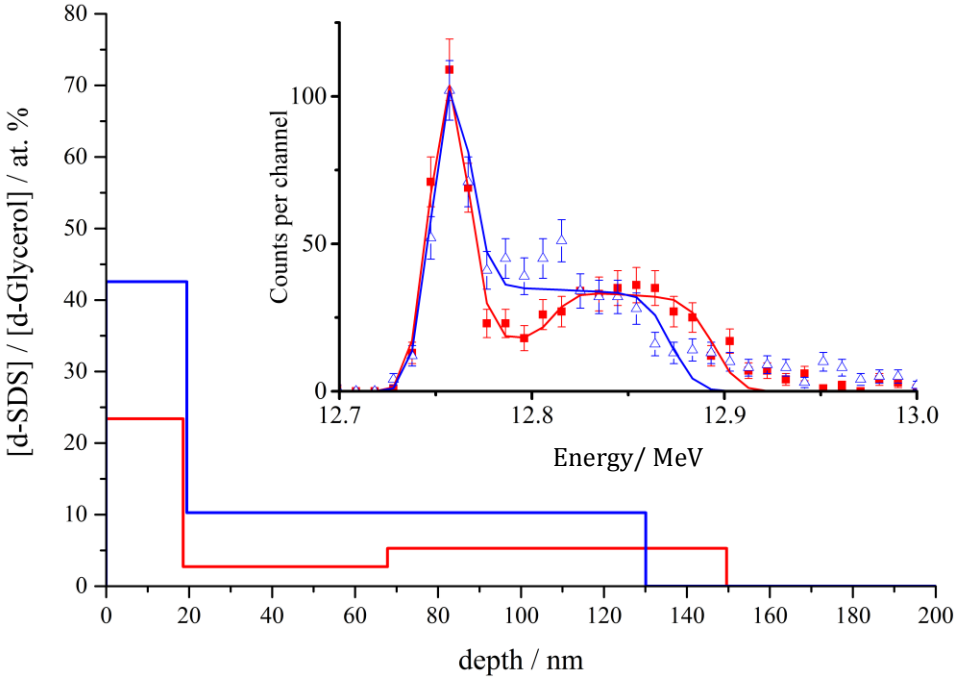

Figure 6.10. NRA data and fits (inset) for 10% (red, squares) and 20% (blue, triangles) d_{25}-SDS in thin PVA films. The derived concentration profiles of d_{25}-SDS correspond to the fitted curves.

Complimentary NR experiments were performed with a similar sample set-up to that described in 5.1. (ambient conditions), which also detected a significant surface excess of d_{25}-SDS, as the NRA results did. It is possible to see that the thickness and concentration of the surface excess detected does differ between the techniques, differences in surface excess characteristics are likely to arise from differences in total film thickness between NRA and NR samples. As NR offers increased depth resolution in comparison to NRA, it is perhaps more likely that a higher concentrated, thinner surface excess has formed in both sample environments, but it could not be resolved with NRA. The surface excess detected with NR is still thick enough to correspond to a wetting layer however, being over twice the length of an all-trans SDS molecule. A similar feature is seen to what was apparent with d_{25}-$C_{12}E_5$, where the concentration of the surface excess does not exceed beyond a particular point, regardless of surfactant concentration. For $C_{12}E_5$ this concentration maximum was reached at 70 at. %. Figure 6.11. shows the NR data for d_{25}-SDS in binary films with PVA, as can be seen at concentrations ≥ 10 w%, a maximum is again reached at ~ 70 at. %, with any additional surfactant being found in the bulk. The fact that a similar limiting surface excess concentration was found for each surfactant implies that a pure layer (100 at. %) of surfactant cannot form in binary films, and PVA must be present as a significant portion of the excess in order to stabilise it. The humidity results from chapter 5 do however suggest that moisture absorbed from the atmosphere is also capable of contributing to the stabilisation of surfactant layers, allowing pure surfactant layers to form on the surface of the films, stabilised by interstitial layers of water-plasticised PVA. As part of the neutron proposal for these experiments the effects of temperature variation on surfactant segregation was studied. Samples containing 20 w% d_{25}-SDS were analysed at room temperature, 30 °C and 40 °C (Figure 6.12.). As can be seen varying the temperature with a remote

temperature stage during analysis causes no discernible change in surfactant segregation. Although storage temperature is certainly a problem for industrial films, as it can increase the rate of migration of compounds from the bulk, or cause the polymer to deteriorate, studying temperature changes in thin films did not indicate any contribution to instability from surfactant distribution.

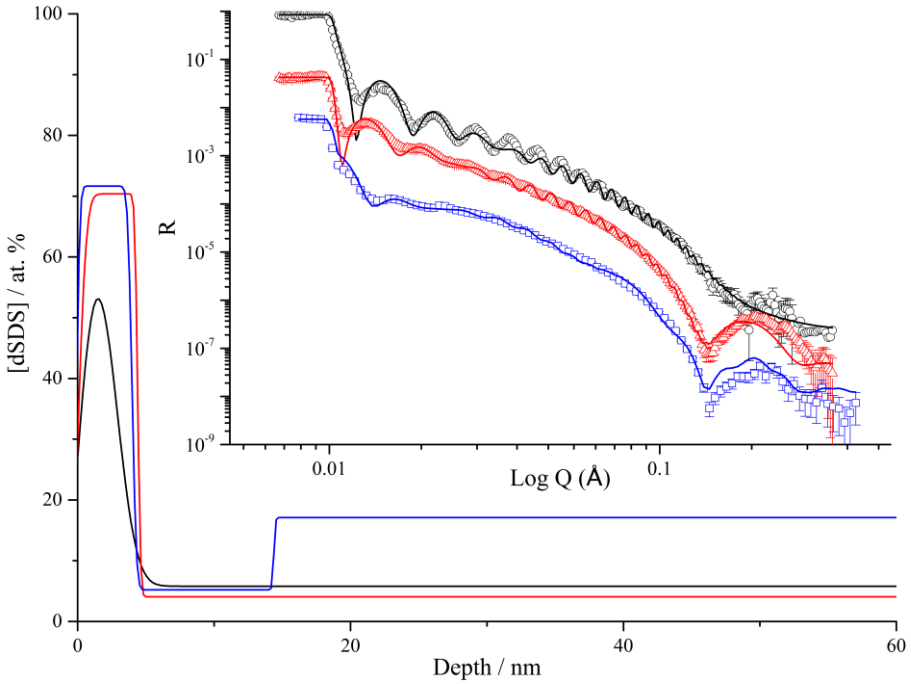

Figure 6.11. Neutron reflectometry data (offset) and fits for 5% (black, open circles), 10% (red, open triangle) and 20% (blue, open circles) d_{25}-SDS in thin PVA films. The derived concentration profiles of d_{25}-SDS correspond to the fitted curves.

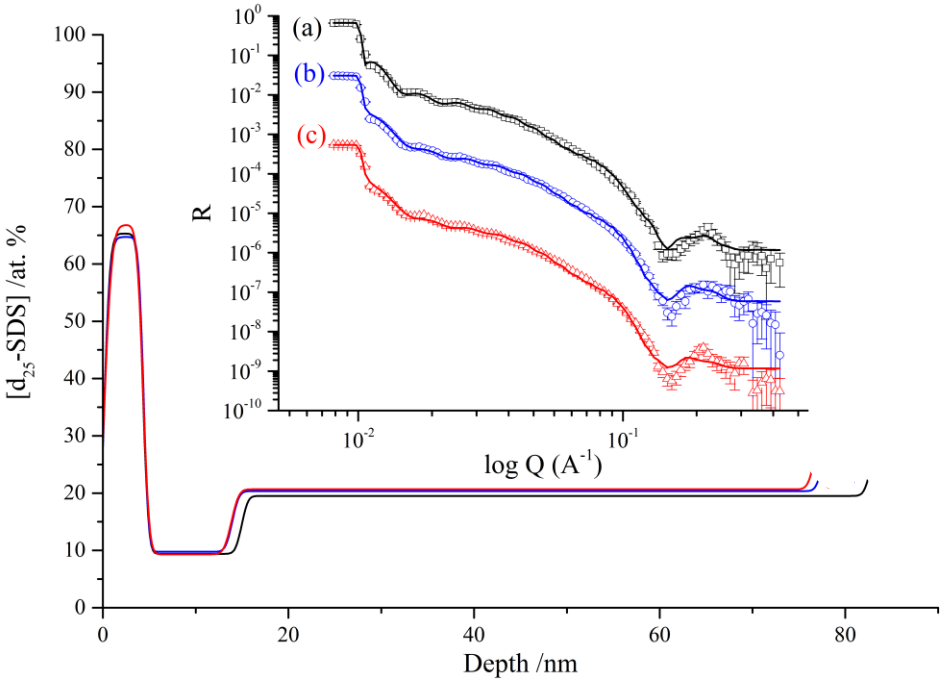

Figure 6.12. NR data for a thin spin cast PVA film cast from a 4 w% solution containing 20 w% d_{25}-SDS, analysed at room temperature (open triangles, red), 30 °C (open circles, blue) and 40 °C (open squares, black).

6.2.2. Segregation of SDS in Ternary, Plasticised PVA Films

So far glycerol has shown opposing effects on a non-ionic and cationic surfactant, decreasing the surface activity of one and increasing the other, despite showing no inherent surface activity itself. This is explained by the increased compatibility between the non-ionic surfactant, glycerol and PVA, induced by the large number of H-bonding sites present on all molecules, compared to the lack of H-bonding sites present on CTAB, which therefore causes no such increased affinity. SDS has a similar sized head-group to CTAB, also containing four polar bonds as CTAB does, so may be expected to exhibit similar segregation behaviour to the anionic surfactant in binary films with PVA, it does however have a significantly shorter alkyl chain. Affinity to glycerol has however been shown to be very important in determining segregation behaviour, therefore if the S-O moiety present in SDS can more effectively H-bond to glycerol compared to the N-H moiety in CTAB, segregation behaviour may be very different in plasticised films. Figure 6.13. shows NRA data, fits and depth profiles for ternary SDS films. It can be seen that glycerol does in fact decrease the compatibility of surfactant and polymer significantly, causing the volume of surface excess of d_{25}-SDS to more than double. Within the depth resolution of NRA, glycerol appears to remain homogeneously distributed within the film, whilst causing additional surfactant to segregate, similar to the result seen for CTAB, suggesting little favourable interaction between surfactant and plasticiser. When analysing similar samples with NR however, significantly more information is gained due to having a depth resolution of < 0.5 nm. Figure 6.14. shows the scattering and calculated d_{25}-SDS concentration profiles for 5, 10 and 20% d_{25}-SDS in plasticised (20 w%) films. Similarly to what was seen previously for $C_{12}E_5$ under humidity control a Bragg peak at high Q (~0.15 Å^{-1}) is present. Fitting this Bragg peak in

plasticised SDS films again reveals significant surfactant structuring within the surface excess. As there are relatively thin regions between each of the surfactant-rich layers, inclusion of the roughness parameter may cause the results to be misinterpreted, so depth profiles are plotted from thickness and SLD parameters only, an example highlighting the differences between a concentration profile with and without roughness considerations is given in 12.3. No structuring is evident at the lowest surfactant concentration of 5% d_{25}-SDS, suggesting that it requires a higher loading of surfactant within the film to have the required quantity to form a multilayer. At 10% loading of SDS the film exhibits presence of a single additional layer, and upon increasing to 20% a series of surfactant-rich layers can be seen. This suggests that the extent to which SDS forms multi-layers in PVA films is directly correlated to the loading of surfactant. Here, 20 w% was the highest concentration studied but it would be of interest to explore the extent to which a stable multilayer can form as surfactant concentration is increased further. It is worth noting that the concentration of the surfactant-rich layers in ternary films is capable of increasing past the 'cap' at 70 at. % as was found in binary films. It would appear that glycerol addition removes the need for PVA to be present in the film surface. To explore the routes by which this occurs the deuterium labelled components were again switched, to resolve the influence of h-SDS on d_5-glycerol.

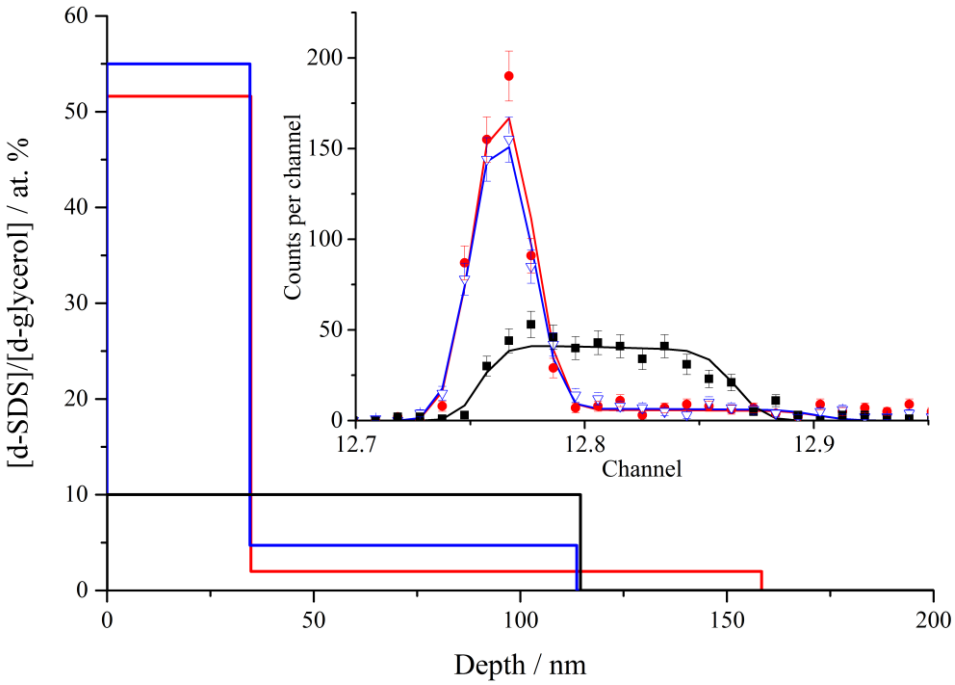

Figure 6.13. NRA data, fits and composition profiles for 20% d_{25}-SDS and 10% h-glycerol (red, circles), with 20% d_{25}-SDS and 20% h-glycerol (blue, triangles) and 20% h-SDS and 10% d_5-glycerol (black, squares) in thin PVA films.

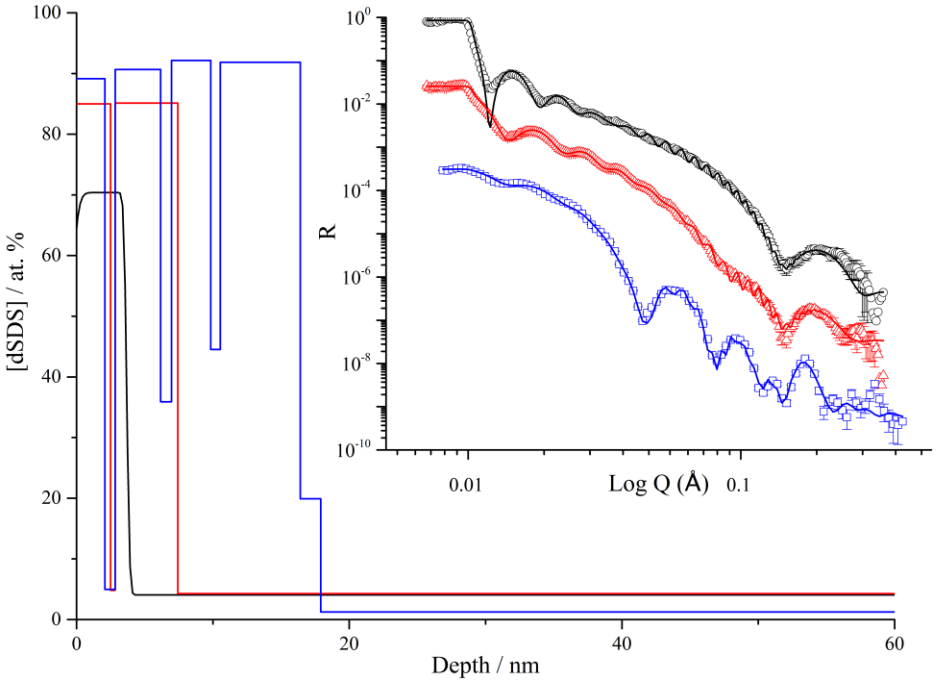

Figure 6.14. NR data (offset), fits and composition profiles for 5% d_{25}-SDS and 20% glycerol (black, open circles), 10% d_{25}-SDS and 20% glycerol (red, open triangles), 20% d_{25}-SDS and 20% glycerol (blue, open squares) in thin PVA films.

Previously, it was shown for $C_{12}E_5$ containing samples under relative humidity control (5.1.5.) that both plasticiser and water were present in the regions of depleted SLD seen in between surfactant-rich layers. As the initial SDS samples studied here were analysed under ambient conditions however, the presence of water in the sample was note explored directly. It is expected that glycerol is primarily supporting the formation of the SDS multilayers seen in Figure 6.14., as it is unlikely that PVA resides in these interstitial regions, or a multi-layered surface feature like this would have been seen in binary SDS films (Figure 6.12.). Exchanging of the labelled components yielded the scattering seen in Figure 6.15. There is noticeably an increase in the size of the error bars at Q ~0.02 Å^{-1} in the d_5-glycerol sample; this may be due to a problem when the NR data from the first and second measurements at 0.25 and 0.65 φ was 'stitched' together. If the data from the two angles were not overlapped precisely it could give the increased error values when extracting the data. A change in film thickness over the course of the experiment would also produce a similar increase in error, but as no evidence of a change in film thickness has been reported previously this is deemed unlikely. Nevertheless the data over the rest of the Q range is of sufficient quality to analyse with MotoFit. An example of how increasing structuring within the surface excess can provide progressively better fitting of a Bragg peak at high Q is visible in Figure 6.15. The best fit was achieved when four discrete glycerol concentrated layers were included in the model composition profile, signifying significant glycerol structure at the surface.

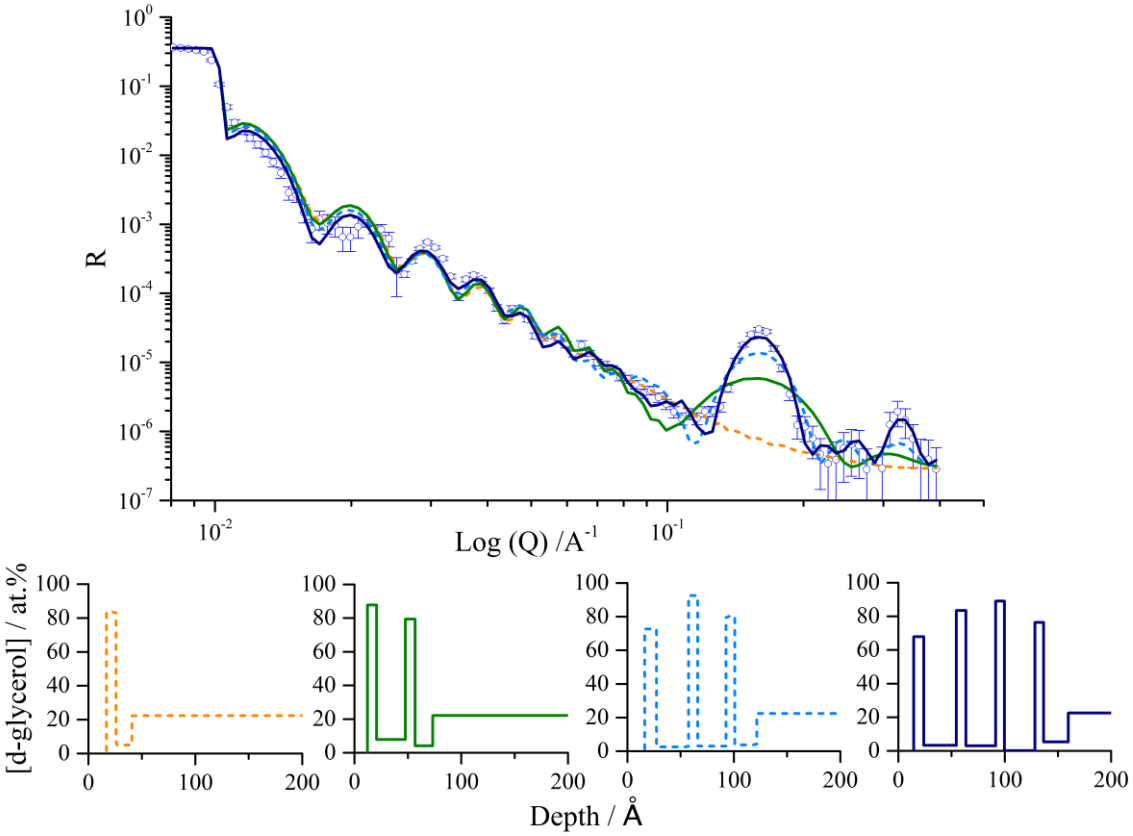

Figure 6.15. NR data, fit and depth profile for 20% h-SDS, 20% d_5-glycerol in a thin PVA film, plus 4 trial fits for increasing layers of glycerol at the surface of the film.

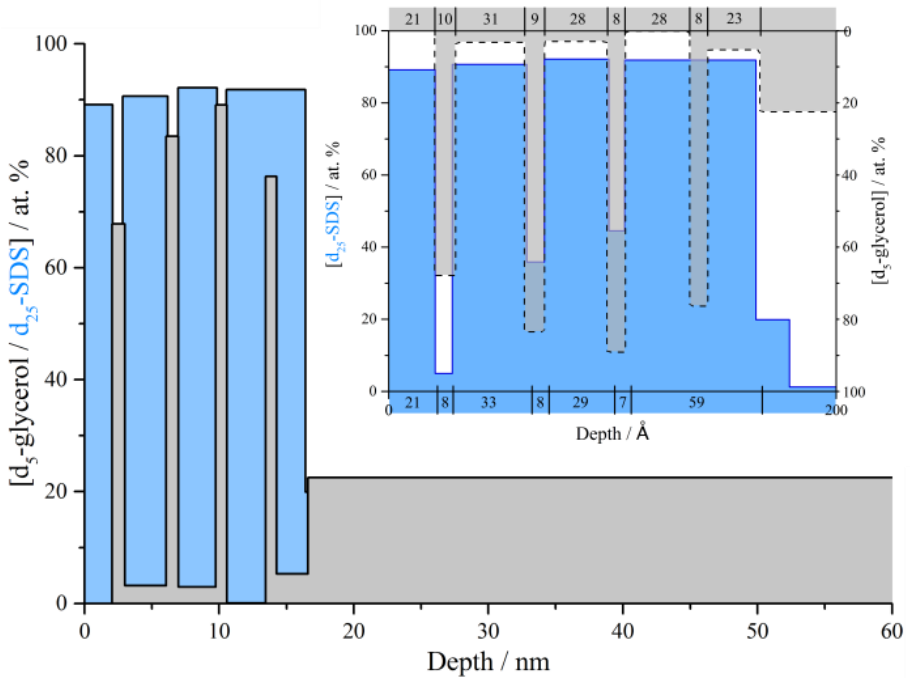

Figure 6.16. Combined plot of the previous data, plus the complementary sample (20% d_{25}-SDS, 20% glycerol) with removal of the roughness parameters. A zoomed plot of the surface excess (inset), h-SDS

profile inverted (grey) with layer thickness values displayed for each profile outside of axis displaying the degree to which the plots agree.

Overlaying the two depth profiles for 20 w% d_{25}-$C_{12}E_5$ and 20 w% d_5-glycerol provides a visual insight into the surfactant multilayer structure on the surface of these films (Figure 6.16.). The overlaid plots for complimentary profiles are in excellent agreement. The thickness of each layer of the fit is given in the inset of the previous figure and as can be seen the values for both the SDS layers and glycerol layers are in excellent agreement. One discrepancy between the two fits is the discovery of an additional segregated layer in the d_5-glycerol sample, it appears that another surfactant depleted layer should have been present closest to the bulk of the film rather than the 59 Å layer, as the concentrated glycerol layer directly intersects this region. However, considering that the two samples are completely separate from one another and subject to some variance in film thickness and composition, the agreement between the plots is still astounding regardless of this discrepancy. The thickness values in Å of each layer can provide an insight in to the nanostructure of the surfactant which is discussed in the following section.

6.2.3. SDS Nanostructure

Due to the sensitivity of NR, some information on the spatial arrangement of the surfactant within the matrix has been established. Figure 6.18. depicts the proposed surfactant nanostructure, it is thought the surface excess could be accounted for by ellipsoidal micelles, arranged in this fashion from the obtained thickness and concentration values. Hammouda [146] established by small-angle neutron scattering (SANS) on aqueous SDS solutions of varying concentration and temperature, that the longest half axis (R_a) of an ellipsoidal SDS micelle is ~21 Å at 20 °C. This means the longer diameter of a SDS micelle is ~42 Å, which is roughly the thickness of the SDS surface excess in Figure 6.11. The shortest half axis (R_b) is approximately 15 Å, so assuming micelles are packing adjacently in the same orientation at the surface, they would occupy ~ 19.8 nm^3 each, taking a cuboid of the same dimensions (Figure 6.17., 37.8 nm^3) would mean that the maximum concentration of surfactant at the surface would be 52.4%. This calculated value is lower, but comparable to the surface excess maximum (65-70 %) discovered from the NR results. As surfactant molecules exist in equilibrium between their monomer and micelle state [83] it is possible that there may be additional surfactant present between each micelle in the polymer matrix, causing the surfactant concentration at the surface to increase slightly. Note that while ellipsoidal micelles are consistent with the thickness of the layer, they do not account for surface activity since the hydrocarbon chains are not on the film surface.

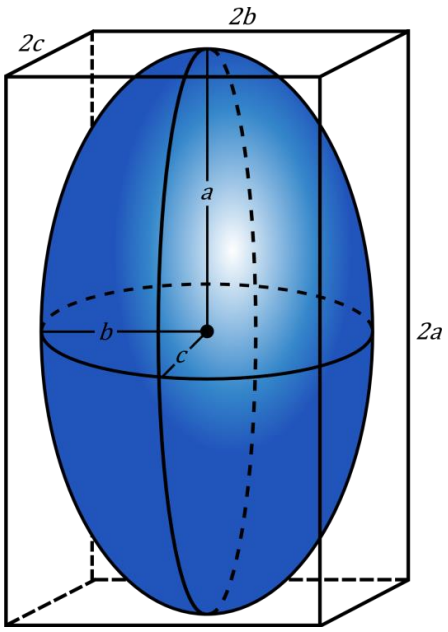

Vol. ellipsoid (V_{ell});

$$V_{ell} = \frac{4}{3}\pi\, abc$$

Vol. cuboid (V_{cub});

$$V_{cub} = 2a \cdot 2b \cdot 2c$$

%Vol. ellipsoid;

$$\%\, V_{ell} = \frac{V_{ell}}{V_{cub}} \cdot 100$$

Figure 6.17. Schematic representation of how maximum ellipsoidal volume is calculated in surfactant surface excess if micelles are forming, a=21 Å, b=15 Å and c=15 Å.

In the presence of plasticiser, it appears that the ellipsoidal micelle breaks down to form a multi-lamellar structure, consisting of a series of SDS bi-layers separated by regions of glycerol. It is possible that the uppermost surfactant layer could present low surface energy hydrocarbon chains to the film surface. From the NR results collected this appears to be the only logical nanostructure as no other arrangements could give such pure surfactant layers of the observed thickness, separated by highly concentrated layers of glycerol. Formation of SDS lamellae parallel to a substrate has been previously documented by evaluation of surface charge density, scanning-electron microscopy and AFM.[223] Thickness of SDS lamellae have also been characterized by Coiro et al.[224] to be of ~4 nm, with a separating phase in low water containing solutions of ~2 nm. These values are similar to the thickness of SDS and glycerol layers calculated in this study. The micelles to lamellae transition (discussed more in chapter 2.2.2.) has also been observed in aqueous solution for a surfactant with similar structure to SDS; sodium dodecylbenzenesulfonate (NaDoBS).[225] Here, dehydration of the head-group by addition of a salt causes an increase in counter-ion binding, allowing electrostatic repulsions between head-groups to be overcome more easily, hence facilitating closer surfactant packing and lamellae formation. Coiro et al.[224] also state that the presence of water in the middle of the 'polar slab' encourages lamellae development as it screens the ion-ion interactions and forms hydrogen bonds between the sulphate groups of opposing monolayers. It is proposed that the addition of glycerol similarly allows increased H-bonding between the head groups of neighbouring surfactants, again overcoming electrostatic repulsions and allowing closer packing, leading to the formation of lamellae. Figure 6.19 depicts the proposed lamellar structure, as well as possible hydrogen bonding interactions in the 'polar slab'. These results suggest that plasticisation in PVA films will enhance the surface segregation of some ionic surfactants, which may have implications when plasticised PVA films are present in surfactant-rich environments as blooming of surfactants to the film surface will occur.

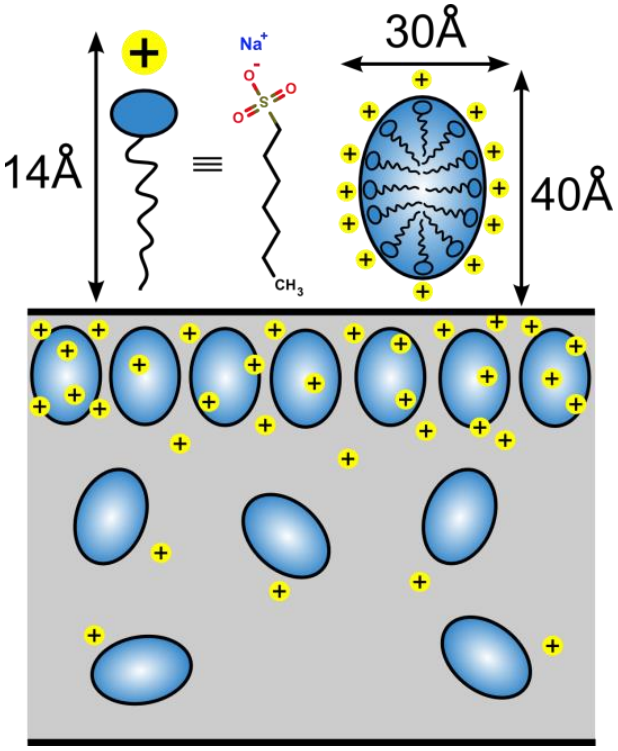

Figure 6.18. Schematic representation of theorised ellipsoidal micelle arrangement in a binary film of d_{25}-SDS (blue) and PVA (grey). Length of SDS and dimensions of ellipsoidal micelle obtained from reference Sammalkorpi [222] and Hammouda [146] respectively.

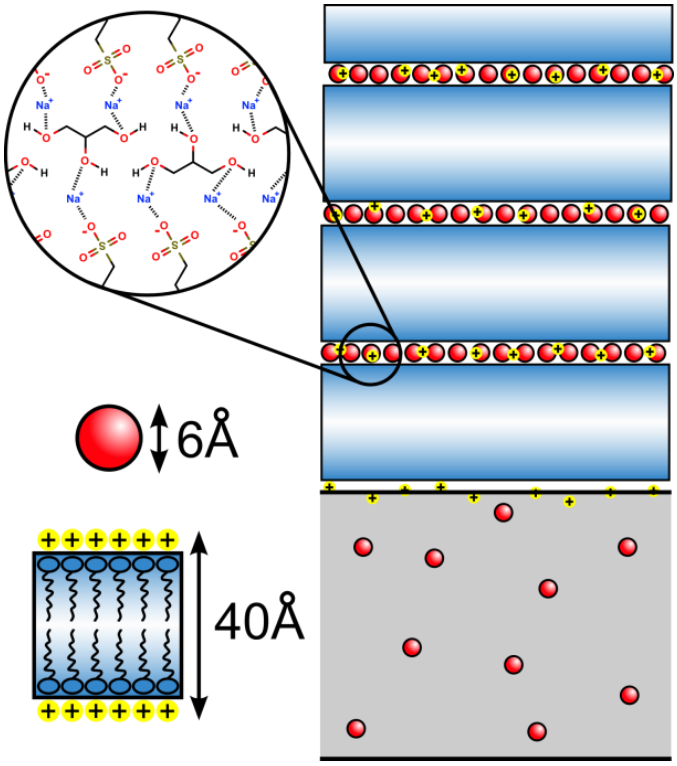

Figure 6.19. Schematic representation of theorised multi-lamellae arrangement in a ternary plasticised film of SDS (blue), glycerol (red sphere) and PVA (grey). Diameter of glycerol and width of lamellar obtained from Kiyosawa[226] and Coiro[224] respectively.

6.2.4. Surface Topography of Thin, SDS-Containing PVA Films

Previously the surface effects of plasticisation and $C_{12}E_5$ addition were studied with AFM and significant changes in the height and adhesion maps were observed with the build-up of surfactant at the air interface. As SDS has been shown to form a larger surface excess than $C_{12}E_5$, containing complex surfactant-glycerol structures under ambient conditions, it is predicted that this should also be detectable when analysing the films surface topography. The same method used previously is applied here, whereby the validity of each AFM image is tested by taking five separate scans at various points on the film, and compared to each other in order to see if similar features are observable. If there was very little variation between the AFM images, then the best quality image was chosen and plotted in the figures shown. Firstly a non-plasticised PVA film containing SDS was studied (Figure 6.20.), the range of height obtained from this sample is the same as what was found for PVA (Figure 5.14.), so although the film appears rougher visibly, there is little evidence for surfactant structures situated on the surface of the film when analysing the height map alone. The level of adhesion is greatly increased however which may be caused by SDS as the samples only differ by the presence of surfactant. As the melting point of SDS lies between 204-207 °C,[227] pure SDS is solid at room temperature, so an increase of adhesion with surfactant addition is unexpected. From the IBA and NR experiments SDS is known to segregate to the surface of these films at approximately 70 at. %, with PVA making up the remaining concentration. If the micelle structures suggested in the previous section are forming at the surface, mixed with PVA, this could perhaps be used to explain the increase in adhesion. If non-adhering micelles are present just below the films surface, with filled PVA regions between them, as is depicted in Figure 6.21., then they could affect the adhesion profile of the film without being detected in the height map. This structure would lead to thinner PVA regions just above the micelles, which would exhibit a reduced adhesion compared to regions where there is more polymer present. So although the overall adhesion of the film is not increasing upon the addition of SDS, the range of adhesion is being affected significantly due to the large contrast between surfactant and PVA rich regions depicted by the arrows of varying length in Figure 6.21. It is also possible that the SDS micelles are hydrated,[228] hence their polar shells have retained some water content. This could cause slight plasticisation of the polymer surrounding SDS micelles, hence changing their adhesive properties. Upon plasticisation of these films, NR results show formation of large surfactant-glycerol multi-layers on the surface, due to the large contrast in height compared with the PVA film these features should be easily detectable with AFM (Figure 6.22.).

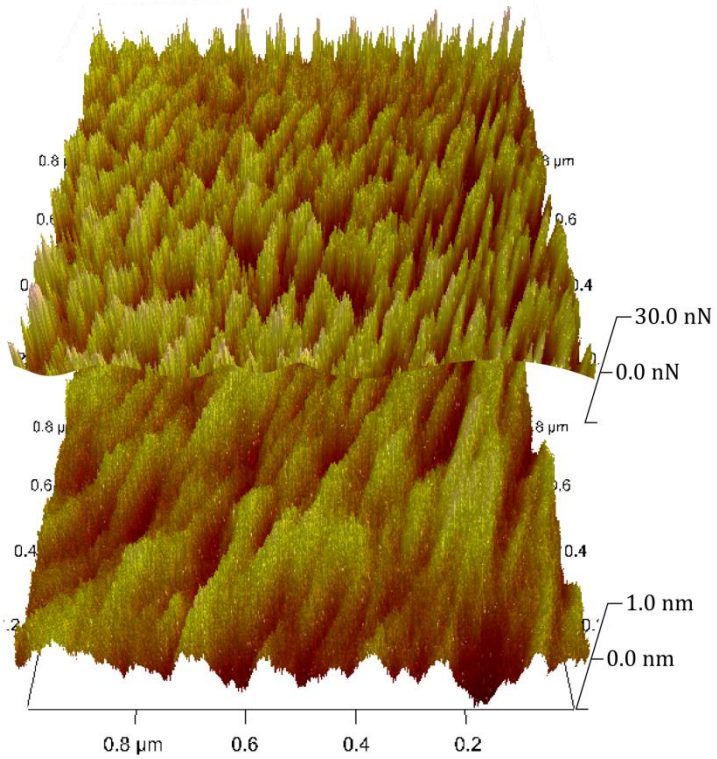

Figure 6.20. AFM topographic height map (bottom) and adhesion (top) for a thin spin-cast 20% SDS, 80% PVA film on silica substrate.

Table 6.1. List of surface properties obtained from NanoScope Analysis for films containing PVA, glycerol and SDS.

Sample	Height Range/ nm	Adhesion Range/ nN	R_q/ nm	R_a/ nm	Kurtosis
PVA	1.0	10.0	0.19	0.15	3.34
PVA + 20 w% Glycerol	1.7	17.5	0.25	0.19	5.36
PVA + 20 w% SDS	1.0	30.0	0.21	0.16	2.94
PVA + 20 w% SDS + 20 w% Glycerol	2.5	115.0	1.14	0.71	3.08

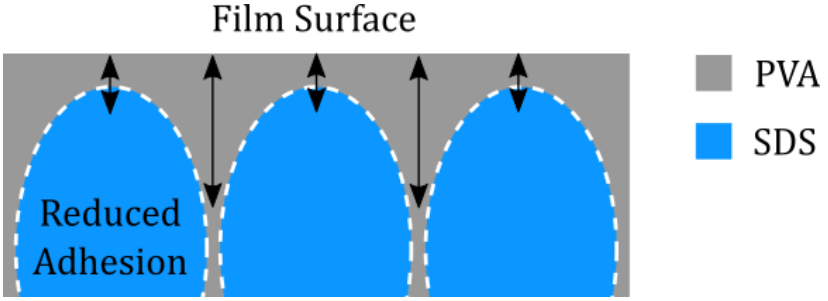

Figure 6.21. Schematic representation of how ordered micelle phase at the surface of the film can create regions of reduced adhesion without being detected in the height map.

Figure 6.22. shows the adhesion and height map for a 20 w% SDS, 20 w% glycerol and 60 w% PVA film, large changes in both maps are visible with plasticisation. The film appears to develop large, relatively flat, structures on the surface of the film, which have reduced adhesion. Overlapping of these features is clearly visible in Figure 6.23. Surface features of this magnitude can only be accounted for by the formation of the SDS-glycerol structures seen in ternary films with NR. It has been suggested by the binary films that SDS structures will likely exhibit reduced adhesion. Hence if pure SDS lamellae are forming on the films surface as the NR data suggests, it would be expected that these structures exhibit crystalline behaviour. This would explain the reduction in adhesion as the probe is less likely to adhere less to a crystalline material in comparison to a plasticised polymer. By performing cross-sectional analysis through the surface features using the NanoScope software, the approximate height of the features was found to be ~3 nm. This is much thinner than the thickness of the surface structure observed with NR (~17 nm). It is possible that only a single SDS lamella is present on the surface of the film, causing these features, as the established thickness of SDS lamellae is ~4 nm, comparable to the height observed here. Despite this difference in excess thickness between techniques, the increased surface segregation of SDS with the addition of glycerol has now been shown by NRA, NR and AFM. The presence of water as a plasticiser in non-ionic surfactant films was also shown to have interesting implications on segregation (chapter 5.6.). Humidity control NR experiments similar to those performed for the non-ionics are done for SDS in the following section.

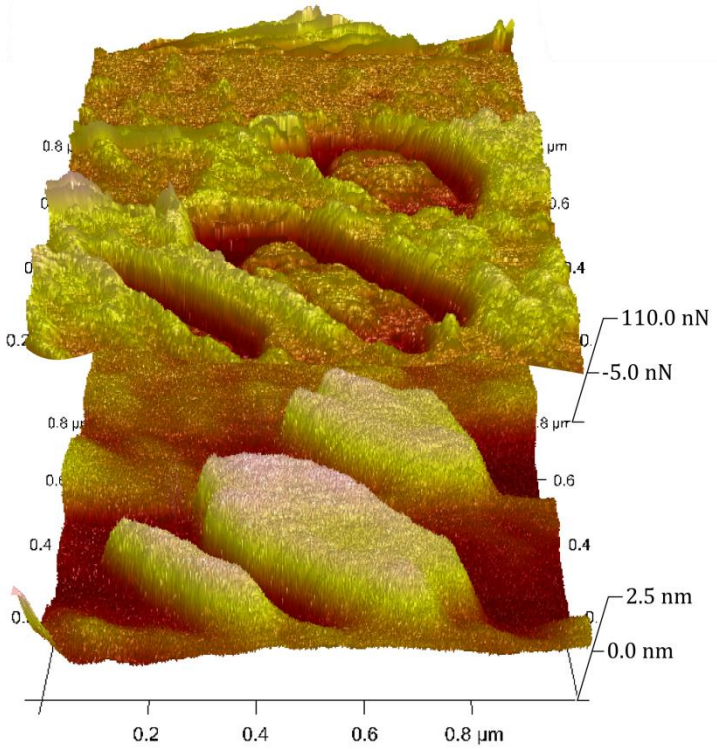

Figure 6.22. AFM topographic height map (bottom) and adhesion (top) for a thin spin-cast 20% SDS, 20% glycerol, 60% PVA film on silica substrate.

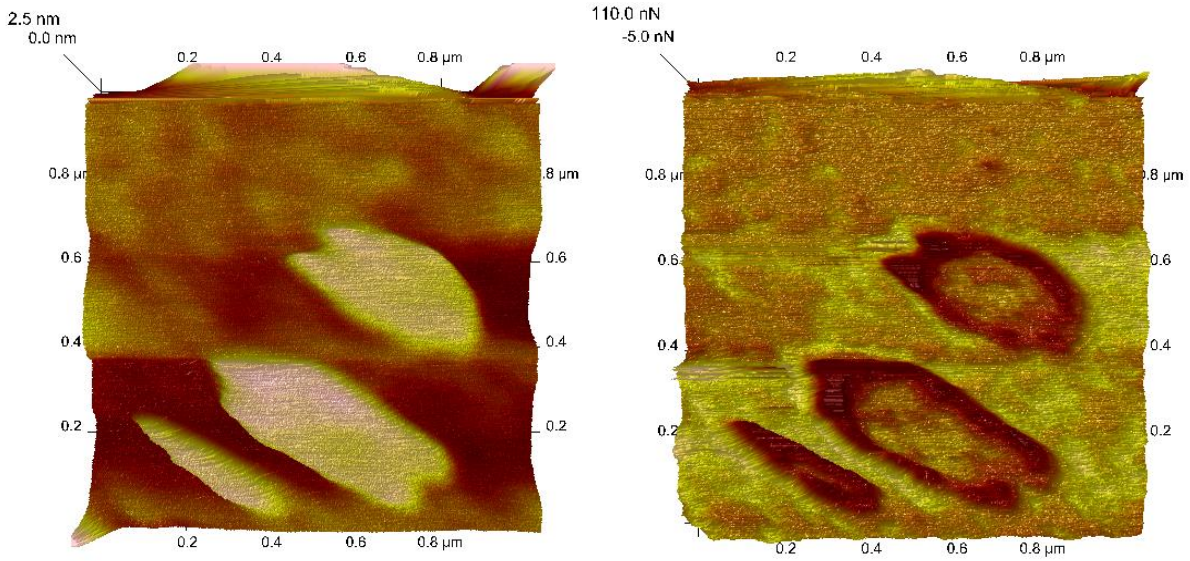

Figure 6.23. Top-down view of the height (left) and adhesion (right) maps for 20% SDS and 20% glycerol in 60% PVA spin cast thin film on a silica substrate.

6.2.5. SDS Segregation Under Humidity Control

Humidity control with NR has so far yielded varying results. It was found that increased humidity caused increased water absorption in to thin films, resulting in an increase in film thickness. The total amount of plasticiser (water + glycerol) hence increased with increasing humidity. In non-ionic surfactant containing films which were co-plasticised by water and glycerol it was seen that as humidity, and hence water concentration in the film increased, surfactant segregation was also increased. This was unexpected as plasticisation with glycerol caused a decrease in surface excess under ambient conditions (chapter 5.1.3.), so it is unexpected that further plasticisation with water would reverse this effect. It was also found that water would replace glycerol in the interstitial regions between surfactant-rich layers (chapter 5.2.2.) which appeared to cause increased segregation. Figure 6.24. shows NR data for binary films of SDS and PVA, in comparison with the samples studied without humidity control the surface excess has increased significantly. Furthermore, the bulk concentration of surfactant has also decreased to levels seen in plasticised PVA films under ambient conditions. This could be a feature of the reduced film thickness measured for samples studied under humidity control, as there is less polymer for the surfactant to be dispersed in with a thinner film, hence increased segregation may occur. Regarding this particular sample set however, the exact same solution and sample preparation method was used to create all four samples, so in the initial, spin-cast state should be identical for all samples. Therefore any change in surfactant behaviour and film thickness here is a result of the varying humidity, not a change in the amount of polymer in the film. It appears plasticisation with water is having a similar effect to plasticisation with glycerol, in allowing more surfactant to segregate at the surface. Interestingly, reduced structuring within the excess is seen compared to the glycerol plasticised atmospheric samples (Figure 6.14.), which either implies that water is not permitting the same level of complex structures to be formed when it is the only plasticiser present, or there is a loss of resolution in the measurement as

there may be water adsorbed on the films surface. This decrease in resolution may mean that structuring cannot be detected to the same extent as it could previously. There does not appear to be a specific trend concerning the surface excess with increasing humidity however, and the only notable change at higher humidity is a depleted surfactant region on the surface of the film, followed by an increased excess of SDS below this. This could be caused by significant water adsorption on the surface of the film, which only contains a small amount of surfactant and PVA, under which a surfactant-rich layer resides.

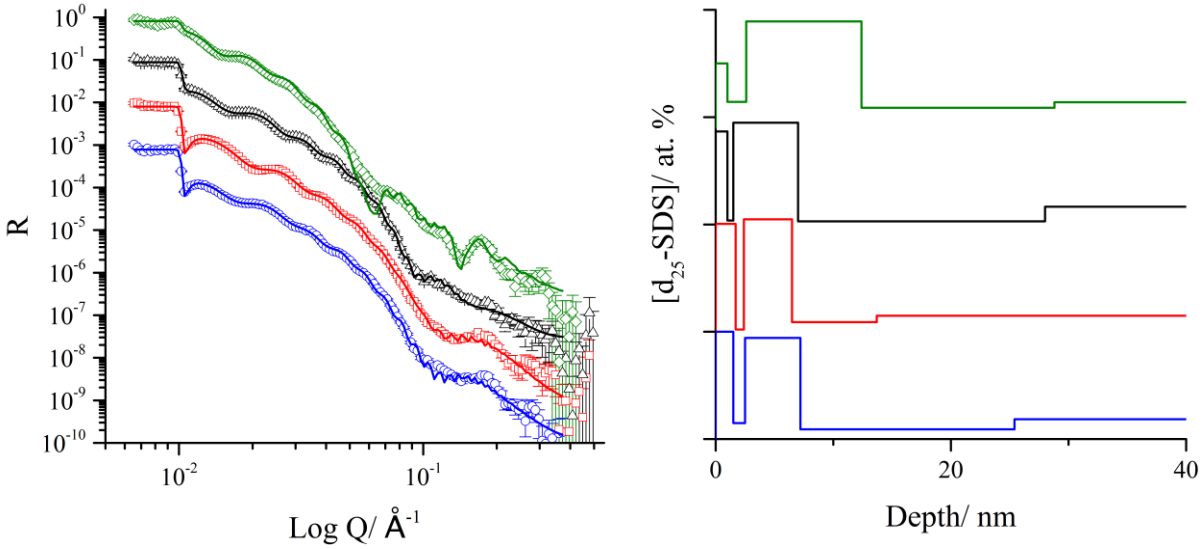

Figure 6.24. NR data (offset), fits and composition profiles for 20w% d_{25}-SDS PVA films subjected to 23%RH (blue), 33%RH (red), 55%RH (black) and 85%RH (green) environments. Each increment on the depth profile accounts for 0 to 100 at. % of d_{25}-SDS.

Under atmospheric conditions addition of glycerol caused a significant increase in the amount of SDS seen at the surface. Here the same conclusion was reached when studied under humidity control. A multi-lamellar structure is seen on the surface of each film at 23, 33 and 55 %RH (Figure 6.25.), although the total thickness of the excess (~ 10 nm) appears reduced compared to samples studied under atmospheric conditions (~ 17 nm). The 85 %RH sample data could not be fitted using this model, but it is notable that the particularly sharp Bragg peak at Q ~0.15 Å^{-1} is clearly evident, suggesting a very well-defined multi-lamellar structure is also present at 85 %RH. The thickness of the individual surfactant layers is not as consistent as was found for the ambient samples, so the exact SDS nanostructure could not be established for this set of samples. Although the data for 23, 33 and 55 %RH look very similar, the Bragg peaks at Q ~0.2 Å^{-1} are relatively broad, therefore do not correspond to a single, well-defined layer spacing. The differing profiles obtained shows that the fits cannot be considered to be truly unique. There does appear to be increased surfactant segregation with increasing humidity however, as both the 33 and 55 %RH samples exhibited a surface excess with three surfactant-rich layers, whereas the 23 %RH sample exhibited an excess with only two. This result is in line with what was seen for the binary SDS samples and plasticised $C_{12}E_5$ samples, suggesting a decrease in compatibility of SDS with the PVA film upon increasing plasticisation with water and glycerol, which was also seen for the ambient samples.

Exchanging of the labelled components as done before will reveal whether water or glycerol is occupying the regions between the surfactant-rich layers. The non-ionic results (chapter 5.2.) showed that water possesses the ability to replace glycerol in the interstitial regions at high relative humidity.

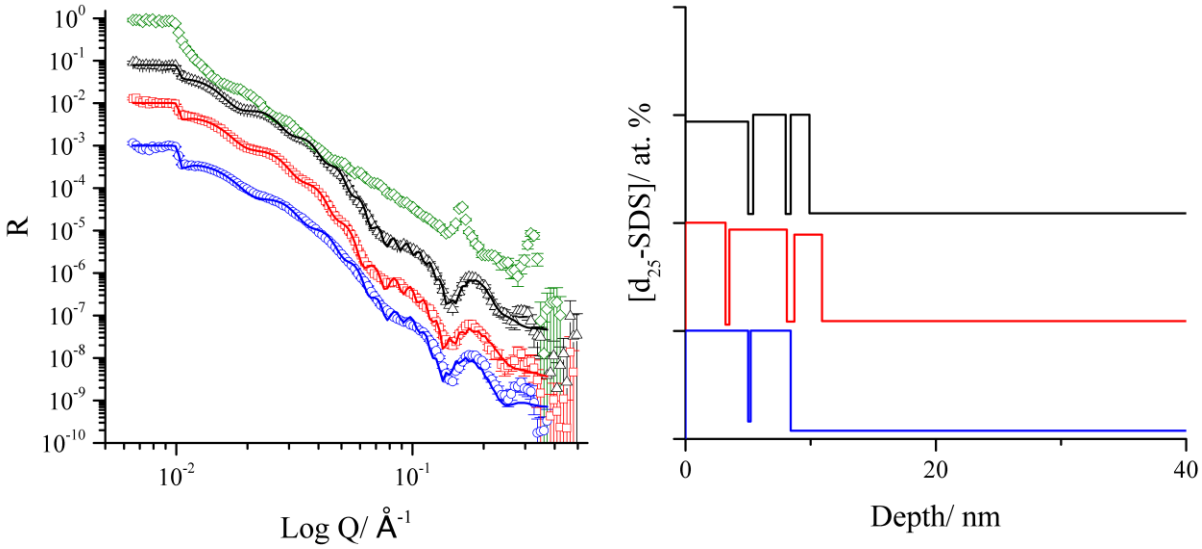

Figure 6.25. NR data (offset), fits and composition profiles for 20 w% d_{25}-SDS, 20 w% h-glycerol PVA films subjected to 23%RH (blue), 33%RH (red), 55%RH (black) and 85%RH (green) environments. Each increment on the depth profile accounts for 0 to 100 at. % of d_{25}-SDS.

Figure 6.26. shows the depth profiles for deuterated glycerol within these samples. Some surface segregation of plasticiser is found in all ternary samples, but in comparison to the data obtained without humidity control, the segregation appears vastly reduced. Where before there were highly concentrated interstitial layers of glycerol separating the SDS layers, now the glycerol concentration within these layers is reduced. There is some evidence for a small amount of glycerol being present between the surfactant layers, as the peaks in the d_5-glycerol data correspond roughly to the depleted regions between the SDS layers in Figure 6.25. It is possible that as water and glycerol are sufficiently compatible they are co-existing between the surfactant-rich regions. As the SLD of water (-0.56×10^{-6} Å^{-2}) is lower than that of d_5-glycerol (4.91×10^{-6} Å^{-2}) any water co-located with glycerol would cause a reduction of the SLD, which when analysing the SLD profiles produced via fitting would give a lower final concentration of plasticiser. This postulate is supported by the decrease seen in surface concentration of glycerol with increasing humidity. If more water is present in the system, especially in the interstitial regions as humidity increases, a reduced SLD would be expected, and therefore the calculated glycerol concentration would be reduced. From Figure 6.26. this is evident as the glycerol concentration at 85 %RH is much smaller than what is seen at 23 %RH. Within the uncertainty of the fit, it is debatable whether the d_5-glycerol excess is real. The presence of water acting as a plasticiser and allowing the formation of surfactant multilayers is apparent, signifying that complex surface structures can be formed even in binary PVA films if there is sufficient humidity.

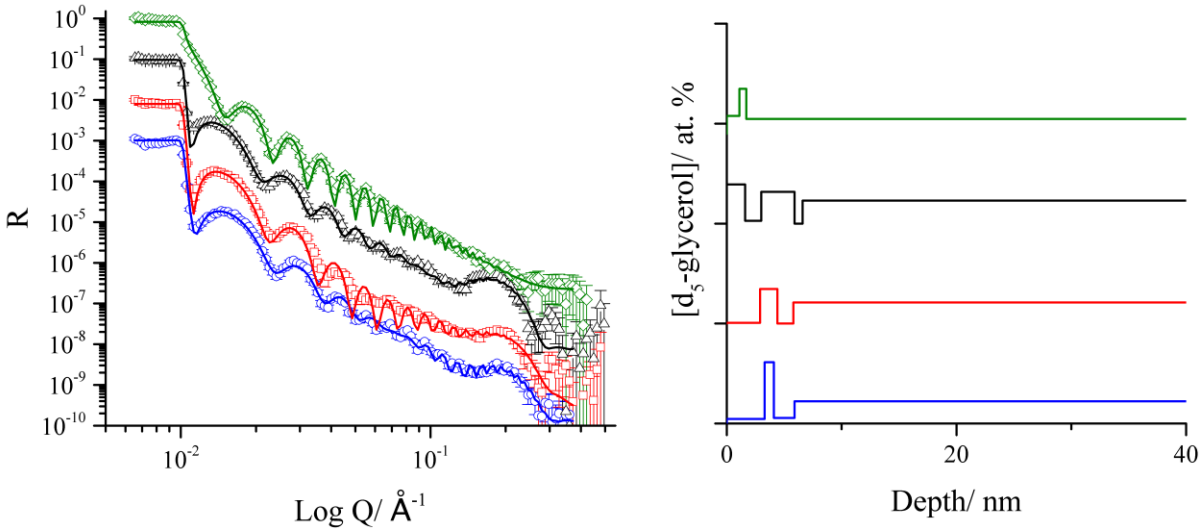

Figure 6.26. NR data (offset), fits and composition profiles for 20 w% h-SDS, 20 w% d_5-glycerol PVA films subjected to 23%RH (blue), 33%RH (red), 55%RH (black) and 85%RH (green) environments. Each increment on the depth profile accounts for 0 to 100 at. % of d_5-glycerol.

6.2.6. Summary of SDS Segregation Patterns

The segregation behaviour of SDS in PVA has been studied in a variety of environments. In binary films with PVA the surfactant showed spontaneous segregation to the surface of thin PVA films, thought to be brought about the reduced surface energy of the surfactant compared to PVA. It was apparent that there existed a concentration 'cap' for the amount of SDS which could be present at the surface in binary films, due to the concentration and thickness of this capped excess, plus suggestions from AFM analysis, it was theorised that a layer of SDS ellipsoidal micelles were present just below the surface of the thin films. Upon plasticisation of these films with glycerol the amount of surfactant seen at the surface increased significantly. This was explained by formation of a SDS-glycerol multi-lamellar arrangement at the surface of the film, where the plasticiser allowed closer head-group packing of SDS, causing a transition from micellar to lamellar structure. The study of non-plasticised PVA films under controlled relative humidity gave much the same results as this, again suggesting formation of a surfactant multilayer, except water now comprised some of the 'polar slab' regions in-between surfactant-rich layers. By increasing the relative humidity around these samples whilst keeping sample composition the same it was found that as a result of increasing water concentration in the film, and hence increased plasticiser concentration, SDS surface segregation was increased further. These results suggest that the inclusion of ionic surfactants into plasticised, solution-cast, PVA films could lead to substantial spontaneous migration of surfactants to the films surface. Significant build-up of surfactant structures on the polymer surface have potential to interfere with the binding and inter-diffusion process of the polymer films used to form seals in industry if surfactants such as these are present in the film formulation.

6.3. Additional Surfactant Segregation in Thin PVA Films

The primary surfactants used in this study have now had their distribution behaviour discussed, but these were not the only surfactants trialled for analysis. In the following section the behaviour of two additional surfactants in PVA film is discussed. These were chosen for their relevance to industrial formulations for unit dose detergent applications.

6.3.1. Sodium Dodecylbenzenesulphonate (SDBS) Segregation in Binary Films

SDBS (Sigma-Aldrich, 289957) was purchased and studied with RBS. This surfactant has the same sulphonate head group as SDS, but contains a hydrophobic tail-group of significantly increased mass by presence of a benzene moiety between the head-group and the hydrocarbon tail (Figure 6.17.), giving it a HLB of 5.9. This surfactant falls into a group known as linear alkylbenzene sulphonates (LAS), a set of compounds found more commonly in detergents than the ones studied so far. [71] Although a deuterated analogue of sodium dodecylbenzenesulphonate (SDBS) could not be obtained, it was known from the SDS work in chapter 6.2.1. that at least a surface excess would be detectable with IBA by using RBS to probe the position of the sulfur atom present in the surfactant. Samples were made containing 20 w% of SDBS in PVA and spin-cast.

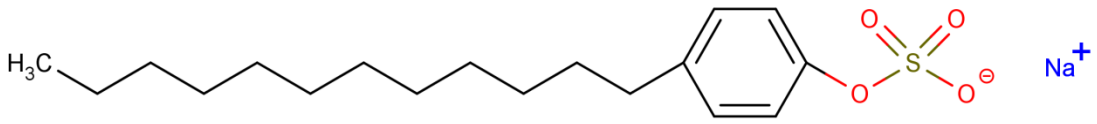

Figure 6.27. Chemical structure of sodium dodecylbenzensulphonate (SDBS)

The resulting scattering is presented in Figure 6.28.; as was apparent with SDS, a surface excess of SDBS is visible at ~ 0.9 MeV. The scattering from SDBS produced much clearer peaks than for SDS, perhaps due to a smoother film being formed for SDBS, which allowed for better analysis. As before, two peaks are visible above 0.7 MeV, a lower energy peak representative of Na and a higher energy peak for S. Fitting the surface excess is relatively straight-forward as scattering from sulfur is easily distinguishable from the other scattering within the sample; however it was also possible to quantify a buried excess due to the clarity of data obtained. Figure 6.29. shows the scattering from the sample plus two fits, one for a surface excess of SDBS followed by even distribution (solid, black) and another which contains a substrate excess (solid, blue). As can be seen from the zoomed plot and depth profile, the initial fit characterises the higher energy peak well, but underestimates the counts per channel of the sodium peak. Initially it was thought that perhaps more than one sodium counter-ion was present per surfactant molecule (i.e. additional salt was present), which would give the same effect (increased counts per channel at ~0.7 MeV), however after some consideration it appeared that the thickness of the film (~260 nm) gives exact overlapping of the substrate S and surface Na. Therefore it is possible to quantify a

substrate excess of SDBS, although not as accurately as what could be achieved with a deuterated analogue. By increasing the amount of SDBS present at the substrate the counts could be increased until a reasonable fit was achieved. It is intriguing that there appears to be a substrate excess for SDBS, whereas with SDS there was not, with the molecules only differing in chemical structure by introduction of a benzene ring. The surface tension values of the two surfactants also differ very little,[229] so this could not be used to explain the substrate segregation. SDBS does however contain a larger hydrophobic portion, so is therefore less compatible with the polymer matrix; this could lead to increased exclusion from the bulk and therefore increased segregation.

Although it is apparent that surface energy values are what determine whether migration will occur or not, it is still unclear what determines whether a surfactant will be surface segregating, substrate segregating, or both. The increase in molecular weight from SDS to SDBS could be the cause of substrate migration, which has perhaps resulted in a change in micelle shape and structure, affecting migration behaviour. The reduced HLB of SDBS (5.9) compared to SDS (8.3) could also be influential, as the increased molecular weight of the hydrophobic tail-group causes the surfactant to have a similar HLB to CTAB (6.9), which also exhibited substrate segregation. Without further investigation it is difficult to pinpoint one property that determines this characteristic. In order to observe and investigate SDBS micelle structure either a deuterated surfactant would need to obtained, which has proven difficult, or a SANS experiment in deuterated solvent could also be performed, unfortunately time did not permit another neutron experiment to be performed to investigate this further.

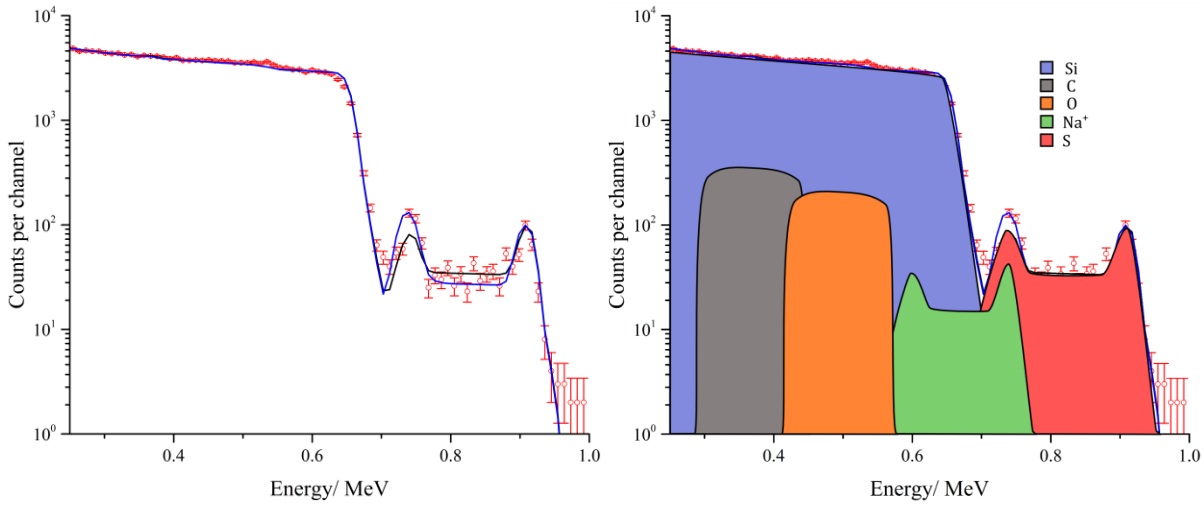

Figure 6.28. RBS data for 20% SDBS in PVA plus fits for surface excess of SDBS only (black), and surface excess plus substrate excess (blue). Separated spectra displaying the scattering contributions of each individual element (colour coded).

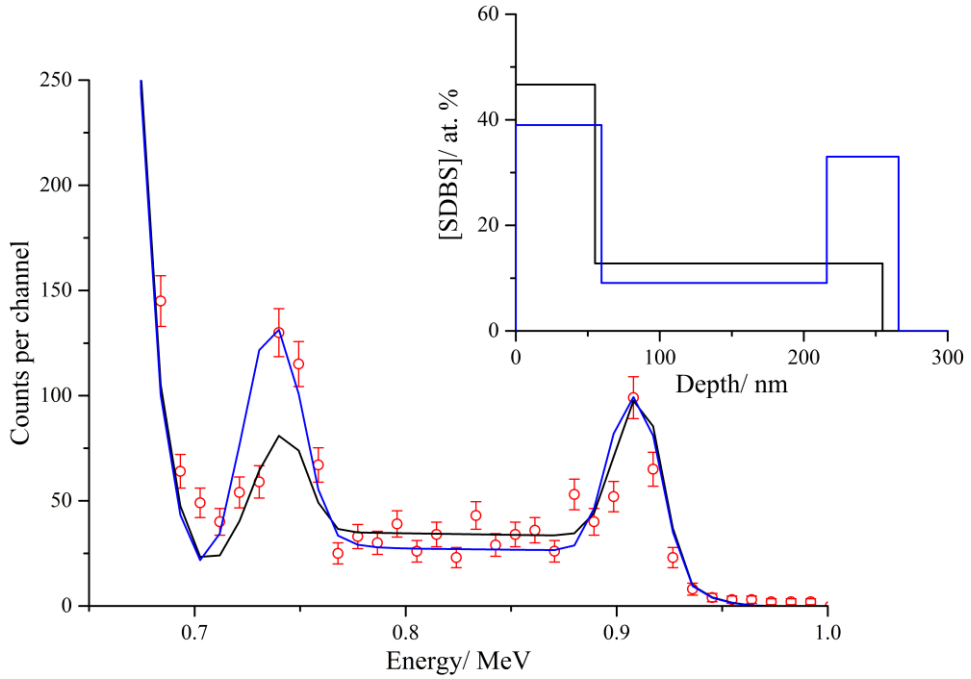

Figure 6.29. Zoomed plot of RBS data from Figure 6.28., with associated depth profiles presented in the inset.

6.3.2. Amine-Oxide Segregation in Ternary, Plasticised PVA Films

Previously it has been shown that surfactants capable of significant hydrogen bonding form glycerol-surfactant complexes, which in-turn perturb glycerol distribution in ternary films. It was proposed that monitoring glycerol distribution in surfactant containing films could help predict surfactant migration behaviour for surfactants which contained no elements to differentiate them from the polymer matrix. C_{12}-alkyldimethylamine oxide ($C_{12}AO$) is a surfactant of interest for inclusion in PVA film and detergents due to its effectiveness in cool or cold fabric laundering operations.[230-231] The structure of $C_{12}AO$ is displayed in Figure 6.30. Comparing the surfactant to SDS, it has three fewer hydrogen bonding sites, and it has been previously noted that SDS does not form a complex with the plasticiser. It is therefore unlikely that amine oxide will, as it only contains one H-bonding site on the terminal amine oxide group, however SDS was an ionic surfactant, so its H-bonding sites were shielded by the presence of the sodium counter-ion. Amine oxides are zwitterionic, so it is plausible that the lack of a counter-ion may cause the H-bonding site to be more exposed, hence increasing the likelihood of favourable interaction with glycerol. If there is sufficient H-bonding between the surfactant and glycerol it may be possible to predict $C_{12}AO$ behaviour indirectly, by studying the distribution of d_5-glycerol. It has been shown in chapter 5.1.3. that this is possible for the non-ionic $C_{12}E_5$. As all other groups of surfactant had been studied; non-ionic, cationic, anionic, it was of interest to explore the behaviour of the last remaining group (zwitterionic) also. A solution of 20 w% d_5-glycerol in PVA was made and 2, 5, 10 and 20 w% $C_{12}AO$ was added. NRA was performed on a thin film spin cast from each solution, the results of which are displayed in Figure 6.31.

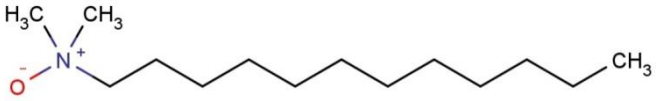

Figure 6.30. MarvinSketch structure of C_{12} alkyldimethylamine oxide

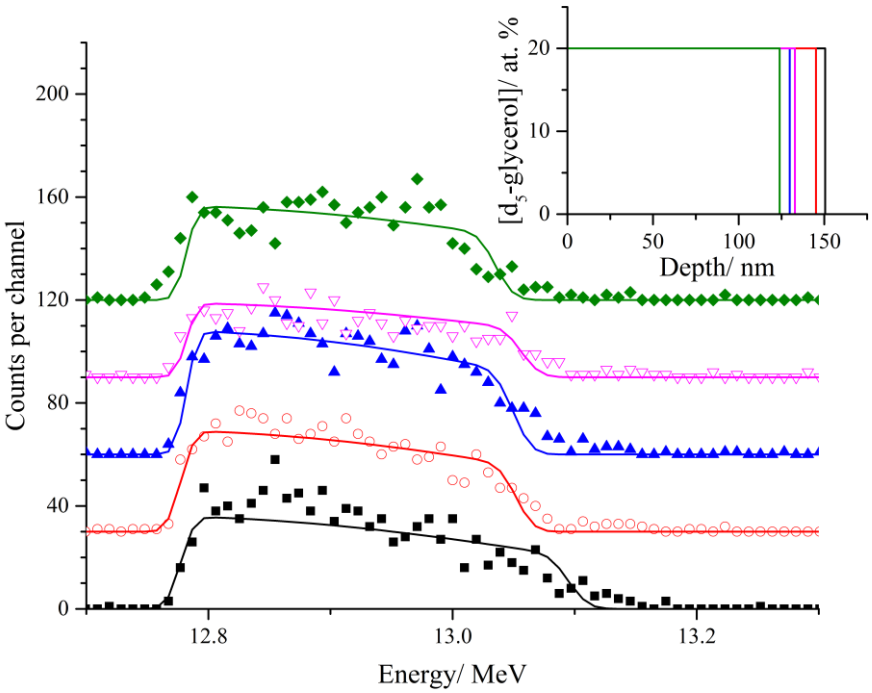

Figure 6.31. NRA data and fits for 0% (solid squares, black), 2% (open circles, red), 5% (closed triangles, blue), 10% (open triangles, magenta) and 20% (closed diamonds, green) C_{12}AO plus 20% d_5-glycerol in thin PVA films. The calculated depth profiles are displayed in the inset.

All samples exhibited homogeneous glycerol distribution, meaning that either the ability of C_{12}AO to hydrogen bond to the surfactant is insufficient to disturb the distribution of plasticiser, or the surfactant itself does not migrate. As the number of H-bonding regions on the surfactant is low, it cannot be concluded that the surfactant does not migrate, simply that there is little to no interaction between surfactant and plasticiser. If interaction had been sufficient at least a surface excess of glycerol would have been expected as C_{12}AO has a surface tension of 31.9 mNm^{-1} at 20 °C. This is lower than the established ST of PVA, estimated to be ~40 mNm^{-1}, hence surfactant adsorption would be favourable.

In summary of the current chapter; ionic surfactant segregation has been studied in thin PVA films for both CTAB and SDS. CTAB was shown to be non-surface segregating when in binary films with PVA, indicating good compatibility with the host polymer. Upon plasticisation with glycerol, segregation is initiated to both the substrate and surface excess, thought to be due to reduced compatibility between the surfactant and glycerol. SDS segregation was shown to occur in both binary and ternary PVA films under ambient conditions, with plasticisation causing a significant increase in the amount of surfactant in the surface excess. Using NR, some information about the SDS nanostructure in plasticised PVA films is

uncovered. Formation of a multi-lamella of SDS, with interstitial regions of glycerol on the surface of the film was found, thought to be facilitated by the presence of the plasticiser. As no such lamellar structures were found in binary films with PVA under ambient conditions, but some structuring of the SDS surface excess was observed in binary films under relative humidity control, where water had clearly been absorbed from the atmosphere, it can be said that plasticisation by water also facilitates formation of complex SDS nanostructures in PVA films. The increased structuring of SDS upon plasticisation with glycerol and water is believed to be due to the H-bonding potential of the plasticisers, allowing closer head-group packing through hydrogen bonding.

Throughout each of the previous chapters, H-bonding has been deemed to be an influential factor in determining the segregation nature of surfactants in non-plasticised and plasticised PVA films. There has been significant evidence for this in chapter 5, where the homogeneous glycerol distribution is perturbed upon the addition of $C_{12}E_5$. Evidence for H-bonding was also suggested in chapter 6, where SDS-glycerol complex was formed on the surface of the film, appearing to be stabilised by H-bonding between each SDS lamella and the plasticiser. The humidity control sections have also alluded to there being some change in the hydrogen bonding nature between all components of the film upon the addition of water. However, despite the evidence suggesting it, the actual presence of hydrogen bonding has not been proven directly. The following chapter aims to quantify the strength of H-bonding between the film components through the use of FTIR spectrometry.

7. Molecular Interactions - Hydrogen Bonding via FTIR

From the surfactant segregation investigations performed in the previous chapters it is clear that there are some interesting interactions taking place between the components of the systems studied. The forces behind these interactions have so far been defined as surface energy and compatibility, with the latter being comprised primarily of H-bonding arguments. While the segregation behaviour indicates the nature of favourable/unfavourable interactions, it is not possible to speculate on the molecular origin of these interactions from NR/IBA techniques, since they do not probe molecular interactions directly. Infra-red spectroscopy on the other hand is a proven technique for studying molecular interactions as it directly analyses bond vibrations, which are largely affected by their molecular surroundings. The following chapter aims to explore the molecular interactions between polymer, surfactant, plasticiser and water in an attempt to explain the molecular detail of H-bonding, in order to support the compatibility theories presented so far. As these compounds are all capable of significant H-bonding, and as H-bonding has been theorised to be one of the most important forms of molecular interaction in the previous chapters, it is deemed that an investigation in this area would provide the most information on the intermolecular forces at play.

As the IBA and NR results have suggested a favourable interaction between $C_{12}E_5$ and glycerol, this interaction was of the most interest to explore. However, it was necessary to validate the method with already studied systems before analysing more complex surfactant systems. The initial experiment performed used a simple, two-component water-glycerol system, similar to what was used by Dashnau et al.[232] If similar results could be achieved despite the use of different spectrometers, then the method would be deemed appropriate for the analysis of more complex systems. Figure 7.1. displays a schematic representation of how H-bonding can be detected with FTIR. For stretching modes, hydrogen bonding causes a weakening of the X-$H^{\delta+}$ bond (see chapter 2.5.), which causes a reduction in mode wavenumber. H-bonding is stronger in glycerol compared to water, hence glycerol exhibits a lower wavenumber νOH stretch, displayed in Figure 7.1. If a straight line is drawn between the wavenumber for a pure glycerol and pure water system it represents the expected wavenumber of any mixed solution of water and glycerol at a given weight fraction. In reality the change in H-bonding does not behave linearly, as will be discussed below, but for initial understanding this representation serves better.

Once this system is established, then the addition of additives to solutions allows study of their effects on H-bonding within the system. If a shift to lower wavenumber upon addition of an additive is observed, it can be derived that H-bonding within the system (regarding that specific vibrational mode) has increased. Alternatively, any increase indicates a reduction in H-bonding. For bending modes, the opposite is true. As bending vibrations become more difficult with increased H-bonding, the wavenumber of their modes increases. Therefore a shift of any bending vibration to higher wavenumber upon addition of an additive indicates increased H-bonding within the system, and vice versa. These effects can be used to probe the hydrogen bonding interactions of compounds within the systems, which have appeared to be critical in determining segregation behaviour in the previous chapters.

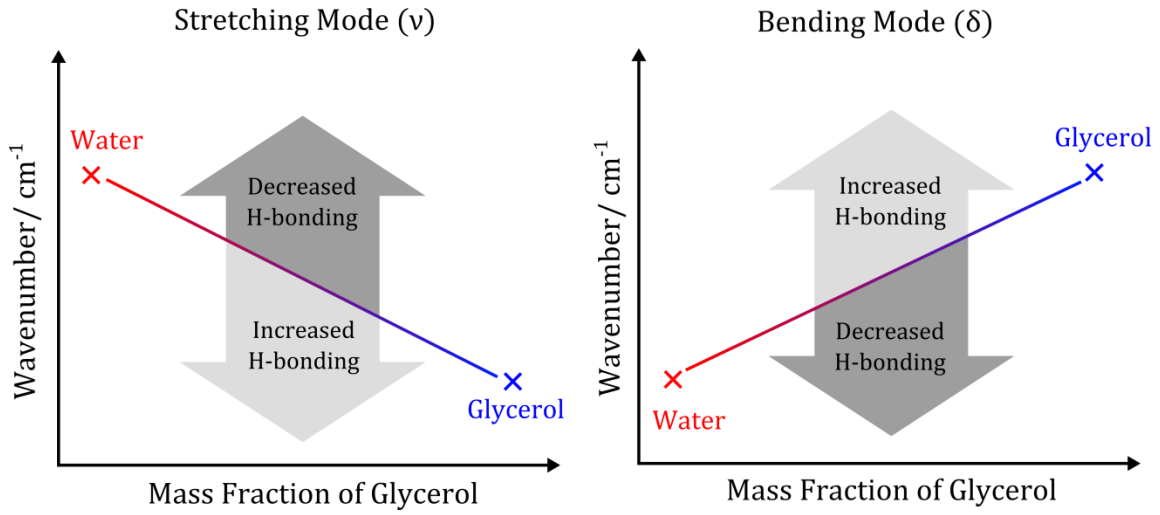

Figure 7.1. Schematic representation of change in stretching and bending mode wavenumber with increasing/decreasing hydrogen bonding

7.1. FTIR Analysis of Hydrogen Bonding in Solutions

To replicate known experiments, and verify the method, glycerol-water solutions of varying glycerol concentration were created and analysed at room temperature (20 °C). FTIR spectra for each solution are displayed in Figure 7.2., the baseline position of each spectrum has been offset to allow easier comparison of the data. It is apparent that each IR spectrum appears slightly noisy. In order to eliminate the noise and calculate the exact wavenumber corresponding to each band maximum/peak minimum, peak fitting was carried out. Using Origin 2015 Sr2 the wavenumber of the maximum of each band could be accurately determined by employing a non-linear curve fit. The exact fitting program used can be found under; category: Polynomial, function: Poly, iteration algorithm: Levenberg Marquardt, within the software, describing a 9th order polynomial (Equation 47). This fit was chosen as in the user's opinion it provided the most accurate representation of peak maxima, an example of a polynomial fit to a νOH stretch is displayed in Figure 7.3., this sample contained 50 w% water mixed with 50 % glycerol. As can be seen, despite the variance in the data around the peak maximum, the fit provides an accurate description of the centre of the band. The same analysis was carried out for several key bands that have been shown to be important when detecting H-bonding; including the OH stretch (νOH),[233-234] CO stretch (νCO)[235] and HOH bend (δOH).[236] The limits for each band when fitting were chosen so only that band was present in the data, if more than one band was present when attempting to fit, an inaccurate representation of band maximum was achieved.

$$y = a0 + a1 * x + a2 * x^2 + a3 * x^3 + a4 * x^4 + a5 * x^5 + a6 * x^6 + a7 * x^7 + a8 * x^8 + a9 * x^9$$

Equation 47

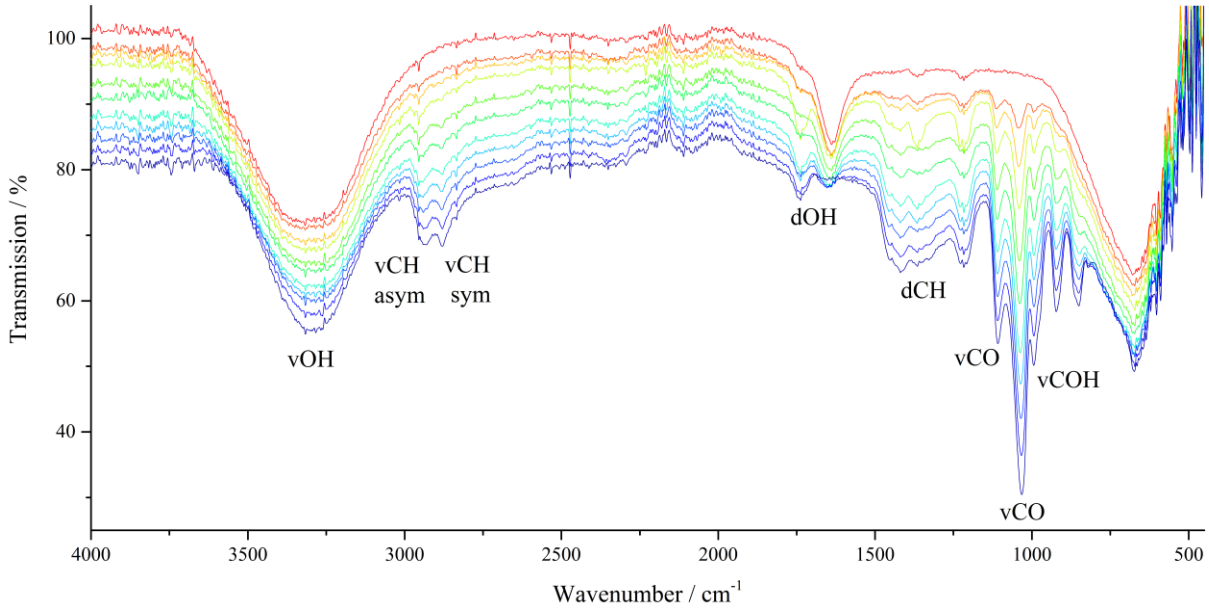

Figure 7.2. Complete FTIR spectra of glycerol-water solutions, ranging from 100% water (solid, red) to 100% glycerol (solid, blue) in 10% increments.

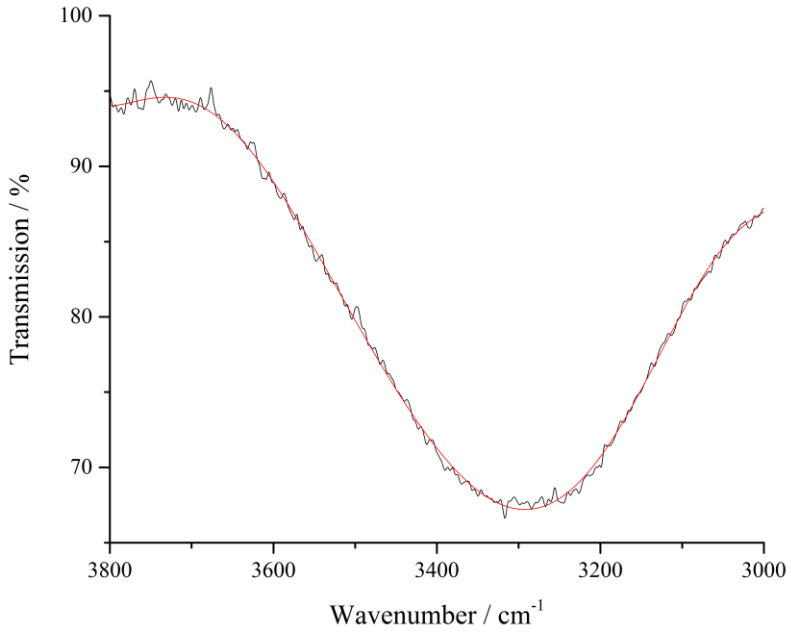

Figure 7.3. FTIR of a solution of 50 w% water, 50 w% glycerol, displaying the νOH stretch raw data (solid, black) and a 9th order polynomial fit (solid, red).

7.1.1. Molecular Interactions Derivable from the νOH Stretch

As all compounds used in this study contain hydroxyl groups, the νOH stretch describes changes in hydrogen bonding for every component of the system, and is hence used as a benchmark for overall H-bonding. For glycerol-water systems, as glycerol concentration in each sample increases, overall H-bonding within the system also increases, expressed as a decrease in wavenumber for νOH.[232] Plots of the νOH stretch for glycerol-water samples are shown in Figure 7.4a. Although not obvious, it is possible to see a decrease in the wavenumber of the νOH stretch as glycerol concentration increases from 0% to 100%. Figure 7.5. shows the peak maxima of each fit plotted against glycerol concentration, and as can be seen from the 'Gly, H_2O' data there is a consistent decrease in wavenumber with increasing glycerol concentration for the νOH stretch. This reiterates what was shown previously by Dashnau et al.[232] and confirms the validity of FTIR testing to detect H-bonding. It is worth noting that the wavenumber detected for high-glycerol containing solutions (60-90 w%) is lower than that for the pure glycerol sample, suggesting H-bonding in these samples reaches a maximum at ~70 w% glycerol. To probe the effects of surfactant and polymer on H-bonding within the samples three more groups of samples were formulated in which the water : glycerol ratio was systematically varied, except this time additives were included in the solution; firstly 10 w% $C_{12}E_5$, then 10 w% PVA, and finally both 10% $C_{12}E_5$ and 10% PVA. The same analysis was performed on each sample group and the fits are displayed in Figure 7.4., as well as the peak maxima versus glycerol concentration in Figure 7.5. The X_{gly} parameter represents the molar fraction of glycerol in each solution, calculated using the following equation;

$$X_{gly} = \frac{100 \cdot [gly]}{[gly] + [H_2O]}$$

Equation 48

where $[gly]$ is the concentration of glycerol in w% and $[H_2O]$ is the concentration of water in w% in each solution. Conclusions from these findings will be drawn in 7.1.4.

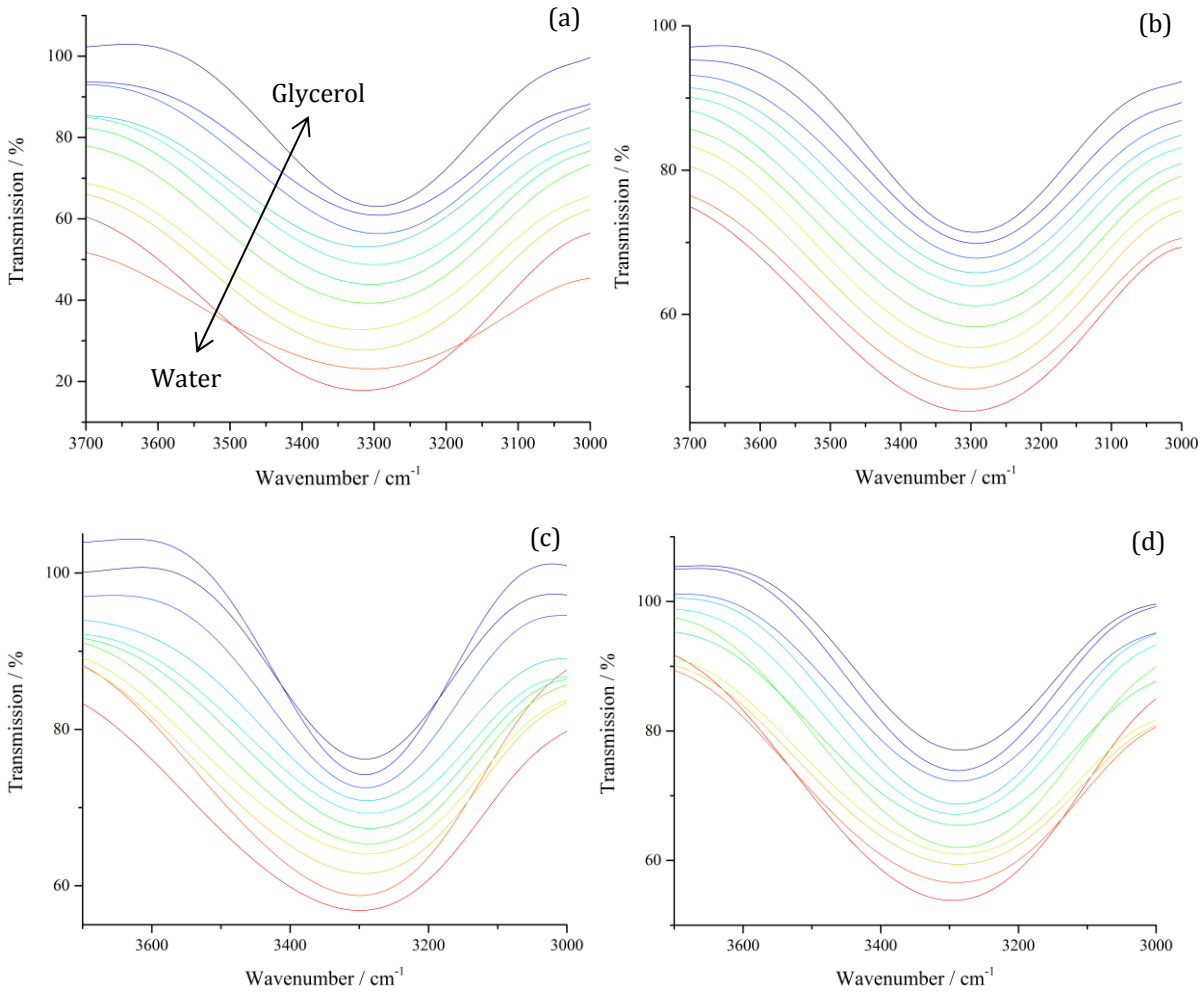

Figure 7.4. νOH stretch from FTIR of several glycerol-water mixtures, ranging from 100% water (solid, red) to 100% glycerol (solid, blue) in 10% increments. (a) glycerol, water, (b) glycerol, water, 10% $C_{12}E_5$, (c) glycerol, water, 10% PVA, (d) glycerol, water, 10% $C_{12}E_5$ and 10% PVA.

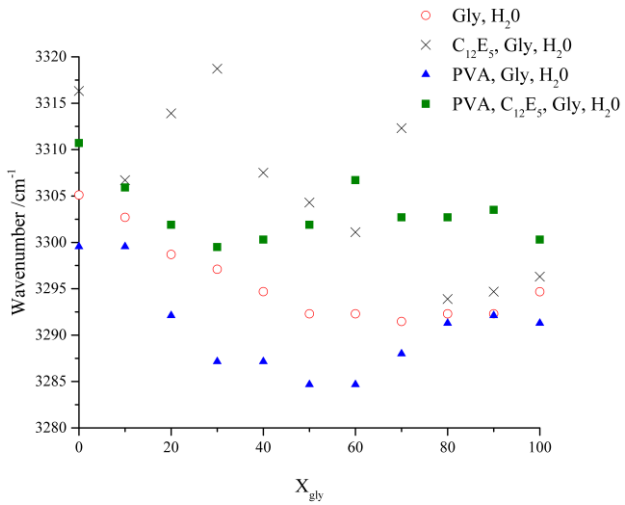

Figure 7.5. Fitted νOH peak maxima for each sample plotted against glycerol concentration,

From Figure 7.5. it is possible to see the effects of each additive on the overall H-bonding within the system; the addition of $C_{12}E_5$ causes a significant increase in νOH wavenumber for all samples, indicating a reduction in the overall H-bonding within the sample. Disruption of the H-bonding network appears to be more significant at lower glycerol concentrations, with H-bonding being mostly restored at glycerol concentrations ≥ 80 w%. The addition of PVA to the glycerol-water system causes a reduction in the νOH wavenumber of each sample, indicating increased H-bonding compared to the binary system, with the difference in wavenumber being less significant at higher glycerol concentrations. When both $C_{12}E_5$ and PVA are present, samples exhibit reduced H-bonding compared with the binary mixtures, however in comparison to the ternary, $C_{12}E_5$-containing samples the quaternary system shows increased H-bonding. This suggests that the presence of PVA somewhat nullifies the H-bonding screening effects of $C_{12}E_5$.

7.1.2. Molecular Interactions Derivable from the δOH Bend

The νOH stretch is not the only band that can be used to obtain information about hydrogen bonding within these systems. The δOH band (or HOH bend) allows monitoring of water's behaviour explicitly, as no other component of the sample contains this moiety; shifts in δOH wavenumber have been shown to be inversely proportional to shifts in the νOH stretching mode.[237] Bending frequencies are generally found at lower wavenumber compared to stretching frequencies and the bending mode of water is usually active between 1500 and 1800 cm^{-1}.[238-239] There are two bands situated very close to each other within this region, one at ~1640 cm^{-1} and another at ~1740 cm^{-1}. As the band at ~1740 cm^{-1} is only prominent in samples containing PVA it must be related to the polymer, therefore the stronger band at ~1640 cm^{-1}, which is present in all plots is the HOH bend associated with water. The data obtained for each spectrum is the same used in the νOH plots, with slight adjustments to the transmission to display the curves in the correct order. Plotting the peak maxima against glycerol concentration gives information on the effects of additive addition (Figure 7.7.). The wavenumber of the δOH bend is seen to increase with increasing glycerol concentration for all samples, indicating an increase in H-bonding strength/number for water molecules within the sample. No δOH band is present at 100 X_{gly} as the moiety does not exist in these solutions. The addition of $C_{12}E_5$ or PVA appears to have no visible effect on the H-bonding of water within the sample for the most part, as the gradient of each dataset remains similar for all samples. There is however a wavenumber increase seen for high glycerol concentration (≥ 70 w%) samples with the addition of PVA, possible reasons for this are presented in 7.1.4.

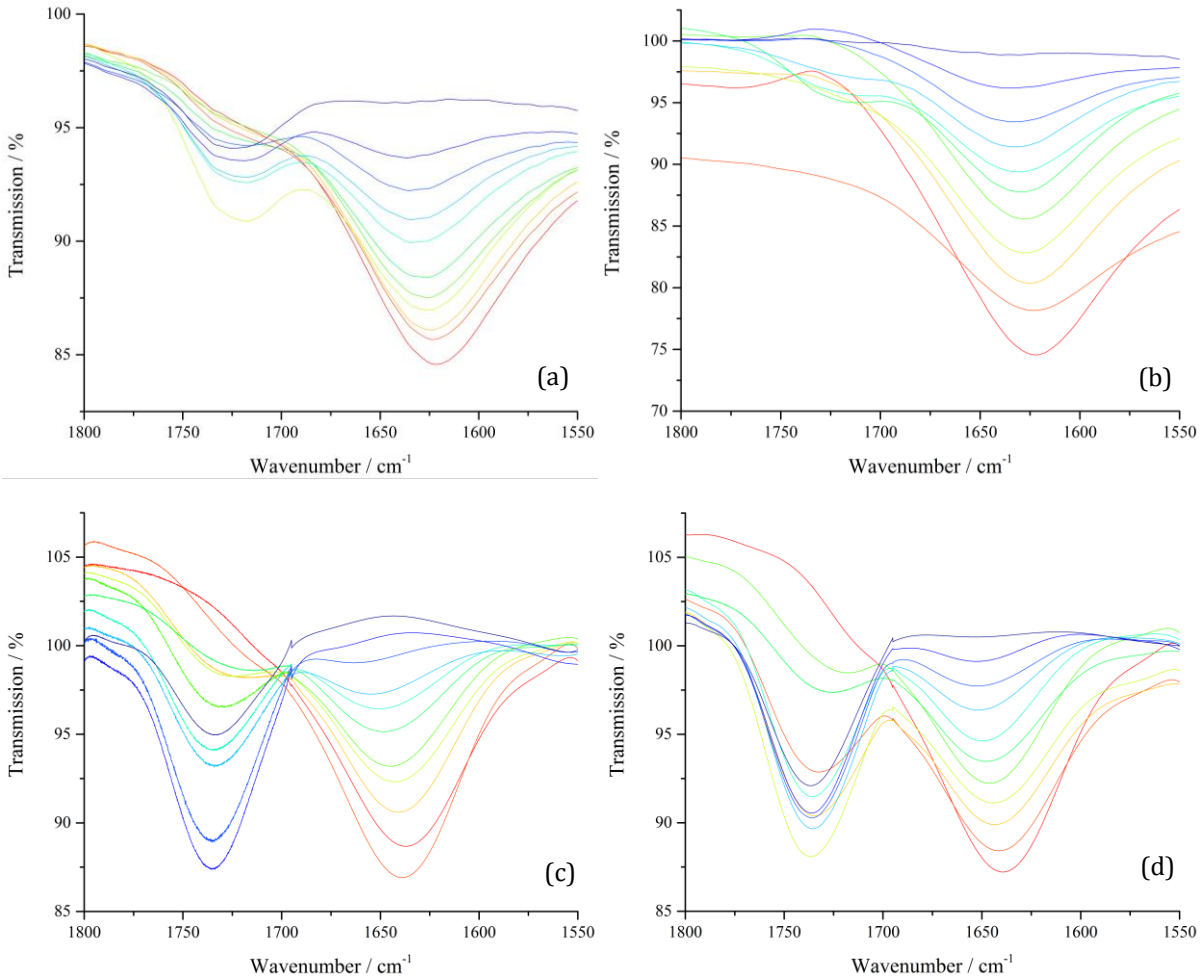

Figure 7.6. δOH bend from FTIR of several glycerol-water mixtures, ranging from 100% water (solid, red) to 100% glycerol (solid, blue) in 10% increments. (a) glycerol, water, (b) glycerol, water, 10% $C_{12}E_5$, (c) glycerol, water, 10% PVA, (d) glycerol, water, 10% $C_{12}E_5$ and 10% PVA.

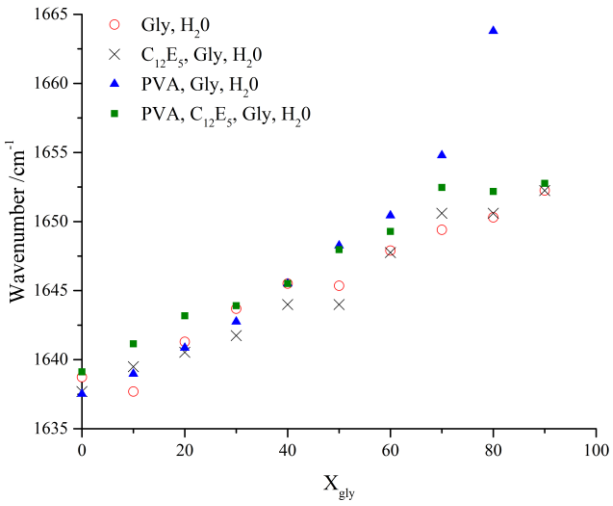

Figure 7.7. Fitted δOH bend (~1640 cm^{-1}) peak maxima for each sample plotted against glycerol concentration,

7.1.3. Molecular Interactions Derivable from the νCO Stretch

The νCO stretch should also provide information on H-bonding within the system, especially between glycerol and other components, as the two lone pairs of the oxygen atoms are also involved in H-bonding. νCO stretches are normally found between 1050 and 1150 cm^{-1}. Three bands are visible in this region, two νCO stretching vibrations at ~1035 cm^{-1} and ~1110 cm^{-1} which arise from primary (R-CH_2-OH) and secondary (RR'-CH-OH) alcohols respectively as 1° < 2° < 3°,[240] and a νCOH stretching band at 995 cm^{-1}. Figure 7.8. displays the vibrational modes mapped on to a glycerol molecule for each of these bands. Unsurprisingly an increase in the intensity of all three bands is seen as glycerol concentration increases, as no C-O-H groups exist in a pure water system and it is only the presence of glycerol that can give rise to these bands. As all bands are stretching vibrations, increased H-bonding should cause a decrease in wavenumber, as was the case with νOH. The peak maxima wavenumber is plotted against glycerol concentration for each sample in Figure 7.10.

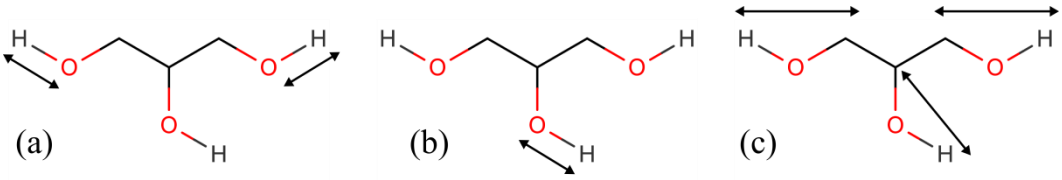

Figure 7.8. Schematic representation of the vibrational modes of glycerol used to detect hydrogen bonding in solution, (a) primary alcohol νCO (R-CH_2-OH) stretch, (b) secondary alcohol νCO (RR'-CH_2-OH) stretch and (c) νCOH stretching band,

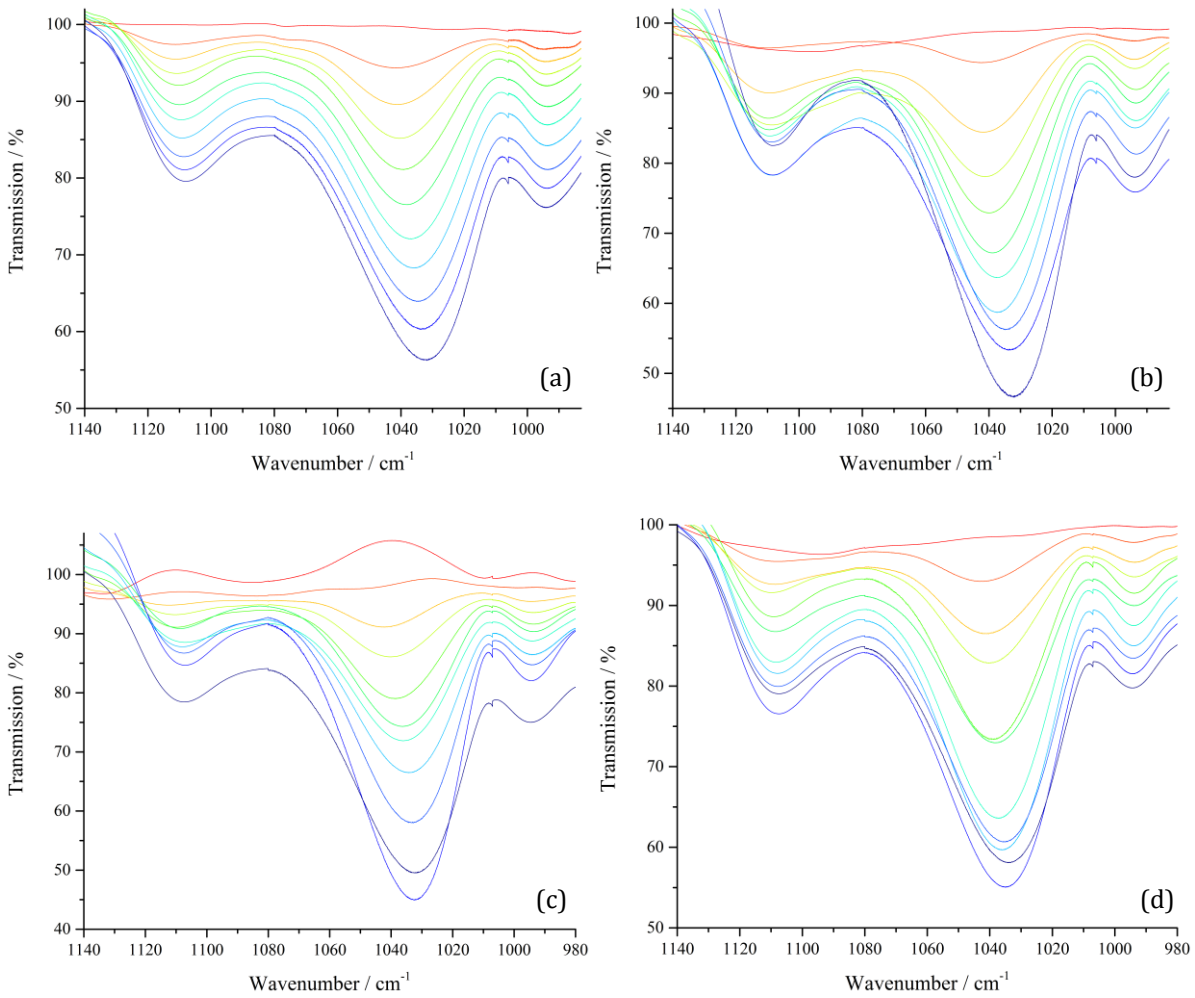

Figure 7.9. νCO stretch from FTIR of several glycerol-water mixtures, ranging from 100% water (solid, red) to 100% glycerol (solid, blue) in 10% increments. (a) glycerol, water, (b) glycerol, water, 10% $C_{12}E_5$, (c) glycerol, water, 10% PVA, (d) glycerol, water, 10% $C_{12}E_5$ and 10% PVA.

In binary mixtures of water and glycerol, the primary νCO stretching band (Figure 7.10a.) shows a relatively linear decrease in wavenumber with increasing glycerol concentration, indicative of increased H-bonding in glycerol as its concentration increases. This mirrors what was found with the νOH stretch. It appears that the additives cause relatively little interference with H-bonding at the terminal primary alcohol groups of glycerol similar gradients and wavenumbers are displayed for all sample groups. However, there is a slight decrease in wavenumber for most samples upon the addition of PVA, indicating an increase in H-bonding to the central hydroxyl group of glycerol. In samples without PVA, the secondary νCO band is unique to glycerol as neither water nor $C_{12}E_5$ contain a secondary CO group, therefore the behaviour of this band can be used to explicitly describe the H-bonding of glycerol.

Although all datasets in Figure 7.10b. have a generally negative gradient somewhat similar to that of the binary glycerol-water samples, when isolating specific glycerol concentrations, some information on the synergy between additives can be realised. Considering PVA, addition caused a consistent decrease in wavenumber (increase in H-bonding) for all samples for the νOH stretch. This is also true for the most

case when observing primary νCO vibrations, however the opposite effects are realised by analysis of the secondary νCO band at low glycerol concentrations. For ≤ 40 w% glycerol, the addition of PVA to the system causes an increase in wavenumber (decrease in H-bonding) when compared to the binary system. Although it may be considered unusual that the two νCO bands exhibit different results; it is possible that as the secondary νCO band includes vibrations from PVA, when the solution contains high water content, the PVA is being primarily solubilised by water. As the νOH band showed that interaction with the polymer causes increased H-bonding, it is possible that glycerol is being outcompeted by water for interaction with PVA, which causes it's H-bonding to be reduced. This leads to an overall reduction in H-bonding for the secondary νCO band. This effect would not be seen in the νOH stretch as the increased H-bonding of water upon the addition of PVA would counteract and overcome the reduced H-bonding of glycerol seen here, as it is the most highly concentrated solvent in these samples. The HSPs of the materials suggest that glycerol (δ = 36.2) has a slightly more favourable interaction with water (δ = 47.8) compared to PVA (δ = 23.7), as its HSP is closer to it. This also suggests that glycerol would be found in the bulk water phase, rather than with PVA, as it prefers to interact more with water, rather than plasticise the polymer in these samples. Water has been shown to have the ability to remove and replace glycerol from its site within thin film samples in the humidity NR experiments also, where water preferentially situates itself between surfactant layers over glycerol in plasticised $C_{12}E_6$ (chapter 5.2.2.) and SDS film (chapter 6.2.5.), so it is plausible that a similar phenomenon is occurring here.

Figure 7.10c. shows the νCOH band maxima for each sample group plotted against glycerol concentration. It is notable that the range of wavenumbers observed is considerably smaller (~3 cm^{-1}) than what has been seen for the other νCO bands (~7-15 cm^{-1}). Therefore any effects of additive addition on the νCOH band may be considered less significant compared to other bands, as the shift is smaller. There does not appear to be any observable trend in H-bonding with increasing glycerol concentration in the binary systems. However, some information regarding the interaction of $C_{12}E_5$ with glycerol water systems can still be obtained from this band. At low glycerol concentrations (≤ 40 w%) the addition of $C_{12}E_5$ causes a significant increase in the wavenumber of the νCOH band, indicating a decrease in H-bonding. This finding elaborates on what was discovered with the νOH band, where it was shown that addition of $C_{12}E_5$ caused a reduction in overall H-bonding within the system, especially at low glycerol concentrations. It now appears that this is at least partly due to a reduction of glycerol H-bonding upon the addition of $C_{12}E_5$, which is discussed further in 7.1.4.

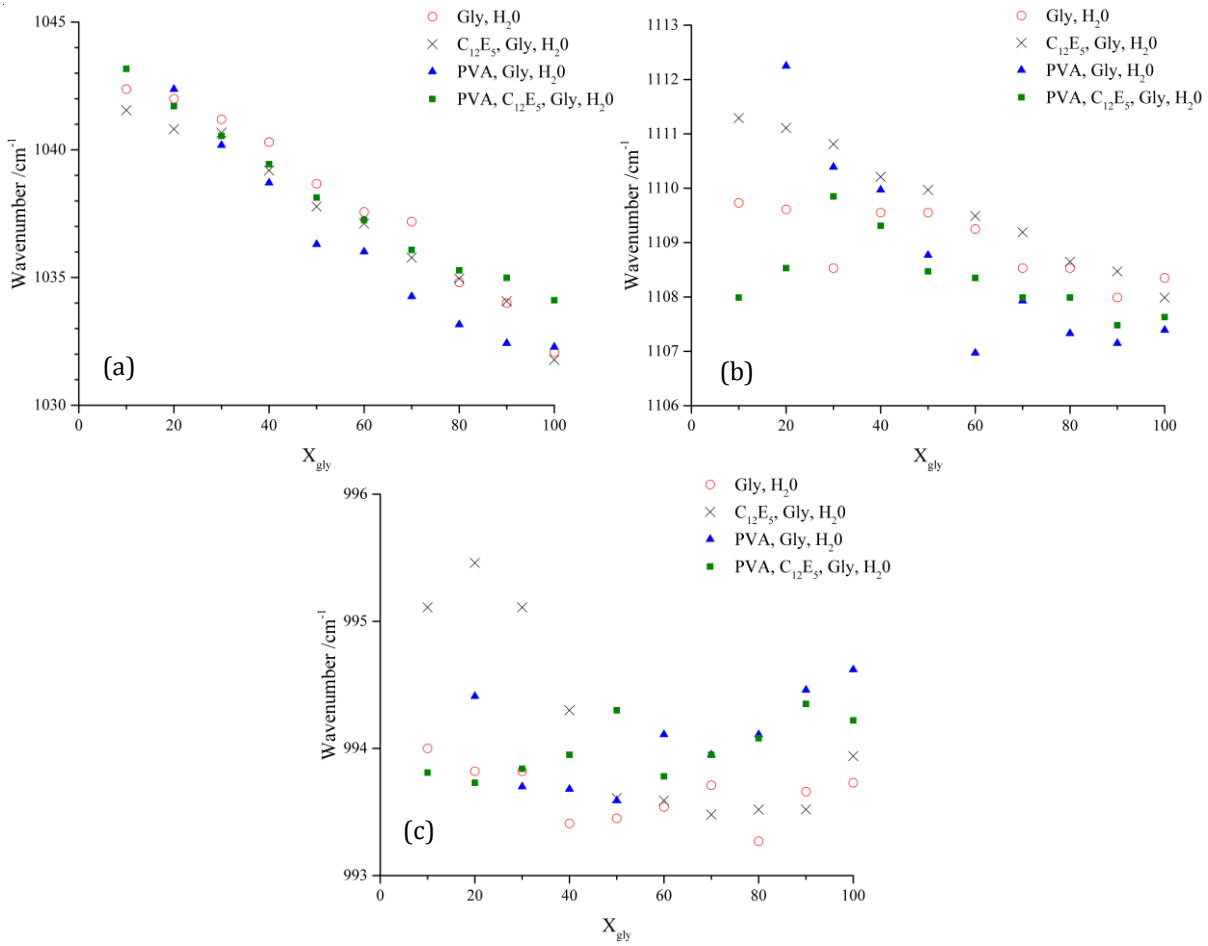

Figure 7.10. Fitted νCO maxima plotted against glycerol concentration for primary alcohol νCO mode (a, 1035 cm^{-1}), secondary alcohol νCO mode (b, 1110 cm^{-1}) and the νCOH vibration (c, 994 cm^{-1})

7.1.4. Discussion of Molecular Interactions and Hydrogen Bonding in Solution Samples

Study of the binary glycerol-water system has mirrored findings by previous authors who have shown an increase in detected H-bonding (reduction of νOH wavenumber) as glycerol concentration increases. Molecular dynamics simulations have been reported on glycerol-water mixtures which suggest the decrease in wavenumber is related to formation of an ordered H-bonding lattice as glycerol concentration increases.[241] A more ordered network of H-bonds results in increased strength of interaction between opposing charged groups O–Hδ+···Oδ-. This causes lengthening of the O-H covalent bond,[109, 242-244] which gives a lower force constant and causes the wavenumber of the stretching vibration to be reduced. Similar findings are exhibited in the case of ice having a lower frequency νOH stretch vibration compared to water due to the ordered network of H-bonds which is formed below 273.15K.[245] In an attempt to represent the H-bonding of water and glycerol in mixtures, a schematic representation of the increased structure visible in higher glycerol concentrations is shown in Figure 7.11. It is possible to see in this schematic how the glycerol H-bonding network forms with increasing glycerol concentration. Several authors have found evidence of glycerol's extensive H-bonding network through molecular

simulations.[246-249] It is the existence of the H-bonding network that gives glycerol the ability to vitrify in to a glassy structure at reduced temperatures.

The increased H-bonding for water molecules within these systems observed by the δOH band is also explained through the formation of this ordered network,[232] which suggests the increased water H-bonding with increasing glycerol concentration is due to clustering (termed linearization) of water, caused by formation of the glycerol-glycerol network. As water becomes clustered at higher glycerol concentration, it has less freedom, and hence becomes more ordered, causing the strength of its H-bonding to increase.

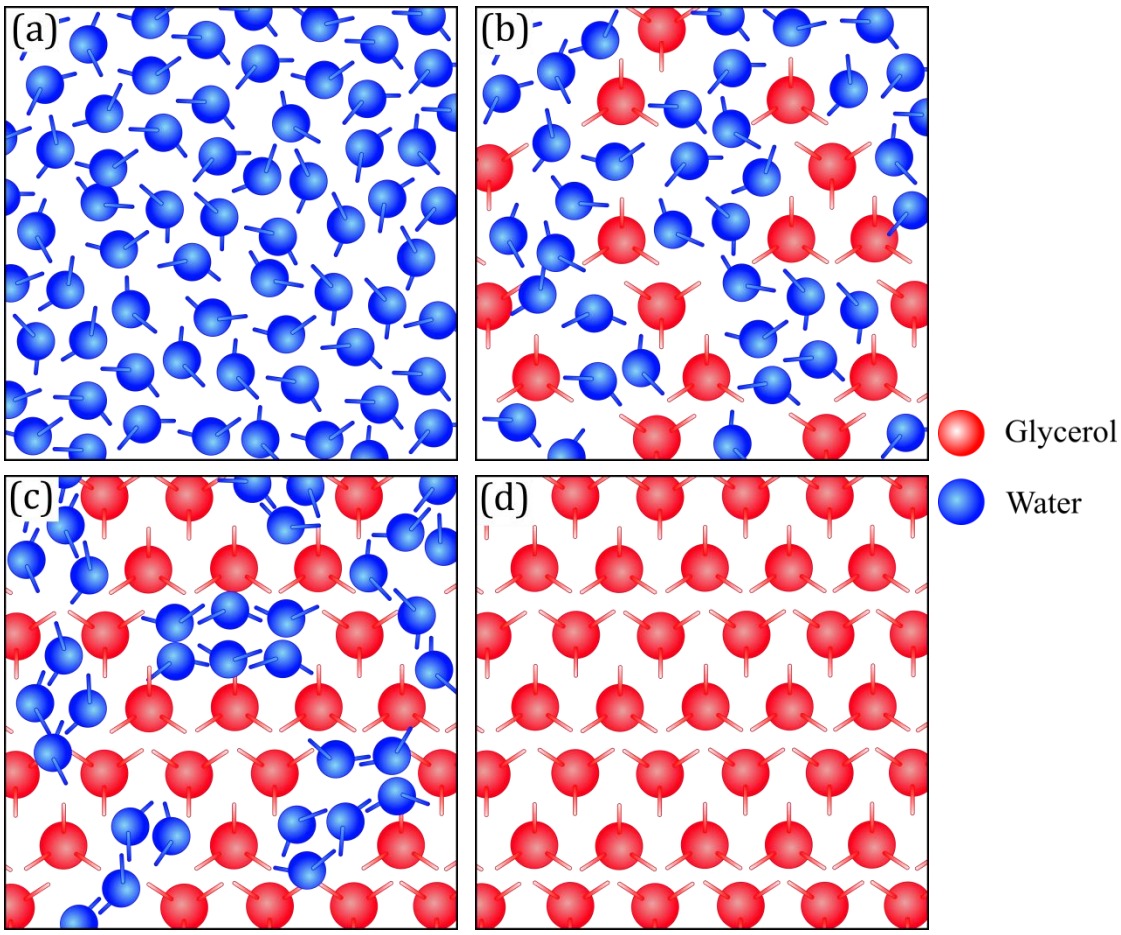

Figure 7.11. Schematic representation of formation of a glycerol (red) H-bonding lattice with increasing glycerol concentration, with groups of water (blue) molecules becoming more isolated and clustered as water concentration drops

Addition of $C_{12}E_5$ to the binary caused relatively little change to the wavenumber of the δOH bend, and hence H-bonding of water within the system. This would mean that the clustering of water occurs similarly in samples which contain $C_{12}E_5$ and in glycerol-water samples. The stretching vibrations (νOH, νCO) do however show a difference upon the addition of surfactant. The wavenumber of the νOH mode increases significantly when $C_{12}E_5$ is included in the solution, indicating a large reduction in the overall H-bonding within the system. This is also true for the secondary νCO stretch. To explain this $C_{12}E_5$ micelle

formation may be used, it is known that $C_{12}E_5$ will form cylindrical micelles in aqueous solution,[250] and it was suggested that these structures may also be capable of forming in thin PVA films in chapter 5.2. Therefore if surfactants are forming in high water/low glycerol concentration solutions, much of the surfactant's H-bonding potential would be concealed within the micelle and be unavailable to H-bond with its surroundings as only the terminal hydrogen in the polar $C_{12}E_5$ head-group would be exposed, visualised in 7.1.2. The calculated diameter for $C_{12}E_5$ cylindrical micelles reported by Li et al.[250] is 5 nm, which is very large compared to the other compounds present in the solutions, hence their potential for disrupting the H-bonding within the sample is significant. This thickness is also remarkably similar to the thickness of the $C_{12}E_5$ surface excess layer (5.6 nm) found in the earlier NR experiments for plasticised, surfactant containing films (Figure 5.11.), supporting the formation of micelles in the solution samples. The fact that H-bonding, as documented by the νOH and secondary νCO modes, is mostly restored at high glycerol concentration solutions (≥ 80 w%) is also interesting. The formation of micelles, or lack thereof, may be used to explain this. As the CMC of $C_{12}E_5$ is increased in glycerol containing solutions [191] due to the reduced water content, micelles are less likely to form. If fewer/no micelles are forming in these solutions, it means that more surfactant monomer will be present, with its H-bonding sites not concealed within the micelle and available to H-bond. This would cause the overall H-bonding within the system to remain relatively similar to binary solutions, as the glycerol-glycerol H-bonding network would not be disturbed, leading to the wavenumber being unchanged upon $C_{12}E_5$ addition, as is seen in Figure 7.5. This effect can be seen in Figure 7.12d. It is also possible that the presence of $C_{12}E_5$ monomer in these solutions does not have a negative effect on H-bonding, as the H-bonding which has been disrupted by the surfactant is restored by the formation of an ice-like H-bonding cage, termed a clathrate cage around the molecule. This change in the H-bonding structure upon addition of non-polar entities is the basis for the hydrophobic effect, which drives the self-assembly of compounds such as surfactants in solution.[251] Clathrate-like structures around the poly(ethylene oxide) region of $C_{12}E_x$ molecules have been proposed[252] and observed with vibrational sum frequency spectroscopy (VSFS).[253] Therefore the overall H-bonding within the system may be relatively unaffected if the polar regions of the surfactant are available to H-bond. If micelles are forming, and these regions are concealed within them, then these effects may not occur, giving rise to the reduced H-bonding observed at glycerol concentrations < 80 w%.

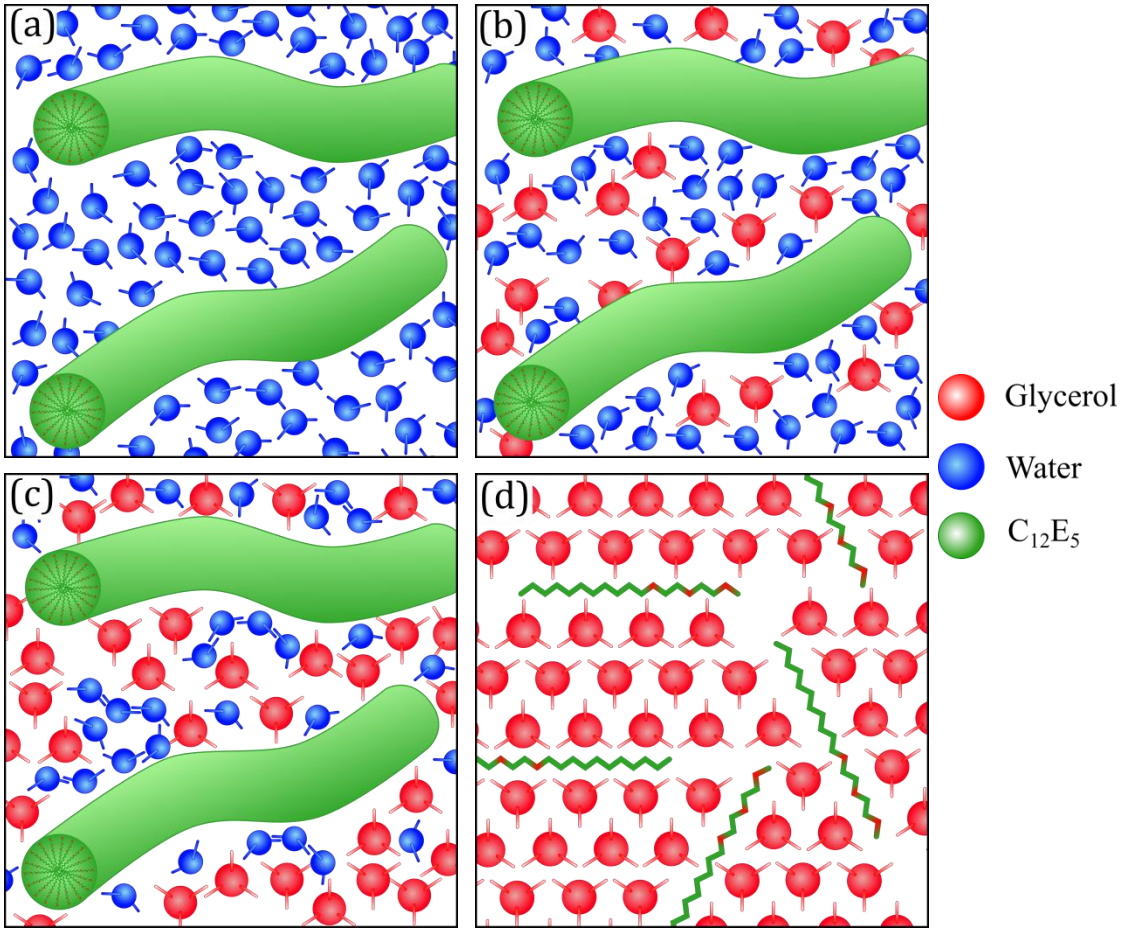

Figure 7.12. Schematic representation of the effects of $C_{12}E_5$ (green) addition on the intermolecular interactions of water and glycerol in solution

Evidence for the increase of overall H-bonding within these systems upon the addition of PVA has also been documented by the νOH stretch. It is thought that H-bonding is encouraged by the addition of PVA as a more structured, rigid network of hydrogen bonds can be formed using the complex polymer suprastructure of PVA in water as a chassis to build on.[254] A schematic representation of this is displayed in Figure 7.13. As the polymer is less free to move in comparison to the glycerol and water molecules surrounding it, as well as containing a significant number of H-bonding sites, it can therefore provide a relatively persistent H-bonding framework for the glycerol and water to bind to. The fact that increased H-bonding seen with PVA addition is less significant at higher glycerol concentration (≥ 80 w%) could either be attributed to phase separation within the system, or PVA crystallising out of solution as the volume of solvent (water) in the solution decreases. PVA has limited solubility in all solvents but water, so increased glycerol concentration within the system would be likely to cause crystallisation. Solid PVA would be less likely to H-bond to glycerol, but may not be as disruptive to the formation of a glycerol H-bonding network as a cylindrical $C_{12}E_5$ micelle as it is not in solution; hence PVA being omitted from Figure 7.13d.

The behaviour of water in these samples, monitored using the δOH bend shows mostly similar behaviour to the binary system at glycerol concentrations < 70 w%, indicating that water clustering is not

affected by the presence of PVA in these samples, similarly to what was seen for $C_{12}E_5$. However the increase in wavenumber seen at 80 w% glycerol concentration for the samples including PVA describes an increase in H-bonding. Unfortunately the strength of the δOH absorbance in the PVA containing solution was too weak to produce a band at 90 w% glycerol, so no information on the behaviour of water could be obtained at this concentration. It is however plausible that at high glycerol concentrations, because of the reduced solubility of PVA in glycerol compared to water, the water present within the system will be primarily being used to maintain dissolution of the PVA. In this case the water would be situated in close proximity to the polymer, which has been shown to increase ordering and H-bonding, therefore exhibiting an increased wavenumber.

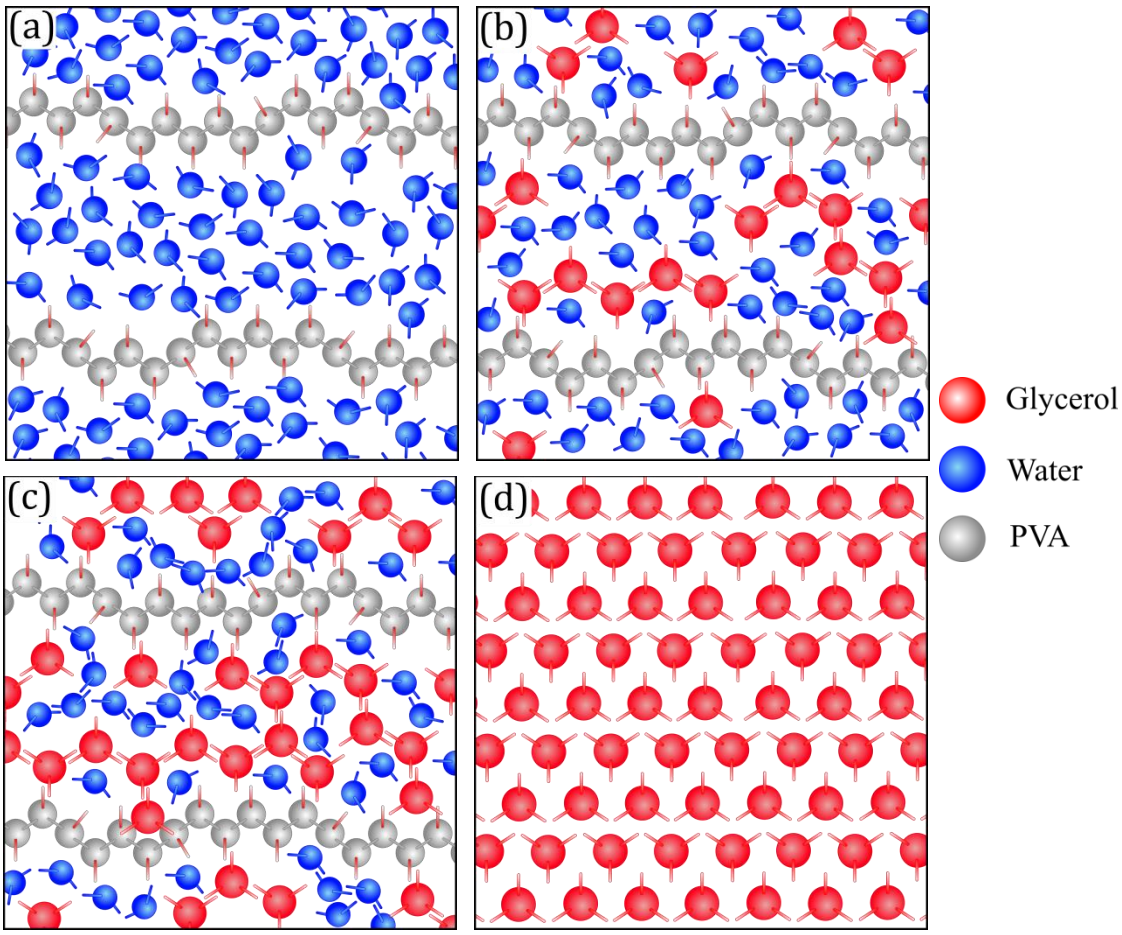

Figure 7.13. Schematic representation of the effects of PVA addition on the intermolecular interactions of water and glycerol in solution

In the quaternary systems containing both $C_{12}E_5$ and PVA it can be seen from most of the vibrational modes that a medium between the strengthening of H-bonding PVA has and the weakening of H-bonding $C_{12}E_5$ has is reached. It appears that this may simply be due to a mix of the two structures being formed in systems where there are sufficient water, and the interaction of the polymer and surfactant is limited.

This part of the investigation has highlighted certain interactions between compounds in liquid samples; addition of PVA to the binary glycerol-water system caused a general increase in the amount of

H-bonding detected within the system, indicating favourable interactions between the three components. Addition of $C_{12}E_5$ caused a decrease in the amount of H-bonding detected compared to the binary system, which suggests an unfavourable interaction between the surfactant and glycerol, water. Study of quaternary systems suggests some favourable interaction between PVA and $C_{12}E_5$ as the H-bonding screening effects of $C_{12}E_5$ are reduced upon the addition of the polymer. These results also shed light on interactions of water and glycerol, where the formation of a complex glycerol network causes clustering of water molecules and increased H-bonding throughout the system. It would appear from the formation of this glycerol H-bonding network that glycerol will preferentially H-bond to itself over water, which may help to explain why water has the ability to force glycerol from the interstitial regions between surfactant-rich layers in thin films. As more water is absorbed through the surface of the film under increasing humidity and water concentration increases, glycerol will migrate away from water-rich regions to maximise its interaction with itself. The formation of more structured water-water and glycerol-glycerol networks within the polymer films may be influential on surfactant segregation. If this increased structuring within the film leads to increased phase separation in the polymer matrix, surfactant may also be more likely to segregate.

Although the ambient NR results suggested favourable interactions between $C_{12}E_5$ and glycerol (chapter 5.1.3.) as the compatibility of the surfactant and PVA appeared to increase upon plasticisation, no such effect could be realised with FTIR. Here the addition of surfactant to the water-based systems caused decreased H-bonding, and the addition of PVA caused increased H-bonding. It was hoped that some synergistic effect on H-bonding would be visible when both surfactant and PVA were present, but the negative effects of surfactant were simply lessened upon the addition of PVA, which may simply be due to mixing of the two components. There may however be some debate as to whether behaviour of surfactants in solution samples containing a small amount of PVA can be used to accurately explain their behaviour in solid polymer films. The contrast of these sample environments may change the way in which the surfactant interacts with other components of the film. A FTIR study in to the effects of additive addition on thick films was initiated but due to time restrictions could not be completed, instead the preliminary experiments on thicker films which prove the effectiveness of the saturated solutions at controlling humidity and show significant water absorption with industrial sized films are discussed in the following section.

7.2. Model Film FTIR Analysis

The use of model, thick (> 10 μm) films not only allows the study of molecular interactions in more relevant, film-based samples compared to the solution samples, but also allows analysis of properties which could not be studied with liquid samples. One such property is humidity, something of significant importance for film stability in industry, as well as thin spin-cast films. Analysis of the 76 μm industrial plasticised PVA film proved difficult as the transmission through the film was too weak to achieve a spectrum. Absorption peaks can start to be realised by stretching the film, however to achieve films of a consistent degree of thickness would prove difficult. The deformation of industrial films also imposes permanent stresses on the material which may interfere with results, for example crystallinity is induced

by stretching the material, which would change the observed spectrum considerably. To prevent these issues model films were prepared by solution casting a PVA (Aldrich, P8136) solution in a vacuum oven for ~90 minutes to remove water and form a solid, dry film. Non-plasticised films were the first to be studied and a FTIR plot of a pure PVA film, approximately 15 μm in thickness is displayed in Figure 7.14.

Each peak of interest has been assigned in the Figure 7.14., if water absorption into these films occurs in a similar way to what was seen for thin films, it would be expected that the νOH and δOH peaks would increase in intensity. Conversely, if water has been lost from the films then the intensity of these bands should decrease. The FTIR absorption spectra for two pure PVA films is given in Figure 7.14. The films were either subjected to ambient conditions of approximately 40 %RH (red), or placed inside of a sealed vessel at 85 %RH (blue) for 24 hours. There appears to be some discrepancy between the starting thicknesses of the two films as the 85%RH data shows stronger absorbance compared to the film left under ambient conditions. This signifies an increase in film thickness, causing the absorbance in the νOH stretch to increase to almost 100%. After allowing the films to equilibrate under ambient conditions for 24 hours and taking another spectrum (dotted lines) any change in film thickness brought about by the absorption or loss of water should be mirrored in the absorbance. Interestingly, it is not just the bands representative of water (νOH, δOH) that show a change in absorbance after this time period, the entire spectrum shows a shift. For both the atmospheric and 85 %RH non-plasticised PVA film an increase in the absorbance of all bands is seen, indicating an increase in thickness for both samples compared to their initial dried state. This would be expected for the sample placed under high humidity as it has been shown that a PVA film is capable of absorbing water as a plasticiser from high-humidity atmospheres in chapters 5 and 6. The fact that the ambient film also shows an increase in film thickness proves the susceptibility of initially dry, non-plasticised films to exhibit water absorption even under standard conditions.

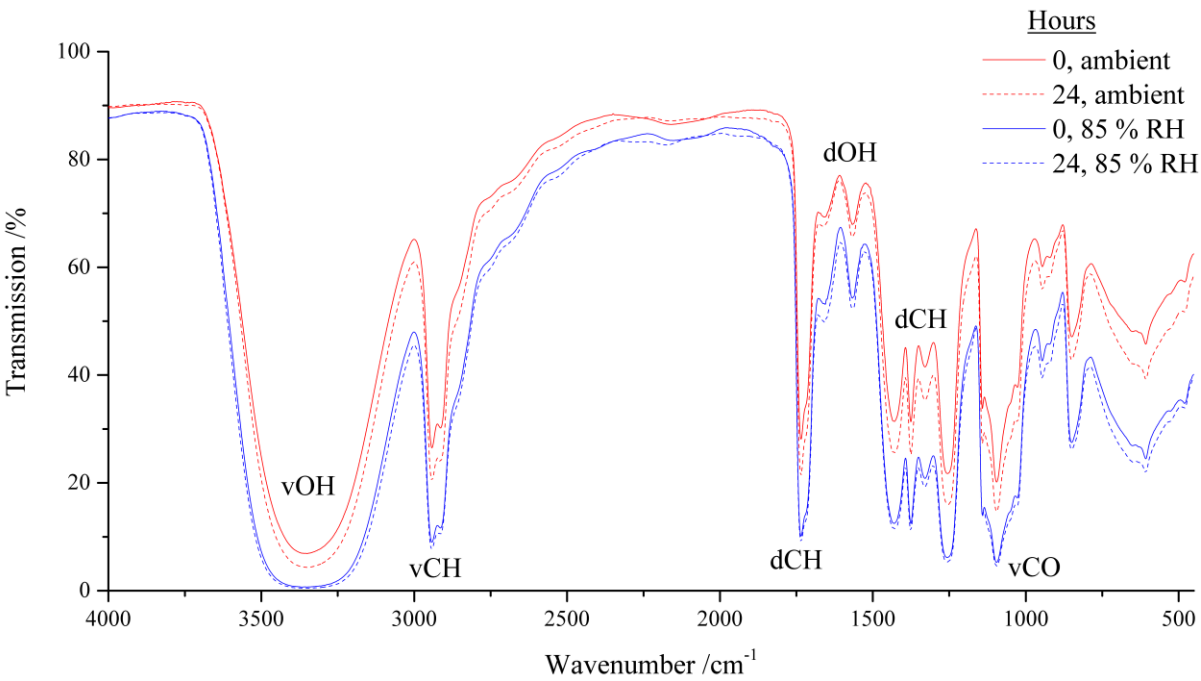

Figure 7.14. FTIR spectra of two separate pure PVA (0 w% glycerol) films, directly after formation (red and blue, solid lines). Another FTIR spectra of the same films after being subjected to 24 hours under ambient conditions (dashed, red) or 85 %RH, achieved using a humidity cell containing a saturated salt solution (dashed, blue).

Next two films containing 10 w% glycerol were studied under the same conditions. The spectra for which are displayed in Figure 7.15., as can be seen both the atmospheric and 85%RH films show relatively little change after 24 hours equilibrating. This suggests that a stable level of plasticisation is reached at 10 w%, where little is being lost to the atmosphere, and there is also little impetus for the film to absorb more plasticiser in the form of water. It is also possible that water was absorbed so quickly after film forming that equilibrium had already been reached in the first 30 minutes; hence all spectra are simply displaying the equilibrium state. Although some loss of plasticiser was detected in thin films which contained 10 w% glycerol over a similar time period, the amount of glycerol present in thin films compared to thicker films is vastly reduced. Therefore assuming glycerol exhibits a similar evaporation rate regardless of film thickness, the amount of plasticiser lost has much more significance for thinner films, and is negligible for thick films considering the large volume present. Although it was suggested from the thin film humidity studies that the presence of glycerol in thin films facilitates increased water absorption from the atmosphere it would be unreasonable to compare thin film humidity control data to these results due to the different plasticiser concentrations. To provide a more direct comparison to thin film results, solution cast films with 20 w% glycerol concentrations were formulated and the same experiments performed.

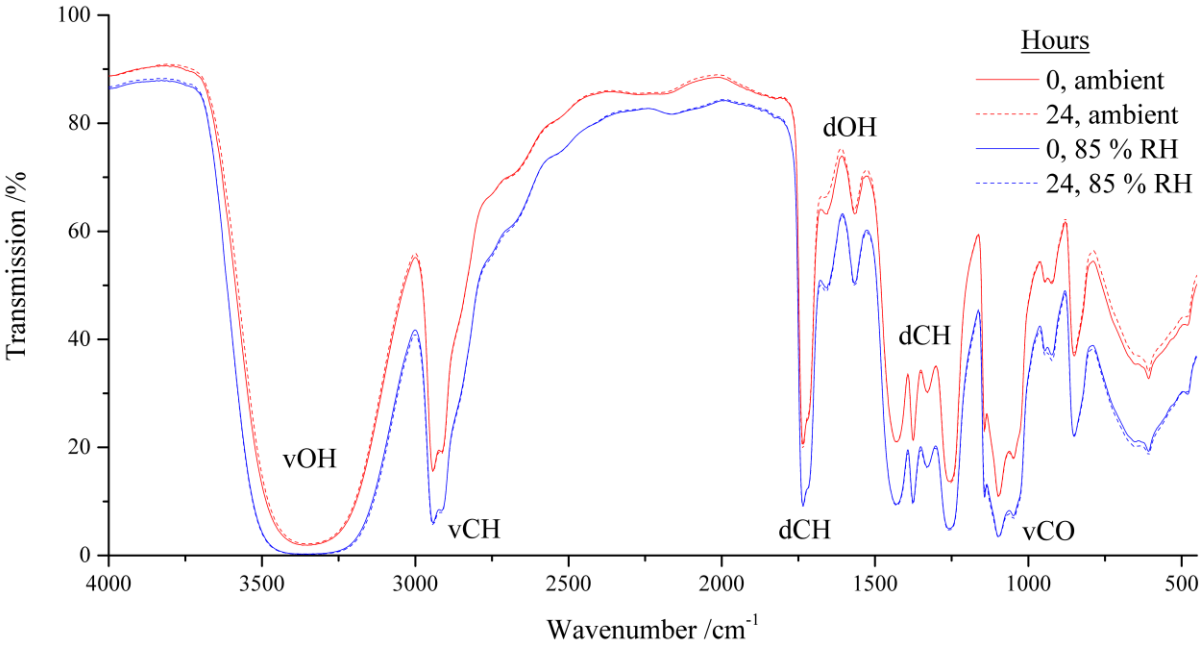

Figure 7.15. FTIR spectra of 10 w% glycerol films directly after formation (red, blue, solid) and after being subjected to overnight under standard laboratory conditions (dashed, red) or 85 %RH (dashed, blue).

Two more films containing 20 w% plasticiser were studied under ambient conditions and 85%RH, the spectra for which are displayed in Figure 7.16. When subjected to ambient conditions a significant reduction in the intensity of most bands, especially the νOH and δCH is seen. Although this effect was not seen for thick films containing 10 w% plasticiser, it is likely that the additional loading of plasticiser at 20 w% is beyond what the film can incorporate in equilibria, so is hence being lost from the film, leading to the observed reduction in thickness. When placed in a high humidity environment the film shows an increase in the absorbance of all bands, which indicates an increase in film thickness. This can only be brought about by the absorption of water from the atmosphere, which has also been indicated for thinner films in chapters 5.1.5, 5.2 and 6.2.5. As more water absorption was observed in 20% plasticised films as opposed to 10%, it suggests that it is glycerol's affinity for water that leads to this increased absorption. This does not explain the absorption of water seen in non-plasticised films however. As pure glycerol was shown to absorb water from the atmosphere previously, and also implied by the non-ionic surfactant results obtained in chapter 5, it would appear that the presence of glycerol largely determines the ability of the PVA film to absorb water from the atmosphere in plasticised films.

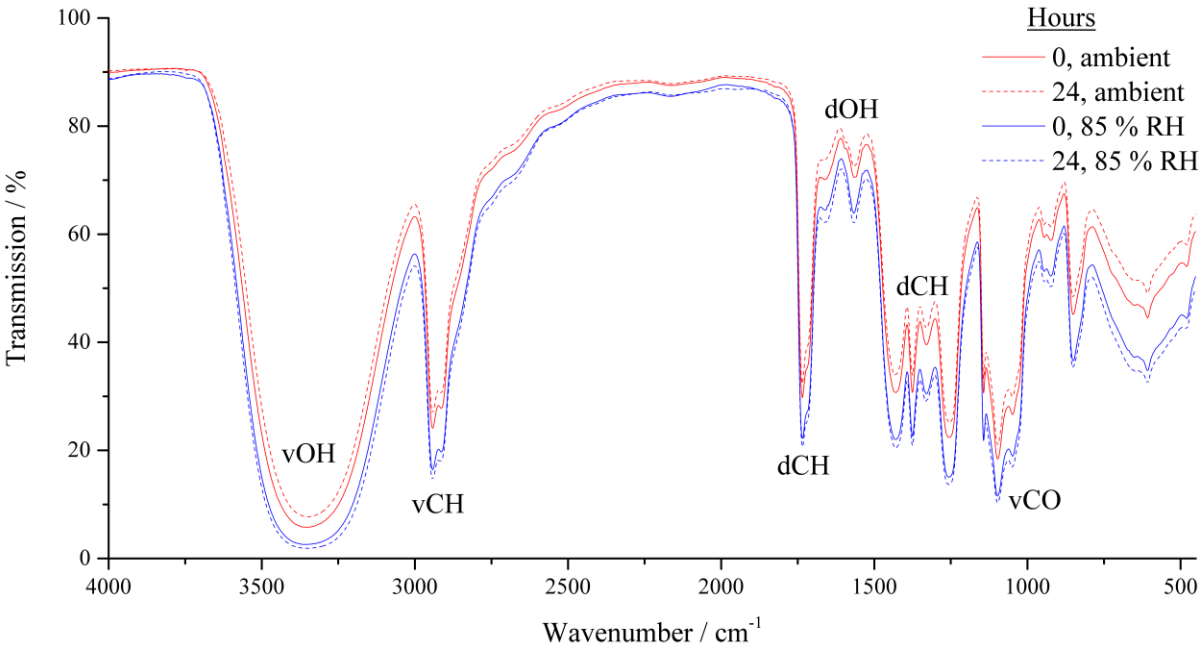

Figure 7.16. FTIR spectra of 20 w% glycerol films directly after formation (red, blue, solid) and after being subjected to overnight under standard laboratory conditions (dashed, red) or 85 %RH (dashed, blue).

From the experiments performed so far PVA films of < 15 μm have shown the ability to absorb significant quantities of water when placed in a high humidity environment. It was proposed that if films could absorb water within the space of a day, then surely they would be able to lose water at a similar rate. To test this theory all samples were subjected to two iterations of the previous experiment. Figure 7.17. and Figure 7.18. display the maximum absorbance (or minimum transmission) for the νOH and δOH bands respectively. These plots include data for 0, 10 and 20 w% glycerol where the horizontal axis is displayed as a time interval with spectra being obtained at each interval; 1 – film freshly formed (after removal from drying oven), 2 – film after placed in 85 %RH humidity cell overnight, 3 – film after being subjected to RTP overnight, 4 – film after 5 hours in 85 %RH humidity cell. Figure 7.17. and Figure 7.18. show the νOH and δOH stretch maxima respectively for the spectra taken at each time interval, the data for 0 and 10% plasticiser films are shown on a separate axis to the 20% films as the 20% film was slightly thinner than the others. As seen in Figure 7.17. each sample shows an increase in absorbance (decrease in transmission) after being placed in the humid environment overnight, regardless of plasticiser concentration. What is also apparent is that after subjecting the films to standard conditions overnight there is a reduction in absorbance in all cases, indicating a loss of water from the sample. Although the magnitude of this reduction is not equal for all films it is clear to see that the level of desorption in most cases is not quite sufficient for the film to return to its original thickness when removed from the drying oven. This implies that the films will hold a certain amount of water after absorbing it, or the rate of loss under atmospheric conditions is simply slower than the rate of absorption in these thicker films. For the final stage films were returned to the high humidity chamber for 5 hours and another spectrum was taken for each sample. An increase in thickness and hence absorption of water can be seen in all but once case, indicating that water absorption can take place even on a shortened

timescale. It would have been interesting to investigate these phenomena further but due to time restrictions with the project this simple study was as far as the line of enquiry could be taken. The next steps would have been to study surfactant containing films and how they affected the rate of absorption/desorption, as well as their effects on the H-bonding in a similar way to what was studied in solution.

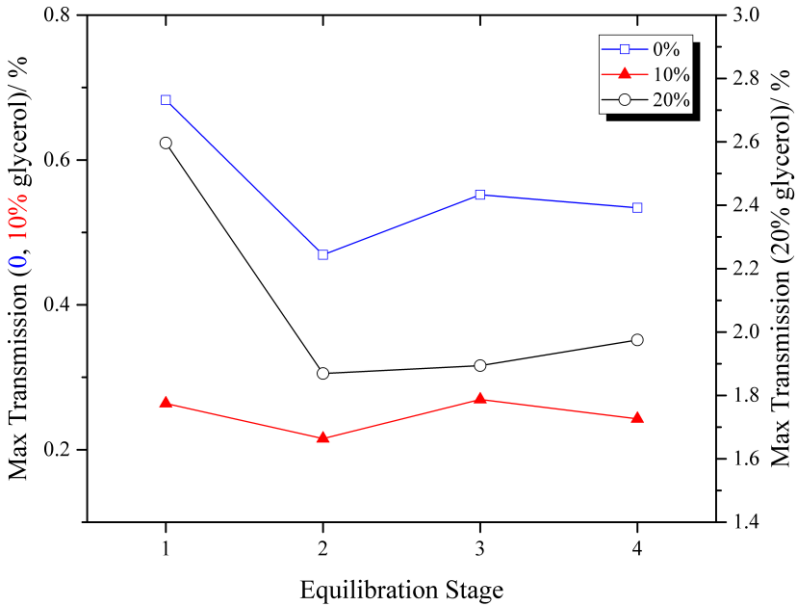

Figure 7.17. Maximum transmission values for νOH stretch obtained through FTIR of 0, 10 and 20 w% glycerol containing PVA films. Stage 1 = film freshly formed (after removal from drying oven), 2 = film after placed in 85 %RH humidity cell overnight, 3 = film after being subjected to RTP overnight, 4 = film after 5 hours in 85 %RH humidity cell.

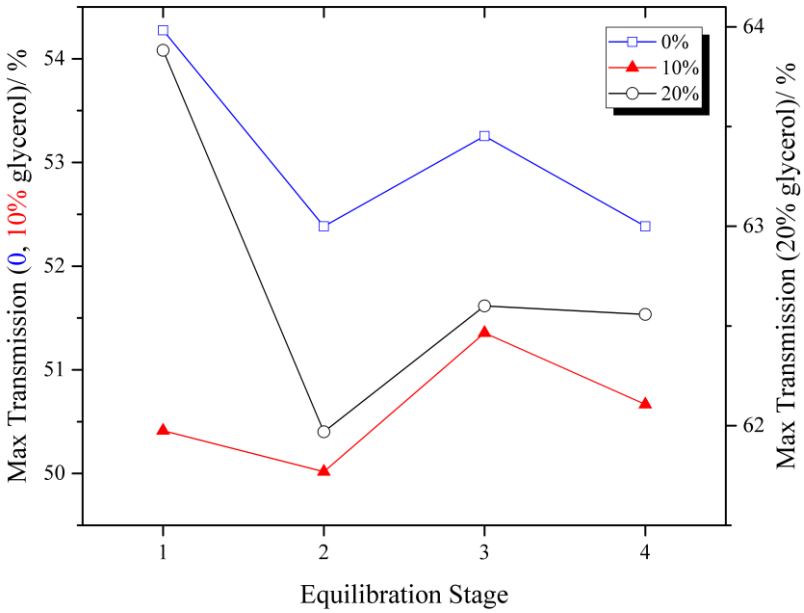

Figure 7.18. Maximum transmission values for δOH stretch obtained through FTIR of 0, 10 and 20 w% glycerol containing PVA films.

7.3. Molecular Interactions Summary

To conclude this chapter; the intermolecular hydrogen bonding within several liquid environments was probed. It was found that the addition of PVA to glycerol, water mixtures caused an increase in the H-bonding of the system, detectable primarily by a decrease in the wavenumber associated with the νOH stretching mode. It is notable that the reduction is of a greater magnitude in solutions which contain a higher water content, which indicates a greater interaction of the polymer with water compared to glycerol. This may help to explain the ability of water to absorb into PVA films and displace glycerol from its sites within the polymer. The addition of $C_{12}E_5$ to the solutions caused a decrease in the overall H-bonding of the system, again detectable primarily from the νOH stretch. This was deemed to be due to cylindrical micelle formation within the solution, which disrupts the formation of a H-bonding glycerol network. It has been suggested that micelles are also forming in thin polymer films in the previous chapters, which could again cause an unfavourable disruption of H-bonding within the system. This unfavourable disruption may lead to the significant surfactant segregation seen in polymer films. Further work in this area may help uncover more information about the complex interactions of these compounds in solution and polymer films.

8. Product Lifetime and Film Properties

A number of scientific studies have been performed throughout this work, most concerning the investigation of more fundamental reasons behind segregation and compatibility of components in polymer films. However, the industrial relevance of the results uncovered within this investigation has always been of importance and is summarised, in brief, in the following chapter. The initial work in chapter 4 highlighted some possible contributors to the failure of industrial films, where the volatility and ability of glycerol to move within and be lost from a PVA matrix was shown. For thin films, the evaporation of glycerol was shown to be significant, losing most of their plasticiser mass in around a week. The significant rate of loss and hence mobility of plasticiser in thin polymer films led to an investigation of this phenomenon in thicker industrial films. Due to the increased timescale of glycerol loss in these films the absorption of glycerol into the film was measured as opposed to the loss. It was found that the rate of absorption was significantly higher than what could be feasible for the rate of loss, so as the detergent the liquitabs encapsulate contains glycerol, the replenishment of plasticiser from the detergent should outweigh the amount capable of being lost. Therefore evaporation of glycerol should not be significant within the lifetime of the product in industrial films. Nevertheless, the phenomenally sensitive test method may be valuable to detect loss of other components, for example perfumes.

Chapter 5 highlighted the segregation behaviour of non-ionic surfactants in thin films, as well as the effects of humidity on this segregation. Surfactants were found to spontaneously segregate to both air and substrate interfaces in non-plasticised and plasticised PVA films. In non-plasticised films this segregation was found to change over time, where surfactant seemed to migrate from the substrate interface to the surface of the film, highlighting the ability of the non-ionic to move through the polymer matrix. This compliments industrial testing where compounds such as surfactants are found, migrated from the detergent, on the external surface of the industrial polymer film, present as a greasy layer. Plasticisation with glycerol was found to reduce the amount of segregated surfactant, but no level of plasticiser tested (10-30 w%) was effective at completely suppressing non-ionic segregation, therefore migration of these compounds is still definitely an issue in plasticised PVA films. This chapter also highlighted the ability of water to absorb into the films under humid conditions, and the fact that increased water content within the film could cause increased surfactant segregation. These findings perhaps provide an explanation as to why the polymer seal formed between two films on many industrial products weakens over time; if significant amounts of surfactant are migrating to the regions between polymer films then a build-up could cause decreased affinity for one PVA film to another, weakening the seal. The ability of the non-ionic surfactant to segregate also had negative effects of on plasticiser distribution, where even small concentrations of $C_{12}E_5$ (1 w%) possessed the ability to perturb the homogeneous behaviour of glycerol. The reorganisation of plasticiser may have implications on the mechanical properties of films which contain even a small amount of surfactant, as homogeneous plasticiser distribution is necessary to maintain polymer functionality for most applications. Hence any deviation from these ideal conditions may lead to plasticiser depleted regions in the polymer which would exhibit decreased elasticity. This would lead to films becoming more susceptible to cracking under strain, something that is undesirable in many industrial applications.

Plasticisation was not only shown to reduce surfactant segregation however, as Chapter 6 describes how the ionic surfactant SDS has its segregation largely increased upon introduction of glycerol. SDS was shown to form significant structures on the surface of films in the presence of a plasticiser or humid conditions. The potential for these structures to form on the surface of thicker films is apparent; if these structures are forming during the film production stage then the ability of two polymer films to inter-diffuse will be heavily impeded. While the segregation of amphiphilic molecules to PVA film surface is not desirable here, there are many other applications in polymer processing where it is. The role identified here of the plasticiser in facilitation and modifying this behaviour may be of value in other areas of polymer processing.

The effects of humidity on industrial PVA film are important in determining product lifetime. By studying the segregation behaviour of surfactants under relative humidity control in thin films, segregation was shown to increase for the non-ionics and SDS when the films became plasticised with water. As previously stated, surfactant segregation may impact product lifetime significantly, if increased humidity is amplifying the segregation behaviour of surfactants in industrial films, this may lead to shorter lifetimes. Results indicated that a lower concentration of plasticiser would cause less water to be absorbed, leading to reduced surfactant segregation. However, reducing the concentration of plasticiser would have adverse effects on the ideal polymeric properties needed for product functionality, so would be difficult to achieve whilst maintaining film efficiency. This suggests the need for a less hygroscopic plasticiser that would not absorb water as readily, but again sufficient compatibility with the polymer is required for plasticisation, hence polar groups, which usually increase the hygroscopic nature of compounds, are needed. It appears that water absorption from the atmosphere will be a persistent problem for the lifetime of PVA films in industry.

9. Final Conclusions

This project has explored new, unchartered areas of surfactant and plasticiser behaviour in thin PVA films, highlighting the segregation of several non-ionic and ionic surfactants. The industrial relevance of these findings has been discussed, but the fundamental understanding of the segregation of materials is perhaps more integral to the heart of this project. Surface energy and tension has provided an insight in to the behaviour of various surfactants in a PVA matrix, where lower SE/ST compounds have been shown to exhibit increased segregation. This concept is relatively simple in its nature as a favourable reduction in the surface energy of the system is achieved by the migration and segregation of lower SE components at the surface. $C_{12}E_x$ surfactants and SDS were shown to spontaneously segregate in binary films with PVA due to their reduced SE compared to PVA, whereas CTAB was shown to exhibit homogeneous distribution in binary films due to its higher SE.

Plasticisation of these films was shown to have mixed effects depending on the concentration of glycerol, chemical structure of the surfactant and relative humidity of the environment. Through chapters 5 and 6 several examples of the varied and intricate surfactant structures capable of forming on the surfaces of thin polymer films are given. These phenomena cannot simply be explained with SE arguments however, and compatibility must be considered. The segregation behaviour of the non-ionic surfactant $C_{12}E_5$ under ambient conditions suggests that surfactant-polymer compatibility increases upon plasticisation, thought to be due to the increased H-bonding potential exhibited by $C_{12}E_x$ surfactants compared to the other surfactants studied. The fact that this behaviour is reversed under humidity control suggests that the presence of water within the thin films reduces the non-ionic surfactant-polymer compatibility. This finding is supported by the FTIR study where addition of $C_{12}E_5$ to systems which have high water content causes a decrease in the overall H-bonding, and hence compatibility within the system.

The ionic surfactants studied also exhibited interesting behaviour, with surface segregation of CTAB being activated upon plasticisation. As the change in surface energy of the polymer is negligible when glycerol is introduced, it is deemed that compatibility between the plasticiser and surfactant must be responsible for CTAB segregation. Monitoring SDS distribution in plasticised films with NR uncovered the formation of a SDS-glycerol multi-lamella arrangement at the surface of the film, facilitated by H-bonding between the surfactant and plasticiser, which allows closer head-group packing of SDS. The ability of water to outcompete glycerol for its favourable interaction with the surfactant was also apparent from the humidity control experiments, showing how humid environments can significantly increase surfactant segregation in polymer films.

This work marks an exploration of surfactant and plasticiser behaviour in PVA films, revealing some of the varied and elaborate segregation exhibited by several surfactants in polymer matrices. It has paved the way for further investigation of these phenomena, and provides a first attempt at explaining the intricate behaviour of surfactants in solid environments. Some suggestions for how this area may be advanced are given in the following section.

10. Suggestions for Further Work

To further this study, increasing the catalogue of surfactants analysed in polymer films would allow better correlation of properties such as HLB and SE/ST to the segregation behaviour. If correlations exist between surface excess (z^*) and these properties then they would provide a series of criteria which could be consulted in order to determine if, and how much, a surfactant will segregate in a polymer film. This could be extremely useful when choosing a surfactant for industrial applications as its segregation nature could choose a surfactant which would exhibit the ideal amount of surface segregation for the role it is set to be used in.

The complex nature of the surfactant-glycerol complexes that can form on the surface of the thin films is of significant interest. It appears that the concentration of surfactant (SDS) in plasticised PVA films determines the number of surfactant lamella, and hence the thickness of the surface excess. As the maximum concentration of surfactant studied was 20 w% it would be of interest to increase the concentration of SDS further, and observe the extent to which an excess can form. The stability of multiple surfactant layers on the surface of polymer and their evolution with time would also be of interest, do they continue to grow both laterally and vertically? Can the structure slide across the surface of a film once formed? Further AFM study on the films as they develop with time and perhaps introduction of some frictional force microscopy would help to answer these questions.

More work on the molecular interactions of surfactants, polymers and plasticisers in film samples would provide a better insight in to the forces determining segregation and compatibility. Continuation of the FTIR study on film samples may have established a greater understanding of the H-bonding potential of the compounds in solid samples. It is clear from this work that there are interesting interactions occurring in the three component systems, and also in the presence of water. Study of the cloud-point of solution samples would allow phase diagrams to be produced, which may help to understand the phase separation of these compounds and hence their interactions in polymer films also.

It would also be interesting to test cases where surfactant migration to polymer surfaces is desired. Surface modification of polymers is a well-used industrial process which can be used to customise not only the appearance and finish of a polymer film, but also its adhesion, wetting and coating characteristics.[212] The functionalisation of polymer surfaces in compounds such as polypropylene (PP) normally requires significant effort. Relatively complex methods such as atmospheric pressure plasma jets[255] and chemical grafting[256] have been used. Within this work the segregation of surfactants to polymer surfaces has been shown to be related to factors such as plasticiser concentration and compatibility, and the structure of these surfactants at the surface has been precisely defined with NR. Therefore this method could be used to study surfactant segregation nature in other polymers with varying plasticisers, allowing investigation of what compounds can be used to achieve maximum surface agglomeration where it is wanted, as well as define the nanostructure of the surfactant in this region.

11. References

(1) Dobb, M. G.; Johnson, D. J.; Saville, B. P. Supramolecular structure of a high-modulus polyaromatic fiber (Kevlar 49). *J. Polym. Sci., Part B: Polym. Phys.* **1977**, *15* (12), 2201-2211.

(2) O'Brine, T.; Thompson, R. C. Degradation of plastic carrier bags in the marine environment. *Marine Poll. Bull.* **2010**, *60* (12), 2279-2283.

(3) Armstrong, R. D.; Wright, D. Polymer protective coatings—the distinction between coating porosity and the wetted metal area. *Electrochim. Acta* **1993**, *38* (14), 1799-1801.

(4) Vallittu, P. K.; Lassila, V. P.; Lappalainen, R. Transverse strength and fatigue of denture acrylic-glass fiber composite. *Dent. Mater. J.* **1994**, *10* (2), 116-121.

(5) Wilson, A. S. *Plasticisers: Selection, Applications and Implications*; Rapra Technology Limited, **1996**.

(6) Rahman, M.; Brazel, C. S. The plasticizer market: an assessment of traditional plasticizers and research trends to meet new challenges. *Prog. Polym. Sci.* **2004**, *29* (12), 1223-1248.

(7) Zaikov, G. E.; Bouchachenko, A. L.; Ivanov, V. B. *Polymer Aging at the Cutting Edge*; Nova Publishers, **2002**.

(8) Holland, B. J.; Hay, J. N. The thermal degradation of poly(vinyl alcohol). *Polym.* **2001**, *42* (16), 6775-6783.

(9) Reich, L.; Stivala, S. S. *Elements of Polymer Degradation*; McGraw-Hill, **1971**.

(10) Lim, L. Y.; Wan, L. S. C. The Effect of Plasticizers on the Properties of Polyvinyl Alcohol Films. *Drug Dev. Ind. Pharm.* **1994**, *20* (6), 1007-1020.

(11) Corti, A.; Solaro, R.; Chiellini, E. Biodegradation of poly(vinyl alcohol) in selected mixed microbial culture and relevant culture filtrate. *Polym. Degrad. Stab* **2002**, *75* (3), 447-458.

(12) Horbaschek, K.; Hoffmann, H.; Thunig, C. Formation and Properties of Lamellar Phases in Systems of Cationic Surfactants and Hydroxy-Naphthoate. *J. Colloid Interface Sci.* **1998**, *206* (2), 439-456.

(13) Yang, B.-S.; Lal, J.; Richetti, P.; Marques, C. M.; Russel, W. B.; Prud'homme, R. K. Interaction of Hydrophobically Modified Polymers and Surfactant Lamellar Phase. *Langmuir* **2001**, *17* (19), 5834-5841.

(14) Kwak, J. C. T. *Polymer-Surfactant Systems*; Taylor & Francis, **1998**.

(15) Dorn, P. B.; Salanitro, J. P.; Evans, S. H.; Kravetz, L. Assessing the aquatic hazard of some branched and linear nonionic surfactants by biodegradation and toxicity. *Environ. Toxicol. Chem.* **1993**, *12* (10), 1751-1762.

(16) DeMerlis, C. C.; Schoneker, D. R. Review of the oral toxicity of polyvinyl alcohol (PVA). *Food Chem. Toxicol.* **2003**, *41* (3), 319-326.

(17) Ghoshal, S.; Denner, P.; Stapf, S.; Mattea, C. Study of the Formation of Poly(vinyl alcohol) Films. *Macromolecules* **2012**, *45* (4), 1913-1923.

(18) Mejía, G. A. I.; López, O. B. L.; Mulet, P. A. Biodegradation of poly (vinylalcohol) with enzymatic extracts of phanerochaete chrysosporium. *Macromol. Symp.* **1999**, *148* (1), 131-147.

(19) Ma, R.; Xiong, D.; Miao, F.; Zhang, J.; Peng, Y. Novel PVP/PVA hydrogels for articular cartilage replacement. *Mater. Sci. Eng., C* **2009**, *29* (6), 1979-1983.

(20) Chaouat, M.; Le Visage, C.; Baille, W. E.; Escoubet, B.; Chaubet, F.; Mateescu, M. A.; Letourneur, D. A Novel Cross-linked Poly(vinyl alcohol) (PVA) for Vascular Grafts. *Adv. Funct. Mater.* **2008**, (18), 2855-2861.

(21) Winterton, L. C.; Lally, J. M.; Sentell, K. B.; Chapoy, L. L. The elution of poly (vinyl alcohol) from a contact lens: The realization of a time release moisturizing agent/artificial tear. *J. Biomed. Mater. Res. Part B: Appl. Biomater.* **2007**, *80B* (2), 424-432.

(22) Poole, T. R. G.; Gillespie, I. H.; Knee, G.; Whitworth, J. Microscopic fragmentation of ophthalmic surgical sponge spears used for delivery of antiproliferative agents in glaucoma filtering surgery. *Br. J. Ophthalmol.* **2002**, *12* (86), 1448-1449.

(23) Peeters, J.; Nguyen, V. S.; Müller, J.-F. Atmospheric Vinyl Alcohol to Acetaldehyde Tautomerization Revisited. *J. Phys. Chem. Lett.* **2015**, *6* (20), 4005-4011.

(24) Bouma, W. J.; Radom, L.; Rodwell, W. R. Structures and thermodynamic stabilities of the C2H4O isomers: Acetaldehyde, vinyl alcohol and ethylene oxide. *Theor. Chim. Acta 56* (2), 149-155.

(25) Mardare, D.; Matyjaszewski, K. "Living" radical polymerization of vinyl acetate. *Macromolecules* **1994**, *27* (3), 645-649.

(26) O'Donnell, J. T.; Mesrobian, R. B.; Woodward, A. E. Vinyl acetate emulsion polymerization. *J. Polym. Sci.* **1958**, *28* (116), 171-177.

(27) Nakabayashi, K.; Mori, H. Recent progress in controlled radical polymerization of N-vinyl monomers. *Eur. Polym. J.* **2013**, *49* (10), 2808-2838.

(28) Olabisi, O.; Adewale, K. *Handbook of Thermoplastics, Second Edition*; CRC Press, **2016**.

(29) Lyoo, W.; Lee, H. Synthesis of high-molecular-weight poly(vinyl alcohol) with high yield by novel one-batch suspension polymerization of vinyl acetate and saponification. *Colloid Polym. Sci. 280* (9), 835-840.
(30) Lyoo, W.; Lee, H. Synthesis of high-molecular-weight poly(vinyl alcohol) with high yield by novel one-batch suspension polymerization of vinyl acetate and saponification. *Colloid Polym. Sci.* **2002**, *280* (9), 835-840.
(31) Hassan, C. M.; Trakampan, P.; Peppas, N. A. Water Solubility Characteristics of Poly(vinyl alcohol) and Gels Prepared by Freezing/Thawing Processes. In *Water Soluble Polymers: Solutions Properties and Applications*, Amjad, Z., Ed.; Springer US: Boston, MA, **2002**, pp 31-40.
(32) Bernstein, J.; Davis, R. E.; Shimoni, L.; Chang, N.-L. Patterns in Hydrogen Bonding: Functionality and Graph Set Analysis in Crystals. *Angew. Chem. Int. Ed. (English)* **1995**, *34* (15), 1555-1573.
(33) Suresh, S. J.; Naik, V. M. Hydrogen bond thermodynamic properties of water from dielectric constant data. *J. Chem. Phys.* **2000**, *113* (21), 9727-9732.
(34) Maksyutenko, P.; Rizzo, T. R.; Boyarkin, O. V. A direct measurement of the dissociation energy of water. *J. Chem. Phys.* **2006**, *125* (18), 181101.
(35) Hassan, C.; Peppas, N. Structure and Applications of Poly(vinyl alcohol) Hydrogels Produced by Conventional Crosslinking or by Freezing/Thawing Methods. In *Biopolymers · PVA Hydrogels, Anionic Polymerisation Nanocomposites*; Springer Berlin Heidelberg, **2000**; Vol. 153, pp 37-65.
(36) Semenzim, V. L.; Basso, G. G.; da Silva, D. A.; de Vasconcellos, A.; Agreli, G.; Lima-Oliveira, A. P. M.; Kawasaki-Oyama, R. S.; Braile, D. M.; Nery, J. G. Synthesis and characterization of novel, highly crystalline poly(vinyl alcohol) microspheres for chemoembolization therapy. *J. Appl. Polym. Sci.* **2011**, *121* (3), 1417-1423.
(37) Bunn, C. W. Crystal Structure of Polyvinyl Alcohol. *Nature* **1948**, *161*, 929-930.
(38) Kwei, T. K. The effect of hydrogen bonding on the glass transition temperatures of polymer mixtures. *J. Polym. Sci., Part C: Polym. Lett.* **1984**, *22* (6), 307-313.
(39) Marten, F. L. Vinyl Alcohol Polymers. In *Kirk-Othmer Encyclopedia of Chemical Technology*; John Wiley & Sons, Inc., **2000**.
(40) Miller, R. L. Crystallographic Data and Melting Points for Various Polymers. In *The Wiley Database of Polymer Properties*; John Wiley & Sons, Inc., **2003**.
(41) Tacx, J. C. J. F.; Schoffeleers, H. M.; Brands, A. G. M.; Teuwen, L. *Polym.* **2000**, *41*, 947-957.
(42) Hassan, C. M.; Peppas, N. A. *Adv. Polym. Sci.* **2000**, *153*, 37-65.
(43) Moukwa, M.; Youn, D.; Hassanali, M. Effects of degree of polymerization of water soluble polymers on concrete properties. *Cem. Concr. Res.* **1993**, *23*, 122-130.
(44) Teraoka, I. Thermodynamics of Dilute Polymer Solutions. In *Polymer Solutions*; John Wiley & Sons, Inc., **2002**, pp 69-166.
(45) Termonia, Y.; Meakin, P.; Smith, P. Theoretical study of the influence of the molecular weight on the maximum tensile strength of polymer fibers. *Macromolecules* **1985**, *18* (11), 2246-2252.
(46) Bhattacharya, A.; Ray, P. Studies on surface tension of poly(vinyl alcohol): Effect of concentration, temperature, and addition of chaotropic agents. *J. Appl. Polym. Sci.* **2004**, *93* (1), 122-130.
(47) Frith, E. M. The interaction of plasticisers and polymers. *Trans. Faraday Soc.* **1945**, *41*, 90-101.
(48) Fox, T. G.; Flory, P. J. *J. App. Phys.* **1950**, *21*, 581-591.
(49) Kelley, F. N.; Bueche, F. Viscosity and glass temperature relations for polymer-diluent systems. *J. Polym. Sci.* **1961**, *50* (154), 549-556.
(50) Hodge, R. M.; Bastow, T. J.; Edward, G. H.; Simon, G. P.; Hill, A. J. Free Volume and the Mechanism of Plasticization in Water-Swollen Poly(vinyl alcohol). *Macromolecules* **1996**, *29* (25), 8137-8143.
(51) Pu-you, J.; Cai-ying, B.; Li-Hong, H.; Yong-hong, Z. Properties of Poly(vinyl alcohol) Plasticized by Glycerin. *J Forest Prod. Ind.* **2014**, *3* (3), 151-153.
(52) Mohsin, M.; Hossin, A.; Haik, Y. Thermal and mechanical properties of poly(vinyl alcohol) plasticized with glycerol. *J. Appl. Polym. Sci.* **2011**, *122* (5), 3102-3109.
(53) Mohsin, M.; Hossin, A.; Haik, Y. *App. Polym. Sci.* **2011**, *122*, 3102-3109.
(54) Flory, P. J. Thermodynamics of High Polymer Solutions. *J. Chem. Phys.* **1942**, *10* (1), 51-61.
(55) Huggins, M. L. THERMODYNAMIC PROPERTIES OF SOLUTIONS OF LONG-CHAIN COMPOUNDS. *Ann. N. Y. Acad. Sci.* **1942**, *43* (1), 1-32.
(56) Jiménez, A.; Peltzer, M.; Ruseckaite, R. *Poly(lactic acid) Science and Technology: Processing, Properties, Additives and Applications*; Royal Society of Chemistry, **2014**.
(57) Titow, W. V. *PVC Plastics: Properties, Processing, and Applications*; Springer Netherlands, **2012**.
(58) Earls, A. O.; Axford, I. P.; Braybrook, J. H. Gas chromatography–mass spectrometry determination of the migration of phthalate plasticisers from polyvinyl chloride toys and childcare articles. *J. Chromatogr. A* **2003**, *983* (1–2), 237-246.

(59) Scott, M. P.; Brazel, C. S.; Benton, M. G.; Mays, J. W.; Holbrey, J. D.; Rogers, R. D. Application of ionic liquids as plasticizers for poly(methyl methacrylate). *Chem. Commun.* **2002**, (13), 1370-1371.
(60) Messadi, D.; Taverdet, J. L.; Vergnaud, J. M. Plasticizer migration from plasticized poly(vinyl chloride) into liquids. Effect of several parameters on the transfer. *Ind. Eng. Chem. Prod. Res. Dev.* **1983**, *22* (1), 142-146.
(61) Lakshmi, S.; Jayakrishnan, A. Photocross-linking of dithiocarbamate-substituted PVC reduces plasticizer migration. *Polym.* **1998**, *39* (1), 151-157.
(62) Jayakrishnan, A.; Sunny, M. C. Phase transfer catalysed surface modification of plasticized poly(vinyl chloride) in aqueous media to retard plasticizer migration. *Polym.* **1996**, *37* (23), 5213-5218.
(63) Ambrogi, V.; Brostow, W.; Carfagna, C.; Pannico, M.; Persico, P. Plasticizer migration from cross-linked flexible PVC: Effects on tribology and hardness. *Polym. Eng. Sci.* **2012**, *52* (1), 211-217.
(64) Wang, R.; Wang, Q.; Li, L. Evaporation behaviour of water and its plasticizing effect in modified poly(vinyl alcohol) systems. *Polym. Int.* **2003**, *52* (12), 1820-1826.
(65) Kovacic, T.; Mrklic, Z. *Thermochim. Acta* **2002**, *381*, 49-60.
(66) Wypych, G. *Handbook of Plasticizers*; Elsevier Science, **2017**.
(67) Wypych, G. Plasticizer Diffusion Rate and the Methods of Study. *Plasticizer Motion and Diffusion* **2013**, *1*, 151-169.
(68) Wypych, G. *Handbook of Plasticizers*; ChemTec Publishing, **2004**.
(69) Yuan, W.; Hansen, A. C.; Zhang, Q. Vapor pressure and normal boiling point predictions for pure methyl esters and biodiesel fuels. *Fuel* **2005**, *84* (7–8), 943-950.
(70) Glycerol; MSDS No. 536407; [Online] Sigma-Aldrich: Gillingham, U.K. 5th Feb, 2013, http://www.sigmaaldrich.com/catalog/product/aldrich/536407?lang=en&region=GB (accessed Apr 2016).
(71) Scheibel, J. J. The evolution of anionic surfactant technology to meet the requirements of the laundry detergent industry. *J. Surfactants Deterg.* **2004**, *7* (4), 319-328.
(72) Seguin, C.; Eastoe, J.; Heenan, R. K.; Grillo, I. SANS studies of the effects of surfactant head group on aggregation properties in water/glycol and pure glycol systems. *J. Colloid Interface Sci.* **2007**, *315* (2), 714-720.
(73) Schott, H. Solubility Parameter and Hydrophilic-Lipophilic Balance of Nonionic Surfactants. *J. Pharm. Sci.* **1984**, *73* (6), 790-792.
(74) Schott, H. Hydrophilic- Lipophilic Balance, Solubility Parameter, and Oil- Water Partition Coefficient as Universal Parameters of Nonionic Surfactants. *J. Pharm. Sci.* **1995**, *84* (10), 1215-1222.
(75) Proverbio, Z. E.; Bardavid, S. M.; Arancibia, E. L.; Schulz, P. C. Hydrophile–lipophile balance and solubility parameter of cationic surfactants. *Colloids Surf., A* **2003**, *214* (1–3), 167-171.
(76) Kruglyakov, P. M. *Hydrophile - Lipophile Balance of Surfactants and Solid Particles: Physicochemical Aspects and Applications*; Elsevier Science, **2000**.
(77) Griffin, W. C. Classification of Surface-Active Agents by 'HLB'. *J. Soc. Cosmet. Chem.* **1949**, *1* (5), 311-326.
(78) Kirkwood, J. G.; Buff, F. P. The Statistical Mechanical Theory of Surface Tension. *J. Chem. Phys.* **1949**, *17* (3), 338-343.
(79) Rasing, T.; Stehlin, T.; Shen, Y. R.; Kim, M. W.; Jr., P. V. Adsorption kinetics of surfactant molecules at a liquid–air interface. *J. Chem. Phys.* **1988**, *89* (5), 3386-3387.
(80) Lin, S.-Y.; Lin, Y.-Y.; Chen, E.-M.; Hsu, C.-T.; Kwan, C.-C. A Study of the Equilibrium Surface Tension and the Critical Micelle Concentration of Mixed Surfactant Solutions. *Langmuir* **1999**, *15* (13), 4370-4376.
(81) Kim, H.-U.; Lim, K.-H. A model on the temperature dependence of critical micelle concentration. *Colloids Surf., A* **2004**, *235* (1–3), 121-128.
(82) Larson, R. G. Self- assembly of surfactant liquid crystalline phases by Monte Carlo simulation. *J. Chem. Phys.* **1989**, *91* (4), 2479-2488.
(83) Danov, K. D.; Kralchevsky, P. A.; Ananthapadmanabhan, K. P. Micelle–monomer equilibria in solutions of ionic surfactants and in ionic–nonionic mixtures: A generalized phase separation model. *Adv. Colloid Interface Sci.* **2014**, *206*, 17-45.
(84) Nagarajan, R.; Ruckenstein, E. Theory of surfactant self-assembly: a predictive molecular thermodynamic approach. *Langmuir* **1991**, *7* (12), 2934-2969.
(85) Chowdhury, M.; Kataky, R. Emulsification at the Liquid/Liquid Interface: Effects of Potential, Electrolytes and Surfactants. *ChemPhysChem* **2016**, *17* (1), 105-111.
(86) Friberg, S.; Jansson, P. O.; Cederberg, E. Surfactant association structure and emulsion stability. *J. Colloid Interface Sci.* **1976**, *55* (3), 614-623.
(87) Asahi, M.; Shirakawa, N.; Kikuta, Y. Water-in-oil emulsion cosmetic. Google Patents, 1991.
(88) Hansen, C. M. The three dimensional solubility parameter. *Danish Technical: Copenhagen* **1967**, 14.

(89) Hansen, C. M. Polymer additives and solubility parameters. *Prog. Org. Coat.* **2004**, *51* (2), 109-112.
(90) Jiang, X.; Tan, B.; Zhang, X.; Ye, D.; Dai, H.; Zhang, X. Studies on the properties of poly(vinyl alcohol) film plasticized by urea/ethanolamine mixture. *J. Appl. Polym. Sci.* **2012**, *125* (1), 697-703.
(91) Yokota, M.; Maibach, H. I. Moisturizer effect on Irritant Dermatitis: an overview. *Contact Derm.* **2006**, *55* (2), 65-72.
(92) Barton, A. F. M. *Handbook of Solubility Parameters*; CRC Press, **1983**.
(93) Young, J. F. Humidity control in the laboratory using salt solutions—a review. *J. Appl. Chem.* **1967**, *17* (9), 241-245.
(94) Rademann, K. P. W. Atkins: Physical Chemistry, 4th Edition, Oxford University Press. *Ber. Bunsenges. Phys. Chem.* **1990**, *94* (10), 1171-1171.
(95) Wexler, A.; Hasegawa, S. Relative humidity-temperature relationships of some saturated salt solutions in the temperature range 0 to 50C. *J. Res. Natl. Stand.* **1954**, *53* (1), 19-26.
(96) Gordon, R. G. Molecular Motion in Infrared and Raman Spectra. *J. Chem. Phys.* **1965**, *43* (4), 1307-1312.
(97) Snyder, R. G.; Hsu, S. L.; Krimm, S. Vibrational spectra in the C□H stretching region and the structure of the polymethylene chain. *Spectrochim. Acta Mol. Biomol. Spectrosc.* **1978**, *34* (4), 395-406.
(98) Shimanouchi, T. Tables of Molecular Vibrational Frequencies Part 5. *J. Phys. Chem. Ref. Data* **1972**, *1* (1), 189-216.
(99) Stuart, B. Infrared Spectroscopy. In *Kirk-Othmer Encyclopedia of Chemical Technology*; John Wiley & Sons, Inc., **2000**.
(100) Colthup, N. *Introduction to Infrared and Raman Spectroscopy*; Elsevier Science, **2012**.
(101) Jorgensen, W. L.; Maxwell, D. S.; Tirado-Rives, J. Development and Testing of the OPLS All-Atom Force Field on Conformational Energetics and Properties of Organic Liquids. *J. Am. Chem. Soc.* **1996**, *118* (45), 11225-11236.
(102) Shim, S.-H.; Gupta, R.; Ling, Y. L.; Strasfeld, D. B.; Raleigh, D. P.; Zanni, M. T. Two-dimensional IR spectroscopy and isotope labeling defines the pathway of amyloid formation with residue-specific resolution. *Proc. Natl. Acad. Sci. U.S.A.* **2009**, *106* (16), 6614-6619.
(103) Muhamadali, H.; Chisanga, M.; Subaihi, A.; Goodacre, R. Combining Raman and FT-IR Spectroscopy with Quantitative Isotopic Labeling for Differentiation of E. coli Cells at Community and Single Cell Levels. *Anal. Chem.* **2015**, *87* (8), 4578-4586.
(104) Middleton, C. T.; Marek, P.; Cao, P.; Chiu, C.-c.; Singh, S.; Woys, A. M.; de Pablo, J. J.; Raleigh, D. P.; Zanni, M. T. Two-dimensional infrared spectroscopy reveals the complex behaviour of an amyloid fibril inhibitor. *Nat Chem* **2012**, *4* (5), 355-360.
(105) Smith, B. C. *Infrared Spectral Interpretation: A Systematic Approach*; Taylor & Francis, **1998**.
(106) Stockton, W. B.; Rubner, M. F. Molecular-Level Processing of Conjugated Polymers. 4. Layer-by-Layer Manipulation of Polyaniline via Hydrogen-Bonding Interactions. *Macromolecules* **1997**, *30* (9), 2717-2725.
(107) Scatena, L. F.; Brown, M. G.; Richmond, G. L. Water at Hydrophobic Surfaces: Weak Hydrogen Bonding and Strong Orientation Effects. *Science* **2001**, *292* (5518), 908-912.
(108) Stuart, A. V.; Sutherland, G. B. B. M. Effect of Hydrogen Bonding on the Deformation Frequencies of the Hydroxyl Group in Alcohols. *J. Chem. Phys.* **1956**, *24* (3), 559-570.
(109) Joseph, J.; Jemmis, E. D. Red-, Blue-, or No-Shift in Hydrogen Bonds: A Unified Explanation. *J. Am. Chem. Soc.* **2007**, *129* (15), 4620-4632.
(110) F. Courchay, P. G., Personal communication, 2013.
(111) Dix, L. R.; Gilblas, R. Lyotropic and interfacial behaviour of an anionic gemini surfactant. *J. Colloid Interface Sci.* **2006**, *296* (2), 762-765.
(112) Jeynes, C.; Colaux, J. L. Thin film depth profiling by ion beam analysis. *Analyst* **2016**, *141* (21), 5944-5985.
(113) Jeynes, C. Ion Beam Analysis: A Century of Exploiting the Electronic and Nuclear Structure of the Atom for Materials Characterisation. *Rev. Accel. Sci. Tech.* **2011**, *04* (01), 41-82.
(114) Zhou, X.-L.; Chen, S.-H. Theoretical foundation of X-ray and neutron reflectometry. *Phys. Rep.* **1995**, *257* (4), 223-348.
(115) Bailey, M. J.; Jeynes, C. Characterisation of gunshot residue particles using self-consistent ion beam analysis. *Nucl. Instr. Meth. Phys. Res. B* **2009**, *267* (12–13), 2265-2268.
(116) Demortier, G. Ion beam analysis of gold jewelry. *Nucl. Instr. Meth. Phys. Res. B* **1992**, *64* (1), 481-487.
(117) Livingston, R. A.; Schweitzer, J. S.; Rolfs, C.; Becker, H. W.; Kubsky, S.; Spillane, T.; Zickefoose, J.; Castellote, M.; de Viedma, P. G.; Cheung, J. Heavy ion beam measurement of the hydration of cementitious materials. *Appl. Radiat. Isot.* **2010**, *68* (4–5), 683-687.

(118) Dran, J.-C.; Salomon, J.; Calligaro, T.; Walter, P. Ion beam analysis of art works: 14 years of use in the Louvre. *Nucl. Instr. Meth. Phys. Res. B* **2004**, *219–220*, 7-15.

(119) Paul, H. Nuclear stopping power and its impact on the determination of electronic stopping power. *AIP Conf. Proc.* **2013**, *1525* (1), 309-313.

(120) Ziegler, J. F.; Biersack, J. P. The Stopping and Range of Ions in Matter. In *Treatise on Heavy-Ion Science: Volume 6: Astrophysics, Chemistry, and Condensed Matter*, Bromley, D. A., Ed.; Springer US: Boston, MA, **1985**, pp 93-129.

(121) Ziegler, J. F.; Ziegler, M. D.; Biersack, J. P. SRIM – The stopping and range of ions in matter (2010). *Nucl. Instr. Meth. Phys. Res. B* **2010**, *268* (11–12), 1818-1823.

(122) Jeynes, C.; Bailey, M. J.; Bright, N. J.; Christopher, M. E.; Grime, G. W.; Jones, B. N.; Palitsin, V. V.; Webb, R. P. "Total IBA" – Where are we? *Nucl. Instr. Meth. Phys. Res. B* **2012**, *271*, 107-118.

(123) Patel, N. J.; Britton, G.; Goodwin, T. W. Use of deuterium labelling from deuterium oxide to demonstrate carotenoid transformations in photosynthetic bacteria. *Biochim. Biophys. Acta - Gen. Subj.* **1983**, *760* (1), 92-96.

(124) Composto, R. J.; Walters, R. M.; Genzer, J. Application of ion scattering techniques to characterize polymer surfaces and interfaces. *Mater. Sci. Eng. R-Rep.* **2002**, *38*, 107-180.

(125) Wang, Y. Q.; Burward-Hoy, J. M.; Tesmer, J. R. Production of high energy and low flux protons using 2D(3He,p)4He for space detector calibrations. *Nucl. Instr. Meth. Phys. Res. B* **2014**, *332*, 432-438.

(126) Livengood, R.; Tan, S.; Greenzweig, Y.; Notte, J.; McVey, S. Subsurface damage from helium ions as a function of dose, beam energy, and dose rate. *J. Vac. Sci. Technol. B Microelectron. Nanometer Struct. Process. Meas. Phenom.* **2009**, *27* (6), 3244-3249.

(127) Kaneko, T.; Watamori, M.; Makita, H.; Araujo, C.; Kano, G. Damage evaluation after ion beam irradiation on polyimide films using ERD and RBS techniques simultaneously. *Nucl. Instr. Meth. Phys. Res. B* **2004**, *219–220*, 236-240.

(128) Abel, F.; Quillet, V.; Schott, M. Degradation of polystyrene thin films under d, 4He and 12C irradiation studied by ion beam analysis: effects of energy loss, sample thickness and isotopic content. *Nucl. Instr. Meth. Phys. Res. B* **1995**, *105* (1), 86-90.

(129) Wong, K. K. H.; Hutter, J. L.; Zinke-Allmang, M.; Wan, W. Physical properties of ion beam treated electrospun poly(vinyl alcohol) nanofibers. *Eur. Polym. J.* **2009**, *45* (5), 1349-1358.

(130) Benzeggouta, D.; Vickridge, I. Handbook on Best Practice for Minimising Beam Induced Damage during IBA. *Spirit Damage Handbook* **2011**, *1* (1), 1-51.

(131) Webster, J.; Holt, S.; Dalgliesh, R. INTER the chemical interfaces reflectometer on target station 2 at ISIS. *Physica B Condens. Matter.* **2006**, *385–386, Part 2*, 1164-1166.

(132) Lee, E. M.; Thomas, R. K.; Cummins, P. G.; Staples, E. J.; Penfold, J.; Rennie, A. R. Determination of the structure of a surfactant layer adsorbed at the silica/water interface by neutron reflection. *Chem. Phys. Lett.* **1989**, *162* (3), 196-202.

(133) Anastasiadis, S. H.; Russell, T. P.; Satija, S. K.; Majkrzak, C. F. The morphology of symmetric diblock copolymers as revealed by neutron reflectivity. *J. Chem. Phys.* **1990**, *92* (9), 5677-5691.

(134) Hillborg, H.; Ankner, J. F.; Gedde, U. W.; Smith, G. D.; Yasuda, H. K.; Wikström, K. Crosslinked polydimethylsiloxane exposed to oxygen plasma studied by neutron reflectometry and other surface specific techniques. *Polym.* **2000**, *41* (18), 6851-6863.

(135) Sears, V. F. Neutron scattering lengths and cross sections. *Neutron News* **1992**, *3* (3), 26-37.

(136) Barradas, N. P.; Jeynes, C.; Webb, R. P. Simulated annealing analysis of Rutherford backscattering data. *Appl. Phys. Lett.* **1997**, *71* (2), 291-293.

(137) Möller, W.; Besenbacher, F. A note on the 3He + D nuclear-reaction cross section. *Nucl. Instr. Meth. Phys. Res. A* **1980**, *168* (1–3), 111-114.

(138) Bucknall, D. G.; Butler, S. A.; Higgins, J. S. Studying Polymer Interfaces Using Neutron Reflection. In *Scattering from Polymers*; American Chemical Society, **1999**; Vol. 739, pp 57-73.

(139) James, C. D.; Jeynes, C.; Barradas, N. P.; Clifton, L.; Dalgliesh, R. M.; Smith, R. F.; Sankey, S. W.; Hutchings, L. R.; Thompson, R. L. Modifying polyester surfaces with incompatible polymer additives. *React. Funct. Polym.* **2015**, *89*, 40-48.

(140) Hardman, S. J.; Hutchings, L. R.; Clarke, N.; Kimani, S. M.; Mears, L. L. E.; Smith, E. F.; Webster, J. R. P.; Thompson, R. L. Surface Modification of Polyethylene with Multi-End-Functional Polyethylene Additives. *Langmuir* **2012**, *28* (11), 5125-5137.

(141) Poly(vinyl alcohol); MSDS No. P8136; [Online] Sigma-Aldrich: Gillingham, U.K. 20th Jan, 2015, http://www.sigmaaldrich.com/catalog/product/sial/p8136?lang=en&region=GB (accessed Apr 2016).

(142) Silicon; MSDS No. 343250; [Online] Sigma-Aldrich: Gillingham, U.K. 8th Apr, 2013, http://www.sigmaaldrich.com/catalog/product/aldrich/343250?lang=en&region=GB (accessed Apr 2016).

(143) Silicon dioxide; MSDS No. 31623; [Online] Sigma-Aldrich: Gillingham, U.K. 2nd Dec 2015, http://www.sigmaaldrich.com/catalog/product/supelco/31623?lang=en&region=GB (accessed Apr 2016).
(144) Glycerol-1,1,2,3,3-d_5; MSDS No. 454524; [Online] Sigma-Aldrich: Gillingham, U.K. 3rd Jan, 2015, http://www.sigmaaldrich.com/catalog/product/aldrich/454524?lang=en&region=GB (accessed Apr 2016).
(145) Pentaethylene glycol monododecyl ether; MSDS No. P8550; [Online] Sigma-Aldrich: Gillingham, U.K. 22nd Feb, 2013, http://www.sigmaaldrich.com/catalog/product/sigma/p8550?lang=en&region=GB (accessed Apr 2016).
(146) Hammouda, B. Temperature Effect on the Nanostructure of SDS Micelles in Water. *J. Res. Natl. Inst. Stand. Technol.* **2013**, *118*, 151-167.
(147) Mehendia, S.; Tomar, A. K.; Goyal, P. K.; Kumar, S. Tuning of refractive index of poly(vinyl alcohol): Effect of embedding Cu and Ag nanoparticles. *J. App. Phys.* **2013**, *113* (7).
(148) Mielenz, K. D.; Nefflen, K. F.; Rowley, W. R. C.; Wilson, D. C.; Engelhard, E. Reproducibility of Helium–Neon Laser Wavelengths at 633 nm. *Appl. Opt.* **1968**, *7* (2), 289-293.
(149) Rezende, C. A.; Lee, L.-T.; Galembeck, F. Surface Mechanical Properties of Thin Polymer Films Investigated by AFM in Pulsed Force Mode. *Langmuir* **2009**, *25* (17), 9938-9946.
(150) Passeri, D.; Rossi, M.; Tamburri, E.; Terranova, M. L. Mechanical characterization of polymeric thin films by atomic force microscopy based techniques. *Anal. Bioanal. Chem.* **2013**, *405* (5), 1463-1478.
(151) Burgos, P.; Zhang, Z.; Golestanian, R.; Leggett, G. J.; Geoghegan, M. Directed Single Molecule Diffusion Triggered by Surface Energy Gradients. *ACS Nano* **2009**, *3* (10), 3235-3243.
(152) Busuttil, K.; Nikogeorgos, N.; Zhang, Z.; Geoghegan, M.; Hunter, C. A.; Leggett, G. J. The mechanics of nanometre-scale molecular contacts. *Farad. Discuss.* **2012**, *156* (0), 325-341.
(153) Kaur, I.; Zhao, X.; Bryce, M. R.; Schauer, P. A.; Low, P. J.; Kataky, R. Modification of Electrode Surfaces by Self-Assembled Monolayers of Thiol-Terminated Oligo(Phenyleneethynylene)s. *ChemPhysChem* **2013**, *14* (2), 431-440.
(154) Gadelmawla, E. S.; Koura, M. M.; Maksoud, T. M. A.; Elewa, I. M.; Soliman, H. H. Roughness parameters. *J. Mater. Process. Technol.* **2002**, *123* (1), 133-145.
(155) Robertson, J. A. Plasticized polyvinyl alcohol composition. Google Patents, 1960.
(156) Sonenstein, G. G. Water soluble films of polyvinyl alcohol and polyacrylic acid and packages comprising same. Google Patents, 1987.
(157) Hedenqvist, M.; Gedde, U. W. Diffusion of small-molecule penetrants in semicrystalline polymers. *Prog Polym Sci.* **1996**, *21* (2), 299-333.
(158) Siracusa, V. Food Packaging Permeability Behaviour: A Report. *Int. J. Polym. Sci.* **2012**, *2012*, 11.
(159) Payne, R. S.; Clough, A. S.; Murphy, P.; Mills, P. J. Use of the D(3He,p)4He reaction to study polymer diffusion in polymer melts. *Nucl. Instr. Meth. Phys. Res. B* **1989**, *42*, 130-134.
(160) Alfassi, Z. B. *Instrumental Multi-Element Chemical Analysis*; Springer Netherlands, **2012**.
(161) Altenhofen da Silva, M.; Adeodato Vieira, M. G.; Gomes Maçumoto, A. C.; Beppu, M. M. Polyvinylchloride (PVC) and natural rubber films plasticized with a natural polymeric plasticizer obtained through polyesterification of rice fatty acid. *Polym. Test.* **2011**, *30* (5), 478-484.
(162) Vieira, M. G. A.; da Silva, M. A.; dos Santos, L. O.; Beppu, M. M. Natural-based plasticizers and biopolymer films: A review. *Eur. Polym. J.* **2011**, *47* (3), 254-263.
(163) Jańczak, W.; Tadych, G. Influence of exudation on the properties of PVC plasticized with blends of phthalate and chlorinated paraffin. *Colloid Polym. Sci.* **1984**, *262* (2), 122-126.
(164) Kennedy, S. P. Liquid laundry detergent in water-soluble package. Google Patents, 1990.
(165) Intelligence, A. M. *Market Report: Global Surfactant Market* [Online]; 4th ed; 2016.
(166) Schick, M. J. *Nonionic Surfactants: Physical Chemistry*; Taylor & Francis, **1987**.
(167) Falbe, J. *Surfactants in Consumer Products: Theory, Technology and Application*; Springer Berlin Heidelberg, **2012**.
(168) Eccleston, G. M. Multiple-phase oil-in-water emulsions. *J. Soc. Cosmet. Chem.* **1990**, *41*, 1-22.
(169) Schmolka, I. R. High foaming liquid shampoo composition. Google Patents, 1984.
(170) Briddick, A.; Li, P.; Hughes, A.; Courchay, F.; Martinez, A.; Thompson, R. L. Surfactant and Plasticizer Segregation in Thin Poly(vinyl alcohol) Films. *Langmuir* **2016**, *32* (3), 864-872.
(171) Lu, J. R.; Li, Z. X.; Thomas, R. K.; Binks, B. P.; Crichton, D.; Fletcher, P. D. I.; McNab, J. R.; Penfold, J. The Structure of Monododecyl Pentaethylene Glycol Monolayers with and without Added Dodecane at the Air/Solution Interface: A Neutron Reflection Study. *J. Phys. Chem. B* **1998**, *102* (30), 5785-5793.
(172) Lu, J. R.; Hromadova, M.; Thomas, R. K.; Penfold, J. Neutron reflection from triethylene glycol monododecyl ether adsorbed at the air-liquid interface: the variation of the hydrocarbon chain distribution with surface concentration. *Langmuir* **1993**, *9* (9), 2417-2425.

(173) Szymczyk, K.; Jańczuk, B. The adsorption at solution–air interface and volumetric properties of mixtures of cationic and nonionic surfactants. *Colloids Surf., A* **2007**, *293* (1–3), 39-50.
(174) Wu, S. Estimation of the critical surface tension for polymers from molecular constitution by a modified Hildebrand-Scott equation. *J. Phys. Chem.* **1968**, *72*, 3332.
(175) Polmanteer, K. E. Current perspectives on silicone rubber technology. *Rubber Chem. and Tech.* **1981**, *54* (5), 1051-1080.
(176) Lee, L. H. Relationships between surface wettability and glass temperatures of high polymers. *J. Appl. Polym. Sci.* **1968**, *12*, 719.
(177) van Oss, C. J.; Chaudhury, M. K.; Good, R. J. Monopolar surfaces. *Adv. Colloid Interface Sci.* **1987**, *28*, 35-64.
(178) Hoftyzer, P. J.; van Krevelen, D. W. The newtonian shear viscosity of concentrated polymer solutions. *Angew. Makromol. Chem.* **1976**, *56* (1), 1-14.
(179) Zuo, B.; Hu, Y.; Lu, X.; Zhang, S.; Fan, H.; Wang, X. Surface Properties of Poly(vinyl alcohol) Films Dominated by Spontaneous Adsorption of Ethanol and Governed by Hydrogen Bonding. *J. Phys. Chem. C* **2013**, *117* (7), 3396-3406.
(180) Sauer, B. B.; Dee, G. T. Molecular Weight and Temperature Dependence of Polymer Surface Tension: Comparison of Experiment with Theory *Macromol.* **1991**, *24* (8), 2124-2126.
(181) Chee, K. K. Molecular weight dependence of surface tension of polystyrene as studied by the corresponding states principle. *J. Appl. Polym. Sci.* **1998**, *70* (4), 697-703.
(182) Moreira, J. C.; Demarquette, N. R. Influence of temperature, molecular weight, and molecular weight dispersity on the surface tension of PS, PP, and PE. I. Experimental. *J. Appl. Polym. Sci.* **2001**, *82* (8), 1907-1920.
(183) Kjellin, U. R. M.; Claesson, P. M.; Linse, P. Surface Properties of Tetra(ethylene oxide) Dodecyl Amide Compared with Poly(ethylene oxide) Surfactants. 1. Effect of the Headgroup on Adsorption. *Langmuir* **2002**, *18* (18), 6745-6753.
(184) Zosel, A. Adhesion and tack of polymers: Influence of mechanical properties and surface tensions. *Colloid Polym. Sci.* **1985**, *263* (7), 541-553.
(185) Tiberg, F.; Joensson, B.; Tang, J.-a.; Lindman, B. Ellipsometry Studies of the Self-Assembly of Nonionic Surfactants at the Silica-Water Interface: Equilibrium Aspects. *Langmuir* **1994**, *10* (7), 2294-2300.
(186) Hexaethylene glycol monododecyl ether; MSDS No. SC-252881; [Online] Santa Cruz Biotechnology: Dallas, U.S. 20th Apr 2015, http://www.scbt.com/datasheet-252881-hexaethylene-glycol-monododecyl-ether.html (accessed May 2016).
(187) Patrick, H. N.; Warr, G. G.; Manne, S.; Aksay, I. A. Self-Assembly Structures of Nonionic Surfactants at Graphite/Solution Interfaces. *Langmuir* **1997**, *13* (16), 4349-4356.
(188) Srinivas, G.; Nielsen, S. O.; Moore, P. B.; Klein, M. L. Molecular Dynamics Simulations of Surfactant Self-Organization at a Solid−Liquid Interface. *J. Am. Chem. Soc.* **2006**, *128* (3), 848-853.
(189) Russell, T. P.; Coulon, G.; Deline, V. R.; Miller, D. C. Characteristics of the surface-induced orientation for symmetric diblock PS/PMMA copolymers. *Macromolecules* **1989**, *22* (12), 4600-4606.
(190) Greenspan, L. Humidity Fixed Points of Binary Saturated Aqueous Solutions. *J. Res. Natl. Bur. Stand. Sec. A* **1977**, *81A* (1), 89-96.
(191) Liao, Y.-C.; Subramani, H. J.; Franses, E. I.; Basaran, O. A. Effects of Soluble Surfactants on the Deformation and Breakup of Stretching Liquid Bridges. *Langmuir* **2004**, *20* (23), 9926-9930.
(192) Zhu, J.; Han, Y.; Kumar, R.; He, Y.; Hong, K.; Bonnesen, P. V.; Sumpter, B. G.; Smith, S. C.; Smith, G. S.; Ivanov, I. N.; Do, C. Controlling molecular ordering in solution-state conjugated polymers. *Nanoscale* **2015**, *7* (37), 15134-15141.
(193) Persson, C. M. Surfactants at Non-Polar Surfaces. Doctoral Thesis, Royal Institute of Technology2002.
(194) Wijaya, E. C.; Separovic, F.; Drummond, C. J.; Greaves, T. L. Micelle formation of a non-ionic surfactant in non-aqueous molecular solvents and protic ionic liquids (PILs). *Phys. Chem. Chem. Phys.* **2016**, *18* (35), 24377-24386.
(195) Patel, T.; Ghosh, G.; Aswal, V.; Bahadur, P. Micellization of sodium dodecyl sulfate and polyoxyethylene dodecyl ethers in solution. *Colloid Polym. Sci.* **2009**, *287* (10), 1175-1181.
(196) Wakeham, D.; Niga, P.; Warr, G. G.; Rutland, M. W.; Atkin, R. Nonionic Surfactant Adsorption at the Ethylammonium Nitrate Surface: A Neutron Reflectivity and Vibrational Sum Frequency Spectroscopy Study. *Langmuir* **2010**, *26* (11), 8313-8318.
(197) Nelson, P. H.; Rutledge, G. C.; Hatton, T. A. On the size and shape of self-assembled micelles. *J. Chem. Phys.* **1997**, *107* (24), 10777-10781.
(198) Menge, U.; Lang, P.; Findenegg, G. H.; Strunz, P. Structural Transition of Oil-Swollen Cylindrical Micelles of C12E5 in Water Studied by SANS. *J. Phys. Chem. B* **2003**, *107* (6), 1316-1320.

(199) Bergstrom, L. M.; Grillo, I. Correlation between the geometrical shape and growth behaviour of surfactant micelles investigated with small-angle neutron scattering. *Soft Matter* **2014**, *10* (46), 9362-9372.
(200) Murray, M.; Thompson, W. F. Rapid isolation of high molecular weight plant DNA. *Nucleic Acids Res.* **1980**, *8* (19), 4321-4326.
(201) Sau, T. K.; Murphy, C. J. Room Temperature, High-Yield Synthesis of Multiple Shapes of Gold Nanoparticles in Aqueous Solution. *J. Am. Chem. Soc.* **2004**, *126* (28), 8648-8649.
(202) Im, S. H.; Jeong, Y. H.; Ryoo, J. J. Simultaneous analysis of anionic, amphoteric, nonionic and cationic surfactant mixtures in shampoo and hair conditioner by RP-HPLC/ELSD and LC/MS. *Anal. Chim. Acta* **2008**, *619* (1), 129-136.
(203) Liu, T.-X.; Stansly, P. A. Insecticidal activity of surfactants and oils against silverleaf whitefly (Bemisia argentifolii) nymphs (Homoptera: Aleyrodidae) on collards and tomato. *Pest Manag. Sci.* **2000**, *56* (10), 861-866.
(204) Neugebauer, J. M. [18] Detergents: An overview. In *Methods in Enzymology*, Murray, P. D., Ed.; Academic Press, **1990**; Vol. Volume 182, pp 239-253.
(205) Rosen, M. J.; Kunjappu, J. T. *Surfactants and Interfacial Phenomena*; Wiley, **2012**.
(206) Rubingh, D. *Cationic Surfactants: Physical Chemistry*; Taylor & Francis, **1990**.
(207) Porebski, S.; Bailey, L. G.; Baum, B. R. Modification of a CTAB DNA extraction protocol for plants containing high polysaccharide and polyphenol components. *Plant Mol. Biol. Report.* **1997**, *15* (1), 8-15.
(208) Sun, X. M.; Chen, X.; Deng, Z. X.; Li, Y. D. A CTAB-assisted hydrothermal orientation growth of ZnO nanorods. *Mater. Chem. Phys* **2003**, *78* (1), 99-104.
(209) Yatcilla, M. T.; Herrington, K. L.; Brasher, L. L.; Kaler, E. W.; Chiruvolu, S.; Zasadzinski, J. A. Phase Behavior of Aqueous Mixtures of Cetyltrimethylammonium Bromide (CTAB) and Sodium Octyl Sulfate (SOS). *J. Phys. Chem. A* **1996**, *100* (14), 5874-5879.
(210) Besson, S.; Gacoin, T.; Ricolleau, C.; Jacquiod, C.; Boilot, J.-P. Phase diagram for mesoporous CTAB-silica films prepared under dynamic conditions. *J. Mater. Chem.* **2003**, *13* (2), 404-409.
(211) Adamczyk, Z.; Para, G.; Warszyński, P. Influence of Ionic Strength on Surface Tension of Cetyltrimethylammonium Bromide. *Langmuir* **1999**, *15* (24), 8383-8387.
(212) Torstensson, M.; Hult, A. Surface modification of polymers using surfactant monomers. *Polym. Bull.* **1992**, *29* (5), 549-556.
(213) Wilkes, C. E.; Summers, J. W.; Daniels, C. A.; Berard, M. T. *PVC Handbook*; Hanser, **2005**.
(214) Schägger, H.; Von Jagow, G. Tricine-sodium dodecyl sulfate-polyacrylamide gel electrophoresis for the separation of proteins in the range from 1 to 100 kDa. *Anal. Biochem.* **1987**, *166* (2), 368-379.
(215) Burnette, W. N. "Western blotting": electrophoretic transfer of proteins from sodium dodecyl sulfate-polyacrylamide gels to unmodified nitrocellulose and radiographic detection with antibody and radioiodinated protein A. *Anal. Biochem.* **1981**, *112* (2), 195-203.
(216) Cleveland, D. W.; Fischer, S. G.; Kirschner, M. W.; Laemmli, U. K. Peptide mapping by limited proteolysis in sodium dodecyl sulfate and analysis by gel electrophoresis. *J. Biol. Chem.* **1977**, *252* (3), 1102-1106.
(217) Zhang, J.; Zhang, J. Study on the interaction of alkaline protease with main surfactants in detergent. *Colloid Polym. Sci.* **2016**, *294* (2), 247-255.
(218) Rhim, J. W.; Gennadios, A.; Weller, C. L.; Hanna, M. A. Sodium dodecyl sulfate treatment improves properties of cast films from soy protein isolate. *Ind. Crops Prod.* **2002**, *15* (3), 199-205.
(219) Banik, R. M.; Prakash, M. Laundry detergent compatibility of the alkaline protease from Bacillus cereus. *Microbiol. Res.* **2004**, *159* (2), 135-140.
(220) Mysels, K. J. Surface tension of solutions of pure sodium dodecyl sulfate. *Langmuir* **1986**, *2* (4), 423-428.
(221) Hernáinz, F.; Caro, A. Variation of surface tension in aqueous solutions of sodium dodecyl sulfate in the flotation bath. *Colloids Surf., A* **2002**, *196* (1), 19-24.
(222) Sammalkorpi, M.; Karttunen, M.; Haataja, M. Ionic Surfactant Aggregates in Saline Solutions: Sodium Dodecyl Sulfate (SDS) in the Presence of Excess Sodium Chloride (NaCl) or Calcium Chloride (CaCl2). *J. Phys. Chem. B* **2009**, *113* (17), 5863-5870.
(223) Bernardes, J. S.; Rezende, C. A.; Galembeck, F. Morphology and Self-Arraying of SDS and DTAB Dried on Mica Surface. *Langmuir* **2010**, *26* (11), 7824-7832.
(224) Coiro, V. M.; Manigrasso, M.; Mazza, F.; Pochetti, G. Structure of a triclinic phase of sodium dodecyl sulfate monohydrate. A comparison with other sodium dodecyl sulfate crystal phases. *Acta Crystallogr., Sect. C: Cryst. Struct. Commun.* **1987**, *43* (5), 850-854.
(225) Sein, A.; Engberts, J. B. F. N. Micelle to Lamellar Aggregate Transition of an Anionic Surfactant in Dilute Aqueous Solution Induced by Alkali Metal Chloride and Tetraalkylammonium Chloride Salts. *Langmuir* **1995**, *11* (2), 455-465.

(226) Kiyosawa, K. Volumetric properties of polyols (ethylene glycol, glycerol, meso-erythritol, xylitol and mannitol) in relation to their membrane permeability: Group additivity and estimation of the maximum radius of their molecules. *Biochim. Biophys. Acta - Biomem.* **1991**, *1064* (2), 251-255.

(227) Sodium dodecyl sulfate; MSDS No. 436143; [Online] Sigma-Aldrich: Gillingham, U.K. 30th Jan, 2015, http://www.sigmaaldrich.com/catalog/product/sial/436143?lang=en&region=GB (accessed May 2016).

(228) Bales, B. L.; Messina, L.; Vidal, A.; Peric, M.; Nascimento, O. R. Precision Relative Aggregation Number Determinations of SDS Micelles Using a Spin Probe. A Model of Micelle Surface Hydration. *J. Phys. Chem. B* **1998**, *102* (50), 10347-10358.

(229) *Surface Phenomena and Additives in Water-Based Coatings and Printing Technology*; Springer US, **1991**.

(230) Ferry, M. W. Detergent compositions containing amine oxide and nonionic surfactants and polyethylene glycol. Google Patents, 1981.

(231) Jadidi, N.; Adib, B.; Malihi, F. B. Synergism and Performance Optimization in Liquid Detergents Containing Binary Mixtures of Anionic–Nonionic, and Anionic–Cationic Surfactants. *J. Surfactants Deterg.* **2013**, *16* (1), 115-121.

(232) Dashnau, J. L.; Nucci, N. V.; Sharp, K. A.; Vanderkooi, J. M. Hydrogen Bonding and the Cryoprotective Properties of Glycerol/Water Mixtures. *J. Phys. Chem. B* **2006**, *110* (27), 13670-13677.

(233) Blainey, P. C.; Reid, P. J. FTIR studies of intermolecular hydrogen bonding in halogenated ethanols. *Spectrochim. Acta Mol. Biomol. Spectrosc.* **2001**, *57* (14), 2763-2774.

(234) Gonjo, T.; Futami, Y.; Morisawa, Y.; Wojcik, M. J.; Ozaki, Y. Hydrogen Bonding Effects on the Wavenumbers and Absorption Intensities of the OH Fundamental and the First, Second, and Third Overtones of Phenol and 2,6-Dihalogenated Phenols Studied by Visible/Near-Infrared/Infrared Spectroscopy. *J. Phys. Chem. A* **2011**, *115* (35), 9845-9853.

(235) Ahmed, M. K.; Ali, S.; Wojcik, E. The C-O Stretching Infrared Band as a Probe of Hydrogen Bonding in Ethanol–Water and Methanol–Water Mixtures. *Spectrosc. Lett.* **2012**, *45* (6), 420-423.

(236) Imoto, S.; Xantheas, S. S.; Saito, S. Molecular origin of the difference in the HOH bend of the IR spectra between liquid water and ice. *J. Chem. Phys.* **2013**, *138* (5), 054506.

(237) Falk, M. The frequency of the HOH bending fundamental in solids and liquids. *Spectrochim. Acta* **1984**, *40A*, 43-48.

(238) Zhang, J.; Zhang, P.; Ma, K.; Han, F.; Chen, G.; Wei, X. Hydrogen bonding interactions between ethylene glycol and water: density, excess molar volume, and spectral study. *Sci. China Ser. B: Chem.* **2008**, *51* (5), 420-426.

(239) Coker, D.; Reimers, J.; Watts, R. The Infrared Absorption Spectrum of Water. *Austr. J. Phys.* **1982**, *35* (5), 623-638.

(240) Coates, J. Interpretation of Infrared Spectra, A Practical Approach. In *Encyclopedia of Analytical Chemistry*; John Wiley & Sons, Ltd, **2006**.

(241) Egorov, A. V.; Lyubartsev, A. P.; Laaksonen, A. Molecular Dynamics Simulation Study of Glycerol–Water Liquid Mixtures. *J. Phys. Chem. B* **2011**, *115* (49), 14572-14581.

(242) Fifer, R. A.; Schiffer, J. Intramolecular Interactions in the Water Molecule: The Stretch–Stretch Interaction Force Constant of Water Molecules in Hydrogen- Bonded Systems. *J. Chem. Phys.* **1970**, *52*, 2664.

(243) Grabowski, S. J. A new measure of hydrogen bonding strength – ab initio and atoms in molecules studies. *Chem. Phys. Lett.* **2001**, *338* (4–6), 361-366.

(244) Gordy, W. A Relation between Bond Force Constants, Bond Orders, Bond Lengths, and the Electronegativities of the Bonded Atoms. *J. Chem. Phys.* **1946**, *14* (5), 305-320.

(245) Zelent, B.; Nucci, N. V.; Vanderkooi, J. M. Liquid and Ice Water and Glycerol/Water Glasses Compared by Infrared Spectroscopy from 295 to 12 K. *J. Phys. Chem. A* **2004**, *108* (50), 11141-11150.

(246) Chelli, R.; Procacci, P.; Cardini, G.; G. Della Valle, R.; Califano, S. Glycerol condensed phases Part I. A molecular dynamics study. *Phys. Chem. Chem. Phys.* **1999**, *1* (5), 871-877.

(247) Chelli, R.; Procacci, P.; Cardini, G.; Califano, S. Glycerol condensed phases Part II.A molecular dynamics study of the conformational structure and hydrogen bonding. *Phys. Chem. Chem. Phys.* **1999**, *1* (5), 879-885.

(248) Padro, J. A.; Saiz, L.; Guardia, E. Hydrogen bonding in liquid alcohols: a computer simulation study. *J. Mol. Struct.* **1997**, *416*, 243-248.

(249) Root, L.; Stillinger, F. Short-range order in glycerol. A molecular dynamics study. *J. Chem. Phys.* **1989**, *90*, 1200-1208.

(250) Li, X.; Lin, Z.; Cai, J.; Scriven, L. E.; Davis, H. T. Polymer-Induced Microstructural Transitions in Surfactant Solutions. *The Journal of Physical Chemistry* **1995**, *99* (27), 10865-10878.

(251) Tanford, C. *The hydrophobic effect: formation of micelles and biological membranes*; Wiley, **1973**.

(252) Kjellander, R.; Florin, E. Water structure and changes in thermal stability of the system poly(ethylene oxide)-water. *J. Chem. Soc., Faraday Trans. 1* **1981**, *77* (9), 2053-2077.

(253) Tyrode, E.; Johnson, C. M.; Kumpulainen, A.; Rutland, M. W.; Claesson, P. M. Hydration State of Nonionic Surfactant Monolayers at the Liquid/Vapor Interface: Structure Determination by Vibrational Sum Frequency Spectroscopy. *J. Am. Chem. Soc.* **2005**, *127* (48), 16848-16859.

(254) Li, H.; Zhang, W.; Xu, W.; Zhang, X. Hydrogen Bonding Governs the Elastic Properties of Poly(vinyl alcohol) in Water: Single-Molecule Force Spectroscopic Studies of PVA by AFM. *Macromolecules* **2000**, *33* (2), 465-469.

(255) David, S.; Andrew, W.; Jerome, B.; Erik, W. Mechanisms behind surface modification of polypropylene film using an atmospheric-pressure plasma jet. *Plasma Sources Sci. Technol.* **2016**, *25* (6), 065018.

(256) Yang, Q.; Xu, Z.-K.; Dai, Z.-W.; Wang, J.-L.; Ulbricht, M. Surface Modification of Polypropylene Microporous Membranes with a Novel Glycopolymer. *Chem. Mater.* **2005**, *17* (11), 3050-3058.

12. Supporting Information

12.1. Tables of Fitted Values for Ion Beam Experiments

Figure	Sample	IBA Branch	Layer	Thickness /nm	Conc. /at%	Roughness /nm	Z*
Figure 4.6.	30% d_5-glycerol	NRA	1	120	27	13.2	-
Figure 5.3.	25% d_{25}-$C_{12}E_5$	ERDA	1	42	24	3.0	8.8
			2	63	3	1.8	
			3	65	80	2.1	
Figure 5.4.	5% d_{25}-$C_{12}E_5$	NRA	1	10	49	0.2	4.7
			2	157	2	1.6	
			3	8	10	2.6	
	15% d_{25}-$C_{12}E_5$	NRA	1	10	71	1.0	6.8
			2	101	3	0.0	
			3	38	23	2.3	
	25% d_{25}-$C_{12}E_5$	NRA	1	10	77	0.5	7.2
			2	93	5	32.5	
			3	28	44	0.6	
Figure 5.8.	25% d_{25}-$C_{12}E_5$ 0 hours	ERDA	1	41	30	-	11.1
			2	63	3	-	
			3	25	99	-	
	25% d_{25}-$C_{12}E_5$ 1 hours	ERDA	1	42	30	-	12.1
			2	47	1	-	
			3	42	50	-	
	25% d_{25}-$C_{12}E_5$ 3 hours	ERDA	1	50	25	-	12
			2	40	1	-	
			3	43	45	-	
	25% d_{25}-$C_{12}E_5$ 6 hours	ERDA	1	46	25	-	11.0
			2	38	1	-	
			3	39	42	-	
	25% d_{25}-$C_{12}E_5$ 24 hours	ERDA	1	37	27	-	9.6
			2	59	1	-	
			3	44	26	-	
	25% d_{25}-$C_{12}E_5$ 48 hours	ERDA	1	60	16	-	9.0
			2	42	1	-	
			3	34	30	-	

Figure 5.10.	0% h-gly: 30% d_{25}-$C_{12}E_5$	NRA	1	15	95	0.3	13.5
			2	99	5	0.0	
			3	39	23	1.2	
	10% h-gly: 30% d_{25}-$C_{12}E_5$	NRA	1	10	96	0.5	9.2
			2	84	4	7.6	
			3	40	21	1.6	
	20% h-gly: 30% d_{25}-$C_{12}E_5$	NRA	1	10	56	0.5	4.7
			2	98	9	10.8	
			3	36	18	2.9	
	30% h-gly: 30% d_{25}-$C_{12}E_5$	NRA	1	10	69	0.0	6.1
			2	86	8	0.0	
			3	14	28	0.0	
Figure 6.3.	25% CTAB	RBS	1	174	25	19.1	
Figure 6.5.	0% h-gly CTAB	RBS	1	174	25	19.1	
	10% h-gly CTAB	RBS	1	174	25	19.1	
	20% h-gly CTAB	RBS	1	19	44	1.9	
			2	131	15	23.6	
			3	17	59	0.7	
	30% h-gly CTAB	RBS	1	23	42	0.0	
			2	126	13	18.9	
			3	13	71	0.0	
Figure 6.6.	10% d_5-glycerol : 20% CTAB	NRA	1	130	10	0.0	
	20% d_5-glycerol : 20% CTAB	NRA	1	123	20	0.0	
	30% d_5-glycerol : 20% CTAB	NRA	1	147	30	0.0	
Figure 6.8.	20% h-SDS in PVA	RBS	1	10	60	0.0	
			2	242	16	0.0	
Figure 6.10.	10% d_{25}-SDS in PVA	NRA	1	18	23	0.0	
			2	45	2	0.0	
			3	86	5	0.0	
	10% d_{25}-SDS in PVA	NRA	1	19	43	0.0	
			2	111	10	0.0	
Figure 6.13.	20% d_{25}-SDS : 10% h-glycerol in PVA	NRA	1	35	52	0.0	
			2	123	2	0.0	
	20% d_{25}-SDS : 20% h-glycerol in PVA	NRA	1	35	55	0.0	
			2	79	5	0.0	

Figure 6.13.	20% h-SDS : 10% d_5-glycerol in PVA	NRA	1	115	10	0.0	
Figure 6.29.	20% SDBS in PVA	RBS	1	55	47	0.0	
			2	200	13	0.0	
		RBS	1	60	39	0.0	
			2	156	9	0.0	
			3	50	33	0.0	
Figure 6.31.	0% h-C_{12}AO : 20% d_5-glycerol	NRA	1	151	20	0.0	
	2% h-C_{12}AO : 20% d_5-glycerol	NRA	1	145	20	0.0	
	5% h-C_{12}AO : 20% d_5-glycerol	NRA	1	130	20	0.0	
	10% h-C_{12}AO : 20% d_5-glycerol	NRA	1	133	20	0.0	
	20% h-C_{12}AO : 20% d_5-glycerol	NRA	1	124	20	0.0	

12.2. Tables of Fitted Values for NR Experiments

Figure	Sample	Layer	Thickness /nm	SLD $\times 10^{-6}$ /Å^{-2}	Conc. /at. %	Roughness /nm	Z*
Figure 4.8.	10% d_5-glycerol (roughness included)	1	70.67	1.13	-	3.0	-
		2	2.43	3.21	-	0.5	
Figure 5.5.	10% d_{25}-$C_{12}E_5$ (roughness included)	1	0.94	4.40	-	0.2	-
		2	68.65	1.10	-	5.1	
		3	2.07	3.30	-	0.5	
	20% d_{25}-$C_{12}E_5$ (roughness included)	1	2.36	4.28	-	0.5	-
		2	61.28	1.45	-	2.0	
		3	2.01	3.0	-	0.5	
	30% d_{25}-$C_{12}E_5$ (roughness included)	1	1.64	4.68	-	1.0	-
		2	17.68	2.77	-	1.0	
		3	52.35	1.67	-	4.9	
		4	1.01	3.00	-	0.5	
Figure 5.11.	20% d_{25}-$C_{12}E_5$ (roughness included)	1	See Figure 5.5.				
		2					
		3					
	20% d_{25}-$C_{12}E_5$: 20% h-glycerol (roughness included)	1	5.66	2.65	-	4.4	-
		2	50.32	1.34	-	2.5	
		3	2.50	3.5	-	0.5	
	20% h-$C_{12}E_5$: 20% d_5-glycerol (roughness included)	1	2.05	4.82	-	1.5	-
		2	60.91	1.30	-	1.5	
		3	2.01	3.10	-	0.5	
Figure 5.21.	PVA in D_2O (23 %RH) (roughness included)	1	63.5	0.83	-	1.2	-
		2	1.0	4.18	-	1.0	
	PVA in D_2O (33 %RH) (roughness included)	1	68.6	0.80	-	1.3	-
		2	1.4	4.18	-	1.0	
	PVA in D_2O (55 %RH) (roughness included)	1	71.7	0.75	-	1.7	-
		2	1.0	4.18	-	0.9	
	PVA in D_2O (85 %RH) (roughness included)	1	94.6	0.74	-	6.6	-
		2	11.3	4.18	-	1.0	
Figure 5.23.	20% d_{25}-$C_{12}E_5$ at 23 %RH (no roughness)	1	1.7	4.14	92.9	3.0	2.41
		2	1.3	0.75	4.6	0.1	
		3	1.5	3.04	64.2	1.3	
		4	27.7	0.80	5.9	0.1	
		5	3.5	4.18	-	0.6	

Figure 5.23.	20% d_{25}-$C_{12}E_5$ at 33 %RH (no roughness)	1	1.4	4.00	89.2	2.7	2.02
		2	1.4	1.23	17.1	0.2	
		3	1.4	2.65	54.1	0.2	
		4	33.2	0.78	5.4	0.0	
		5	3.5	4.18	-	1.0	
	20% d_{25}-$C_{12}E_5$ at 55 %RH (no roughness)	1	2.4	4.13	92.6	1.2	4.30
		2	1.4	2.72	55.9	0.3	
		3	1.6	4.42	100.0	0.2	
		4	42.8	0.79	5.64	0.0	
		5	2.9	4.18	-	1.4	
	20% d_{25}-$C_{12}E_5$ at 85 %RH (no roughness)	1	1.0	3.60	78.8	0.7	4.18
		2	1.8	0.96	10.1	0.4	
		3	2.3	4.38	99.1	0.2	
		4	0.9	0.90	8.5	0.2	
		5	2.4	3.05	64.5	1.8	
		6	51.8	0.89	8.2	1.8	
Figure 5.24.	20% d_{25}-$C_{12}E_5$: 20% h-glycerol at 23 %RH (no roughness)	1	3.5	4.39	99.9	1.5	3.61
		2	1.6	5.1	27.3	0.1	
		3	0.7	3.70	3.8	0.1	
		4	39.2	0.97	82.0	1.0	
		5	2.2	4.18	-	2.3	
	20% d_{25}-$C_{12}E_5$: 20% h-glycerol at 33 %RH (no roughness)	1	2.7	4.28	97.1	1.8	3.90
		2	0.7	1.22	17.4	0.7	
		3	1.6	4.29	97.3	0.3	
		4	40.3	0.86	8.0	0.2	
		5	3.8	4.18	-	3.2	
	20% d_{25}-$C_{12}E_5$: 20% h-glycerol at 55 %RH (no roughness)	1	4.0	4.39	99.9	1.6	5.45
		2	0.6	0.72	4.4	1.3	
		3	1.7	4.40	100.0	0.0	
		4	49.6	0.72	4.4	0.0	
		5	2.9	4.18	-	1.8	
	20% d_{25}-$C_{12}E_5$: 20% h-glycerol at 85 %RH (no roughness)	1	1.3	4.39	99.9	2.1	4.87
		2	2.2	0.75	5.1	0.1	
		3	2.3	4.39	99.9	0.0	
		4	1.1	0.75	5.1	0.1	
		5	3.0	2.52	51.2	3.5	
		6	57.4	0.72	4.4	0.1	
		7	0.1	4.18	-	0.9	

Figure 5.25.	20% h-$C_{12}E_5$: 20% d_5-glycerol at 23 %RH (no roughness)	1	1.8	3.58	63.6	0.5	0.86
		2	37.6	1.23	15.8	1.7	
		3	0.6	4.18	-	0.7	
	20% h-$C_{12}E_5$: 20% d_5-glycerol at 33 %RH (no roughness)	1	3.0	1.29	17.0	0.6	2.43
		2	1.9	4.19	76.1	0.3	
		3	1.1	1.28	16.8	3.0	
		4	1.3	3.89	69.9	0.5	
		5	40.6	0.87	8.4	2.3	
		6	3.4	4.18	-	2.0	
	20% h-$C_{12}E_5$: 20% d_5-glycerol at 55 %RH (no roughness)	1	2.4	2.45	40.6	0.4	0.52
		2	44.2	1.38	18.8	0.2	
		3	0.1	4.18	-	1.3	
	20% h-$C_{12}E_5$: 20% d_5-glycerol at 85 %RH (no roughness)	1	1.1	1.53	21.9	0.2	0.47
		2	1.9	2.71	45.9	0.1	
		3	2.0	0.71	5.2	1.5	
		4	70.9	1.50	21.3	0.2	
Figure 5.29.	20% d_{25}-$C_{12}E_4$ at 23 %RH (no roughness)	1	1.5	4.67	98.0	0.0	1.31
		2	49.0	1.01	10.4	2.4	
		3	0.8	4.18	-	0.9	
	20% d_{25}-$C_{12}E_4$ at 33 %RH (no roughness)	1	1.6	4.59	96.1	0.0	1.36
		2	48.7	1.03	10.9	2.0	
		3	0.8	4.18	-	0.9	
	20% d_{25}-$C_{12}E_4$ at 55 %RH (no roughness)	1	1.3	4.76	100.0	0.0	1.18
		2	46.3	0.95	9.0	1.6	
	20% d_{25}-$C_{12}E_4$ at 85%RH (no roughness)	1	1.2	4.75	99.9	0.3	1.19
		2	59.6	0.60	0.6	0.8	
		3	0.1	4.18	-	1.2	
Figure 5.30.	20% d_{25}-$C_{12}E_6$ at 23 %RH (no roughness)	1	0.9	3.23	74.6	0.3	2.99
		2	1.1	1.08	14.2	0.1	
		3	2.9	4.03	97.1	5.8	
		4	44.7	1.05	13.4-	1.7	
	20% d_{25}-$C_{12}E_6$ at 33 %RH (no roughness)	1	0.9	3.31	76.9	0.3	2.66
		2	1.1	1.28	19.8	0.5	
		3	3.2	3.41	79.7	0.4	
		4	47.4	1.12	15.4	2.3	
		5	15.8	4.18	-	0.0	

Figure 5.30.	20% d_{25}-$C_{12}E_6$ at 55 %RH (no roughness)	1	1.1	3.16	72.7	0.5	2.71
		2	1.0	0.63	1.6	0.5	
		3	2.3	4.28	99.9	0.4	
		4	48.6	0.98	11.4	2.3	
		5	1.7	4.18	-	0.0	
	20% d_{25}-$C_{12}E_6$ at 85 %RH (no roughness)	1	2.8	4.07	98.5	0.3	4.92
		2	0.7	0.16	0.0	1.4	
		3	2.3	4.13	99.9	0.3	
		4	65.7	0.67	2.7	3.6	
Figure 5.32.	20% d_{25}-$C_{12}E_4$: 20% h-glycerol at 23 %RH (no roughness)	1	2.2	4.73	99.9	0.4	2.52
		2	0.8	0.70	3.5	0.8	
		3	2.0	2.00	34.6	0.0	
		4	36.4	0.92	8.8	1.4	
	20% d_{25}-$C_{12}E_4$: 20% h-glycerol at 33 %RH (no roughness)	1	2.0	4.73	99.9	1.3	1.91
		2	0.9	0.92	8.8	0.2	
		3	2.0	1.54	23.6	0.3	
		4	40.8	1.14	14.1	0.3	
	20% d_{25}-$C_{12}E_4$: 20% h-glycerol at 55 %RH (no roughness)	1	1.9	4.73	99.9	0.3	2.01
		2	1.4	0.45	0.0	1.8	
		3	1.7	2.10	37.0	0.4	
		4	51.2	1.16	14.5	4.7	
	20% d_{25}-$C_{12}E_4$: 20% h-glycerol at 85 %RH (no roughness)	No data					
Figure 5.33	20% h-$C_{12}E_4$: 20% d_5-glycerol at 23 %RH (no roughness)	1	2.2	3.28	57.7	0.6	0.86
		2	2.5	1.10	13.3	0.6	
		3	35.7	1.36	18.6	0.1	
	20% h-$C_{12}E_4$: 20% d_5-glycerol at 33 %RH (no roughness)	1	2.8	2.99	51.8	0.5	0.92
		2	2.3	0.33	0.0	2.4	
		3	36.2	1.38	19.0	0.5	
		4	0.1	4.18	-	1.2	
	20% h-$C_{12}E_4$: 20% d_5-glycerol at 55 %RH (no roughness)	1	2.9	2.39	39.6	0.8	0.56
		2	1.4	0.74	6.0	0.1	
		3	43.1	1.45	20.5	0.1	
	20% h-$C_{12}E_4$: 20% d_5-glycerol at 85 %RH (no roughness)	1	2.8	2.32	38.2	0.6	0.65
		2	2.4	0.98	10.9	0.7	
		3	51.1	1.18	15.0	0.6	
		4	0.4	4.18	-	1.6	

Figure 5.34.	20% d_{25}-$C_{12}E_6$: 20% h-glycerol at 23 %RH (no roughness)	1	5.1	2.54	55.8	1.3	2.49
		2	31.3	0.80	7.0	1.6	
		3	1.7	4.18	-	0.4	
	20% d_{25}-$C_{12}E_6$: 20% h-glycerol at 33 %RH (no roughness)	1	1.6	2.73	61.2	0.7	2.59
		2	0.8	0.97	11.7	0.9	
		3	2.5	3.30	77.2	0.5	
		4	31.9	0.85	8.4	1.9	
		5	1.8	4.18	-	0.0	
	20% d_{25}-$C_{12}E_6$: 20% h-glycerol at 55 %RH (no roughness)	1	2.1	2.05	42.1	0.1	3.10
		2	0.8	1.14	16.5	1.3	
		3	3.5	3.13	72.4	0.1	
		4	38.1	0.80	7.0	2.0	
		5	1.4	4.18	-	0.0	
	20% d_{25}-$C_{12}E_6$: 20% h-glycerol at 55 %RH (no roughness)	1	2.5	3.67	87.6	0.1	3.89
		2	1.5	0.70	4.1	0.0	
		3	2.0	3.92	94.6	0.1	
		4	48.4	0.70	4.1	2.1	
Figure 5.35.	20% h-$C_{12}E_6$: 20% d_5-glycerol at 23 %RH (no roughness)	1	1.9	3.01	51.9	3.2	0.63
		2	40.6	1.39	18.9	0.6	
	20% h-$C_{12}E_6$: 20% d_5-glycerol at 33 %RH (no roughness)	1	1.9	2.57	42.9	3.0	0.43
		2	47.9	1.45	20.1	0.7	
	20% h-$C_{12}E_6$: 20% d_5-glycerol at 55 %RH (no roughness)	1	2.0	2.71	45.7	0.6	0.56
		2	49.7	1.33	17.6	0.5	
	20% h-$C_{12}E_6$: 20% d_5-glycerol at 85 %RH (no roughness)	1	1.1	1.97	30.7	5.5	0.29
		2	63.8	1.41	19.3	0.3	
		3	1.4	4.18	-	0.9	
Figure 6.11.	5% d_{25}-SDS (roughness included)	1	2.8	4.55	68.2	1.0	-
		2	88.8	1.02	7.7	1.2	
		3	0.3	4.18	-	2.8	
	10% d_{25}-SDS (roughness included)	1	4.6	5.79	89.5	0.5	-
		2	95.2	0.81	4.1	0.2	
		3	0.3	4.18	-	4.2	
	20% d_{25}-SDS (roughness included)	1	4.6	5.49	84.3	0.3	-
		2	11.5	0.97	6.8	0.3	
		3	83.4	1.84	21.7	0.2	
		4	0.2	4.15	-	0.4	

Figure 6.12.	20% d_{25}-SDS at room temperature (roughness included)	1	4.3	4.98	75.6	0.6	-
		2	10.6	1.24	11.4	0.5	
		3	68.4	1.91	22.9	0.5	
		4	0.2	4.18	-	0.7	
	20% d_{25}-SDS at 35 °C (roughness included)	1	4.4	4.94	74.9	0.6	-
		2	9.6	1.26	11.8	0.4	
		3	64.2	1.97	24.0	0.6	
		4	0.2	4.18	-	0.7	
	20% d_{25}-SDS at 45 °C (roughness included)	1	4.3	5.08	77.3	0.7	-
		2	9.5	1.23	11.3	0.5	
		3	63.4	1.99	24.3	0.6	
		4	0.2	4.18	-	0.7	
Figure 6.14.	5% d_{25}-SDS : 20% h-glycerol at room temperature (roughness included)	1	4.4	4.76	72.2	0.5	-
		2	83.5	0.90	6.0	0.2	
		3	0.3	4.18	-	2.9	
	10% d_{25}-SDS : 20% h-glycerol at room temperature (no roughness)	1	2.5	5.59	86.4	1.2	-
		2	0.3	0.92	6.3	2.2	
		3	4.6	5.60	86.6	0.4	
		4	64.2	0.89	5.8	0.5	
		5	0.3	4.18	-	1.8	
	20% d_{25}-SDS : 20% h-glycerol at room temperature (no roughness)	1	2.8	5.75	89.1	0.3	-
		2	0.8	0.84	4.9	2.4	
		3	3.3	5.84	90.7	0.9	
		4	0.8	2.64	35.8	3.9	
		5	2.9	5.92	92.1	0.3	
		6	0.7	3.15	44.6	2.9	
		7	5.9	5.91	91.9	0.3	
		8	1.5	1.71	19.9	0.9	
		9	60.0	0.63	1.3	1.5	
		10	0.2	4.18	-	3.4	
Figure 6.15.	20% h-SDS : 20% d_5-glycerol 1 Excess (no roughness)	1	1.7	0.40	0.0	0.6	-
		2	0.9	4.60	69.4	0.6	
		3	1.5	0.74	3.2	1.2	
		4	62.6	1.59	17.8	0.0	
		5	0.0	4.18	-	0.9	

Figure 6.15.	20% h-SDS : 20% d_5-glycerol 2 Excess (no roughness)	1	1.2	0.33	0.0	0.5	-
		2	0.9	4.81	73.0	0.6	
		3	2.7	0.88	5.6	0.3	
		4	0.9	4.40	66.0	0.5	
		5	1.7	0.70	2.5	0.4	
		6	58.9	1.58	17.6	0.0	
		7	0.0	4.18	-	0.7	
	20% h-SDS : 20% d_5-glycerol 3 Excess (no roughness)	1	1.6	0.36	0.0	0.3	-
		2	1.1	4.06	60.2	0.3	
		3	3.0	0.62	1.2	0.5	
		4	0.9	5.04	77.0	0.9	
		5	2.7	0.65	1.7	0.3	
		6	0.8	4.44	66.7	0.2	
		7	2.1	0.68	2.2	0.5	
		8	54.9	1.60	18.0	0.2	
		9	0.0	4.18	-	0.8	
	20% h-SDS : 20% d_5-glycerol 4 Excess (no roughness)	1	2.2	0.36	0.0	0.2	-
		2	1.0	3.64	53.0	0.2	
		3	3.2	0.69	2.4	0.2	
		4	0.9	4.57	68.9	1.5	
		5	2.6	0.70	2.5	0.2	
		6	1.0	4.30	64.3	0.5	
		7	2.7	0.41	0.0	0.3	
		8	1.0	3.59	52.1	0.2	
		9	2.3	0.77	3.7	0.6	
		10	50.4	1.58	17.6	0.2	
		11	0.05	4.18	-	0.9	
Figure 6.24	20% d_{25}-SDS 23 %RH (no roughness)	1	1.6	6.41	100.0	1.4	-
		2	0.1	1.44	15.2	2.4	
		3	4.7	6.07	94.6	0.3	
		4	18.2	1.10	9.4	1.6	
		5	32.5	1.65	18.8	2.8	
		6	0.3	4.18	-	0.8	
	20% d_{25}-SDS 33 %RH (no roughness)	1	1.7	6.40	100.3	1.1	-
		2	0.7	0.69	2.4	1.6	
		3	4.1	6.40	100.3	0.4	
		4	7.2	1.10	9.4	2.2	
		5	34.8	1.44	15.2	7.4	

Figure 6.24.	20% d_{25}-SDS 55 %RH (no roughness)	1	6.6	6.05	94.3	1.8	-
		2	20.5	0.78	3.9	1.0	
		3	32.0	1.55	17.1	6.0	
		4	0.1	4.18	-	0.8	
	20% d_{25}-SDS 85 %RH (no roughness)	1	1.0	3.49	50.4	0.0	-
		2	1.6	1.40	14.5	0.3	
		3	9.8	5.77	89.5	0.9	
		4	16.4	1.08	9.0	0.9	
		5	43.1	1.38	14.2	0.0	
Figure 6.25	20% d_{25}-SDS : 20% h-glycerol 23 %RH (no roughness)	1	5.0	6.40	100.3	0.5	-
		2	0.2	1.50	16.3	0.6	
		3	3.2	6.40	100.3	1.4	
		4	36.5	1.0	7.7	1.5	
	20% d_{25}-SDS : 20% h-glycerol 33 %RH (no roughness)	1	3.2	6.40	100.3	2.1	-
		2	0.3	0.90	6.0	1.6	
		3	4.6	6.03	94.0	0.8	
		4	0.6	1.06	8.7	0.3	
		5	2.2	5.76	89.3	2.0	
		6	38.9	1.09	9.2	1.6	
	20% d_{25}-SDS : 20% h-glycerol 55 %RH (no roughness)	1	5.0	6.03	94.0	0.9	-
		2	0.4	1.04	8.4	0.7	
		3	2.6	6.40	100.3	2.5	
		4	0.4	1.04	8.4	0.3	
		5	1.5	6.40	100.3	1.7	
		6	43.5	1.08	9.0	1.5	
Figure 6.26	20% h-SDS : 20% d_5-glycerol 23 %RH (no roughness)	1	3.1	0.72	4.53	0.2	-
		2	1.0	3.51	61.36	0.7	
		3	1.5	0.77	5.55	0.1	
		4	39.3	1.59	22.25	0.0	
	20% h-SDS : 20% d_5-glycerol 33 %RH (no roughness)	1	2.9	0.53	0.66	0.0	-
		2	1.5	2.19	34.47	0.3	
		3	1.4	0.47	0.0	0.2	
		4	41.8	1.53	21.03	0.0	

Figure 6.26.	20% h-SDS : 20% d_5-glycerol 55 %RH (no roughness)	1	1.0	1.41	18.59	0.3	-
		2	2.5	0.85	7.18	1.1	
		3	2.4	2.31	36.92	0.9	
		4	2.0	0.45	0.0	0.0	
		5	40.0	4.18	-	1.2	
	20% h-SDS : 20% d_5-glycerol 85 %RH (no roughness)	1	1.1	0.88	7.79	0.0	-
		2	0.6	2.21	34.88	1.5	
		3	66.6	0.73	4.74	0.0	

12.3. NR Roughness Considerations

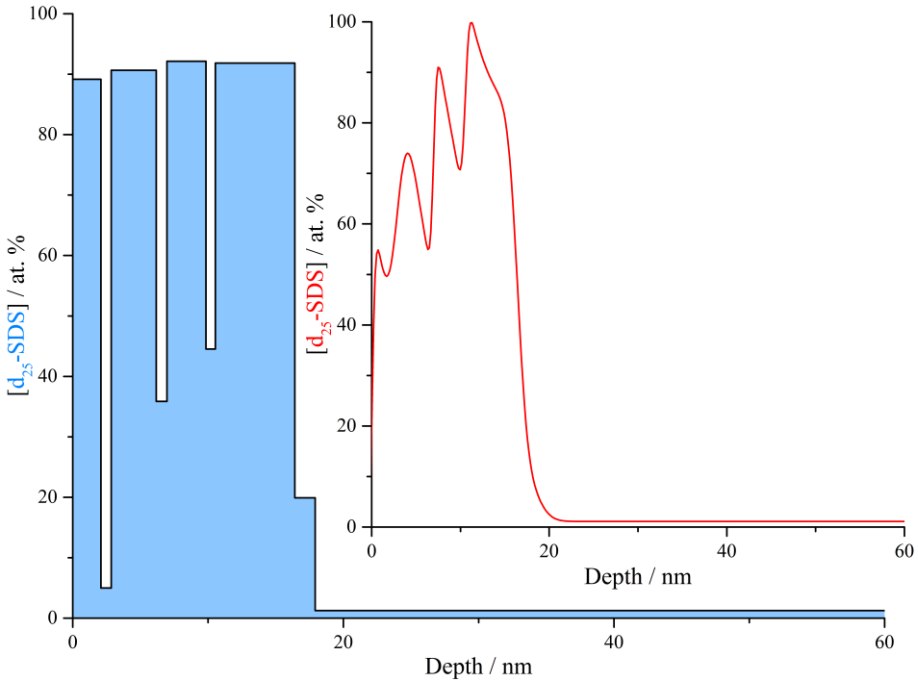

Figure 12.1. Example of NR plot with (inset) and without roughness parameter